An optimized hybrid data reduction strategy in 1D Raman/Rayleigh spectroscopic measurements of turbulent flames

Vom Fachbereich Maschinenbau
an der Technischen Universität Darmstadt
zur
Erlangung des Grades eines Doktor-Ingenieurs (Dr.-Ing.)
genehmigte

D i s s e r t a t i o n

vorgelegt von

M.Sc. Nicola Luciano

aus Neapel, Italien

Berichterstatter:	Prof. Dr.-Ing. C. Hasse
Mitberichterstatter:	Prof. Dr. G. Continillo
Mitberichterstatter:	Prof. Dr. N.J. Dam
Tag der Einreichung:	18.02.2019
Tag der mündlichen Prüfung:	12.06.2019

Darmstadt 2019
D17

Luciano, Nicola: An optimized hybrid data reduction strategy in 1D Raman/Rayleigh spectroscopic measurements of turbulent flames

Darmstadt, Technische Universität Darmstadt,
Year thesis published in TUprints: 2020
Date of the viva voce 12.06.19

NNT : 2019SACLC026

THÈSE DE DOCTORAT DE L'UNIVERSITÉ PARIS-SACLAY ET DE TECHNISCHE UNIVERSITÄT DARMSTADT

préparée à CentraleSupélec.

ÉCOLE DOCTORALE N^{o}579

Sciences mécaniques et énergétiques, matériaux et géosciences.

Spécialité Combustion.

Présentée par

Nicola Luciano

An optimized hybrid data reduction strategy in 1D Raman/Rayleigh spectroscopic measurements of turbulent flames

Thèse soutenue à Darmstadt (Allemagne), le 12/06/2019.

Composition du jury:

Prof. Schiffer, H.P., Professor, Technische Universität Darmstadt, President
Prof. Hasse, C., Professor, Technische Universität Darmstadt, Rapporteur
Prof. Continillo, G., Professor, Università degli Studi del Sannio, Rapporteur
Prof. Dam, N.J., Associate Professor, Technische Universität Eindhoven, Rapporteur
Prof. Fiorina, B., Professor, CentraleSupélec, Paris-Saclay, Directeur de these
Prof. Dreizler, A., Professor, Technische Universität Darmstadt, Directeur de these
Prof. Schabel, S., Professor, Technische Universität Darmstadt, Examinateur
Dr. Renaud, A., Maître de conférences, CentraleSupélec, Paris-Saclay, Examinateur

Laboratoire d'Énergétique Moléculaire et Macroscopique, Combustion
CNRS, CentraleSupélec.

Erklärung

Hiermit erkläre ich an Eides statt, dass ich die vorliegende Dissertation selbstständig verfasst und keine anderen als die von mir angegebenen Hilfsmittel verwendet habe. Ich erkläre außerdem, dass ich bisher noch keinen Promotionsversuch unternommen habe.

Nicola Luciano

Darmstadt, 18.02.2019

Preface

This thesis is the result of my time as doctoral candidate in a European joint doctorate project. The institute of Reactive Flows and Diagnostics (RSM) of the Technische Universität Darmstadt has represented my main establishment, where I have conducted a considerable part of my research and my studies. The Macroscopic Molecular Energy and Combustion Laboratory (EM2C) of CentraleSupélec has hosted me for a not less relevant part of my work. In both the establishments I have found extraordinary environments, with highly qualified researchers and scientists. For this reason, my deepest gratitude goes to Prof. Andreas Dreizler (RSM), who has made possible every single result of my work, representing a limitless source of knowledge, and to Prof. Benoît Fiorina (EM2C), who has given a significant contribution to my research in what has been probably the most crucial part of it. A special acknowledgement goes to Prof. Dirk Geyer, for sharing his exceptional knowledge on Raman spectroscopy and on its data evaluation. First among the colleagues, I wish to thank Dr.-Ing. Silvan Schneider, M.Sc. David Butz and M.Sc Johannes Trabold, who have been members, with me, of the "Raman Group" at the RSM institute; Dr.Ing. Schneider has guided me in the first period of my permanence at the institute; M.Sc. Butz and M.Sc. Trabold made possible this thesis with the huge effort they've put in conducting the measurement campaign at the combustion laboratories of the Technische Universität Darmstadt, whose results are presented in this thesis. Thanks to all the colleagues who, at the RSM and EM2C, contributed in making my permanence at the institutes nice and enjoyable, and at the same time proposing discussions of high interest.

My staying at the RSM institute and at the EM2C laboratory would have not been the same without the many friends I've met during the past years. All of them share with me a small part of this work. A special thanks goes to the Darmstadt Italian/Latinos crew, who recreated a familiar environment in which I've always found a reference. All the many friends who contributed to make my staying in Paris unforgetable merit a particular mention. After the years in Benevento, Giampaolo and Lorella proved me that true friendship knows how to last through years and kilometers. With Alfredo I've shared what have been the most astonishing adventures in Paris, and with him I've discovered secrets and views of the city and its life. *Merci*.

Lastly, I am grateful that the amazing experiences I've done in these years have always been encouraged by my family's unconditioned love. My parents, my sisters and my loved ones made all they could to show me their support. Marta has given all her love in daring to put hundreds of kilometers between us, believing that the wind blows off weak flames, but it stokes vigorous fires up.

Nicola Luciano
Darmstadt, February 2019

Marco Polo descrive un ponte, pietra per pietra.

"Ma qual è la pietra che sostiene il ponte?" chiede Kublai Khan.

"Il ponte non è sostenuto da questa o quella pietra," risponde Marco, "ma dalla linea dell'arco che esse formano."

Kublai Khan rimane silenzioso, riflettendo. Poi soggiunge: "Perché mi parli delle pietre? È solo dell'arco che mi importa."

Polo risponde: "Senza pietre non c'è arco."

Italo Calvino, Le Città Invisibili

Marco Polo describes a bridge, stone by stone.

"But which is the stone that supports the bridge?" Kublai Khan asks.

"The bridge is not supported by one stone or another," Marco answers, "but by the line of the arch that they form."

Kublai Khan remains silent, reflecting. Then he adds: "Why do you speak to me of the stones? It is only the arch that matters to me."

Polo answers: "Without stones there is no arch."

Italo Calvino, Invisible Cities

Contents

List of Tables

List of Figures

Nomenclature

Uppercase Latin letters

$\mathbb{R}$	Real number set	
$\mathbf{S}$	Raman signal	
C_i	Concentration of species i	$\mathrm{kg/m^3}$
I_{Ram}	Raman scattering signal intensity	J
I_{Ray}	Rayleigh scattering signal intensity	J
J	Molecule rotational level	
N	Number density	$\mathrm{m^{-3}}$
R	Universal gas constant	8.314 J/(mol K)
S_{Conv}	Molecule convoluted Raman spectra	
S_{Stick}	Molecule stick Raman spectra	
T	Temperature	K
X	Mole fractions	-
Y	Mass fractions	-

Lowercase Latin letters

$\mathbf{p}$	Electric dipole momentum	C m
$\mathbf{q}$	Molecular nuclear displacement	m
$c_{ij}(T)$	Raman response / crosstalk function	
h	Plank constant	6.62607×10^{-34} J s
k_{ij}	Raman matrix tuner	
p	Pressure	bar
r	Radial coordinate in experiment	mm
z	Axial coordinate in experiment	mm

Greek letters

Γ_{app}	System apparatus function	
ν	Molecule vibrational level	
ϕ	Equivalence ratio	-
ρ	Density	kg/m^3

Dimensionless Numbers

Da	Damköhler number
Ka	Karlovitz number
Le	Lewis number
Re	Reynolds number

Abbreviations

ACR	Automated Calibration Routine
CS	Convoluted Raman spectra
FF	Flat Flame (Burner)
Fl.C	Target flame C
Fl.D	Target flame D
MI	Matrix inversion method
SF	Spectral fitting method
VF	Vertical Flame (Burner)

Chapter 1

Introduction

Motivation

The world gross inland consumption of natural gas in 2005 was 2359 Mtoe and 3035 Mtoe in 2016, with an increase of about 20%. In 2016, it represented 22% of the global consumption, being the third source after petroleum and solid fuels. In EU-28 its role is even more relevant, covering 23.4% of gross inland consumption [1].

Over the past decades the scientific community has risen an alarm about the anthropogenic impact on the biosphere. According to the Intergovernmental Panel on Climate Change [2] (IPCC), "human activities are estimated to have caused approximately 1.0 °C of global warming above pre-industrial levels, with a likely range of 0.8 °C to 1.2 °C. Global warming is likely to reach 1.5 °C between 2030 and 2052 if it continues to increase at the current rate.". The studies conducted by the IPCC predict, among the others, a strong impact of the global warming on hot extremes in most inhabited regions and on the probability increase of drought and precipitation deficits in some regions.

The 21th Conference Of Parties (COP 21) within the UN Framework on Climate Change (UNFCCC), also known as the 2015 Paris Climate Conference, has marked an important milestone in the path to limit the impact of human activities on the biosphere. The proposed "Paris Agreement" has been signed by 174 countries, committed to pursue efforts to limit the temperature increase to 1.5 °C.

Being fossil fuels combustion among the primary sources of CO_2 emissions [3], which is believed to be connected to the mentioned anthropogenic global warming, combustion of hydrocarbons is a key topic in this context. Among different fossil fuels, natural gas, which consists primarily of methane[1], plays a fundamental role. Indeed, according to U.S. Energy Information Administration estimates, the combustion of natural gas produces about 52.7 kg of CO_2 per kJ of converted energy, while diesel fuel and coal contribute to the emission of about 72.6 and 98.5 kg of CO_2 per kJ of energy, respectively.

With that being said is clear that, on one side, fossil fuels represent still a fundamental part of the world energy mix, on the other side they have a strong environmental impact. With its reduced impact, compared to other fossil fuels, natural gas represents at the moment a key fuel in the global scenario.

In the applications where methane is used as fuel in combustion processes, very often turbulent flows are involved. This is on one side a desired effect, given that in

[1] Natural gas consists primarily of methane together with a number of other constituents. [4]

a turbulent flow several intrinsic physical mechanisms might be beneficial for specific applications. Indeed, fundamental phenomena for the combustion processes, such as mixing or heat exhange, are enhanced within turbulent flow fields. On the other side, in many cases the presence of turbulent flows is unavoidable for several reasons. For example, the thermal energy converted from the chemical one by the reactions may generate flow instabilities leading to the transition to turbulent conditions [5].

Clearly, turbulent combustion has a leading role in the modern technological scenario, and will keep it for the foreseeable future. Increasing the efficiency of the processes is a priority for many sectors, from industry, to power generation and transportation. This goal originates from two fundamental reasons: increasing efficiency would lead to reducing fuel consumption, with economical and strategic benefits; also, it is important to keep on reducing pollutant emissions, to compete with increasingly stringent regulations.

State of the Art

In the field of combustion, turbulent premixed regimes are topics of great interest, given their wide use in technical applications. To have an idea about how spread is their utilization, it is sufficient to consider that spark-ignition engines, for example, operate in these conditions. Despite a context of advanced technological and industrial employment, "the progress made by combustion science is much less impressive, especially as far as premixed turbulent flames are concerned" [6].

The complexity of turbulent premixed regimes is the main reason behind the difficulty in fully understanding the phenomena involved. A variety of sub-processes are present in turbulent premixed combustion, and their interaction adds even more complications. The sub-processes composing the complete problem may be divided into two classes: fluid dynamic-related and chemistry-related. Dedicated studies are focused on the two classes alone, as well as on their interaction, investigating configurations with increasing level of complexity. Target flames are established to gain knowledge about turbulence-chemistry interaction [7]. The most simple cases are based on jet flames [8]. Bluff-bodies positioned within the flow [9,10] or the use of pilot flames [11–13] add elements of complexity. Swirl flows are even more complex [14,15]. Imposing a stratification in the flow is a further step [9,12,13,15–17]. Basic configurations in terms of kinetics are represented by hydrogen/air flames [18,19]. The use of hydrocarbons as fuels add a significant component of difficulty, increasing with the complexity of the molecules [7].

In the context of turbulent combustion, multiscalar measurements are highly valuable [7,20]. Thanks to simultaneous information about relevant quantities, such as temperature and species, insights in the flame structures may be gained. Among the different techniques available, simultaneous Raman/Rayleigh spectroscopy is one of the most advanced [21], being able to provide quantitative information about major species and temperature in turbulent hydrocarbon flames [22–24] with satisfying spatial resolution [25] and reduced interference on the investigated flames.

Objectives

Being a pioneer technique with respect to others employed for diagnostics in turbulent combustion, the application of simultaneous Raman/Rayleigh spectroscopy in this context cannot take advance of well established strategies for data reduction. Each application has its own implementation of the reduction strategy, as it will be clarified in chapter 3.

In this thesis, a new data processing strategy is developed, presented and analyzed. It will be demonstrated that significant benefits are obtained thanks to the new routine. Among them, it will be shown that the new routine includes a more rigorous system calibration procedure. Moreover, a relevant reduction of the data processing time will be observed. The developed routine has been tested against different test cases and its performance compared with other data processing routines. The results of the testing are presented in chapter 4. Moreover, the new routine has been applied to two target flames investigated thanks to an experimental campaign. The flames are turbulent premixed methane/air jet flames, and the results of a study conducted on the base of their experimental investigations are presented in chapter 5. While Raman/Rayleigh diagnostics have been applied to several studies of non-premixed and partially premixed flames, a relatively reduced number of studies on premixed flames is available [11], especially considering the recent advances in the technique capabilities in terms of spatial resolution and measurement precision. Few works with appropriate characteristics for investigation of the instantaneous internal scalar structure of turbulent premixed flames are available in literature, including [10, 11]. In the mentioned studies, bluff-body stabilized flames are investigated. In this thesis, the turbulent premixed flames are anchored to the Darmstadt Stratified Burner [12] thanks to a pilot flame, specifically designed and implemented for a reduced impact on the target flame. The absence of the bluff-body removes a series of interferences on the target flames, including possible heat exchange and fluid internal recirculation.

Thesis Structure

This thesis is organized into four main chapters, preceded by this introduction and followed by the final conclusions. The content of the main chapters is summarized in the following:

Chapter 2 The fundamental principles on which this work is based are presented. An overview of the physics background of the Raman/Rayleigh spectroscopy is presented. A second part of the chapter is dedicated to physics of premixed combustion in the gas phase, with a specific focus on turbulent premixed cases. Fundamentals of fluid dynamics of turbulent flows are included as well.

Chapter 3 The methodology applied for the data processing of single shot 1-D Raman/Rayleigh measurements is detailed and the calibration procedure is introduced. Also, a brief description of a typical test rig necessary to apply the technique in turbulent combustion diagnostics is included.

Chapter 4 This chapter presents the modified calibration routine for data processing of single shot Raman/Rayleigh spectroscopy applied in turbulent combustion,

based on optimization techniques. The data processing system is characterized in order to identify the most effective optimization method. A mathematical structure is given to the calibration of the data processing system. Finally, the proposed routine is described and its performances are tested in different data sets. A short overview about principles of most widely used optimization techniques and algorithms is included at the beginning of the chapter, for better understanding the implemented routine.

Chapter 5 The results of an experimental investigation conducted on a turbulent premixed methane/air flame are shown. The data set analyzed is acquired with the introduced measurement technique, and the data processing system is calibrated with the proposed modified routine. Preliminary results on a second turbulent premixed methane/air flame are presented.

Conclusions A summary of the conclusions of this work is provided, with reference to the modified calibration routine and to the investigated flames. Key aspects for future investigations are proposed.

Chapter 2

Physics Background

Summary

This chapter provides an overview of the theoretical principles on which this thesis is based.

A background of the physics underlying the Raman/Rayleigh scattering processes is included in sec.2.1, followed by a focus on the state of the art for the applications of Raman/Rayleigh spectroscopy in turbulent combustion diagnostics in sec.2.2. The theoretical background is mostly based on the works by Smith and Dent [26] and by Ferraro, Nakamoto and Brown in [27].

In sec.2.3 the focus is on turbulent premixed combustion. A basic theory describing reactions in gas mixtures is provided, followed by the fundamentals of turbulent reactive flows.

2.1 Physics Background of Raman/Rayleigh scattering

For a better understanding of the Raman and Rayleigh processes it is reasonable to start with an explanation of the energy levels in a molecule. It is beyond the interest of this paragraph to detail the theory supporting the representation reported below, rather a brief overview is presented for a simple diatomic molecule. This overview is preceded with details about the vibrations of a molecule. An introduction on the energy levels in a molecule, sec.2.1.2, will guide to the basics of Raman/Rayleigh scattering, sec.2.1.3.

2.1.1 Molecular vibrations

If a molecule has N atoms, it can have a maximum of $3N$ degrees of freedoms to describe its motion in the three dimensional space. Three of these degrees of freedom are taken up to describe the rigid translation of the molecule and three to describe rotational movements about the three principal axes of rotation, which pass through the center of gravity (except for linear molecules, where only two rotations are possible). As a consequence, the number of vibrational degrees of freedom is $3N - 6$ for all molecules, while it is $3N - 5$ for the linear ones. This number also corresponds to the number of possible vibrations of a molecule. A diatomic molecule will then show only one vibration (a stretch along the bond between the two atoms), while 3-atoms molecules can have three vibration modes: symmetrical and asymmetrical stretch, plus a bending

or deformation mode. This last example is illustrated in fig.2.1 for CO_2 and H_2O molecules.

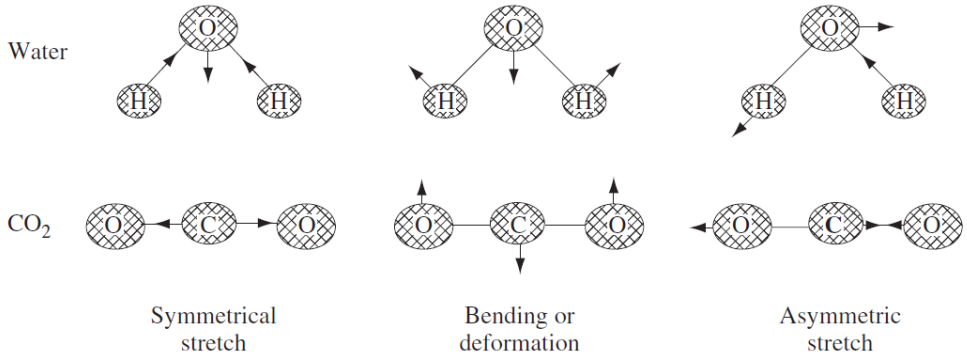

Figure 2.1: Representation of the three vibrational modes for H_2O and CO_2, representing a non-linear and a linear molecule, respectively. The bending for deformation takes place in two directions: parallel and perpendicular to the represented plane. Reproduced from [26]

The vibrations of the molecule can have more complex patterns than the ones shown in fig.2.1, due to the superposition of different motions, but it will always be possible to decompose the pattern into a superposition of the basic modes.

When the molecules have a more complex structure, for example with an increasing number of atoms, the vibration modes can be harder to find. Usually the group theory and symmetry analogies are used to help the analysis.

To have an estimation of the order of magnitude of the energy involved in a molecular vibration, it is possible to use a simplification, modelling a diatomic molecule as a mass-spring system. This approach is referred to as "harmonic approximation". The most simple mass-spring system can be solved following the classic theory of the harmonic oscillator, as explained by Feynmann in his Lectures on Physics [28].

A slightly more complex system, closer to the condition of the diatomic molecule, is shown by Ferraro et al. [27], and is composed of two masses m_1 and m_2, representing the two atoms, connected by a linear spring which is a representative of the chemical bond. A schematic representation of this system is reported in fig. 2.2. It is possible

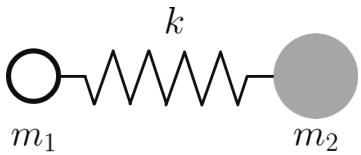

Figure 2.2: Representation of a diatomic molecule modelled as a two masses - spring system.

to demonstrate that the frequency of the system's motion is given by [26]:

$$f_0 = \frac{1}{2\pi}\sqrt{\frac{k}{\mu}} \tag{2.1}$$

where μ is a "reduced mass" of the system and k is characteristic of the spring. Equation (2.1) makes it easy to understand the relative order of the energies of specific vibrations. In [26] it is highlighted indeed that the lighter the atoms, the higher the frequency will be. Thus, for example, C–H vibrations are at higher frequencies than C–I vibrations, being the H atom lighter than the I atom. The force constant k is a measure of bond strength. The stronger the bond, the higher the frequency will be.

In addition to vibrations, molecules can undergo other types of motions. In the context of this thesis, rotations have a primary relevance. Different models can be used to describe rotational motions of molecules. The rigid rotor is typically the most simple one [29]. It assumes a diatomic molecule to be rotating about its center of mass, with the bond behaving like a rigid connection between the atoms. Of course this is a rude approximation and molecules exhibit non-rigid rotations. In addition to that, interactions between rotations and vibrations are present, and have to be properly taken into account. Indeed, these interactions are so relevant that it is common to describe molecular spectra in terms of "rovibrational" models.

2.1.2 Energy levels in a molecule

Figure 2.3 schematically represents the energy levels of a diatomic molecule, reported as segments. The levels marked with the letter ν are vibrational levels, while the J is for the rotational levels. The electronic transitions are in reality much more spaced than what is shown in the figure, while the rotational levels are much closer. It is possible to notice that for each electronic state (long horizontal lines), there are several vibrational levels ν (medium-length lines); for each vibrational levels, several rotational levels J are present (short lines).

The actual energy levels of the molecule are described by the Morse potential diagram, in which the potential energy of the molecule is plotted against the internuclear distance. This representation is more accurate than the one in fig.2.3, which is indeed a simple schematic diagram. An example of Morse potential is reported in fig.2.4 for an electronic state of a diatomic molecule. The vibrational levels are indicated by the ν, and for each of the ν there is a set of sub-levels, each corresponding to one rotational level (not shown in the figure).

Since Raman scattering is fast compared to the time fo the nuclear movements [26], there is no appreciable change in the nuclear separation during any of the scattering events. Thus, in the Morse potential representation of fig.2.4, there is no variation along the x-axis. As a consequence, for a simple description of the process the simplified representation of fig.2.3 is used, with energy changes in the molecule plotted as vertical lines and states as horizontal lines. The organization of the energy levels in terms of electronic, vibrational and rotational are the same as the Morse case.

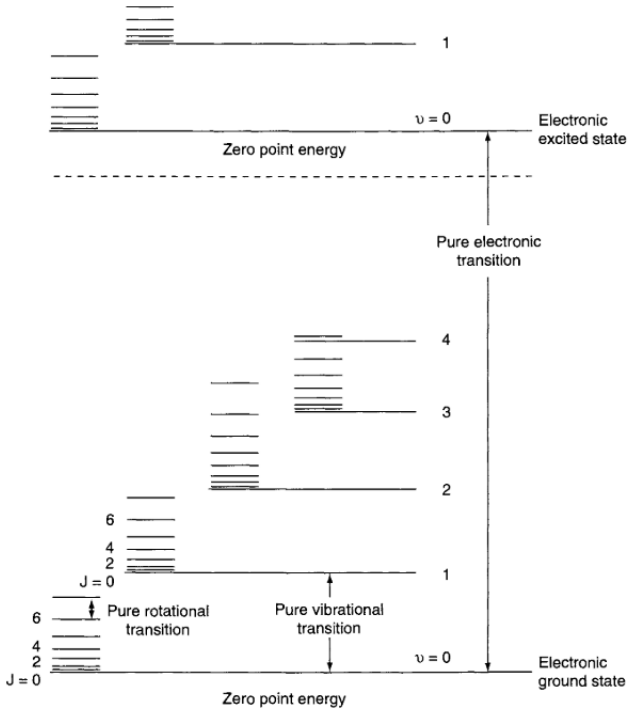

Figure 2.3: Schematization of the Energy levels of a diatomic molecule. Electronic states are represented as long horizontal lines. For each electronic state, there are several vibrational levels ν (medium-length lines). For each vibrational levels, several rotational levels J are present (short lines). Reproduced from [27].

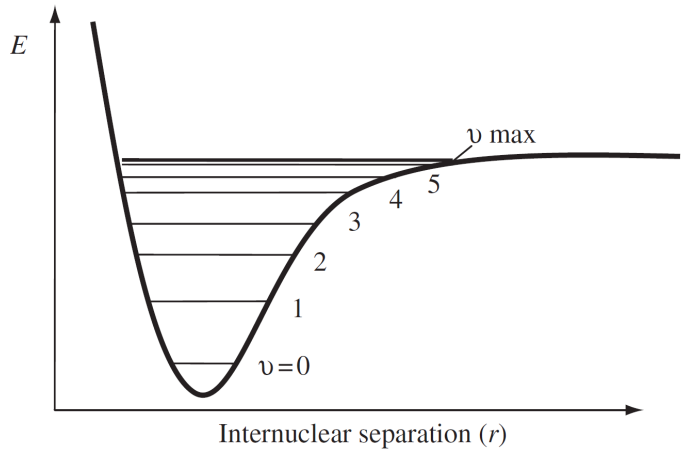

Figure 2.4: Representation of the Morse potential curve for a diatomic molecule in a defined electronic state. The vibrational levels, ν, are indicated by the numbers. For each of the ν's there is a set of sub-levels, each corresponding to one rotational level (not shown). Reproduced from [26].

2.1.3 Raman/Rayleigh scattering

When light and matter interact, the photons which compose the light may be absorbed or scattered, or may not interact with the material. If the energy of an incident photon corresponds to the energy gap between the ground state of a molecule and an excited state, the photon may be absorbed and the molecule promoted to the higher energy

excited state. However, it is also possible for the photon to interact with the molecule and being scattered. In this case there is no need for the photon to have an energy which matches the difference between two energy levels of the molecule.

This is exactly the case of Raman and Rayleigh scattering processes. Even if closely related one to the other, the Raman and the Rayleigh scatter processes have fundamental differences. Both the processes have origin when a molecule is excited by a photon with energy $E = h\omega_0$, where h $[J \cdot s]$ is the Planck constant[1], and ω_0 $[s^{-1}]$ is the frequency.

When the above-mentioned photon interacts with a molecule, elastic or non-elastic light scattering occurs: the elastic scatter, which is also the strongest, is named "Rayleigh", while the inelastic, weaker one is defined spontaneous "Raman" scatter.

A simple model for vibrational Raman According to the classic theory, these scatter effects can be explained as follows, with respect to a diatomic molecule.

The electric field[2] of an electromagnetic wave (for example a laser beam) is given by

$$\mathbf{E} = E_0 \cos(2\pi\omega_0 t) \tag{2.2}$$

where $E_0\,[N/C]$ or $[V/m]$ is the magnitude of the field, $\omega_0\,[s^{-1}]$ its frequency, while $t\,[s]$ represents the time. When $\mathbf{E}$ interacts with a molecule whose polarizability is denoted by α, an electric dipole momentum $\mathbf{p}$ is induced:

$$\mathbf{p} = \alpha\mathbf{E} = \alpha E_0 \cos(2\pi\omega_0 t) \tag{2.3}$$

The polarizability $\alpha\,[Cm^2/V]$ is a measure of how easy it is to induce a moment in an atom when it is influenced by an electric field. It can be assumed to be a scalar constant, when the mean to which it refers is isotropic, i.e. α is the same in any direction. More generally, when the hypothesis of isotropy cannot be applied, the polarizability has to be expressed as a tensor with 9 components in a Cartesian system [30]. An example of the polarization of a diatomic molecule is in fig.2.5.

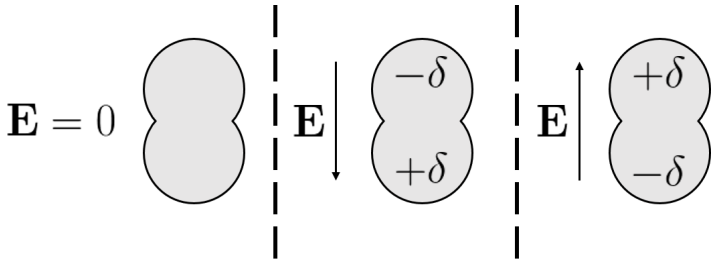

Figure 2.5: An example of the polarization of a diatomic molecule. On the left, if the electric field applied is equal to zero, the charges in the molecule are balanced and no positive or negative charge is highlighted. The other two cases are representative of a non-zero electric field, cause of a migration of the charges in molecule, which will finally show a positive and a negative charge, represented by $\pm\delta$.

[1] Planck constant $h = 6.62606896(33) \cdot 10^{-34} Js$

[2] As well known from the Maxwell's equations the electric field $\mathbf{E}$ and the magnetic field $\mathbf{M}$ are interconnected. Here for simplicity the discussion will focus on $\mathbf{E}$, keeping in mind that the light can be indeed described as an electromagnetic wave.

In fig.2.5 it is shown that before the influence of an electric field **E**, the centers of the positive and negative charges in the molecule are located in the same position, resulting in a net zero charge for the molecule. After the application of **E** (or $-\mathbf{E}$) the electronic cloud will migrate according to the orientation of the electric field, causing an unbalance of the charge in the molecule, which will finally highlight a positive and a negative charge.

If the molecule is vibrating with a frequency ω_m and an amplitude q_0, the nuclear displacement **q** can be written as:

$$\mathbf{q} = q_0 \cos(2\pi\omega_m t) \tag{2.4}$$

The polarizability, seen in eq. 2.3, can be written as a linear function of the displacement, if the amplitude of the vibration is small (from a truncated Taylor series):

$$\alpha = \alpha_0 + \left(\frac{\partial\alpha}{\partial q}\right)_0 q_0 + o(q_0^2) \tag{2.5}$$

In the eq.(2.5) α_0 is the polarizability at the equilibrium position, and $(\partial\alpha/\partial q)_0$ is the rate of change of α with respect to the change of the displacement of the nucleus, evaluated at the equilibrium position.

The induced momentum of dipole of the molecule, vibrating at frequency ω_m with amplitude q_0 and interacting with the electric field **E** can be written using the equations (2.4) and (2.5) in (2.3), leading to the following expression:

$$\begin{aligned}\mathbf{P} &= \alpha_0 E_0 \cos(2\pi\omega_0 t) + \left(\frac{\partial\alpha}{\partial q}\right)_0 q_0 E_0 \cos(2\pi\omega_0 t)\cos(2\pi\omega_m t) = \\ &= \underbrace{\alpha_0 E_0 \cos(2\pi\omega_0 t)}_{\text{Rayleigh}} + \\ &+ \underbrace{\frac{1}{2}\left(\frac{\partial\alpha}{\partial q}\right)_0 q_0 E_0 \cos[2\pi(\omega_0+\omega_m)t]}_{\text{Anti-Stokes}} + \underbrace{\frac{1}{2}\left(\frac{\partial\alpha}{\partial q}\right)_0 q_0 E_0 \cos[2\pi(\omega_0-\omega_m)t]}_{\text{Stokes}}.\end{aligned} \tag{2.6}$$

The model described by eq.(2.6) is referred to as "Simple Harmonic Oscillator" (SHO). Despite its simplicity, when interpreted according to the semi-classic theory, it provides a number of information about the Raman and Rayleigh scatter processes. The first term of the equation represents a dipole oscillating at the frequency ω_0, i.e. the frequency of the forcing **E**, and explains the Rayleigh scatter, which is indeed at the same frequency of the incoming light. The second and third terms give instead an explanation to the Raman scattering: they represent dipoles vibrating at frequencies shifted from ω_0 by $\pm\omega_m$ (the molecule vibrational frequency). Thus the light scattered by the Raman process can be seen as formed by two components: the Anti-Stokes, shifted to a shorter wavelength, and the Stokes, at a longer wavelength than **E**. The SHO leads to very simple selection rule for the molecules, namely that the vibrational quantum number can change only by 1: $\Delta v = \pm 1$. Considering rotational Raman, the selection rules are $\Delta J = 0, \pm 2$, with $\Delta J = 0$ identifying the Q branch, $\Delta J = +2$ and $\Delta J = -2$ the O branch and the S branch, respectively.

The same eq.(2.6) gives also the conditions for a molecule to be Rayleigh and/or Raman active. The Rayleigh component requires that the molecule has a non-zero polarizability in the equilibrium condition, $(\partial\alpha/\partial q)_0$. This condition is fulfilled in practice by all the molecules, which are indeed always showing a Rayleigh scattering when they are interacting with light.

For the molecule to be Raman active, instead, the requirement is to have a non-zero rate of change of the polarizability, with respect to the nuclear displacement, around the equilibrium position. In other words, when the molecule is excited from the equilibrium position, it has to show a change in the polarizability tensor $\underline{\underline{\boldsymbol{\alpha}}}$. These changes can be induced by some of the molecular vibrations: a relative change in the position of the atoms in the molecule will generate a change in the distribution of the charges and, consequently, will change how the molecule interacts with the electromagnetic field.

As said, the change of the polarizability has to be intended in terms of its tensor structure, and then a change of just one component is enough for having a Raman-active vibration. The complete structure of the eq.(2.3) is indeed given by:

$$\begin{bmatrix} P_x \\ P_y \\ P_z \end{bmatrix} = \begin{bmatrix} \alpha_{xx} & \alpha_{xy} & \alpha_{xz} \\ \alpha_{yx} & \alpha_{yy} & \alpha_{yz} \\ \alpha_{zx} & \alpha_{zy} & \alpha_{zz} \end{bmatrix} \begin{bmatrix} E_x \\ E_y \\ E_z \end{bmatrix} \tag{2.7}$$

A very useful representation is the one given by Ferraro et al. in [27] and reproduced in the fig.2.6. It shows the change of the so-called "polarizability ellipsoid" for the CO_2 molecule due to the three vibrational modes. This solid surface is obtained plotting the polarizability in one direction α_i from the center of gravity in all the directions (actually for an easier representation $1/\sqrt{\alpha_i}$ is plotted). Using this representation, a vibration is Raman-active when the ellipsoid changes its size, shape or orientation during the normal vibration about the equilibrium position q_0.

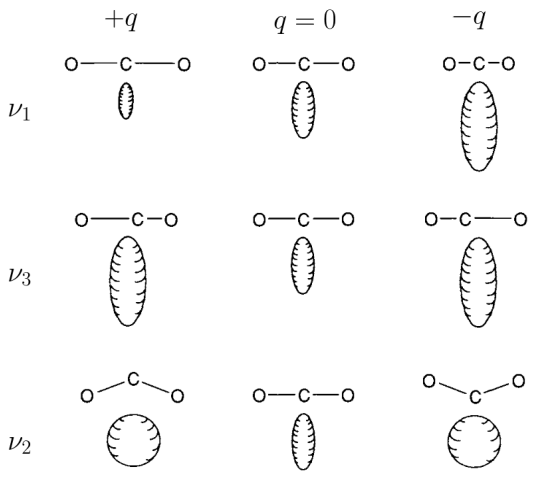

Figure 2.6: Change in the polarizability ellipsoid for the CO_2 molecule. $\pm q$ is the nuclear displacement, while the ν_i are three different vibrating modes of the molecule. Reproduced from [27].

Analysing the fig.2.6 it is possible to comment that the mode ν_1 is Raman-active, because the ellipsoid is changing its shape during the vibrational displacement. The other two modes ν_2 and ν_3 are instead non Raman-active, because the ellipsoid is exactly the same at the two extremes: this means that, around the equilibrium

position q_0, the rate of change of the polarizability is null (it has to be null because it is increasing symmetrically on the two sides). As a general rule, the simultaneous change of all the diagonal elements α_{ii} of $\underline{\underline{\boldsymbol{\alpha}}}$ will scale the size of the ellipsoid. If the α_{ii}'s are changing with a different rate, the ellipsoid will change its shape and size. If the change is in the off-diagonal elements α_{ij}, the orientation of the ellipsoid will be altered.

Improved models Despite the important information they contain, as anticipated the SHO and the rigid rotor are rude simplifications of the Raman/Rayleigh scattering physics, considering only harmonicities, no interactions between rotations and vibrations nor variations of internuclear spacing. Anharmonic effects, together with non-ideal and/or coupled rotational and vibrational motions of the molecules have to be accounted for. Anharmonic vibrations lead to the already mentioned Morse potential for the molecule, rather than the parabolic-like one, and are accounted for using appropriate coefficient for second (and higher) terms of the vibrational energy definition. The fact that the average internuclear spacing is function of the vibrational energy causes the so called "vibrational stretching", i.e. rotational motions depend on the molecule vibrations. Rotations are also affected by centrifugal distortion, because of the average internuclear spacing dependence on the rotational energy. Influence of vibrational motions on rotations is also caused by the "Coriolis coupling": Coriolis forces arise due to one component of each degenerate vibration exciting the other components. There will be then an angular momentum of vibration interacting with angular momentum of rotation. The oveall effect on the motion can be observed in the atoms moving along circles or ellipses rather than straight lines.

It results clear from the mentioned effects that a more complete treatment has to rely then on more complex phenomena. In the following some details about improved models are introduced, following the Placzek's theory of polarizability. The main reference for this part is the work by Long [31], together with [24, 32] for information specific to the application of Raman/Rayleigh spectroscopy in turbulent combustion. Long's book represents a milestone in the treatment of Raman effect physics, and the reader can rely on it for further information.

The line intensity of a Raman transition is proportional to the squared transition moment, R. The latter is proportional to the transition probability, and can be identified as:

$$R = \int \psi'^{*}\, p_i\, \psi''\, d\tau \tag{2.8}$$

where ψ'' and ϕ' are the wavefunction of the respectively initial and final states, while p_i is the mentioned induced dipole momentum. From eq.(2.3) (or eq.(2.7), equivalently), and considering that E_0 may be considered as constant in the area of the molecule, it follows:

$$R = E_0 \int \psi'^{*}\, \alpha\, \psi''\, d\tau \tag{2.9}$$

The polarizability tensor, with respect to the given initial and final states, is then:

$$[\alpha_{xy}]_{fi} = \int \psi'^{*}\, \alpha\, \psi''\, d\tau. \tag{2.10}$$

If one considers a typical Raman/Rayleigh illumination-observation geometry (laser beam linearly polarized propagating along *haty* with non-zero component only along

$\hat{z}$, observation in the xy plane, and sufficiently small viewing angle in the $\hat{x}$ direction), it follows that the dipole momentum has only two components:

$$\mathbf{P}_{fi} = [\alpha_{yz}]_{fi} E_{0,z} + [\alpha_{zz}]_{fi} E_{0,z} \tag{2.11}$$

which are respectively the parallel and perpendicular components of the scattered light, generally treated separately with respect to its polarization direction relative to the scatter plane.

The components of α_{fi} relevant to the determination of the induced dipole momentum for the transition $f \leftarrow i$ depend on the electronic wavefunction and have to be determined in order to calculate the transition moments. Polarizabilities can be calculated from quantum chemical *ab initio* computations within different orders of accuracy, depending on the used level of approximation, or via semi-empirical computations (see [32] p. 14 for a list of reference).

Term values $E(v, J)$ for diatomic molecules such as N_2, CO and H_2 are computed as sum of the vibrational and rotational energies. Anharmonic vibrations and non-rigid rotation corrections have to be accounted for, as well as rotation-vibration interactions[3] [33]:

$$\begin{aligned} E(v, J) &= G(v) + F_v(J) = \\ &= \left[\omega_e(v + 1/2) - \omega_e x_e(v + 1/2)^2 + \omega_e y_e(v + 1/2)^3\right] + \\ &+ \left[B_v\, J(J+1) - D_v(J(J+1))^2\right] \end{aligned} \tag{2.12}$$

with the rotational parameters are corrected to account for rotation-vibration interactions with $B_v = B_e - \alpha_e(v + 1/2) + \gamma_e(v + 1/2)$ and $D_v = D_e - \beta_e(v + 1/2)$ [33].

For a simulation of O_2 spectra useful for typical Raman/Rayleigh in turbulent combustion, in addition to vibration-rotation interactions, the triplet structure of the electronic ground state and contributions from excited electronic states have to be taken into account [32].

Triatomic or polyatomic molecules have additional complexities respect to the diatomic ones. In the context of Raman/Rayleigh in turbulent combustion, H_2O spectra are computed thanks to simulations including up to twenty six thousand transitions (see [32] for details). CH_4 spectra are calculated using different polyades, resulting in half a million transitions. CO_2 presents a Fermi doublet $v_1 + 2v_2$, due to an accidental degeneracy caused by the first overtone of the v_2 band being nearly resonant with the fundamental of v_1. The two vibrational modes are strongly coupled by radiative and collisional exhanges, leading to normally weak overtone band transition moments being strongly enhanced. Perturbation theory is applied to compute CO_2 transition modes, firstly computing unperturbed transitions and then using appropriate coupling effects to account for the effects of perturbations. Up to 30 polyades are included into the spectra simulation.

The equations and comments above give an explanation about the two processes in terms of frequency/wavelength, and explain the nature of the Raman and Rayleigh scattering processes. But these can also be "visualized" in terms of energy transitions of the molecule, recalling the interaction with a photon of energy $E = h\omega_0$ and figg. 2.3 and 2.4.

[3] See [33] for details and for the values of the equation coefficients.

The Rayleigh scatter firstly brings the molecule to an excited state from where it returns, being the scatter elastic, to its original quantum state. The interaction with the photon that leads to the Raman effect is instead followed by a net exchange of energy, which might change the vibrational or rotational quantum level of the molecule (more generally, in fact, the term "ro-vibrational" level is used). The change in the molecule energy can be positive or negative, and the balance required by the energy conservation is closed by the energy contained by the photon, which will be accordingly and specularly changed.

Figure 2.7 schematizes the Rayleigh and the spontaneous Raman (Stokes and anti-Stokes) scattering processes when a molecule is excited to a virtual state by a photon with energy $h\,\omega_0$. ω_m is the molecule characteristic frequency (see eq.(2.6)).

One interesting observation that can be clearly derived from fig.2.7 is that, following the Boltzmann distribution law, the population of molecules at the rotational level $\nu = 0$ (QS_0 on the figure) is much larger than that at $\nu = 1$ (QS_1 on the figure). Thus, the Raman Stokes scatter is usually stronger than the anti-Stokes one and is therefore used for measurements.

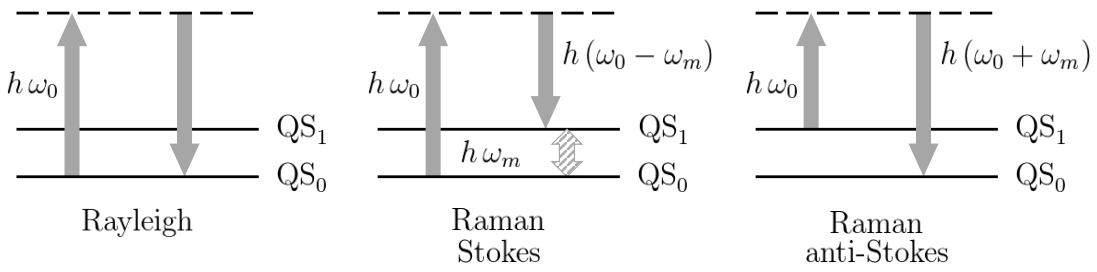

Figure 2.7: Schematization of the Spontaneous Raman Scattering (Stokes and anti-Stokes) and the Rayleigh scattering. QS_0 is the ground quantum state of the molecule, while QS_1 is an excited ro-vibrational state. The dashed line is representative of a virtual state. ω is for the frequencies, with ω_0 being the excitation frequency and ω_m the molecule characteristic frequency (see eq.(2.6)).

It is reported in a variety of relevant works, [27, 29, 31, 34] among the others, that both Raman and Rayleigh cross sections are defined in accordance to the Boltzmann distribution for the fraction of molecules in an energy level. If the populations in all the quantum levels obey Boltzmann distribution, the species may be said to be in local thermodynamic equilibrium [29]. If this condition is not met, the formulas used in literature to describe Raman and Rayleigh scattering are not valid.

In Raman scattering the energy of a $C = C$ vibration may typically be between $1.6e3$ and $1.0e3\ cm^{-1}$ but the energy of a green laser will be about $20e3\ cm^{-1}$ [26]. Very often, as in fig.2.7, the energy of the laser radiation $h\,\omega_0$ is not scaled accurately because the desire is to show the vibration spacing clearly, and plotting the true excitation energy would lead to a very large separation between the ground state and the virtual state (dashed lines of the figure) reducing the space to show the vibronic levels.

2.2 Raman/Rayleigh spectroscopy in combustion

The content of sec.2.1 has shown background of the physics of the Raman and Rayleigh scattering processes. The practical applications of those processes are many and spread among a number of different fields. In this part, the goal is to understand how those scattering processes are used for spectroscopic measurements of combustion processes.

2.2.1 Overview

A first sketch of a Raman/Rayleigh system as it could be applied for a measurement in a (reacting) gas flow is illustrated in fig.2.8.

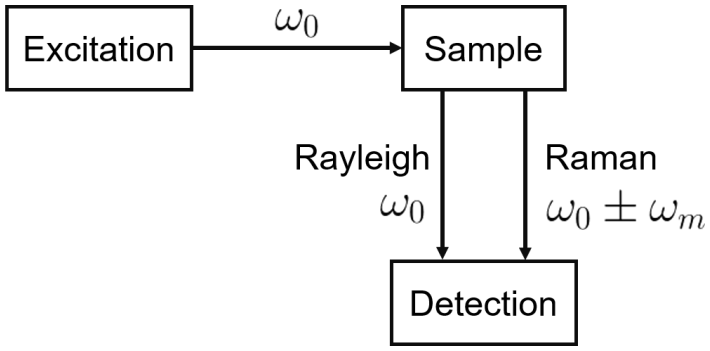

Figure 2.8: Scheme of a Raman/Rayleigh system used for measurement of a sample. The arrows represent the paths of the photons. ω is for the frequencies, with ω_0 being the excitation frequency and ω_m the molecule characteristic frequency (see eq.(2.6)).

From fig.2.8 it is possible to deduce that the sample object of the measurement has to be excited with a light beam at a given frequency, which is usually provided by a laser. The scattered light has to be collected, at a certain angle, in order to be analysed and deliver the desired information. All these parameters, such as the excitation system, the detection system, the frequencies and the detection angle, are crucial for the measurement to carry useful information. Also a number of other components in between the boxes drawn in the figure are present in a real system.

In the following part some details about the main part of a Raman-Rayleigh measurement system for applications in turbulent fluid dynamic context are given.

For better understanding the following part, it is useful to provide another formulation for the Raman effect, which helps to derive other fundamental principles.

The intensity of the Raman scattering may be expressed as [35]:

$$I_{\mathrm{Ram}} \propto \eta\, \omega_0^4\, I_o\, N \left(\frac{\partial \alpha}{\partial q}\right)^2 \tag{2.13}$$

where:

$\omega_0\,[s^{-1}]$ is the frequency of the excitation source;

$I_o\,[J]$ is the incident energy of the excitation;

$N\,[cm^{-3}]$ the number of scattering molecules in a given state;

η is an overall efficiency of the system (accounting for example for the optic path);

$\frac{\partial \alpha}{\partial q}$ the change in the polarizability with respect to the displacement.

It is clear, as well as intuitive, that a high incident energy will give a higher scattering intensity. A very important role is also played by ω_0 with a dependence of the 4th power. Moreover, it appears clear that the intensity is depending also on the number of molecules: this means that the Raman scattering can provide a quantitative information about the molecule concentration in the excited probe volume. The qualitative information about the nature of the molecules is instead already explained by the eq. 2.6 with the presence of ω_m which depends on the molecule.

The Rayleigh intensity can be re-written in order to read [36]:

$$I_{\text{Ray}} \propto \eta\, I_0\, N\, \frac{\partial \sigma}{\partial \Omega}\bigg|_{\text{Eff}} \tag{2.14}$$

where the last term of the RHS in eq. 2.14 is the differential Rayleigh effective cross section, with $\sigma\,[cm^2]$ being the total cross section and $\Omega\,[sr]$ the collection solid angle. In σ it is again present a dependence from ω_0^4. The differential cross section has to be integrated over Ω, and then the bigger is the detection solid angle, the higher will be the intensity of the Rayleigh scattering intensity. Above all, it is important to notice the dependence of I_{Ray} from N. Assuming the validity of the ideal gas law and being T the temperature of the excited probe volume, then $T \propto N^{-1}$. Reading the eq. 2.14 with this relation, it is possible to write that:

$$T \propto N^{-1} \Rightarrow I_{\text{Ray}} \propto T^{-1} \tag{2.15}$$

The relation of eq.(2.15), coming from the eq.(2.13) and together with the Ideal Gas law, state that, knowing the pressure of the system and having a reference Rayleigh signal in known (p, T) conditions , it is possible to calculate the temperature of the probe volume by measuring the intensity of the Rayleigh scattering signal. The effective Rayleigh cross section can instead be written as a weighted average of the molecules cross sections present in the probe volume. Being X_s and σ_s respectively the mole fraction and cross section of the s-th species in the probe volume:

$$\frac{\partial \sigma}{\partial \Omega}\bigg|_{\text{Eff}} = \sum_s X_s \frac{\partial \sigma_s}{\partial \Omega} \tag{2.16}$$

The eq.(2.16) means that the measure of the temperature through the Rayleigh scattering effect requires the knowledge of the probe volume composition. On the other side, as will be shown after, the Raman intensity scales non-linearly with the temperature. Thus to exactly measure the composition of the probe volume, it is important to know T. From these two considerations it is clear that the Raman and the Rayleigh scattering effects are strongly interconnected also in terms of information provided from the measurement.

Moreover, from considerations related to the probability of the scattering events (again related to the Boltzman distribution), it is possible to see that the Rayleigh

scattering is the most probable event and the scattered intensity is ca. 10^{-3} less than that of the original incident radiation, while the Raman scattering is far less probable, with an observed intensity that is ca. 10^{-6} of the incident radiation [35]:

$$I_{\text{Ray}} \sim 10^{-3}\, I_0 \qquad ; \qquad I_{\text{Ram}} \sim 10^{-6}\, I_0 \tag{2.17}$$

2.2.2 Excitation and Detection

Excitation

The excitation part of the system has a crucial role, with several fundamental tasks to fulfill, that in a first instance can be summarized by the requirement of providing a high number of photons in a short period of time. They come from two main reasons: on one side a high number of photons passing through the probe volume means that a (relatively) high number of photons can be scattered and produce the Raman and Rayleigh effects. The second reason, related to the time, comes from the demand of the technique to be able to resolve the smallest time scales characteristic of a turbulent flow field. In addition to that, the excitation source influences also the spatial resolution achievable.

Lasers are ideal excitation sources for Raman spectroscopy [27], due to the specific characteristics of a laser beam. Among them it is possible to highlight that:

- The energy typically convoyed by the beam of a solid state laser can easily reach 2 J [9].
- The beam is highly monochromatic. This requirement is important because the peaks of the Raman scattering spectra are sharper than the one usually detected in the visible region phoenomena, and are measured as a shift from the energy of the excitation source [26].
- Most laser beams have millimiter-size diameters, which can be reduced to submillimiter-size by using simple lens systems, as seen for example in [37].

From the eq.(2.13) and eq.(2.14) it is already clear that the intensity of the scattering increases with the intensity of the exciting laser. In principle, the highest the laser energy the better is for the detectability of the scattered light. In practice upper limits are set by some undesired effects, and among them it is worth citing the optical break down. DeMichelis describes the break down as follows [38]: "the phenomenon consists in the fact that at the very high field strength, [...] ($1e6 - 1e7$ V/cm), gases that are usually transparent to optical frequencies break down, i.e., they become highly ionized. This is accompanied by a light flash and a sharp sound, just as in an ordinary gas discharge". The effect can also be triggered by dust particles present in traces in the gas flows. The high intensity light emission can result in damages on the image detectors of the experimental test rig, and then usually the pulse length of the laser is stretched temporally to reduce the peak power of the laser without reducing its average energy [39].

The choice of the wavelength is also relevant for measurement set-up. The eq.(2.13) shows that the intensity of the Raman scattering signal scales with the fourth power of the frequency and thus it is inversely proportional to the fourth power of the wavelength: the shorter the wavelength, the highest the intensity of the Raman

scatter. Having an exciting laser emitting in the UV would be positive for this requirement, but it would on the other hand increase the probability of laser-induced fluorescence, interfering especially with Raman scattering.

Some clarifications must be done respect to the spatial and temporal resolution requirements.
Later in this chapter it will be shown that in turbulent (reactive) flows the Kolmogorov space and time scales are the smallest scales of great interest [40], when it comes to fundamental understanding of turbulent combustion. Thus the ideal measurement technique is able to resolve the quantities of interest on both the sides: the temporal information must be averaged over a time period shorter than the Kolmogorov time scale, and there should be at least two points from which are extracted the information within one length of the Kolmogorov length scale to spatially resolve the physical structures in the flow.

Typical Kolmogorov time-scales are at the order of few microseconds, in a typical industrial application as the one shown in [41]. Consequently, scalars measurements should resolve at least one microsecond. In practice, this requirement is accomplished with pulsed lasers in the submicrosecond regime, with Nd:YAG[4] lasers providing pulse widths of 10 ns and repetition rates ranging from 10 to 100 Hz [23].

Among the others, single shot Raman/Rayleigh is applied at the experimental facilities available at the Technical University of Darmstadt, the German Aerospace Center (DLR) in Stuttgart, at the Combustion Research Facility of the Sandia National Laboratories in the USA and at the Technical University of Eindhoven.

All the experimental setup operated in these facilities count on a Nd:YAG pulsed laser as excitation source. More specifically, a flashlamp-pumped dye laser ($\lambda = 489$ nm, 3 μs pulse duration) was used for the excitation at the DLR, as described for example in [42]. The source used in the Sandia laboratories is described in [10]. Here it is reported to be based on four frequency doubled Nd:YAG lasers ($\lambda = 532$ nm), fired sequentially with a temporal offset of about 80 ns one from the other. The beam path is composed by three optical delay lines, to superimpose the pulses to a single pulse of about 400 ns delivering energy higher than 2 J. The superimposing and stretching of the pulses is used to lower the occurrence of lased induced optical breakdown. The Darmstadt test rig will be shown in the dedicated section in the next chapters.

Detection

A proper design and implementation of the system detection apparatus is fundamental to acquire all the information contained in the light scattered by the sample after the excitation of the laser beam. The state of the art in the most of Raman applications in combustion diagnostic is the use of Charge Coupled Devices (CCDs). Some of the information contained in the following description of CCDs are provided by Nikon Instrument Inc.[5], or from [27].
A CCD is a thin silicon wafer, i.e. a semiconductor element, composed by an array of

[4] "Nd:YAG" stands for neodymium-doped yttrium aluminum garnet. It is a crystal used as a lasing medium for solid-state lasers.

[5] https://www.microscopyu.com/digital-imaging/introduction-to-charge-coupled-devices-ccds

photosensitive elements. Each fundamental light-sensing unit of the CCD is a metal oxide semiconductor (MOS) capacitor operated as a photodiode, and is schematically reported in fig.2.9. A common size for a pixel in these devices is 20x20 μm. Moreover,

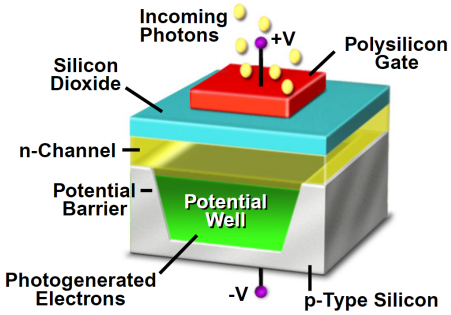

Figure 2.9: Schematic representation of a Metal Oxide Semiconductor (MOS) with its main parts. (© 2018 Nikon Instruments Inc.)

accumulated charge packets from adjacent pixels in the CCD array can be combined to form a reduced number of superpixels. This process is referred to as pixel binning, and can be used for detecting small amount of photons (that is the case of the Raman scattering).

The major advantages of the CCD relative to other multichannel detectors are the low readout noise, which makes optical intensification unnecessary, and high quantum efficiency and sensitivity in a wide wavelength range (120 - 1000 nm) [27]. Currently back-illuminated CCDs detectors are the devices available to the imaging community which can provide the highest sensitivity [43].

Other components might be necessary for the detection, as well as for the operation of the test rigs, depending on the specific application and its requirements. More detailed information about the equipment used within this work will be given in the dedicated chapter.

2.3 Combustion and Combustion Regimes

The third part of this chapter is dedicated to provide a background of combustion, specifically to the cases where this process takes place in presence of turbulent flow fields, i.e. "turbulent combustion". The most of the theoretical content is based on books which are at the present standard in the field, namely the Poinsot and Veynante [44], Warnatz, Maas and Dibble [45], Law [46], Lipatnikov [6], Glassman and Yetter [47], Pope [40].

Turbulent premixed combustion is a particularly complex process, where a number of fundamental sub-phenomena are interacting. In this chapter a basic description of the chemical processes is provided in sec.2.3.1. The role of fluid dynamics is clarified in sec.2.3.2, with specific focus on turbulent flows. Closing the chapter, sec.2.3.3 provides a description of relevant peculiarities of turbulent premixed combustion regimes.

The reactants of a combustion process can be in solid, liquid or gas form (plus other special cases such as plasma); in this context only the case of reactants in gas phase will be considered.

2.3.1 Reacting Gas Mixtures

Basic Definitions

It is common to consider the reacting mixture to be an ideal gas, described by the ideal gas state equation

$$p = \frac{\rho}{MW} RT \tag{2.18}$$

begin

ρ [g/m^3] the density of the mixture

MW [g/mol] is the molecular weight of the mixture

$R = 8.314$ J/mol K the universal gas constant

T [K] the temperature

A first assumption can be safely made using the fundamental quantities of the eq.2.18: the variation of the molecular weight of the mixture will be neglected [6]. Then, if the subscript 0 denotes the state of the mixture before the combustion, while the quantities without subscript refer to a general state after the initial one:

$$\frac{p}{\rho T} = \frac{p_0}{\rho_0 T_0} \tag{2.19}$$

In addition to that, in this work only subsonic propagation will be considered, i.e. only deflagration processes are studied. In this case the pressure changes through the domain are considered small, according to [47] the pressure of the burnt mixture can drop to a value of 0.98–0.976 p_0 . Consequently:

$$\rho T = \rho_0 T_0 \tag{2.20}$$

The quantities from the equation of state, eq.(2.18), are related to the gas mixture. It is useful to recall the relations for these quantities in the case one wants to refer to the single component of the mixture. If ρ_k [kg/m^3] is the density of the species k-th, i.e. the ratio between the mass of k divided by the volume occupied by the mixture, then

$$\rho = \sum_k \rho_k \tag{2.21}$$

The partial pressure of the k-th species is p_k, measured in Pascal in SI units (remembering that 1 Pa = 1 N/m^2). The ideal gas law then reads:

$$p_k = \frac{\rho_k}{MW_k} RT \tag{2.22}$$

If N is the number of species in the mixture, $\sum_{k=1}^{N} p_k = p$

To describe the amount of components in the gas mixture, it is very helpful to use the mole fractions X_k or the mass fraction Y_k, both dimensionless in SI units.

Being C_k [mol$_k$/m^3] the concentration of a species in the mixture, defined as the number of moles of k per unit volume of mixture, and C the concentration of the mixture [mol/m^3]:

$$X_k = \frac{C_k}{C} \tag{2.23}$$

The mass fraction is instead defined as the mass of species per unit mass of the mixture, i.e.:

$$Y_k = \frac{m_k}{m} \tag{2.24}$$

It is easy to show that

$$\sum_{k=1}^{N} X_k = 1 \qquad ; \qquad \sum_{k=1}^{N} Y_k = 1 \tag{2.25}$$

First and Second Laws, Thermodynamic Functions

If U is the internal energy of a closed system[6], and heat and work are denoted with Q and W, the first law of the thermodynamics can be written, in terms of infinitesimal process[7], as

$$\delta Q = dU + \delta W \tag{2.26}$$

As already stated, the variations of pressure are neglected, then the work can be performed only through volume changes:

$$\delta Q = dU + pdV \tag{2.27}$$

The second law, stating the non-reversibility of the thermodynamic transformations, introduces the entropy S ($dS/dt > 0$) and can be arranged in order to read:

$$dE \leq T\,dS - p\,dV \tag{2.28}$$

[6] In a closed system no mass exchanges take place with the environment.

[7] The symbol "d" is used to define the infinitesimal change of the internal energy because it is a property of the system. Work and heat variations are instead noted with δ because they are dependent on the specific thermodynamic transformation.

if E is the energy of the closed system.

If the closed thermodynamic system is monocomponent, its status can be defined using two functions. If the system is instead multicomponent, the composition also has to be specified. Then the energy will be a function, for example, of S, V and of the composition.

Omitting some steps not necessary in this context, it is possible to write the specific energy [J/kg] for the i-th species of a reacting system as:

$$e_i = \underbrace{\int_{T_0}^{T} c_{v,i}\, dT - RT_0/MW_i}_{\text{Sensible}} + \underbrace{\Delta h^0_{f,i}}_{\text{Chemical}} \tag{2.29}$$

where a reference value of temperature T_0 has to be chosen. Any temperature could be picked as choice, for simplicity the standard reference state at 298.15 K is used. In the eq.(2.29) the "sensible" part is related to the temperature changes, while the "chemical" one is due to the reference chemical status of i, and is called "enthalpy of formation". It accounts for the energy necessary to form the species i starting from its single elements. It is usually a mass quantity, for example measured in [J/kg], or it can be on molar base. While the sensible term is associated to an increase in the thermal energy when the temperature increases from T_0 to T, the energy stored in the chemical bonds may be released in chemical reactions, that is converted into thermal energy: this process is defined "heat release". The heat release has the effect of increasing the temperature of the combustion products, with respect to the reactants.

In parallel with the equations for the energy, it is useful to recall also the (specific) enthalpy [J/kg] definition:

$$h_i = \underbrace{\int_{T_0}^{T} c_{p,i}\, dT}_{\text{Sensible}} + \underbrace{\Delta h^0_{f,i}}_{\text{Chemical}} \tag{2.30}$$

In the energy and enthalpy equations, eq.(2.29) and eq.(2.30), are included the heat capacities c_p and c_v [J/kg K], referred to a pressure constant or volume constant transformation, respectively:

$$c_v = \left.\frac{\partial e}{\partial T}\right|_{V\,=\,\text{const.}} \quad ; \quad c_p = \left.\frac{\partial h}{\partial T}\right|_{p\,=\,\text{const.}} \tag{2.31}$$

Both the relations come directly from the First Principle. For the ideal gas case, it is true the Mayer relation:

$$c_p - c_v = R.$$

Using the definitions of the mass/molar fractions, it is possible to derive the following relations for energy, enthalpy and heat capacities of a mixture:

$$e = \sum_i^N e_i\, Y_i \quad ; \quad h = \sum_i^N h_i\, Y_i \tag{2.32}$$

$$c_p = \sum_i^N c_{p,i}\, Y_i \quad ; \quad c_v = \sum_i^N c_{v,i}\, Y_i \tag{2.33}$$

Chemical Reactions

Generally speaking, when a chemical reaction is written as

$$rR \rightarrow pP \tag{2.34}$$

the meaning is that r moles of the reactants R are converted into p moles of the products P. In this context it is interesting to define some quantities associated to the chemical reactions of combustion, useful for the analysis of the combustion processes, as they can be found in all the basic text book about the subject. Remembering that this kind of reaction is an oxidation, where the conversion takes place when a chemical species reacts with oxygen, it is possible to analyze a basic oxidation of a hydrocarbon C_xH_y (which is in this case the "fuel"):

$$C_xH_y + o\,O_2 \rightarrow c\,CO_2 + h\,H_2O \tag{2.35}$$

This reaction is often defined a "global reaction". It is just a simplified representation of a chain of a great number of elementary reactions, and describes the complete conversion of the fuel and the oxidizer into carbon dioxide and water. To this reaction it is associated the maximum possible amount of thermal energy released. This energy mostly comes from the chemical energy bound in the fuel, and has the main effect of heating up the gas mixture itself, which therefore experiences an increase of the temperature.

The full conversion of C_xH_y and O_2 into CO_2 and H_2O is only possible if the concentrations of fuel and oxidizer respect a given ratio, called stochiometric, which depends on the fuel formula. Looking at the reaction (2.35), it is easy to derive that $c = x$ from the conservation of the carbon atoms. From the conservation of H and O it comes that $2h = y$ and that $2o = 2c + h$. From these considerations it is possible to prove that

$$o = x + y/4 \tag{2.36}$$

that is, for a full oxidation of the fuel, the fresh unburnt mixture has to contain $x + y/4$ moles of oxygen. When this requirement is exactly met, the mixture is defined "stochiometric".

Apart for some exceptions, normally the oxygen necessary for the oxidation of the fuel is provided to the process from air. Thus a significant amount of N_2 is also present in the fresh mixture (plus all the other gases and aerosols usually present in air). In a first approximation the nitrogen can be considered as an inert in the process, even if it is well known its contribution to the reactions chain, with the NOx formation for example. As inert it is participating to the global reaction without conversion, but still playing an important role in terms of heat exchange. The global reaction (2.35) with the N_2 contribution then reads:

$$C_xH_y + o\,(O_2 + 3.762\,N_2) \rightarrow c\,CO_2 + h\,H_2O + 3.762\,o\,N_2 \tag{2.37}$$

considering a volumetric air composition of 21% O_2 and 79% N_2. For each O_2 mole provided to the reaction, 3.762 moles of N_2 are fed.

Not always the fresh gas mixture is in stochiometric conditions: intentionally or not, the combustion process can take place even when a different amount of oxygen is available. This change can lead to a very different outcome from the process, in terms of product species, temperature, luminosity and heat release. In literature it is common to define a parameter to identify the condition of the fresh mixture in terms of composition, namely the "equivalence ratio", ϕ [-]:

$$\phi = \frac{(X_F/X_O)}{(X_F/X_O)_{\mathrm{St}}} = \frac{(Y_F/Y_O)}{(Y_F/Y_O)_{\mathrm{St}}} \tag{2.38}$$

where the subscript "F" is for the fuel, and the "O" is for the oxidizer. From this definition follows:

- $\phi = 1$: **stochiometric** mixture. The amount of oxygen available is exactly the amount required from the stoichiometry of the global reaction. In principle all the fuel is converted to the products, but in practice limitations due for example to the non perfect mixing of the fresh gas mixture can cause some fuel to remain unburnt.
- $\phi < 1$: (fuel) **lean** mixture. The mixture has less fuel than the stoichiometric ratio, and then there is abundance of oxygen. Also in this case all the fuel is oxidated. This condition is often used in those applications where it is important for emissions limits or economical reasons to avoid the exit from the process of any unburnt fuel.
- $\phi > 1$: (fuel) **rich** mixture. The mixture has more fuel than the stoichiometric ratio, and then there is not enough oxygen to oxidate all of it.

To give an idea about the different characteristics of the reaction in the different ϕ regimes, the plot of the adiabatic flame temperature is shown as function of the equivalence ratio in fig.2.10. This temperature will be introduced in the next part. For the moment, it is enough to consider that it may be thought as the maximum temperature that can be reached in the combustion process, given the mixture thermodynamic state.

Simplified approaches: Adiabatic Temperature and Equilibrium Chemistry

A general expression for a single irreversible reaction may be written as:

$$F + O \rightarrow P \tag{2.39}$$

where the fuel F and the oxidizer O react to form the product P.

Assuming that the reaction is adiabatic, there is not change in the enthalpy between the unburnt and the burnt states; to be more precise, the sensible and formation parts of the enthalpy will re-distribute in order to have:

$$h_u = h_b \ . \tag{2.40}$$

Using eq.(2.30), eq.(2.32) and eq.(2.33), it is possible to re-write the balance of eq.(2.40) as follows[8]:

$$\int_{T_0}^{T_u} c_{p,u} dT + Y_F \ \Delta h^0_{f,F} + Y_O \ \Delta h^0_{f,O} = \int_{T_0}^{T_b} c_{p,b} dT + Y_P \ \Delta h^0_{f,P} \tag{2.41}$$

[8] If $T_u = T_0$ the sensible contribution of the LHS is null.

An assumption often used in simple calculations is based on the hypothesis that the heat capacity c_p is constant with the temperature [9], i.e.:

$$c_{p,i}|_{T=T_u} = c_{p,i}|_{T=T_b} = c_{p,i}. \tag{2.42}$$

In addition, it is assumed also that $c_{p,F} = c_{p,O} = c_{p,P}$, that is all the species have the same heat capacity. Using this simplifications, eq.(2.41) reads:

$$c_p(T_b - T_u) = Y_F\ \Delta h^0_{f,F} + Y_O\ \Delta h^0_{f,O} - Y_P\ \Delta h^0_{f,P} \tag{2.43}$$

which is confirming what already said above: the temperature increase between reactants and products (LHS) is given by the energy released by the re-assembling of the elements from the reactants to the products (RHS). The RHS of the eq.(2.43) is by definition the heat released by the reaction, q, called "specific heat of reaction".

The product temperature can be explicated rearranging eq.(2.43):

$$T_b = T_u + \frac{Y_F\ \Delta h^0_{f,F} + Y_O\ \Delta h^0_{f,O} - Y_P\ \Delta h^0_{f,P}}{c_p} = T_u + \frac{q}{c_p}. \tag{2.44}$$

Given that no heat exchange with the environment is considered, because the adiabaticity hypothesis has been done, the product temperature T_b is referred to as "adiabatic flame temperature", T_{ad}. This is the maximum temperature achievable with the considered reaction: removing the adiabaticity hypothesis, a portion of the heat release q will be exchanged with the environment[10], and $T_b < T_{ad}$.

Figure 2.10 shows how the adiabatic temperature changes over the equivalence ratio, fixed the pressure and temperature for the fresh mixture.

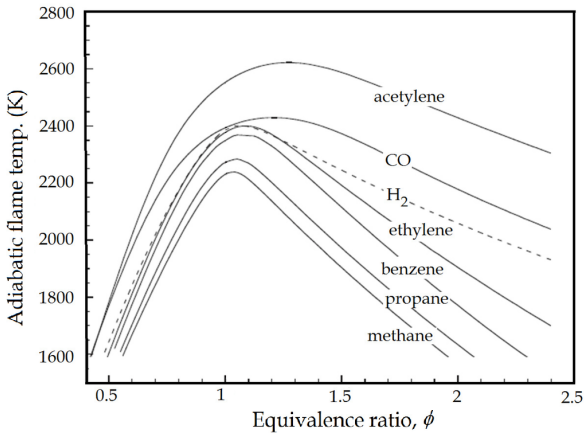

Figure 2.10: Adiabatic flame temperautre as a function of fuel equivalence ratio, ϕ, for several fuel-air mixture at STP. Reproduced from [46].

As one can see from fig.2.10, the maximum adiabatic flame temperature values are located around the stoichiometric values of ϕ; this is explained by the fact that in this condition the fraction of inert is at the minimum. For leaner conditions, there is

[9] In general this hypothesis is not verified, with $c_{p,i} = c_{p,i}(T)$. The functional form is usually expressed as a polynomial of T.

[10] Considering that the temperature of the environment is lower than the combustion products temperature.

proportionally more inert absorbing the energy released by the reaction. On the richer side, the temperature also decreases because the fuel acts as inert diluent. The figure is obtained with a relation more complex then the one in eq.(2.44): given the linear correlation expressed by this equation, the $T_{ad}(\phi)$ would result in a broken line with vertex at $\phi = 1$.

The described approach that leads to the calculation of the adiabatic temperature is effective, but extremely simplified. It does not allow to accounting for the dependence of the heat capacities on the temperature and not even on the differences in this quantities between different species.

A slightly less simplified approach can yield to more realistic results, and is based on the assumption that the reaction reaches the equilibrium condition. The relations describing this status can be derived with a number of different approaches, e.g. from the energy or enthalpy balance, as well as from the definition of Gibbs free energy. If the products of the reaction are composed by N species, to fully describe the thermodynamic state the unknowns to be defined are:

- the N species masses m_i
- the temperature T_b;
- the pressure p;
- the density ρ_b;

ending with a total of $N + 3$ variables. To saturate these degrees of freedom, an equal number of equations describing the system has to be defined and solved.

The first equation is given by the assumption of constant pressure. The ideal gas state equation and the energy balance are two additional laws valid in the system (which can be used to calculate T_b and ρ_b). The N species mass balances saturate the remaining degrees of freedom. A mass balance for a species can be written as follows:

$$\text{Inlet} = \text{Outlet} + \text{Accumulation} + \text{Reaction} \tag{2.45}$$

If no transient effects are significant, and then the accumulated quantity is zero, the unsolved term is the one related to the reaction. This depends (linearly or not) on the species concentrations and on the reaction constant, which is specific for each reaction. The reaction rate will be positive or negative, depending on whether the species is consumed or produced within the reaction. More details about the forms of this term can be found in [48].

To know the reaction constant, the equilibrium condition is applied. Given a generic equilibrium reaction, where S_i is the generic i-th species,

$$\sum_{i=1}^{N} n_i \, S_i \leftrightarrow \sum_{i=1}^{N} m_i \, S_i \tag{2.46}$$

the equilibrium condition can be defined with respect to the partial pressures of the species, and then reads

$$K_p(T) = \frac{\prod_{i=1}^{N} p_i^{m_i}}{\prod_{i=1}^{N} p_i^{n_i}}. \tag{2.47}$$

with $K_p(T)$ the equilibrium constant, that can be written also in terms of other quantities. For the reaction $fF + oO \rightarrow pP$, it is valid what follows:

$$K_X(T,p) = \frac{X_P^p}{X_F^f \, X_O^o} = \frac{p_P p}{p_F p_O} = pK_P(T) \tag{2.48}$$

The dependence of the K's on T (together with the polynomial form of $c_p(T)$ and the values for the enthalpy of formation) are usually taken from the NIST-JANAF Thermocemical Tables.

The equilibrium chemistry approach allows enough simplification of the problem to provide, in some cases, analytical solutions for flame structures [44]. The assumption implies that chemical reactions proceed locally so fast that equilibrium is instantaneously reached. This may true when a 0-D domain is considered, as it has been done until now, but when a multidimensional field is studied the hypothesis might not hold true. In these cases other effects have to be considered, which can limit the reaction rates.

2.3.2 Fluid Dynamics

The physical phenomena involving fluids, heat exchange and chemical reactions are governed by the principles of mass, momentum and energy balances.

Those balances can be referred to a defined domain in the space, usually called "control volume" (CV). In fact, generally speaking, to study the dynamics of a continuum system it is possible to adopt a reference system that can be *eulerian* or *lagrangian*. In a lagrangian system, the observer moves with a control mass moving through the control volume; in the eulerian system the analysis is referred to a region of the problem fixed in the space.

In the following, an eulerian system will be used to derive the equations describing general combustion problems involving fluid in laminar or turbulent motions.

Balance Equations

The system of equations describing a turbulent flow, being reactive or non reactive, are one of the most well known set of equations in physics and mathematics. Firstly because they describe the physics of a huge variety of problems, but also because it has not yet been proven whether a solution always exists in three dimensions and, if it does exist, whether it is smooth. More rigorously, the so-called "Navier-Stokes equation" describes the momentum conservation for such a case, but it is common to use this naming to refer to all the three balance equations.

Hypothesis The fundamental hypothesis of the equations reported below are here listed:

- Newtonian Fluid: the viscous stresses are linearly proportional to the local strain rate (as will be seen later in eq.(2.54)). In other words, the stresses are proportional to the rates of change of the velocity field.

- Isotropic Fluid: the properties of the fluid are independent from the spatial direction.
- Local thermodynamic equilibrium: in the neighborhood of a point, the fluid is in mechanical, chemical, nuclear and electromagnetic equilibrium. This is a fundamental condition to describe unequivocally the state of a system.

Other hypothesis will be clarified in the single sections.

Mass Balance Considering a closed surface $\partial\Omega(t)$, defining a control volume $\Omega(t)$, the total mass conservation, in the most general form, reads:

$$\frac{dm}{dt} = 0. \tag{2.49}$$

From this general formulation, it is possible to obtain the following expression:

$$\frac{\partial\rho(\mathbf{x},t)}{\partial t} + \frac{\partial}{\partial x_i}(\rho(\mathbf{x},t)u_i) = 0 \tag{2.50}$$

where $\mathbf{x}$ is the spatial vector, $\mathbf{u}$ is the flow velocity and t is the time. The Einstein notation is used for the index i[11]. In a steady state case (or when the density does not vary with the time), the eq. 2.50 is simplified including only the divergence of the flow velocity.

The global mass balance is not impacted by the combustion process, and stays the same in reactive and non reactive cases. It is possible to express the mass balance also for a single species k in the system:

$$\frac{\partial\rho Y_k}{\partial t} + \frac{\partial}{\partial x_i}(\rho\, u_i\, Y_k) = +\frac{\partial}{\partial x_i}\left(\rho\,\mathcal{D}_k\frac{\partial Y_k}{\partial x_i}\right) + \dot{\omega}_k$$

being $\mathcal{D}_k$ the molecular diffusivity of the species k in the mixture. An alternative approach may be based on the use of the binary diffusion coefficient of k respect to the dominant species. Clearly, a simplification is made in the assumption of considering only diffusion of k respect to a dominant species (N_2, for example). The diffusion effect may be described with the Fick's law[12] (see eq.(2.60)). The last term of the RHS, $\dot{\omega}_k$, is the reaction rate of k.

[11] Given a vector field $\mathbf{F} = \{F_x\hat{x}, F_y\hat{y}, F_z\hat{z}\}$ continuously differentiable, the divergence of $\mathbf{F}$ is noted as follows:

$$\nabla\cdot\mathbf{F} = \frac{\partial F_x}{\partial x} + \frac{\partial F_y}{\partial y} + \frac{\partial F_z}{\partial z}.$$

With the Einstein notation the RHS can be written equivalently as follows:

$$\frac{\partial F_i}{\partial x_i}$$

meaning that the index i is used in place of the (generally) n dimension of $\mathbf{F}$ and a summation is applied over it.

[12] There are also other approaches to model this effect, for example the use of a diffusion velocity V_k for each species. The Hirschfelder and Curtiss approximation allows for the calculation of V_k:

$$V_k X_k = -D_k\nabla X_k$$

where D_k depends on the species binary diffusion coefficients.

Momentum Balance This balance comes directly from the second Newton principle:

$$\frac{d(m\mathbf{u})}{dt} = \sum \mathbf{F} \tag{2.51}$$

where the **F**'s are the forces applied on the fluid. They can be:

- Surface forces: applied on the surface of the control volume (pressure, stresses, surface tension, ...)
- Body forces: involving the entire volume, that can be described as applied of the center of mass of the control volume.

The Navier-Stokes reads:

$$\frac{\partial}{\partial t}(\rho u_j) + \frac{\partial}{\partial x_i}(\rho\, u_i\, u_j) = -\frac{\partial p}{\partial x_j} + \frac{\partial \tau_{ij}}{\partial x_i} + \rho \sum_{k=1}^{N} Y_k f_{k,i} \tag{2.52}$$

rearranged in:

$$\frac{\partial}{\partial t}(\rho u_j) + \frac{\partial}{\partial x_i}(\rho\, u_i\, u_j) = \frac{\partial \sigma_{ij}}{\partial x_i} + \rho \sum_{k=1}^{N} Y_k f_{k,i} \tag{2.53}$$

where $f_{k,j}$ is the volume force acting on the species k in direction j.

The tensor $\underline{\underline{\tau}}$ in eq.(2.52) is called "viscous tensor", and accounts for the interaction between an element of fluid and the surrounding elements:

$$\tau_{ij} = \mu\left(\frac{\partial u_i}{\partial x_j} + \frac{\partial u_j}{\partial x_i} - \frac{2}{3}\frac{\partial u_k}{\partial x_k}\delta_{ij}\right) \tag{2.54}$$

with δ_{ij} the Kronecker delta and μ the dynamic viscosity. It is clear from the definition itself that when the fluid is not in motion ($\mathbf{u} = 0$), the tensor is null. The first components of the $\underline{\underline{\tau}}$ definition in the eq.(2.54) represents, apart from a constant, the rate of strain tensor, usually noted $\underline{\underline{S}}$ [5], composed by the velocity gradients:

$$S_{ij} = \frac{1}{2}\left(\frac{\partial u_i}{\partial x_j} + \frac{\partial u_j}{\partial x_i}\right) \tag{2.55}$$

It describes the rate of change of the deformation of the fluid.

Given that the static pressure p is a force uniformly applied on the surfaces of the elementar cube of fluid, it is common to combine the surface stresses included into $\underline{\underline{\tau}}$ and the ones applied by the pressure in a unique tensor $\underline{\underline{\sigma}}$

$$\underline{\underline{\sigma}} = \underline{\underline{\tau}} - p\underline{\underline{I}} \tag{2.56a}$$

or

$$\sigma_{ij} = \tau_{ij} - p\delta_{ij} = -p\delta_{ij} - \frac{2}{3}\mu\frac{\partial u_k}{\partial x_k}\delta_{ij} + \mu\left(\frac{\partial u_i}{\partial u_j} + \frac{\partial u_j}{\partial u_i}\right) \tag{2.56b}$$

Commenting eq.(2.53) with Poinsot and Veynante [44], there are no explicit reaction terms (as for example in the species balance). Despite of that, the impact of the combustion process on the balance derives from the changes in some of the quantities in the equation. The variation of the temperature in a ratio of 1:8 or 1:10 implies a strong change also in the dynamic viscosity and in the density. The velocities are also increased by the dilatation through the flame front.

Energy Balance The energy balance can take a number of different forms, depending also on which terms are neglected or if simplifications are applied. A balance for the energy, including the sensible and chemical contributions:

$$\frac{\partial \rho e}{\partial t} + \frac{\partial}{\partial x_i}(\rho u_i e) = -\frac{\partial q_i}{\partial x_i} + \frac{\sigma_{ij}\partial u_i}{\partial x_j} + \dot{Q} \tag{2.57}$$

An analysis of the terms in the eq.(2.57) is helpful. The term **q** accounts for the thermal energy fluxes. It includes conduction and diffusion. The conductive part is usually described by the Fourier's Law:

$$q_i^c = -\lambda \frac{\partial T}{\partial x_i} \tag{2.58}$$

where λ [J/mKs] is the thermal conductivity.
The diffusion term can be written in different expressions, one of the most used is

$$q_i^d = \sum_{k=1}^{N} h_k J_{k,i} \tag{2.59}$$

where the Fick's law is used for the flux **J**:

$$J_{k,i} = -\rho \mathcal{D}_k \frac{\partial Y_k}{\partial x_i} \tag{2.60}$$

Another approximation is done considering negligible the Dufour effect, i.e. that there is no thermal energy transfer forced by the concentration gradients. The term $\dot{Q}$ accounts for external thermal sources as a spark, for example, or for radiative heat transfer. This last case is particularly complex, and usually requires a specific treatment, with an appropriate modelling. The effect of volume forces on the species has been neglected in the formulation of the eq.(2.57).

Impact of Turbulence

A universally accepted definition of turbulence does not exist in literature. Speaking about "turbulence" alone is not formally correct, but rather one should use the term to indicate a characteristic of a flow or a motion; it is then more correct to talk about "turbulent flow" or "turbulent motion". Some peculiarities of a turbulent motion can be highlighted, being:

- Intrinsically unsteady; quantities such velocity, pressure, density and concentrations show a clear time dependence, even in cases with steady boundary conditions.
- Three dimensional; the flow structures develop in the space, and cannot be confined on a line or a plane.
- Stochastic; a strong sensibility on initial conditions is always present.
- Characterized by a wide range of dimensional scales; both length and time scales vary over several orders of magnitude. This brings the need of describing very small scales as well as phenomena taking place at larger scales.
- Dissipative; the viscosity is responsible for converting the kinetic energy of the flow into internal energy.
- Capable of intense mixing; the flow mixing in presence of turbulence is enhanced if compared to the mixing in a laminar flow.

A fundamental non dimensional parameter used to characterize a turbulent flow is the Reynolds number:

$$Re = \frac{u\rho\ell}{\mu} = \frac{u\ell}{\nu} = \frac{\text{Inertial Forces}}{\text{Viscous Forces}} \tag{2.61}$$

with u and ℓ respectively a characteristic velocity and length of the flow, while μ is the kinematic viscosity.

A high Re results in flows in which the inertial forces are dominant over the viscous forces, while small Re are typical of the inverse case. This aspect is explained by another characteristic of a turbulent flow: the general structure of a turbulent flow is one that consists of large eddies created by abstracting energy from the mean flow motion. These eddies then continuously break up into smaller ones until a certain size range is reached over which viscous dissipation becomes effective. This is the "cascade" concept of turbulent flows and will be later better explained. Large Re promotes the existence of turbulent flows because a large amount of kinetic energy is needed to sustain the generation of turbulent eddies, which are eventually dissipated through viscous action [46].

Generally speaking, it is possible to refer to the following classification (which has to be intended in terms of order of magnitude) for a generic pipe flow, with respect to the Reynolds number [49]:

- $Re < 2000$: laminar flow;
- $2000 < Re < 4000$: transition regime;

- $Re > 4000$: turbulent flow.

Glassman et al. highlight that, approximately, $\nu \propto T^2$ [47]. Thus, a change in temperature by a factor of 3 or more, quite modest by combustion standards, means a drop in Re by an order of magnitude. Thus, energy release can damp turbulent fluctuations.

Reynolds and Favre Decompositions The unsteady and three-dimensional nature of a turbulent flow field, together with the small scale variations of turbulent quantities, as well shown by the fig.2.11, make useful to separate, in a generic flow characteristic quantity, an average part from a fluctuating contribution:

$$f(\mathbf{x}, t) = \bar{f}(\mathbf{x}, t) + f'(\mathbf{x}, t) \tag{2.62}$$

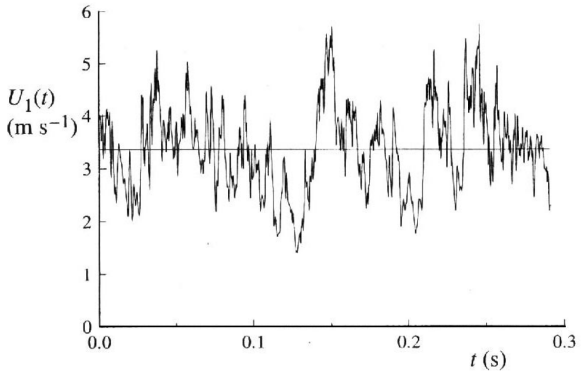

Figure 2.11: The time history of the axial component of velocity on the centerline of a turbulent jet. From the experiment of Tong and (1995). Reproduced from [40]

The mean part can be calculated using different averaging processes:

- Time averaging:

$$\bar{f}_i(\mathbf{x}, t) = \frac{1}{T - t_0} \int_{t_0}^{T} f_i(\mathbf{x}, t')dt'$$

  where $T - t_0$ is a time interval long enough for not affecting the result of the integration. For a steady mean flow, the quantity does not depend on the time: $\overline{\bar{f}_i(\mathbf{x})} = \bar{f}_i(\mathbf{x})$.

- Spatial averaging:

$$\bar{f}_i(\mathbf{x}, t) = \frac{1}{V} \int_V f_i(\mathbf{x} + \mathbf{r}, t)d\mathbf{r}$$

  If the results of the integration does not depend on the integration domain V, then the flow is called a spatially uniform (homogeneous) mean flow [6].

- Ensemble averaging:

$$\bar{f}_i(\mathbf{x}, t) = \frac{1}{N} \sum_{n=1}^{N} f_{i,n}(\mathbf{x}, t_n)$$

  In this case the average of a large number of realizations at the same location of the same flow field is calculated, and is applicable when it is possible to statistically replicate a flow field motion.

Given the above mentioned averaging techniques, the decomposition in mean and fluctuating part can be achieved using two approaches, the Reynolds and the Favre decompositions. The Reynolds one is the already presented eq.(2.62), while the Favre (or mass weighted) is given by:

$$f(\mathbf{x},t) = \tilde{f}(\mathbf{x},t) + f''(\mathbf{x},t) \tag{2.63}$$

where $\tilde{f} \equiv \frac{\overline{\rho f}}{\bar{\rho}}$. The Fabre decomposition is useful when describing flows with a significant variation of the density.

Given these decompositions it is possible to introduce the turbulence intensity:

$$I = \frac{\sqrt{\overline{(f')^2}}}{\bar{f}} \tag{2.64}$$

i.e. the ratio between the root mean square of the fluctuations f' and the man value $\bar{f}$, and is an indicator about the turbulence strength [50].

The turbulence intensity is anyway not sufficient to characterize a turbulent flow (nor reactive or non-reactive), for several reasons. Among them, it is worth to mention that some turbulent fluctuations are associated with the largest scales of the problem, and some to the smallest one. Later in this section some information will be given about the mentioned scales, but first another important concept has to be pointed out.

Homogeneous Isotropic Turbulence In real turbulent flows the spatial components of the vector fields are not equal one to another. A physical description would then be very complex. To overcome to this difficulty it is common to use a simplified model. Generally the concept of statistically stationary, homogeneous and isotropic turbulence is used for this purpose [40]:

- Statistically stationary: all the averaged quantities of turbulence are invariants under a shift of time, while instantaneous pulsations (i.e. the terms with the apex of eq.(2.62)) depend on t.
- Statistically homogeneous: the averaged quantities are invariants under arbitrary translation of coordinate axes.
- Statistically isotropic: the average quantities are invariants under arbitrary rotations of coordinate axes. In formula: $\overline{(f_i')^2} = \overline{(f_j')^2} = \overline{(f_k')^2}$, while $f_i'(\mathbf{x},t) \neq f_j'(\mathbf{x},t) \neq f_k'(\mathbf{x},t)$.

In the following the hypothesis above described will be assumed.

Energy cascade, Length Scales and Timescales According to Richardson's view, as reported by Pope [40], the turbulence can be considered to be composed of eddies of different sizes. Given a size, say ℓ, an eddy also has a characteristic velocity $u(\ell)$ and a timescale $\tau(\ell) \equiv \ell/u(\ell)$. The definition of "eddy" is not broadly accepted (on the contrary of the concept itself, which is instead widely used). In general, an eddy identifies an area of the turbulent motion with coherent characteristic [40]. An eddy can also contain smaller eddies.

The largest eddies have a length scale close to the flow scale, the "integral scale" ℓ_0. Their Reynolds number is high, being $Re(\ell_0) \propto \ell_0$ (see eq.(2.61)) and being this length scale the highest existing in the system. The effects of viscosity are indeed small for these eddies, as expected for high Re. These eddies are then unstable and tend to break up, transferring their energy to smaller scales in the fluid, where smaller eddies are formed. Those eddies experience the same kind of process and transfer their energy - taken from the larger eddies - to even smaller scales. This process is called for clear reasons "energy cascade", and takes place in the motion down to the scales where the molecular viscosity can play a role in dissipating the kinetic energy, stabilizing the eddies. A sketch illustrating this process is reported in fig.2.12. From

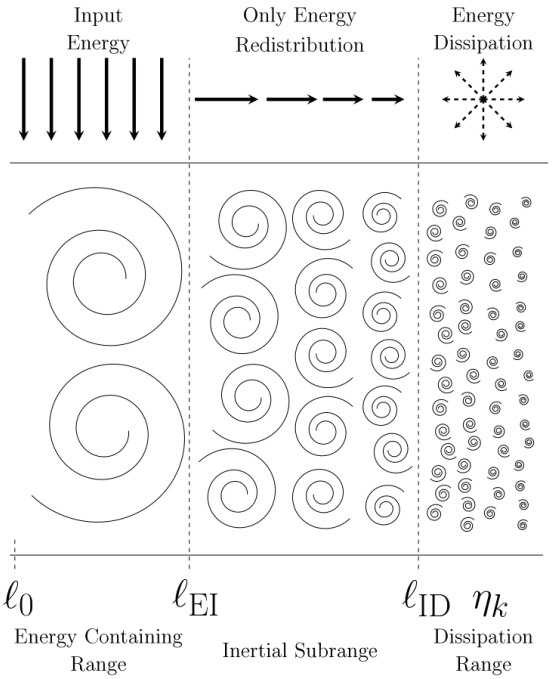

Figure 2.12: Sketch representing the energy cascade process in a fully developed turbulence. The energy input occurs by the eddies at the integral scale, between ℓ_0 and ℓ_{EI} (where the subscript "EI" remarks the separation from the energy and the inertial subranges). The energy is redistributed through the inertial subrange and is dissipated for the eddies smaller than ℓ_{ID}. Adapted from [51]

the description reported by Pope [40], it is also pointed out that the rate at which the energy is transferred is determined by the first step of the cascade, and is afterwards constant till the viscous dissipation. This rate is easily estimated considering that, if the largest eddies have a characteristic velocity u_0 and a timescale $\tau_0 = \ell_0/u_o$, the rate of transfer, indicated with ε is

$$\varepsilon = u_0^2/\tau_0 = u_0^3/\ell_0 \tag{2.65}$$

As already said, the cascade effect proceeds as long as the inertial forces are dominant over the viscous ones, with the Reynolds number decreasing more and more from the integral scale to a unitary value. The lower limit determines the smallest scale found in the turbulent flow [44], the Kolmogorov scale η_k, defined by ν and ε:

$$\eta_k = \left(\frac{\nu^3}{\varepsilon}\right)^{1/4} \tag{2.66}$$

The definition of η_k is based on ν and ε, from the Kolmogorov theory (1941), because those are defining the two dominant processes in the cascade, namely the transfer of energy and the viscous dissipation. Together with η_k, it is possible also to find from the same two parameters that:

$$u_k = (\varepsilon\,\nu)^{1/4} \qquad ; \qquad \tau_k = (\nu/\varepsilon)^{1/2} \tag{2.67}$$

and it is easy to prove, as stated, that:

$$Re(\eta_k) = \frac{u'_k\,\eta_k}{\nu} = \frac{\varepsilon^{1/3}\,\eta_k^{4/3}}{\nu} = 1 \tag{2.68}$$

remembering that it is possible to write that $\varepsilon = u_k^3/\eta_k$.

It is possible to find that the ratio between the integral length scale and the Kolmogorov scale is given by:

$$\frac{\ell_0}{\eta_k} = \frac{u^3/\varepsilon}{(\nu^3/\varepsilon)^{1/4}} = Re_{\ell_0}^{3/4} \tag{2.69}$$

where Re_{ℓ_0} is referred to the integral scale.

2.3.3 Premixed Combustion

After an overview of the reacting gas mixtures and of the peculiarities of the turbulent flows, in this part premixed combustion will be analyzed. The section will start from laminar premixed flames, and then will proceed adding the complexity of turbulence to premixed combustion.

A premixed flame can be seen as a deflagration wave propagating in a gas mixture that lies within the flammability limits. The flame front propagates towards the fresh mixture, where exist the conditions for the reaction to take place, and leaves behind a burnt mixture of combustion products at a temperature in the order of the adiabatic flame temperature, in a condition close to the chemical equilibrium[13]. As usual for deflagration processes, the pressure change across the wave is not significant, while the density ratio is $\sigma = \rho_u/\rho_b = 6 \div 8$ [6] (in the order of T_b/T_u).

Laminar Premixed Flame

A simple yet effective overview of the phenomenology of the physical mechanism of a laminar premixed flame is given by Lipatnikov [6].

The core process controlling the flame propagation are the molecular transport and the chemical reactions: as seen, one of the effects of the chemical reactions is the release of thermal energy. A portion of this energy is transported by molecular heat conductivity to the fresh gas mixture, increasing its temperature, in the region ahead the zone where the system's reactivity is high and from which the thermal energy is released. The temperature increase triggers the reactivity in the heated area of the fresh mixture, and the flame propagates toward this zone. The flame is then "self sustained", because the thermal energy necessary to activate the reactions in the fresh mixture is provided by the flame heat release.

Fundamental quantities of this type of flames can be computed analytically using for example the thermal theory of laminar premixed flames, also known as "activation-energy asymptotic", developed by Zel'dovich and Frank-Kamenetskii (1938). It is beyond the goal of this work to detail this approach, and only selected results will be shown and commented from this theory[14].

Laminar Flame Speed The notation s_L^0 is used to indicate the propagation speed of a planar, 1-D, steady, adiabatic flame. A sketch of such a flame is reported in fig.2.13, where the premixed flame is seen as a propagating deflagration wave. The subscript u is for the quantities characterizing the unburnt mixture, while b is for the burnt one. The arrows show the direction of the flow velocities. The velocity s_L^0 is called "laminar flame speed". Perturbations such as heat losses or non uniformities will have an impact on the flame speed, but usually the impact itself is small when compared to s_L^0.

Applying the continuity equation to the case reported in fig.2.13, it is possible to demonstrate that the mass flow rate through the flame is constant [5]. This allows for a definition of s_L^0:

$$(\rho u)_{-\infty} = \left(\rho s_L^0\right)_u \tag{2.70}$$

[13] If complete combustion has taken place.

[14] For a complete treatment it is possible to refer, among the others, to [5, 6, 44, 46].

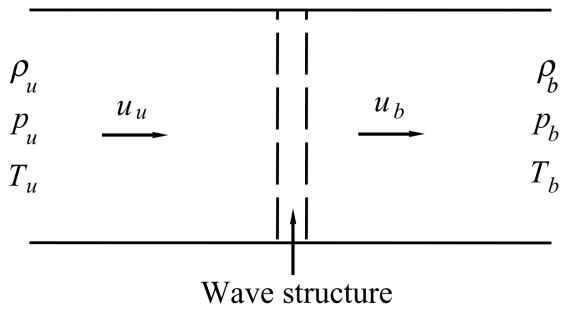

Figure 2.13: Schematic of the one-dimensional planar combustion wave in a mixture. The subscript u is for the quantities characterizing the unburnt mixture, while b is for the burnt one. The arrows show the direction of the flow velocities. Reproduced from [46].

where the subscript $-\infty$ refers to the unperturbed fresh mixture, far from the flame.

A simple approach for finding the laminar flame velocity in a different configuration is presented by Peters, using a kinematic balance on a steady oblique flame recalling the one which can be established on a Bunsen burner, as shown in fig.2.14.

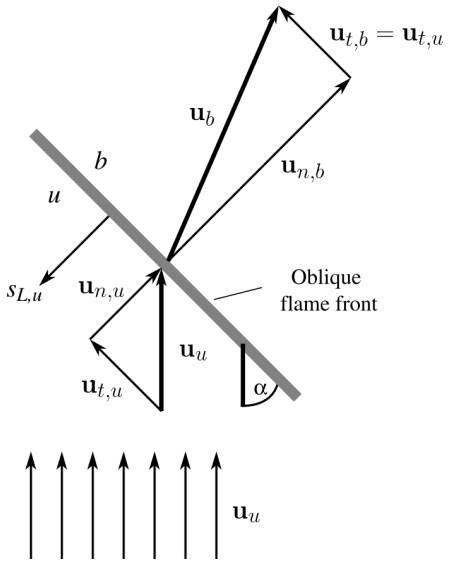

Figure 2.14: Kinematic balance on an oblique flame. Adapted from [5]

The flow velocity of the fresh gases, noted $\mathbf{u}_u$, as shown in fig.2.14, can be split into two components:

$$\mathbf{u}_u = \mathbf{u}_{t,u} + \mathbf{u}_{n,u} \tag{2.71}$$

One component is normal to the flame front (subscript n) and the other is tangential (t).

The mass continuity must hold through the flame front:

$$(\rho \mathbf{u}_n)_u = (\rho \mathbf{u}_n)_b \Rightarrow \mathbf{u}_{n,b} = \mathbf{u}_{n,u} \frac{\rho_u}{\rho_b} \tag{2.72}$$

From this relation, considering that $\rho_b < \rho_u$, it follows that $\mathbf{u}_{n,b} > \mathbf{u}_{n,u}$, that is the normal velocity component on the burnt gas side is larger than the one on the unburnt side because of the gas thermal expansion within the flame front.

An analog continuity relation can be derived for the tangential component, with the difference that in this case no gas expansion is involved, and then $\mathbf{u}_{t,b} = \mathbf{u}_{t,u}$.

Reconstructing $\mathbf{u}_b = \mathbf{u}_{t,b} + \mathbf{u}_{n,b}$, follows that the velocity on the burnt side points in a direction deflected from the direction of the velocity in the unburnt mixture [5] and has larger magnitude.

Peters also highlights that "since the flame front is stationary in this example, the burning velocity with respect to the unburnt mixture must be equal to the flow velocity of the unburnt mixture normal to the front":

$$s_L^0 = u_{n,u} = u_u \sin\alpha \tag{2.73}$$

if α is the angle between the flame and the vertical line.

Characteristic lengths The definition of some flame characteristic lengths will be given in the following part.

The "preheat zone" is the region of the flame where the reaction rate is neglegible, and its structure is controlled by convection and molecular transport. The "reaction zone" is on the contrary the region where convection plays a minor role and the structure is controlled by the reaction rate and molecular transport.

The reaction zone is much thinner than the preheat zone, and the flame thickness is approximately equal to the thickness of the preheat zone. The dimension of this region can be estimate using the temperature profile [44]:

$$\delta_L^0 = \frac{T_b - T_u}{\max\left(\left|\frac{\partial T}{\partial x}\right|\right)} \tag{2.74}$$

The laminar flame thickness may be expressed also on the base of laminar flame speed and thermal diffusivity[15] a_u [6], leading to:

$$\delta_L^0 \equiv \frac{a_u}{s_L^0} \tag{2.75}$$

Again in the Lipatnikov description of the thermal theory, a ratio between the preheat zone thickness and the reaction zone thickness, δ_r is given, with

$$\delta_r = \delta_L^0 / Ze \quad \text{with} \quad Ze = \Theta \frac{T_b - T_u}{T_b^2} \tag{2.76}$$

being Θ defined as an activation temperature for the singe-reaction model on which the thermal theory is based (Θ = 15e3 ÷ 20e3 K).

The ratio coming from eq.(2.76), with $\delta_L^0 >> \delta_r$, is a direct consequence of the hypothesis on which the thermal theory is based on, i.e. single-step chemistry and high activation temperature. In real cases, even if it is valid that the reaction zone is thinner than the preheat zone, a more realistic relation would be

$$\delta_r = 0.2 \div 0.5\ \delta_L^0$$

[15]This formula comes from a manipulation of the progress variable that leads to write $\delta_L^0 = (\rho_b D_b)/(\rho_u s_L^0)$. Using the assumptions that ρD = const and replacing the molecular diffusivity D_u with the thermal diffusivity a_u under the hypothesis that $Le = 1$, from this expression for the flame thickness comes that $\delta_L^0 \equiv a_u / s_L^0$.

due to several effects not included in this description, as the complex chemistry.

Figure 2.15 shows two schematizations of laminar premixed flames. In both the cases the temperature profile is plotted on the spatial coordinate, together with the oxidizer mass fraction. The first schematization, fig.2.15a, reflects the thermal theory, with the reaction zone thickness significantly smaller than the flame thickness. The second case, fig.2.15b, is a more realistic representation and accounts for more complex effects. It is indeed possible to notice that the reaction rate has a significant value only within the reaction zone thickness. The latters remains thinner than the flame thickness, but is wider than in fig.2.15a.

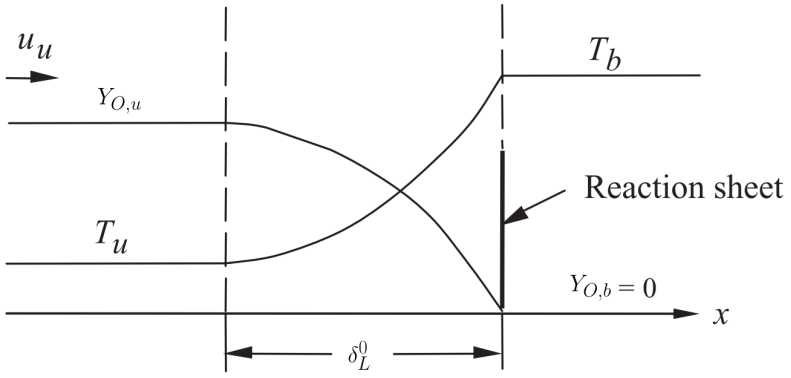

(a)

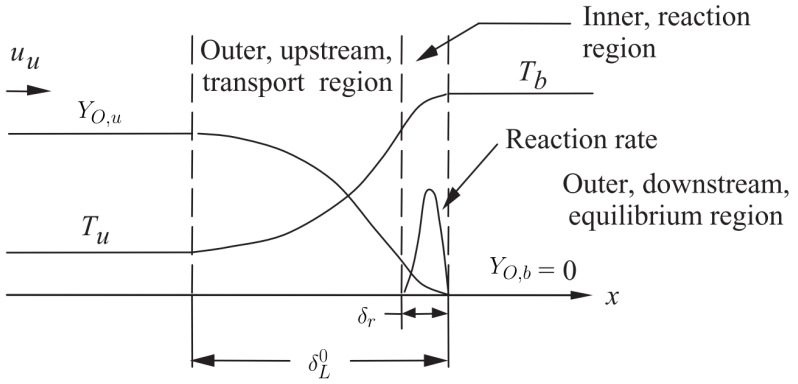

(b)

Figure 2.15: Flame structure as described by the thermal theory (a) and a more realistic structure of a laminar premixed flame (b). Temperature and oxidant mass fraction profiles are plotted in the spatial coordinate. In (b) also the reaction rate is qualitatively plotted. Adapted from [46].

Turbulent Premixed Flame

The presence of turbulence in the flow field may have a strong impact on the structures and the phenomena of a premixed flame.

Among the impacts, Lipatnikov highlights a thicker flame brush, respect to a laminar flame case (see fig.2.16); Poinsot and Veynante add also that the interaction between the laminar flame and the eddies of the turbulent flow can lead to a strong increase of the mass consumption rate.

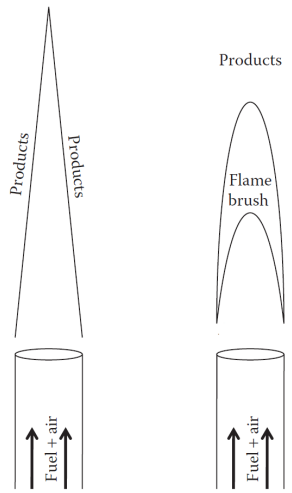

Figure 2.16: Schematic representation of laminar (left) and turbulent (right) Bunsen premixed flames. Note as the mean flame brush in the turbulent case is thicker than the laminar one. In addition, the thickness of the case on right increases while moving downstream from the burner exit. Adapted from [6].

Flame Wrinkling The most visible effect of the difference between a turbulent and a laminar premixed flame is probably the flame wrinkling. As reported in [44], Damköhler in 1940 introduces wrinkling as the main mechanism controlling turbulent premixed flames. In this theory a turbulent flame speed s_T is defined as the velocity needed at the inlet of a control volume V to keep a turbulent premixed flame stationary in the mean inside this volume. This velocity can be related to the laminar flame speed by the ratio of the turbulent flame surface and the cross section of V, A:

$$\frac{s_T}{s_L^0} = \frac{A_T}{A} \equiv \Xi \tag{2.77}$$

where Ξ is a flame wrinkling factor, and increases with the Reynolds number.

This relation explains the increase of the turbulent flame speed if compared to the laminar flame speed as depending on a higher flame surface, with a consequent higher fuel consumption rate.

Figure 2.17 helps to visualize the wrinkling effect of the turbulence. The figure refers to the case in which the inner structures of the flame are not influenced by the turbulent eddies, i.e. the asymptotic case of an infinitely thin laminar flame. In the figure for the turbulent flame an instantaneous flame front is sketched, as well as a thickness of

the mean flame brush and its location. Lipatnikov explains that, if it is true that the effect of the turbulence flow on the combustion is restricted only to the wrinkling of an inherently laminar flame, then the burning rate is controlled by the self-propagation of the front at speed s_L^0 and by the above mentioned increase of the flame surface.

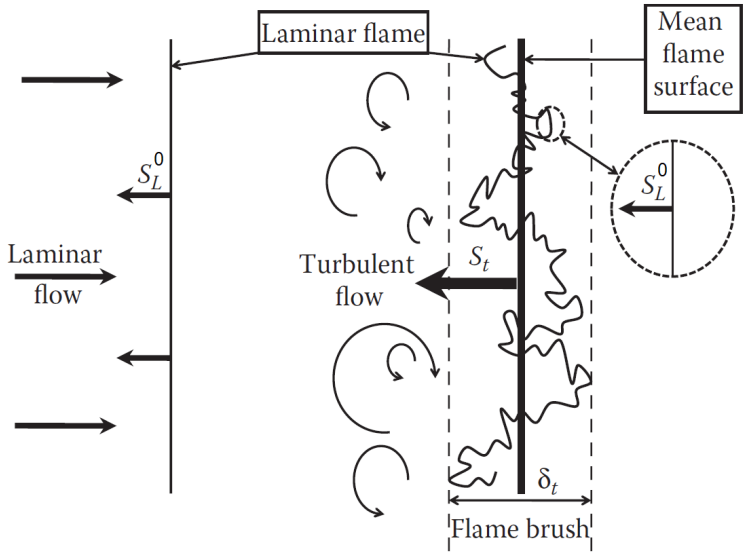

Figure 2.17: A sketch of laminar (left) and turbbulent (right) premixed flame. The sketch shows the local portion of the wrinkled flame self-propagating at velocity equal to s_L^0, whit the whole flame propagating at the turbulent velocity s_T. Reproduced from [6].

Flame Stretch When a flame propagates in non uniform flows, it might experience strain and curvature effects, leading to a change in the flame area referred to as "stretch" k [s^{-1}] and defined as

$$k = \frac{1}{A}\frac{dA}{dt} \tag{2.78}$$

For a detailed analytical description of the flame stretch it is possible to refer, for example, to [44]. Here it is sufficient to report that "the orientation of flame fronts relative to velocity gradients is a critical parameter for flame stretch: only velocity gradients in the flame tangent plane induce flame stretch". Another contribution to the stretch is given by the curvature effects, and describes the change in A as a curved surface propagates normally to itself [52].

The interaction geometry shown in fig.2.18 is commonly employed to explain the interaction between the flame and the turbulence structures, following the first applications by Poinsot, Veynante, Candela and many others[16]. In this canonical configuration, a pair of 2-D counter rotating vortices are impinged on a planar laminar flame. The interaction between these structures will generate a positive strain-rate along the centerline, and the flame will be wrinkled with a structure concave towards the reactants (negative curvature). After the interaction, the flame surface continues to propagate normal to itself and a cusp with high negative curvature develops. Even if widely accepted, this example is a simplification, given that in a turbulent flow not only isolated counter rotating vortices are present.

[16]See [52] for a wide list of works

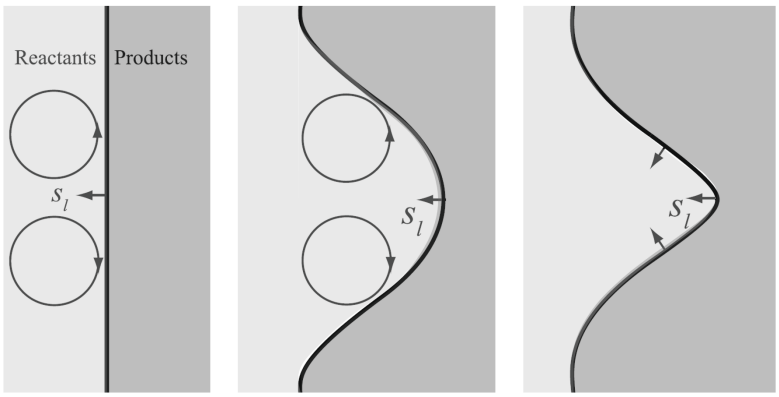

Figure 2.18: Canonical flame–vortex interaction, adapted from [52].

Despite the simple configuration, the representation of fig.2.18 allows for relevant considerations regarding the effects of the curvature on the flame behavior. Indeed, depending on the curvature, the diffusion mass flow and the heat flux will have different orientations. For a better understanding, in fig.2.19 the two fluxes are schematically represented in two cases, one with negative curvature, the other with positive curvature. From the representation of fig.2.19 it is possible to notice that in the case with

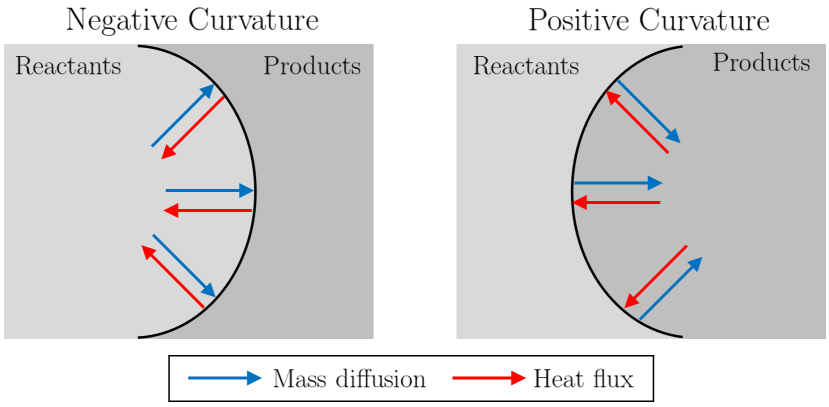

Figure 2.19: Diffusion mass flux and heat flux orientations in negative (*left)* and positive (*right*) curvature cases. The black line sketches the flame position.

positive curvature the heat flux is divergent towards the reactants, meaning that it is divergent also towards the flame preheat zone. This will result in reductions of the local temperature and of the flame speed. The diffusion of reactants to the flame surface is instead enhanced by a convergent orientation, contributing to increase the propagation velocity. The result of these counter-acting phenomena depends on the dominance of their respective effects.

In this context it is useful to introduce the "Lewis number", Le. This dimensionless number is used to compare the diffusion of heat and species. If λ is the heat diffusion coefficient [W/mK] and $\mathcal{D}_k$ [m^2/s] is the diffusion coefficient of the species k in the rest

of the mixture[17], the Lewis number is defined as

$$Le_k = \frac{\text{Thermal Diffusion}}{\text{Molecular Diffusion}} = \frac{\lambda}{\rho C_p \mathcal{D}_k} \; [=] \; \frac{\frac{W}{mK}}{\frac{kg}{m^3}\frac{J}{kgK}\frac{m^2}{s}} \; [=] \; - \tag{2.79}$$

Being $\lambda/\rho C_p$ the heat diffusivity coefficient, it is clear how Le expresses indeed the relation between heat and species diffusivity.

The role of Le is, as anticipated, important for the understanding of the effects of the curvature on the flame speed. In cases with $Le > 1$, as for heavy hydrocarbons, and in presence of positive curvature, the net effect of heat and mass diffusion will be a reduction in the flame speed because the effects of the divergent thermal flux dominates the effects of the converging mass flux. Duality is valid with $Le > 1$ and negative curvature. This situation is stable: the flame front will straighten out as a consequence of the reduction/increase of the flame speed in positive/negative curvature flames.

The cases with $Le < 1$, such as hydrogen/air premixed flames, will experience an increase/decrease of the flame speed in presence of positive/negative curvature [5]. In both the cases the curvature will increase, resulting in an unstable configuration: a self-induced wrinkling may result even in planar, laminar flames.

Being methane characterized by $Le \simeq 1$, the described mechanisms activated by the flame curvature don't play a relevant role, being the fluxes balanced in terms of their effects. Methane flame are then relatively insensitive to the flame curvature [53].

Flame effects on the turbulence Up to this point the focus of this section was mostly on the changes induced on the flame structure by the presence of a turbulent flow field. It is also true that the interaction takes place in the other "direction": the flame structure, with its reactivity, can cause effects on the turbulent flow field.

Poinsot and Veynante in [44] provide an interesting yet simple insight on this aspect, highlighting the consequences of the temperature change between the reactant side and the product side of a flame. Considering that (in air) the kinematic viscosity increases with the temperature according to the relation $\nu(T) \propto T^{1.7}$, and that in a typical flame configuration $T_b/T_u \simeq 8$, it follows that $Re_b \simeq Re_u/40$:

$$\begin{cases} \nu(T) \approx T^{1.7} \\ T_b/T_u \simeq 8 \end{cases} \quad \text{and} \quad Re \propto \nu^{-1} \Rightarrow \quad Re_b \simeq \frac{Re_u}{40} \tag{2.80}$$

This change of more than one order of magnitude, can induce a "relaminarization" on the flow, that is, the turbulent flow might become laminar after the heat release zone.

A second effect of this interaction, also pointed out by the same authors, is the flow acceleration through the flame front. The continuity equation (ρu = const.) written in the flame reference frame can prove that the flow velocity downstream the flame front is higher that the one upstream, by an additive factor proportional to $s_L^0 \, T_b/T_u$: considering a laminar flame velocity of 0.5 m/s, the difference can then be in the order of 4 m/s.

[17] The diffusion process is intrinsically involving two species and it is more correct to consider the binary diffusion coefficient of a species into another. Nevertheless, the hypothesis that there is a dominant species (in terms of concentration) in the mixture, allows for the simplification widely adopted of using a law including only $\mathcal{D}_k$ [44].

Turbulent Premixed Combustion Regimes

In the previous part some general features of laminar and turbulent premixed combustion have been presented. A focus on the turbulent cases will be here proposed, specifically on the different regimes that can be established in this context. The classification of different cases into groups with analogies and similar peculiarities is based on the analysis of characteristic lengths and time scales.

A first classification is based on a time scale analysis, through the analysis of the Damköhler number [-]:

$$Da = \frac{\tau_m}{\tau_c} \tag{2.81}$$

If τ_m is a characteristic time scale of the turbulent mixing, and τ_c is instead a time scale for the chemistry, Da allows for quantifying which one, among the two, is the time limiting process:

> $\boldsymbol{Da >> 1} \rightarrow \tau_m > \tau_c$: the chemistry is faster than the turbulent mixing. It follows then that the turbulence is not able to modify significantly the chemistry, and more in general that it is not able to interact with the inner structures of the flame. The latter remains then close to a laminar flame wrinkled by the turbulent motion: this case is defined "flamelet".
>
> $\boldsymbol{Da << 1} \rightarrow \tau_m < \tau_c$: the turbulent mixing happens in a short time if compared to the chemical reactions. As a consequence the turbulence can change the reaction dynamics. If the mixing is significantly faster then the chemistry, the flame is similar to a Perfectly Stirred Reactor (PFR) and reactants and products are continuously mixed in a time shorter than the chemical time.

It can be useful to describe the Damköhler number also in terms of other quantities, simply considering that a time scale is given by the ratio of the relative length scale and velocity:

$$Da = \frac{\tau_m}{\tau_c} = \frac{\ell_t / u'}{\delta / S_L^0} \tag{2.82}$$

remembering that ℓ_t is referring to the integral length scale and δ to the flame thickness.

The turbulence characteristic time depends on the length scale at which it is computed, and this dependence is also transferred to Da. Several choices can be made for τ_m, and the most common is the integral time scale τ_t. Nevertheless the need of defining another non-dimensional number arises, to help in the analysis: the Karlovitz number, Ka [-]. It is referred to the smallest scales, i.e. the Kolmogorov scale η_k, and is indeed the ratio between the chemical time scale and the turbulent time scale referred to η_k:

$$Ka = \frac{\tau_c}{\tau_k} \tag{2.83}$$

It can be proved that, if Re_t is the Reynolds number referred to the integral time scale, $Re_t = Da^2\, Ka^2$. The Karlovitz number can be equivalently written in terms of length scales:

$$Ka = \frac{\delta / S_L^0}{\eta_k / u'(\eta_k)} = \left(\frac{\delta}{\eta_k}\right)^2 \tag{2.84}$$

where δ is the flame thickness and (as usual) η_k the Kolmogorov scale.

The use of Ka defined as above allows for a sub-classification of the cases in which $Da > 1$:

- $Ka < 1 \rightarrow \delta < \eta_k$: the flame thickness is smaller than the size of the Kolmogorov turbulence structures. This is the case properly defined as "flamelet regime", with a thin flame wrinkled by the turbulent flow, without any impact of the turbulence on the inner structures of the flame.

- $Ka > 1 \rightarrow \delta > \eta_k$: the Kolmogorov structures and the flame thickness are in such a ratio that the smallest turbulent structures could penetrate the flame structure. In such a case, remembering the scheme presented in figure 2.15b, given that the reaction zone thickness δ_r is smaller than the preheat zone, it is more likely that the turbulent mixing affects only the latter, without a direct alteration of the flame reaction layer.

- There is also the case in which the turbulence is so intense that its structure may penetrate the reaction layer, too. This possibility is met when the Kolmogorov scale is comparable to this flame inner layer, i.e.: $\eta_k = \delta_r$. Applying this condition to the definition of Ka it is possible to find a transition value Ka_r:

$$Ka_r = \left(\frac{\delta}{\delta_r}\right)^2 \tag{2.85}$$

  Given that, for most premixed flame, $\delta/\delta_r \simeq 10$ [44], it follows that $Ka_r \simeq 100$.

As anticipated, the cases in which $Ka > 1$ can be thought as another sub-category, while Damköhler remains greater than unity:

- $\boldsymbol{1 < Ka < Ka_r} \rightarrow \eta_k < \delta \ ; \ \eta_k > \delta_r$: the Kolmogorov structures interact with the flame pre-heat zone, but not with the reaction zone. This regime is referred to as "thickened-wrinkled flame regime" or "thin reaction zone regime".

- $\boldsymbol{1 < Ka_r < Ka} \rightarrow \eta_k < \delta \ ; \ \eta_k < \delta_r$: the Kolmogorov structures are so small that they can interact also with the flame reaction layer. In this extreme case, no laminar structure could be identified. This regime is called "thickened flame regime" or "broken reaction zone" and is close to the condition of a Perfectly Stirred Reactor (PSR).

The scheme in fig.2.20 sums up the combustion regimes established in premixed conditions, on the base of the relative dimensions of the flame thickness δ, the reaction zone thickness δ_r and the Kolmogorov length scale η_k.

The regimes described above can be represented on a diagram as functions of ℓ_t/δ (integral length scale over flame thickness) and u'/S_L^0 (velocity of turbulent motion over laminar flame speed), as proposed by Peters in [54] and later in [55]. This representation is reported in fig.2.21. In the log-log diagram of fig.2.21 Da and Ka scale with different trends. The Da lines pass for the axes origin and change the angle with the horizontal axes for different values of Da (the higher Da the smaller the angle). The Ka lines shift upward with increasing Ka.

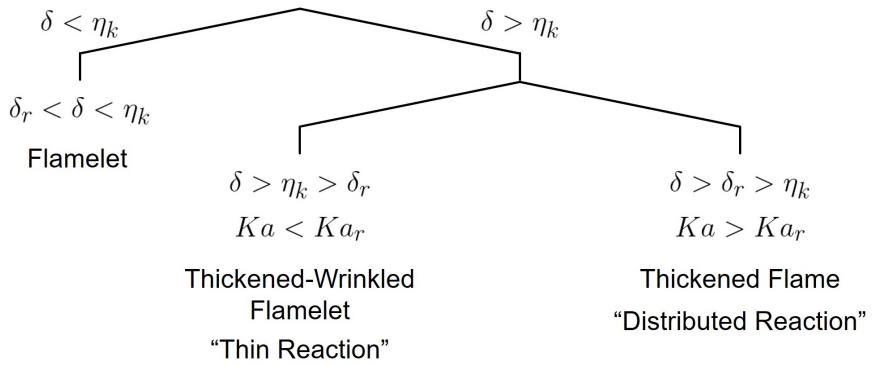

Figure 2.20: Scheme representing the different combustion regimes established in premixed conditions, based on the relative dimensions of the flame thickness δ, the reaction zone thickness δ_r and the Kolmogorov length scale η_k.

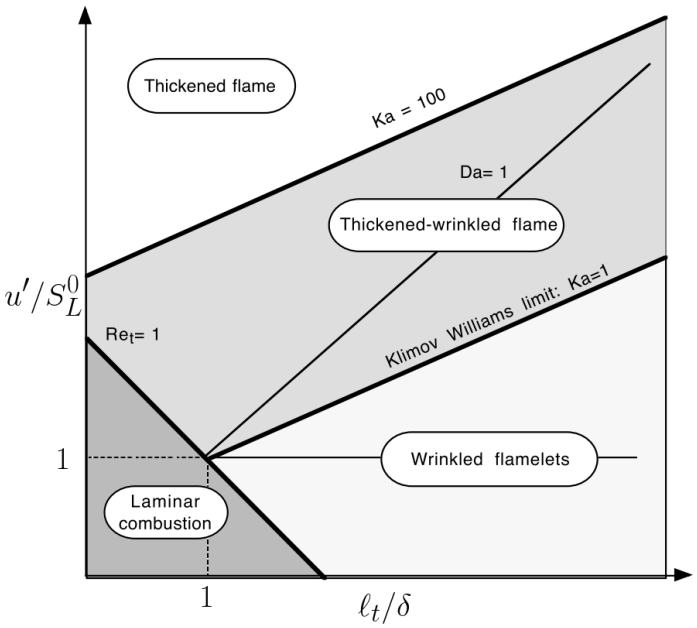

Figure 2.21: Premixed combustion regimes as proposed by Peters in [55] in log-log scale. The different regimes are identified from length and velocity ratios. Reproduced from [44].

Given the peculiarities of each regime, with its different length scales, it is possible to sketch a representation of the flame structures in the different cases. A useful example is offered by Borghi and Destriau [56] and is reported in fig.2.22. The case (a) of fig.2.22 is the "classic" flamelet regime, with a thin flame front wrinkled by the turbulent motion. The case (b) shows a flame of the thickened-wrinkled region, where the Kolmogorov eddies interact with the flame preheat zone. In the case (c) the turbulent structures are able to penetrate also the flame reaction zone, in the thickened flame (distributed reaction) zone.

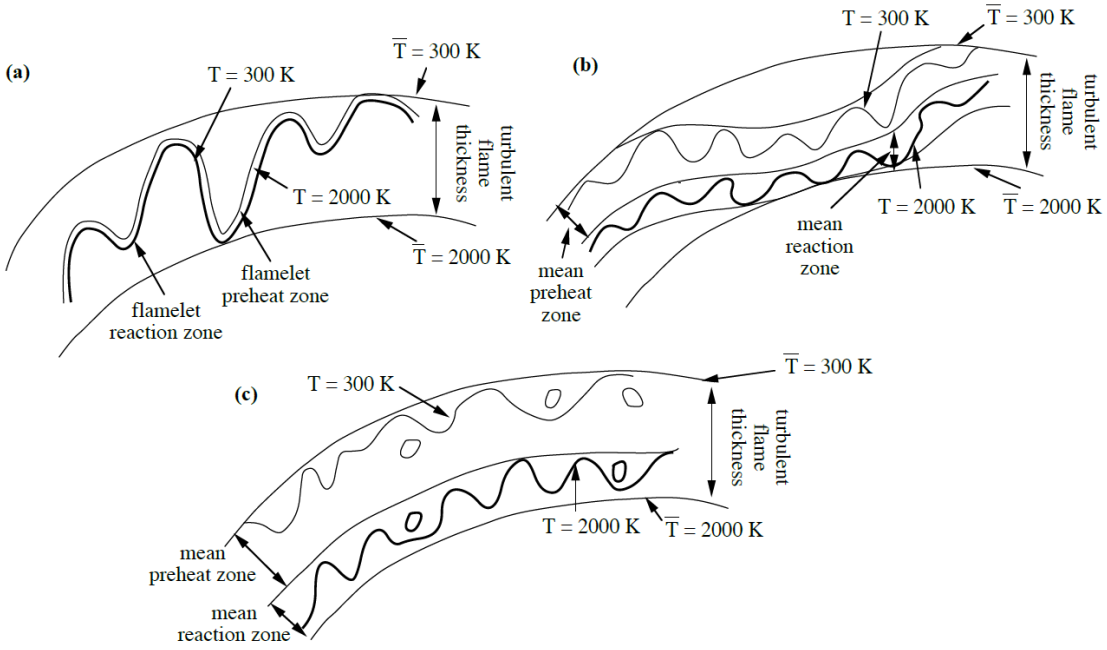

Figure 2.22: Turbulent premixed flame structures as proposed by Borghi and Destriau [56]. The fresh and burnt gas are at 300 and 2000 K respectively, and is possible to see: (a) wrinkled flamelet, (b) thickened-wrinkled flame, (c) thickened flame. Reproduced from [44].

Flamelet Model As mentioned above, the flamelet regime is expected to be established when the characteristic time of the chemical reactions is significantly faster than the turbulent mixing one. In terms of dimensional comparison of characteristic length scales, the flame thickness has to be smaller than the size of the smallest turbulent scales (i.e. Kolmogorov structures). The flamelet concept was first developed by Williams in the frame of turbulent diffusion flames, viewed as consisting of an ensemble of stretched laminar flamelets. Later Peters derived flamelet equations based on the mixture fraction as independent variable, and successively he reviewed the flamelet concept in order to describe turbulent premixed flames too, using a progress variable in place of the mixture fraction. This brief paragraph summarizes the most relevant points of his description, useful to better understand the discussions of chapter 5 (sec.5.2 and sec.5.3). Flamelets are described by Peters [5] as "thin reactive-diffusive layers embedded within an otherwise nonreacting turbulent flow field". In his description, Peters depicts the chemical time scale of the fuel consumption reaction as very short, and identifies the most chemically active region in a thin layer named "inner layer" (see fig.2.15). The location of the inner layer defines the flame surface, more precisely identified as an iso-surface of a nonreacting scalar (whose equations do not include a source term, consequently), that are the mixture fraction or a progress variable. As already seen in the previous analysis of the turbulent premixed combustion regimes, if this layer is thin compared to the size of a Kolmogorov eddy, it is embedded within the quasi-laminar flow field. In this case, the assumption of a laminar flamelet structure is justified. On the other hand, it might be that turbulence is so intense that Kolmogorov eddies become smaller than the inner layer and can penetrate into it. When this is verified, these eddies are able to destroy the layer's structure, eventually leading to

flame extinction.

Detailed treatment of the flamelet concept, including model equations for turbulent premixed combustion, can be found in Peters' book [5] or in his previous works from 1984 and 1986, to which his book refers.

Chapter 3

Data Processing for Raman/Rayleigh Spectroscopy in Turbulent Combustion

Summary

In this chapter details will be given about the treatment of the data provided by the single shot Raman/Rayleigh spectroscopy applied to diagnostics in turbulent combustion. The data treatment includes the acquisition, the processing and the reduction strategies.

The first part, sec.3.1, provides information about relevant burner configurations and about the burner used to investigate selected fundamental processes, as well as a brief description of the test rig. This part is included for a better understanding of the rest of the thesis and is not part of the results of work conducted by the author. For more details, the reader can refer to [12, 57, 58], where similar test rigs have been used.

The second part of the chapter, sec.3.2, will focus on the data treatment, from the pre-processing to the reduction. Section 3.3 will present the principles of the calibration routine applied for the single shot Raman/Rayleigh measurements.

3.1 Experimental Setup

The general equipment needed for Raman/Rayleigh experiments has already been presented in sec.2.2. In sec.3.1.1 details about the test rig present at the TU Darmstadt combustion laboratories are presented. In sec.3.1.2 the Darmstadt Stratified Burner is presented, and in sec.3.1.3 the calibration burners are described.

3.1.1 Excitation and Detection Systems

The test rig is capable to providing data about temperature and main species concentrations (CO_2, O_2, CO, CH_4, N_2, H_2O, H_2) along a 1-D probe volume, represented by a 6 mm line.

A general sketch of the test rig is reported in fig.3.1. From the figure it is possible to identify the excitation and detection sections of the system, described in the following.

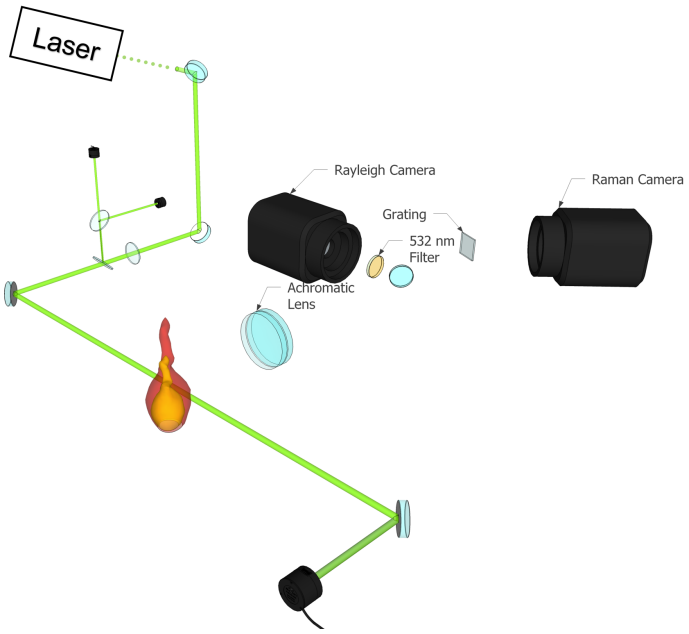

Figure 3.1: Sketch of the Raman/Rayleigh test rig operated at the Darmstadt laboratories for diagnostic in turbulent combustion.

Excitation The laser beam is generated by four separated and identical modules, produced by InnoLas. Each of them is a Nd:YAG laser, with a wavelength of 1064 nm, an energy of ca. 1000 mJ and a pulse duration of ca. 8 ns.

The four beams are then superimposed and frequency doubled, ending with a total energy of about 2000 mJ at 532 nm. They also pass through a delay lines system, to stretch the overall pulse duration up to about 500 ns. This is done to avoid a very high pulse power, which would increase the possibility to have optical breakdown. When focused, the beam width is less than 200 μm ($1/e^2$). This is made possible by using a spherical lens

More details about the laser system can be found in the master thesis by R. Merkel [59], or in the doctoral thesis by S. Schneider [57].

Energy meters are installed in several positions of the beam path, in order to allow for a compensation of the shot-to-shot laser energy fluctuations. The compensation is done *a posteriori* in the data evaluation process.

Detection The scattered light is collected by an achromatic lens and convoyed into a custom built spectrometer. Detailed information about this part of the system can be found in the doctoral thesis by S. Schneider [57]; here only a brief description will be reported.

A sketch of the custom built spectrometer, plus other optical equipments, is shown in fig.3.2, adapted from [57].

An effect typically caused by this kind of spectrometer is the so called "bowing effect" [60]. When it is present, the image of a straight entrance slit or laser beam is

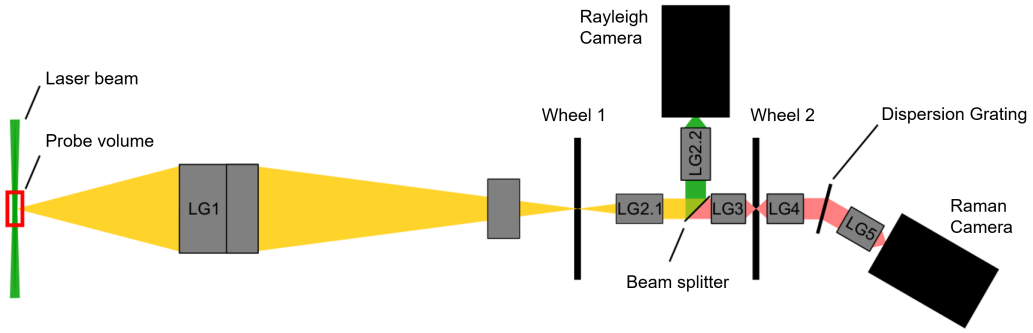

Figure 3.2: Sketch view from above of the costum built spectrometer. Adapted from [57].

optically distorted or bowed. This effect has to be specifically accounted for, as it will be cleared in the next section.

Virtually following the light path after the scattering process, the first optical component (LG1) is an achromatic lens. It fulfills the task of maximizing the number of detected photons, which is beneficial for increasing the intensity of the detected scattered light.

Several lenses are put in place for beam guiding and focusing. A crucial component is the custom built mechanical shutter system, based on counter rotating wheels: its main role is to allow for a reduction of the background luminosity and other interferences without cutting out information from the scattered light beam.

A transmission grating is used to spectrally disperse the scattered light onto the Raman camera chip, over a range of wavelength $\lambda \simeq 550 \div 700$ nm.

The cameras specifics are:

- **Rayleigh**: CCD Princeton Instruments Pixis 400F. Chip size: 1300x400 Px. Pixel size: 0.02 mm.
- **Raman**: CCD Princeton Instruments Pixis 1300B. Chip size: 1300x1340 Px. Pixel size: 0.02 mm.

3.1.2 Darmstadt Stratified Burner

The so called "Darmstadt Stratified Burner" has been designed and developed at the combustion laboratories of the Darmstadt Technical University to investigate relevant combustion phenomena arising in technical applications. A comprehensive description of the burner can be found in [12]. Here, relevant characteristics will be presented.

The burner, shown in fig.3.3, has three staged concentric tubes with inner diameters of D_p = 14.8 mm, D_1 = 37 mm, and D_2 = 60 mm. The hydraulic diameters of slots 1 and 2 are d_{h1} = 21.2 mm and d_{h2} = 20.0. The feed lines have a wall thickness of 2.0 mm and 1.5 mm for the outer and inner tube, respectively, enough to guarantee a temperature rise of the premixed gases in the first annular slot below 1 K. The tube length is about 25 hydraulic diameters.

The burner is placed inside a circular coflow with diameter of 600 mm issuing a filtered air flow at 0.1 m/s. It is designed to shield the flames from the laboratory environment and prevent penetration by dust particles.

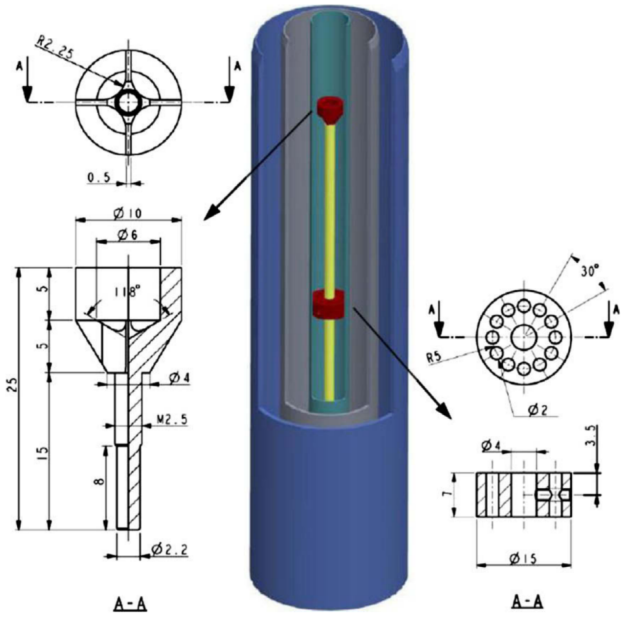

Figure 3.3: Stratified burner. *Middle*: 3D elevation of the nozzle consisting of the ceramic pilot tube and the two concentric steel tubes. The flame holder and the turbulence enhancing perforated plate can be seen inside the pilot. *Left*: technical drawing of the flame holder. *Right*: technical drawing of the turbulence enhancing perforated plate. Reproduced from [12].

The pilot flame is anchored above a retractable flame holder and turbulence is enhanced by a perforated plate positioned upstream. During the flame operations, the flame holder is moved upstream in the pilot tube in order to provide a uniform exhaust gas flow at the tube exit, capable to ignite the fresh mixtures issuing from the burner slots.

Velocity and compositions of the flows in the three burner sections are independently controlled. This allows for a number of different configurations, from fully premixed to non-premixed and partially-premixed and/or stratified. The velocity control can induce different levels of shear among the flows.

The burner has been operated in several conditions, providing an experimental database for model validation in numerical simulations, including the works presented in [12, 25, 37].

In this work, measurements of two flames stabilized on the stratified burner are used. The data have been employed, as it will be clarified in the next chapters, for a double purpose. On one side the analyzed flames are characterized by peculiarities of interest, useful to gain insights in the context of premixed turbulent combustion. These aspects will be discussed in the final chapter. On the other side, the data are used as a test case for the modified calibration routine developed in this work, and applied to single shot Raman/Rayleigh (chapter 3).

3.1.3 Calibration Burners

Other burners are employed in the routine necessary for the application of the Raman/Rayleigh investigation. The reasons for these needs will be detailed in the next

sections. Here the most important calibration burner configurations will be presented.

Flat Flame Burner

The Flat Flame Burner (also "FF" in the following) has been designed and developed at the combustion laboratories of the Darmstadt Technical University and is presented in [58]. As for similar cases, for details the reader can refer to the cited publication, while here will find the relevant specifics. The burner is shown in fig.3.4.

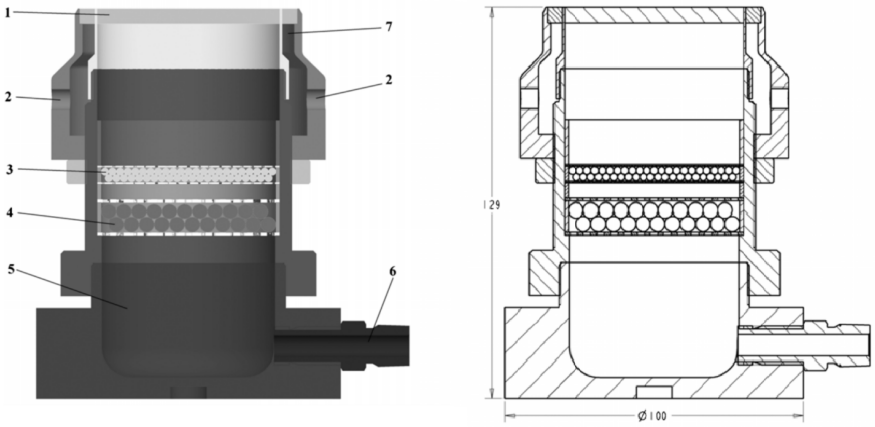

Figure 3.4: Laminar Flat Flame Burner. (1) Sinter plate, (2) gas inlet coflow, (3) sphere packing (d = 1 mm), (4) sphere packing (d = 5 mm), (5) plenum chamber, (6) gas inlet, (7) co-flow. Reproduced from [58]

The burner is designed to be fueled with premixed methane/air. After passing through a plenum chamber, the mixture is laminarized in two steps thanks to two sequential packs of glass spheres. The gas mixture leaves the burner through a porous sinter plate acting as the flame holder, with a 60 mm diameter. No cooling systems are necessary, due to the operation with detached flames.

Surrounding the burner exit, a 5 mm wide concentric nitrogen coflow shields the flame from ambient air or particles entrainment.

Vertical Flame Burner

The Vertical Flame Burner (also "V-Flame" in the following) has the peculiarity of anchorating a flame to a ceramic rod placed atop the burner exit. Subsequently, a two branches flame is established, attached to the rod. The burner is equipped with a rotational mechanism which allows for positioning one of the two flame branches vertical to the laboratory coordinates and perpendicular to the 1-D probe Raman/Rayleigh probe volume. A representation of a burner section cut, with the rod in position (the turning mechanism is not shown), is reported in fig.3.5. A fuel / air mixture flows in a central tube (D = 31 mm), surrounded by a coflow (D = 88 mm), operated with N_2.

The burner presents a sintered bronze plate (5 mm thickness, 20 μm pore size), three nets (mesh width 1.0, 0.6 and 0.4 mm) and a nozle for flow homogenization. The burner operates in laminar conditions. For further details, the reader can refer to [57].

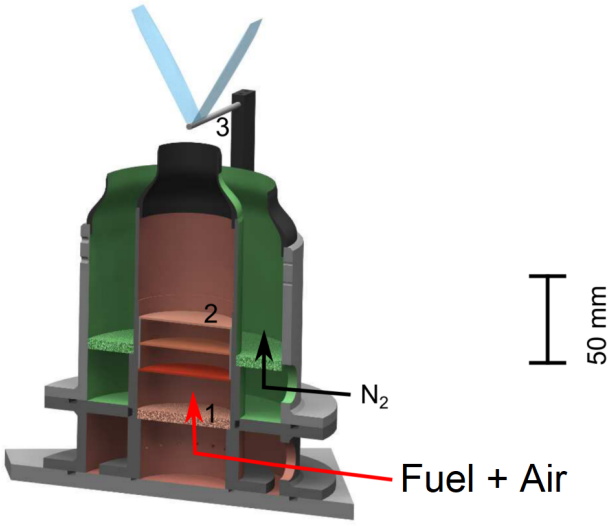

Figure 3.5: Section cut of the vertical flame burner. (1) Sinter plate. (2) Nets. (3) Ceramic Rod. Reproduced from [57].

Figure 3.6 shows scaled experimental spectra obtained from single shots, acquired in the exhaust region of a laminar premixed CH_4/Air flame using the test rig described in sec.3.1.1 and the FF burner (sec.3.1.3).

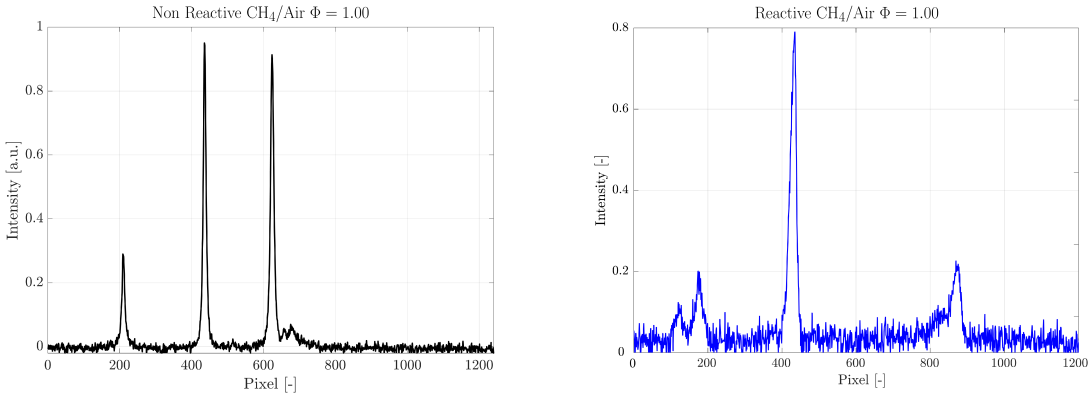

(a) **(b)**

Figure 3.6: Single shot scaled experimental spectra acquired in the exhaust region of a premixed CH_4/Air flame: (a) non reactive case; (b) reactive case.

3.2 Data Processing: the Hybrid Method

3.2.1 Context

The data treatment for the single shot Raman/Rayleigh spectroscopy applied to turbulent hydrocarbon combustion requires a specific approach. Currently three different methodologies are available: the "spectral fitting" (SF), the "matrix inversion" (MI) and a combination of both, called the "hybrid method".

Spectral Fitting This method needs the calculation of individual rovibrational Raman transitions for each species, contributing to the construction of rovibrational Raman bands after an appropriate manipulation with system-specific transfer functions. The molecules temperature dependent Raman bands compose a spectral library which has to be calibrated to an experimental spectrum measured in a gas sample with known mole fraction and temperature, accounting for specific experimental conditions. The species concentrations can be computed directly by fitting measured spectra with the calibrated libraries, using the routine described in [32].

Matrix Inversion This method has been used, among the others, in [61–64]. The Raman signals, including background luminosity and fluorescence, are integrated over a specific set of regions in the spectral dimension obtained thanks to on-chip binning. This procedure partially compensates the signal weakness of the Raman scattering, but has the drawback of causing a reduction of detail: some spectral information on broadening and shifting of Raman bands with increasing temperature is lost, as are spectral details of interferences.

Hybdrid Method Fuest et al, in [65], highlight advantages and disadvantages of the two different approaches described above. The Matrix Inversion returns a stronger Raman signal and on-chip binning allows for low readout noise. The drawbacks of this procedure is the extensive calibration required, which also leaves margin of error in the temperature ranges which are not directly calibrated. The Spectral Fitting, relying on quantum mechanical models, reduces the required calibration to only one per species. It preserves more spectral information but has to pay the price of a higher readout noise, a slower data acquisition rate and an intensive procedure to obtain the Raman bands. In the same work Fuest developed an alternative procedure [24, 65] to the above mentioned, the "Hybrid Method", which is indeed combining SF and MI. The Hybrid Method has been proven to allow for better results than SF and MI in single shot measurement of multiple scalars in combustion-related applications. It retains benefits of on-chip binning (similarly to the MI method), such as suppression of camera readout noise, faster data acquisition, smaller raw data volume, and faster processing. Moreover, being based on the theoretical Raman spectra (similarly to the SF method), the needs for calibrations is significantly reduced respect to the Matrix Inversion, reducing uncertainty at conditions where calibrations are difficult.

The Hybdrid Method will be detailed in the following. In sec.3.2.2 the procedure to construct the spectral libraries used to analyze the measured Raman spectra is

described. Further, in sec.3.2.3, the effects of the temperature on the libraries are shown. Concluding, the procedure will be framed within a mathematical structure in sec.3.2.4.

3.2.2 Spectral Library

The Hybrid Method adopts from the MI the requirement of a library of simulated/-calculated Raman scattering spectral intensity, covering the temperature range of the measured mixtures. The libraries contain also the intensities of the crosstalks between different species and background or fluorescence effects. The process to compose the Raman libraries includes different steps, explained in the following.

Theoretical Raman spectra generation

The first step is the generation of the theoretical spectra. This procedure is done using RAMSES [32] for CO_2, O_2, CO, N_2, H_2O and H_2, while for CH_4 an experimental spectrum is used, because no reliable quantum mechanics models are accepted in the temperature range of interest [65]. The output consists of the so-called "stick spectra", i.e. theoretical Raman spectra of the molecules, as the one shown in fig.3.7 for H_2 at 300 K.

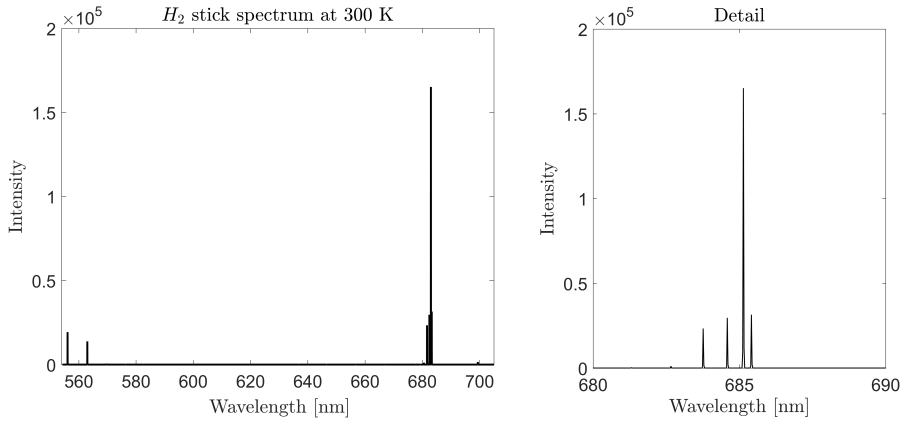

Figure 3.7: (Left) Hydrogen Raman stick spectrum at 300 K plotted in the wavelength domain. (Right) Detail of the same spectrum.

The stick spectra report the spectra in terms of "shift", i.e. the position in the wavelength space is reported using as a reference the emitting wavelength of the exciting source (532 nm, in this case).

Dispersion Function The impact of the spectrometer dispersion is specifically accounted for, thanks to the information obtained from an emitting source with known spectra. Measuring the emission of this calibration source, it is possible to compose a correlation defined as "dispersion function" between the wavelength and the pixels on the Raman camera chip; the dispersion function returns an indication about which wavelength excites a specific chip region.

Spectra Convolution

The laser beam characteristics as well as the spectrometer specifics affect how the Raman spectra are recorded on the camera chip. To know how the stick spectra would account for this aspects, a convolution operation is required. The stick spectra are indeed convoluted with an "apparatus function", which returns the impact of the system, from the laser beam to the camera chip. This function is constructed using the Rayleigh scattering image of the laser beam, ad is indicated with Γ_{app}. An example is shown in fig.3.8. Appropriate scaling is applied to Γ_{app}, in order to retrieve correspondence between the convoluted spectrum and a spectrally resolved acquisition of nitrogen. The described operation is deeply explained in [24], chapter 2.

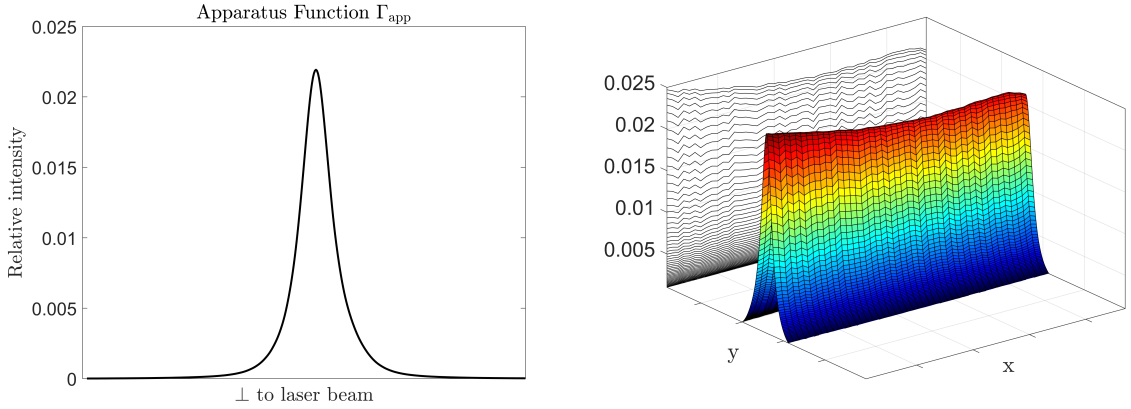

(a) **(b)**

Figure 3.8: (a) Example of apparatus function Γ_{app}, obtained from the Rayleigh scattering image in air at room temperature. The horizontal axis represents the spatial dimension perpendicular to the laser beam. (b) The same Γ_{app}, seen across all the Raman camera chip: the x axis is for the spatial dimension, the y axis is the direction perpendicular to the laser beam (corresponding to the Raman channels).

To simplify the description of that approach, too detailed for the context, it is possible to define here an alternative mathematical treatment. This keeps the exact same procedure to obtain the convoluted spectra and simply proposes another mathematical formulation.

It is possible to define a function including all the Raman transitions of interest for a given molecule, i.e. the above mentioned stick spectra. This function can be named S_{Stick}, and is continuous in the spectral region of interest by definition and given by the sum of the single spectra. In principle S_{Stick} is a function of the specific molecule, of T and of the frequency (or equivalently wavelength). Focusing the analysis on one molecule only, and leaving implicit the temperature dependence, which will be in the next section detailed, it is possible to write simply $S_{\text{Stick}} = S_{\text{Stick}}(\nu)$.

Γ_{app} is also indirectly depending on the wavelength: the shape of the Rayleigh image will be slightly different on the different chip regions, due to already mentioned effects, such as the nonlinear dispersion or bowing.

The convoluted spectrum for the molecule of interest can then be given by the convolution between the apparatus function and the function of the stick spectra:

$$S_{\text{Conv}}(\nu) = \Gamma_{app}(\nu) * S_{\text{Stick}}(\nu) \tag{3.1}$$

where, as usual in literature, the star symbol is for the operation of convolution.

Being the convolution a linear operation, and being S_{Stick} fairly well approximated by a finite summation of finite-height impulses, it is easy to understand that the result of the convolution will be given by the sum of the apparatus function translated in the frequency space where the Raman transitions are located, and scaled by the intensities of the transitions.

Figure 3.9 shows a detail of the convolution between S_{Stick} and the Γ_{app} at a 300 K for H_2 in the central region of the camera chip.

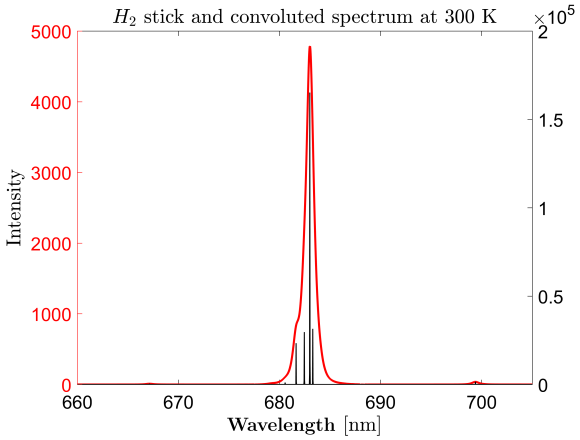

Figure 3.9: Convoluted spectrum and stick spectrum for H_2 at 300 K (detail). The apparatus function used for the convolution is the one shown in fig.3.8.

Integration over the Raman Channels

Once the convoluted spectra are obtained for the species of interest, the Hybrid Method takes from the Matrix Inversion the use of channels on the Raman camera chips. The "channles" are fixed spectral regions, which also correspond to pixel regions on the camera chip, defined in the case of interest by the on-chip binning[1]. Their use is related to the calculation of the species Raman response and crosstalks.

To obtain the species Raman responses and to quantify the crosstalks between two species, the libraries of convoluted spectra S_{Conv} are integrated over the specific channels. Considering two species I and J, and given that the univocal relation between spectral and pixel spaces allows to use the discrete variable Pix instead of the frequency ν:

- The binning region (br) limits can be noted, for I, as $\text{br}(I)_{\text{lb}}$ and $\text{br}(I)_{\text{ub}}$, where "lb" stands for "lower boundary" and "ub" stands for "upper boundary". Equivalent notation is used for J.

- The Raman response for I, if for brevity $CS(I) \equiv S_{\text{Conv}}(I)$, is given by

$$\int_{\text{br}(I)_{\text{lb}}}^{\text{br}(I)_{\text{ub}}} CS(I)\, d\text{Pix}$$

[1]This is the common approach where a CCD is used as detector. With other systems, such as photomultipliers employed in earlier approaches, several devices are placed in different locations.

- The crosstalk of J over I, i.e. the portion of $CS(J)$ falling between $\mathrm{br}(I)_{\mathrm{lb}}$ and $\mathrm{br}(I)_{\mathrm{ub}}$ is given by (note the differences in the integral limits and the S)

$$\int_{\mathrm{br}(I)_{\mathrm{lb}}}^{\mathrm{br}(I)_{\mathrm{ub}}} CS(J)\, d\mathrm{Pix}$$

Figure 3.10 reports a sketch of two spectra for I (black) and J (grey):

- The response function for I is given by the black area under $CS(I)$ in $[\mathrm{br}(I)_{\mathrm{lb}}\ ;\ \mathrm{br}(I)_{\mathrm{ub}}]$.
- The response function for J is given by the grey area under $CS(J)$ in $[\mathrm{br}(J)_{\mathrm{lb}}\ ;\ \mathrm{br}(J)_{\mathrm{ub}}]$.
- The crosstalk of I onto J, noted $J << I$, is the black area in $[\mathrm{br}(J)_{\mathrm{lb}}\ ;\ \mathrm{br}(J)_{\mathrm{ub}}]$.

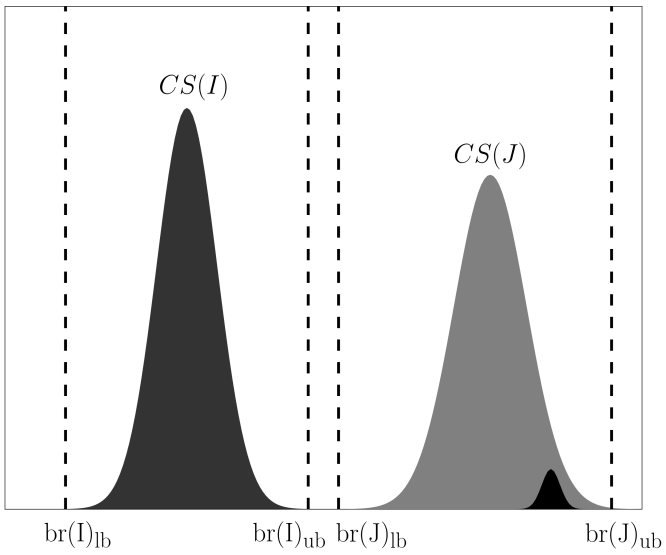

Figure 3.10: A sketch of I and J convoluted spectra and binning regions. The colored areas are the Raman responses of I and J and the crosstalk $J << I$.

The integration is performed multiple times, shifting the boundaries of the binning regions, in order to account for the effects of bowing[2] and beam steering[3]. The results are stored in tabular form, after a normalization respect to the response functions at 0 pixel shift and 290 K. When processing a single shot, the actual shift is determined from the Rayleigh image and used to properly access the tables.

The binning regions are defined after the frequency of the Raman transitions of the molecules of interest, as reported in table 3.1.

[2]As already said, the bowing effect optically distorts or bows the image of a straight entrance slit or laser beam [60].

[3]Beam steering is an effect, caused by the turbulent flame, which may alter the position of the imaged laser beam on a detector in line-imaging applications [7].

Table 3.1: Range of wavelength containing the Raman transitions of interest for the molecules. Adapted from [24].

Molecule	Wavelength [nm]	
CO_2	568	578
O_2	578	584
CO	597	603
N_2	603	611
CH_4	622	643
H_2O	651	665
H_2	678	689

3.2.3 Temperature Dependence

It has already been pointed out that the effects involved in the Raman scattering, from the stick spectra to the response functions and crosstalks, have a dependence on the temperature. In this part the effects of this dependence will be detailed, given its importance on the following of the work.

A plot of the stick spectra at different temperatures, as the one reported in fig.3.11, can clarify the temperature dependence. In fig.3.11, the hydrogen spectra are reported

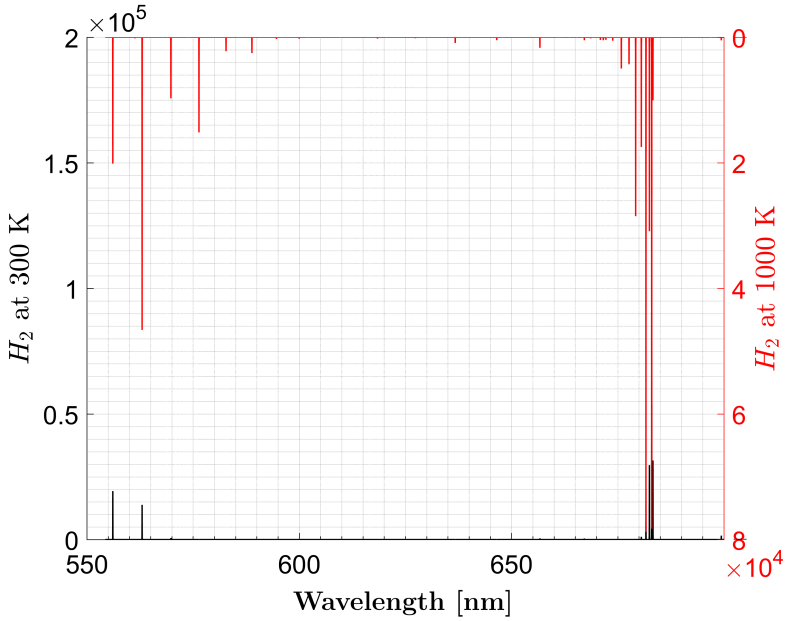

Figure 3.11: $S(H_2)_{\text{Stick}}$ at 300 K (left y-axis) and 1000 K (right y-axis, reverse) in the wavelength domain.

at 300 K and 1000 K. It appears clear that with increasing temperature the intensities of the peaks can change significantly (see different scales on the two vertical axis). Also, peaks become evident at locations where they were not. The first aspect is mostly impacting the Raman response of the species, while the rising of other peaks along the spectral space can have a big impact in terms of crosstalks: a peak of a species J can be present in the Raman channel of I only from a certain temperature, and also can

change its intensity with further fluctuations in T.

It is clear that the dependence on T of the Stick spectra affects directly the Convoluted spectra and, as briefly mentioned, the Raman responses and the crosstalks obtained with the integration. Consequently the integration has to be performed for several values of temperature. More specifically, the libraries are composed from spectra ranging from 250 to 2500 K, with a discretization of 10 K. As an example, some response functions and crosstalks are reported in fig.3.12. As said, they are the results of the integration over the Raman channels of the convoluted spectra. The functions are normalized with respect to their value at 300 K.

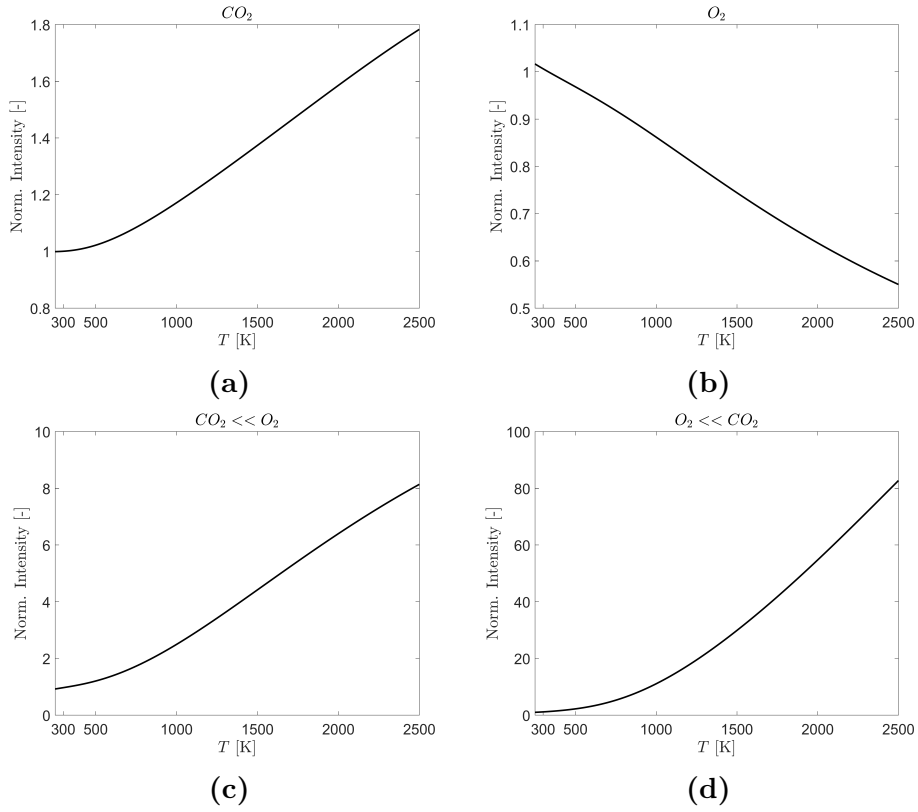

Figure 3.12: Four examples of temperature effects on response functions and crosstalks: (a) CO_2 response function; (b) O_2 response function; (c) CO_2 << O_2 crosstalk; (d) O_2 << CO_2 crosstalk. Note the different scales of the intensities and the non-monotonic trend. All the curves are obtained with the same apparatus function. The functions are normalized with respect to their respective value at 300 K and are then not normalized respect to a unique value.

Figure 3.12 confirms a significant effect on the intensity, with orders of magnitude of change, especially on the crosstalks. It is notable also that the curves are not monotonic and present some inflection point. It can also be noted that the influence depends on the molecule: the change in intensity and the number of additional peaks can change significantly. A very useful representation to fully understand the impact of the temperature can be found in [65] and is reported in fig.3.13.

The temperature dependences and the boundaries of the Raman channel seen in fig.3.13 can change with the setup and/or measurement conditions, but qualitatively the highlighted effects will remain present. It can be noted, for example, how CO_2

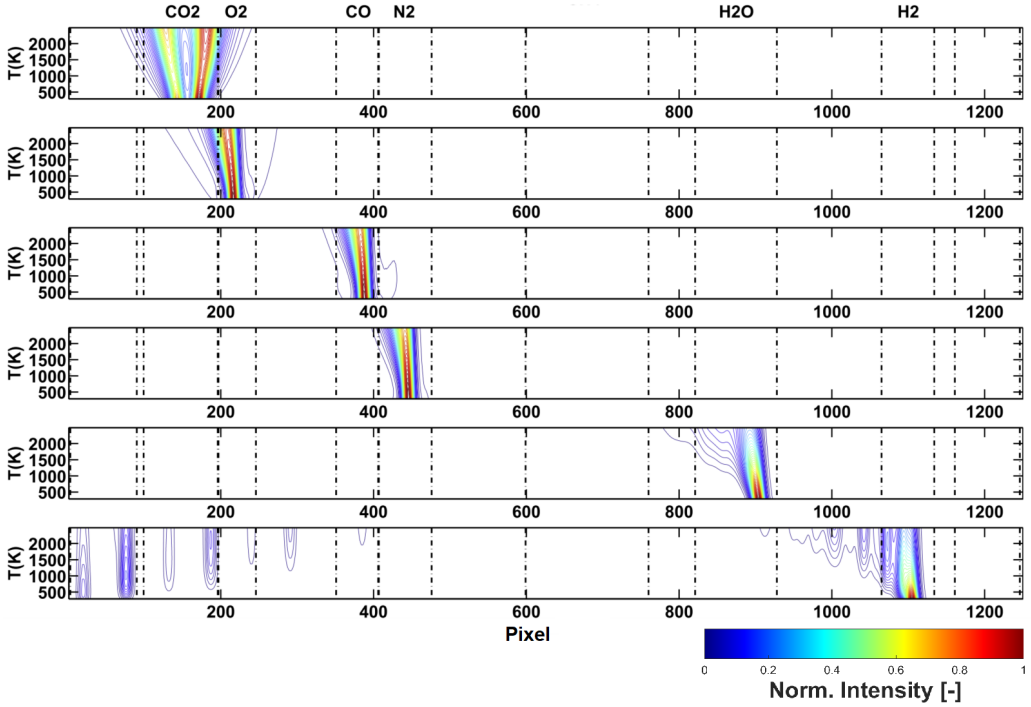

Figure 3.13: Calculated temperature dependence of relative Raman scattering spectral intensities from CO_2, O_2, CO, N_2, H_2O, and H_2. Dashed vertical lines indicate the pixel boundaries for the Raman channel. Reproduced from [65].

and O_2 mutual crosstalks are strong, and also how H_2 is presenting peaks in different channels.

Look-up Tables Once the Raman responses and the crosstalks are calculated for the different temperature values and pixel shifts, the results are stored in tabular form to compose a set of look-up tables, accessed during the solution of the Raman equation, introduced in the next section. For the cases not inlcuded or derived from RAMSES, specific polinomials are used.

3.2.4 Mathematical Structure

After presenting the peculiarities of the Hybrid Method and its first fundamental steps, it is possible to provide the mathematical structure on which it is based. This is mostly based on the Matrix Inversion method.

First, the function describing the Raman response of a molecule i can be identified by $\tilde{c}_{ii} = \tilde{c}_{ii}(T, i)$. Considering that more than one Raman channel can be used for i across the camera chip, it is possible to express the multiple integration described above as:

$$\tilde{c}_{ii}(T, i) = \sum_{\mathrm{br}(i)_{\mathrm{lb}}}^{\mathrm{br}(i)_{\mathrm{ub}}} \frac{T}{T_0} CS(\mathrm{Pix}, T, i) \tag{3.2}$$

where the index i is spanning the seven species, while the summation is performed, for each species, over all its binning channels. The temperature normalization by T_0

is employed to mitigate the effect of signal decrease with increasing temperature (as shown in eq.(2.13)).

The Raman response used in the Hybrid Method is obtained after a normalization expressed by

$$c_{ii}(T,i) = \frac{\tilde{c}_{ii}(T,i)}{\tilde{c}_{ii}(T_{\text{norm}},i)} \tag{3.3}$$

where $\tilde{c}_{ii}(T_{\text{norm}},i)$ is the response function at 290 K.

With similar symbolism, the non normalized crosstalk of j onto i noted $i << j$ is given by:

$$\tilde{c}_{ij}(T,i<<j) = \sum_{\text{br}(i)_{\text{lb}}}^{\text{br}(i)_{\text{ub}}} \frac{T}{T_0}\, CS(\text{Pix},T,j) \tag{3.4}$$

After the normalization procedure:

$$c_{ij}(T,i<<j) = \frac{\tilde{c}_{ij}(T,i<<j)}{\tilde{c}_{ij}(T_{\text{norm}},i<<j)} \tag{3.5}$$

As seen in sec.3.2.3, the c's have a polynomial structure in the temperature space - see fig.3.12 for example.

As for the MI method [23, 62–64], Raman signals and background radiation, once integrated across the Raman channels, compose a signal vector[4] $\boldsymbol{S}$. From this information the number densities of the probe line can be deducted on a single shot base, using the relations contained in the Raman responses, the Rayleigh information about the temperature and other secondary but still relevant information (e.g. single shot based laser energy). If with $\boldsymbol{N}$ the vector of the number densities is indicated, the relation will be expressed by

$$\boldsymbol{S} = \underline{\underline{M}}(T)\ \boldsymbol{N} \tag{3.6}$$

modified from the equation reported in [24] and above mentioned works, with $\underline{\underline{M}}$ referred to as "Raman matrix".

In eq.(3.6), the noise term is enclosed in the signal vector. Denoising techniques may be used to improve the quality of the signal. Wavelet denoising approaches have been successfully tested and implemented in Raman/Rayleigh single-shot measurements in HC flames, yielding improvements in both measurement precision and effective spatial resolution. (see [9, 15, 17, 37, 66–68], for examples of application).

Being the probe line discretized, it can be helpful to point out that an equation as the (3.6) can be written for each segment of the discretized line: the Raman matrix will stay the same, while S, and subsequently N, will differ. For the same single shot, if s_n is the n-th segment of the probe line:

$$\boldsymbol{S}^{s_n} = \underline{\underline{M}}(T)\ \boldsymbol{N}^{s_n} \tag{3.7}$$

[4] In this thesis the "bold" notation is used for vectors (e.g. $\boldsymbol{u}$) and the double underline for matrices. The signal vector and the number density vector follow the same rule, even though they would be more rigorously referred to as "arrays". Similarly, matrices are indicated by a double underline, and so the Raman Matrix even if it is a two-dimensional array. This exception is done to avoid the specification of the size of the arrays, that would result in an over-complicated reading, and to remain coherent with the naming used in the previous works on the topic. When necessary to avoid misunderstanding, the square brackets are used to define an array (e.g. $[C]$).

If s_m is the m-th segment of the discretized proble line, in general:

$$\boldsymbol{S}^{s_n} \neq \boldsymbol{S}^{s_m} \tag{3.8}$$

Figure 3.14 shows a sketch of the segment discretization of a probe line sector: each segment s_i generates a signal vector $\boldsymbol{S}^{s_i}$, which will be processed to give $\boldsymbol{N}^{s_i}$.

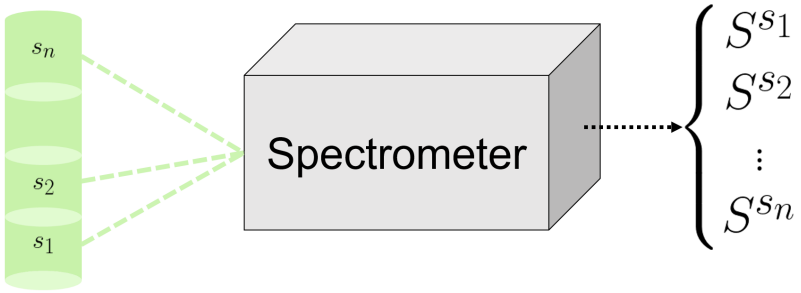

Figure 3.14: Sketch representing the segment discretization of a probe line sector: each segment s_i generates a signal vector S^{s_i}.

In the coming sections, when the signal vector $\boldsymbol{S}$ is used, it has to be intended as the signal vector $\boldsymbol{S}^{s_i}$ of a general segment i of the probe line, if not differently specified.

Solving the Raman equation

Equation (3.6) has to be inverted to obtain the number densities. In this part, focus is given on the Raman matrix $\underline{\underline{M}}$ and about the solution of the Raman equation.

Considering that

$$\boldsymbol{S} = \begin{bmatrix} s_{CO_2} & s_{O_2} & s_{CO} & s_{N_2} & s_{CH_4} & s_{H_2O} & s_{H_2} \end{bmatrix}'$$

the Raman equation can be made explicit as following:

$$\begin{bmatrix} s_{CO_2} \\ s_{O_2} \\ s_{CO} \\ s_{N_2} \\ s_{CH_4} \\ s_{H_2O} \\ s_{H_2} \end{bmatrix} = \begin{bmatrix} m_{11} & m_{12} & & & m_{15} & m_{16} & m_{17} \\ m_{21} & m_{22} & & & m_{25} & m_{26} & m_{27} \\ & & m_{33} & m_{34} & m_{35} & & m_{37} \\ & & m_{43} & m_{44} & m_{45} & & \\ & & & & m_{55} & m_{56} & \\ & & & & & m_{66} & m_{67} \\ & & & & & m_{76} & m_{77} \end{bmatrix} \begin{bmatrix} n_{CO_2} \\ n_{O_2} \\ n_{CO} \\ n_{N_2} \\ n_{CH_4} \\ n_{H_2O} \\ n_{H_2} \end{bmatrix} \tag{3.9}$$

Equation (3.9) is directly inverted to obtain the unknown number density from the known, measured, signal. The element m_{ij} of the Raman matrix is composed as $m(T)_{ij} = k_{ij} \cdot c(T)_{ij}$, where

$$c(T)_{ij} = \begin{cases} \text{Raman Response of } i & \text{if} \quad i = j \\ \text{Crosstalk } i << j & \text{if} \quad i \neq j \end{cases}$$

k_{ij} is referred to as "multiplier" or "tuner".

The element $c(T)_{ij}$ gives the temperature dependence to the Raman equation, coming directly from the temperature dependence of the Raman spectra and crosstalks as seen in eq.(3.3) and eq.(3.5). The temperature necessary to obtain c_{ij} is given by the local instantaneous temperature from the simultaneously measured Rayleigh scattering. Because the effective Rayleigh cross section depends on the gas composition, an iterative procedure is applied. The first guess Rayleigh temperature is used to access the tables with the $c(T)$'s and the Raman equation is solved. The resulting gas composition is used to find the effective Rayleigh cross section and to compute then a new guess for the temperature. This value is used to correct the previous $c(T)$ and the procedure is repeated until the temperature change in the iteration is arbitrary small. The main steps of the procedure to solve the Raman equation, using the Rayleigh information to correct the temperature, is reported in fig.3.15. Other inputs are needed to properly treat the Raman and Rayleigh signals before feeding them into the system, as for example the energy referencing or the flat field correction files[5].

The knowledge of the crosstalks and/or Raman responses is not sufficient to compute the species number densities from the inverted matrix. The tuners have also to be determined. The tuners k_{ij} are used to calibrate the system against defined conditions, relevant to the measured ones. Their values are found thanks to a calibration procedure that involves both acquiring signals from specific experimental conditions and a proper setting of the data processing routine. A detailed explanation about their role, and in general about the calibration procedure for the simultaneous Raman/Rayleigh single shot measurement in turbulent flames is provided in sec.3.3.

Other Raman channels can be used, and their signal will be appended to S, as well as new elements m's can be present in the Raman matrix. Such an approach is used for example for specific background treatment, where one or more background channels are added in the space left in between the species channels.

[5]The energy referencing accounts for variations in the laser energy from one shot to the other. If not accounted for, a fluctuation in the laser energy from one shot to the other would lead to a false interpretation of the scattered signal intensity. The "flat field correction" accounts instead for spatial distortion in the detected image, using as a reference a flat profile.

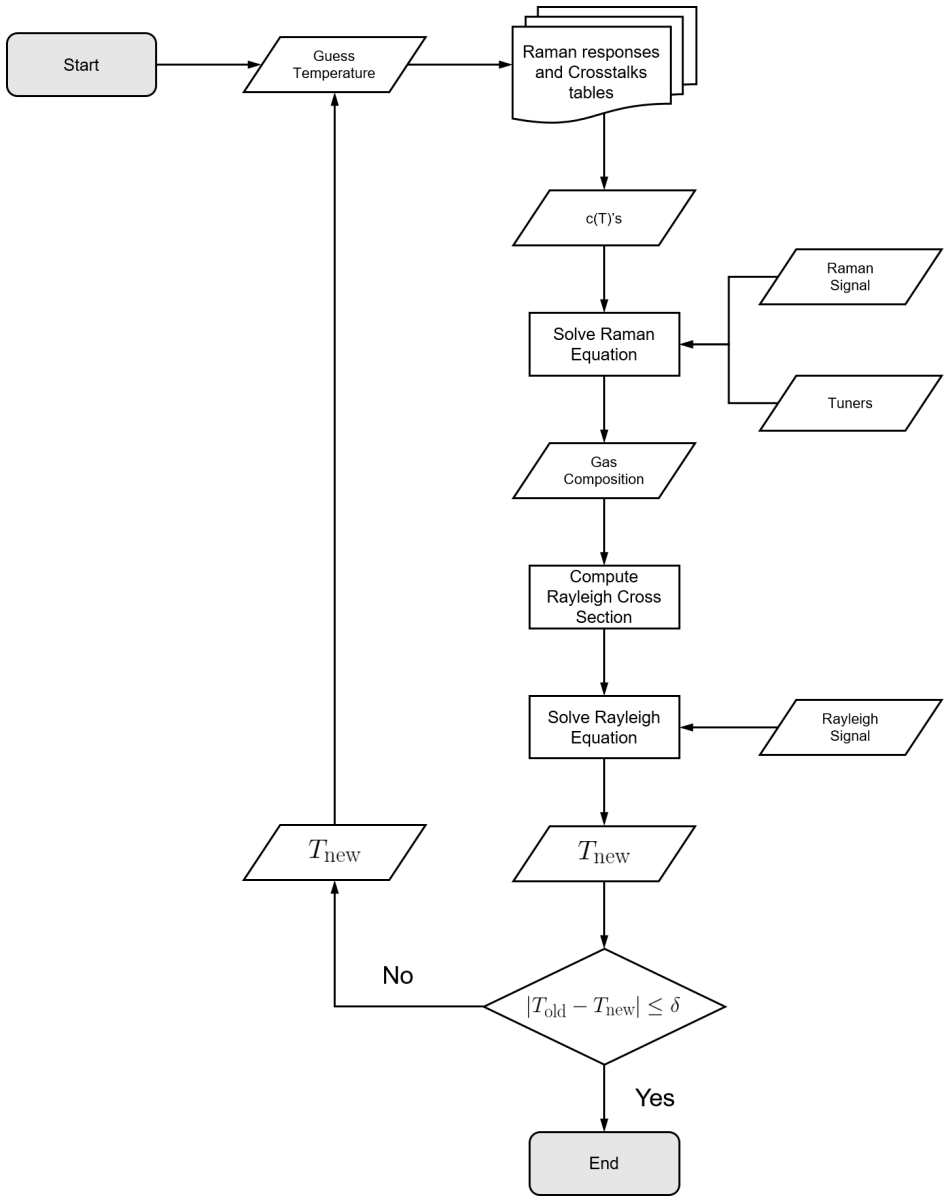

Figure 3.15: Flow chart representing the main steps to solve the Raman equation, using the local instantaneous temperature from the simultaneously measured Rayleigh scattering, given the Raman signal vector S.

3.2.5 Limits of the Technique in Combination with the HM

As said, the described technique has the capability to detect the major species involved in the HC combustion. It is out of doubt that in presence of complex hydrocarbons, polycyclic aromatic hydrocarbons (PAHs) formation and soot formation, chemistry becomes more complex, with intermediate species and soot precursors growing in relevance [45]. For example, PAHs and fuel pyrolysis products, such as unsaturated hydrocarbons, produce a broad fluorescence interference spectrum. In these class of cases, different approaches may be put in place to successfully apply Raman/Rayleigh single-shot measurements. One option is to take advantage of their polarization properties to separate the interference from the Raman signal, as it is done in [69] (where the Hybrid Method is applied) and in [70–72]. Here it is demonstrated that "record-

ing both components of the polarization separately, allows removing the interference terms and obtaining useful Raman measurements, even in the mildly sooty region of hydrocarbon flames" [69].

3.3 Calibration Conditions

3.3.1 Principles

The Raman responses and the crosstalks account for several system-dependent characteristics, such as optical dispersion and apparatus function. Nevertheless, the polynomials expressing those functions need to be calibrated in specific conditions, given that the $c(T)$'s are normalized and expressed in relative terms, as one can see in eqs. (3.3) - (3.5).

The calibration procedure makes use of different conditions to find a unique value for each of the k's present in the Raman matrix $\underline{\underline{M}}$, valid in the entire specific measurement session. In special cases the calibration can be repeated during or after the session, to confirm or modify the tuners values.

The set of tuners found with the calibration procedure is used in the Raman equation to process the target flames measurements, in which every measured point is in an unknown thermochemical state. The conditions at which the system is calibrated compose a set of known thermochemical states, that are selected in order to present comparable characteristics with the target flames of interest. The calibration is based on the key hypothesis that the target flames unknown thermochemical states are included within the range of known states, against which the system is calibrated. Subsequently, the set of k's found for the known conditions stays valid in the unknown conditions, too. The calibration can not be guaranteed for states that are not included within the calibration range. Figure 3.16 shows a sketched representation of the described principle, considering a general thermochemical state identified by a couple $(T_i, [C]_i)$, where $[C]_i$ is the species of interest concentrations array. The procedure used for finding the k's

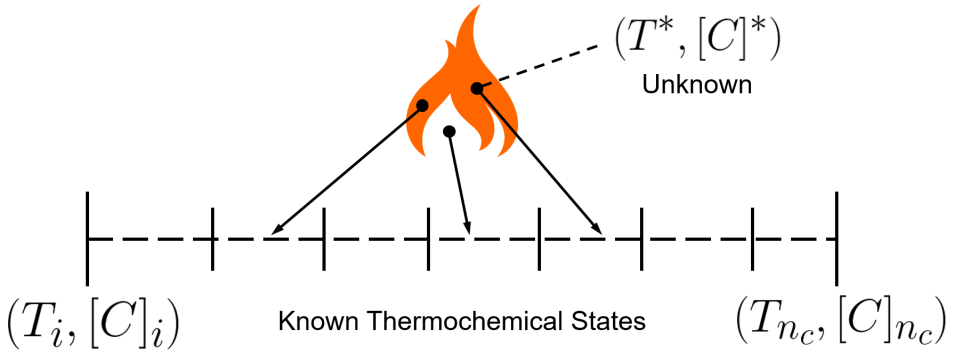

Figure 3.16: Sketched representation of the calibration approach: the calibration conditions compose a set of known thermochemical states $[(T_i, [C]_i) - (T_{n_c}, [C]_{n_c})]$, while each point of the target flames is in unknown condition, generically identified here with $(T^*, [C]^*)$. The unknown conditions will lye in between the set formed by the known conditions, and this will assure that the system is well calibrated for all the possible thermochemical states measured.

values will be detailed in the next chapter, while in this section the calibration conditions used are introduced. Different operative conditions have to be employed, because of the different effects that the temperature change has on the response functions and on the crosstalks, but also to account for the different combustion characteristics which are likely to be found in the target flames. Given that some of the k's are associated to

Raman response functions, more specifically the one on the diagonal of $\underline{\underline{M}}$, and some to the crosstalks (off diagonal elements), in the following they will also be referred to as "species multipliers / tuners" or "crosstalks multipliers / tuners", respectively. The operative conditions used to find the tuners values are:

- Filtered, dry ambient air.
- Gas mixtures at ambient temperature, with known composition.
- Laminar flames, at both burnt and unburnt conditions.

3.3.2 Calibration Operative Conditions

Gas Mixtures and Air at Ambient Temperature

These gas mixtures are used to provide calibration conditions at room temperature. The ambient air is processed in the laboratories facilities using a series of condenser and compressors. After this procedure, it is filtered to possibly remove remaining particles or other residuals. The other gas mixtures employed are instead composed as following, considering values in volume %:

- 20% CH_4 – 80% N_2;
- 20% CO_2 – 80% N_2;
- 2% CO – 35%H_2 – 63% N_2.

Laminar Flame

To calibrate the system in conditions close to the flame and post flame zone, a premixed methane air laminar flame is used. The burner used to stabilize the laminar flame is the Flat Flame Burner (FF burner) described in sec.3.1.3. The employed conditions span equivalence ratios in a range from lean to rich conditions, e.g. $\phi \in [0.80 - 1.3]$, are used to calibrate unburnt as well as fully burnt conditions, with the probe volume placed in the exhaust region for the latter. A sketch of the burner with an approximate position of flame and probe line is shown in fig.3.17a: when measuring the burnt conditions, the laser is focused above the flame, in order to pass through the exhaust gases. For the unburnt conditions, the flame is shut down.

Vertical Flame

The vertical flame burner, as presented in sec.3.1.3 is used to perform additional adjustments using a premixed methane / air unstretched laminar flame. The probe volume in this case is placed across the flame front, such that different conditions can be simultaneously monitored, including Raman and Rayleigh cameras alignment. A sketch cut of the positions of the flame brushes and probe line is shown in fig.3.17b.

The species concentrations and the temperatures used as setpoint for the calibration in the high temperature range are validated against several experimental and numerical characterizations of the burners employed for this task, that are the described FF and VF. Those characterizations are performed internally and in different, independent, institutions. Moreover, the described calibration burners and their respective setpoints have been used in a number of scientific publications, including [10, 11, 13, 17, 73].

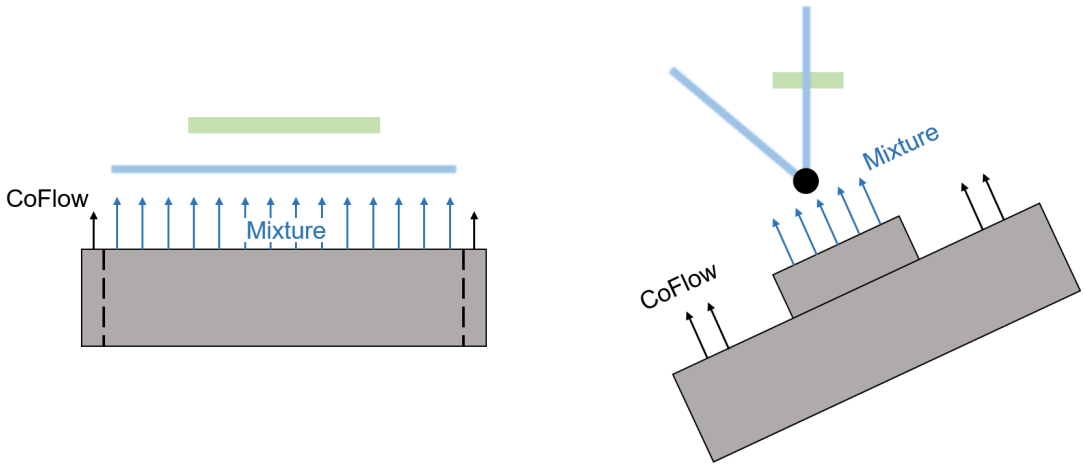

(a) **(b)**

Figure 3.17: Sketches representing the FF (a) and VF (b) burners, used for the calibration procedure. The light blue thick lines represent the flames, while the green ones the laser beam constituting the probe lines.

Chapter 4

Automated Calibration Routine

Summary

The present chapter is dedicated to the calibration routine implemented in the data processing for the simultaneous Raman/Rayleigh single shot in turbulent combustion. Given the deep specificity of the experimental technique and its implementation, no commercial or industrial packages are available to process the data from the raw condition to the desired output of temperature and species profiles. For this reason, a dedicated routine has been developed through the years at the RSM institute, in cooperation with the Sandia laboratories. In this context specific details will be given about the procedure to find the system tuners k's, introduced in the previous chapter. Further, an alternative approach will be presented.

For a better understanding of the methodology applied and the results commented, this chapter is introduced by a section (sec.4.1) where a background about optimization techniques is proposed.

The second part of the chapter is instead dedicated to the results obtained within this work about the developed routine. Section 4.2 reports the results of the analysis and synthesis operated on the data processing system operated in calibration mode. The problem of the tuners finding is then framed within a mathematical structure. More specifically, in sec.4.2.1 the structures and properties of the quantities involved in the experiments, such as the signal vector and the number densities are clarified, together with the tuners. In addition, the characteristics of the functions describing the Raman responses and the crosstalks will be analyzed. In sec.4.2.2 and sec.4.2.3 the problem setup and its formulation are presented. In sec.4.2.3 an alternative formulation for the problem is also introduced. The details about the implementation of the alternative approach are presented in sec.4.3, followed by an analysis of its performances.

4.1 Optimization Techniques: Principles and Review

For a better understanding of the proposed routine, some general remarks are reported here from literature on optimization problems, with specific regard to numerical optimization.

4.1.1 General Definitions

Nocedal in [74] introduces the optimization as the minimization or maximization of a function subject to constraints on its variables. The fundamental problem variables are:

$\boldsymbol{x} = \{x_1, x_2, \ldots, x_n\}$, the vector of unknown variables, also referred to as design variables.

$f(\boldsymbol{x})$, the objective function, i.e. the function to minimize / maximize.

$\boldsymbol{h}(\boldsymbol{x})$, set (array) of m_1 equality constraint functions.

$\boldsymbol{g}(\boldsymbol{x})$, set (array) of m_2 inequality constraint functions.

then the optimization problem can be written as:

$$\min_{\boldsymbol{x}\in\mathbb{R}^n} f(\boldsymbol{x}) \quad \text{with} \quad \begin{cases} \boldsymbol{h}(\boldsymbol{x}) = 0 \\ \boldsymbol{g}(\boldsymbol{x}) \leq 0 \end{cases} \tag{4.1}$$

The objective function and the constraints are functions of the design variables. In the basic cases they are such that $\mathbb{R}^n \to \mathbb{R}$, but in several problems they are functions such that $\mathbb{R}^n \to \mathbb{R}^m$. In a number of cases, the domain of functions and variables is not the set of the real numbers, but it might be restricted to only integers, positive / negative real numbers, or extended to complex numbers etc. In this case $\mathbb{R}$ is used as an exemplification, but the formulation does not lose validity if $\mathbb{Q}$, $\mathbb{Z}$, $\mathbb{N}$, ..., are used. Normally in those cases other constraints are added, to account for the peculiarities of the set in which the variables are defined. In fig.4.1 a geometrical representation of an optimization problem is shown.

A vector $\boldsymbol{x}^*$ is called "optimal" and provides a solution for the optimization expressed in (4.1), if:

$$f(\boldsymbol{x}^*) \leq f(\boldsymbol{x}) \quad \forall\, \boldsymbol{x} \,:\, \begin{cases} \boldsymbol{h}(\boldsymbol{x}) = 0 \\ \boldsymbol{g}(\boldsymbol{x}) \leq 0 \end{cases} \tag{4.2}$$

A general classification for optimization problems is based on the presence of constraints and on their specifics, as well as on the form of the objective function:

Constrained Optimization Problem if there are explicit constraints on the variables, the problem is defined "constrained". The constraints can span from simple bounds on the variables values, to complex relations among several variables, to limit the objective functions.

Unconstrained Optimization Problem if no explicit constraints are expressed. Sometimes constrained problems may be reformulated as unconstrained, with a proper mathematical treatment and/or modifications to the objective function.

Linear Optimization Problem if all the functions describing the constraints and the objective are linear functions in the design variables.

Nonlinear Optimization Problem if at least one function among constraints and objective presents nonlinearity in $\boldsymbol{x}$. They are also referred as "NLP", (Non Linear Programming problems).

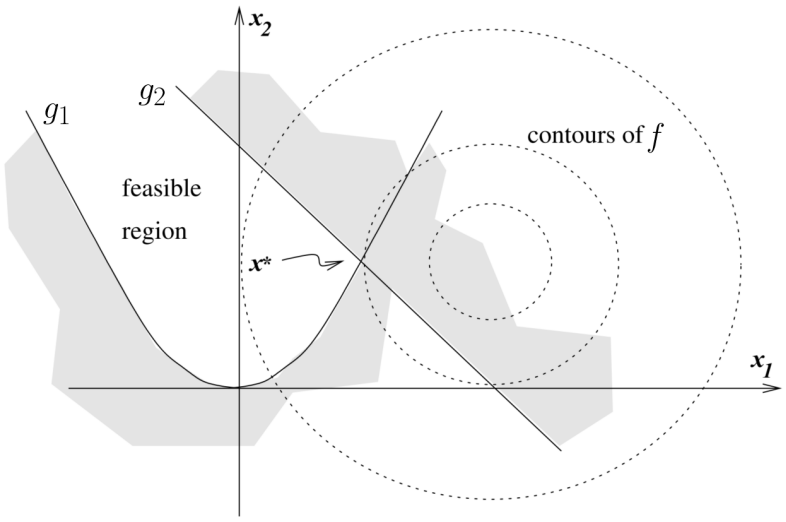

Figure 4.1: A geometrical representation of an optimization problem, in $\mathbb{R}^2$, with two inequality constraints g_1 and g_2, respectively linear and quadratic. The dark area marks the half-planes where the solutions cannot be accepted, for each constraint. The optimum is $\boldsymbol{x}^*$. Adapted from [74].

Local and Global Optima

If the goal of an optimization problem is to minimize $f(\boldsymbol{x})$, a point $\boldsymbol{x}^*$ is defined a "global minimizer" if

$$f(\boldsymbol{x}^*) \leq f(\boldsymbol{x}) \quad \forall \text{ feasible } \boldsymbol{x}. \tag{4.3}$$

The global minimum can be hard to find, because usually in practical applications the knowledge of f is only local. It is more common that the solution of a problem can be defined as a "local minimizer", i.e. a point in which the function has a minimum value within a certain neighborhood N: a point $\boldsymbol{x}^*$ is a local minimizer if:

$$\exists\, N(\boldsymbol{x}^*) \,:\, f(\boldsymbol{x}^*) \leq f(\boldsymbol{x}) \quad \forall\, \boldsymbol{x} \in N. \tag{4.4}$$

Generally speaking, *minima* and *maxima* can be referred to as *extrema* of a function.

Convexity

A fundamental property in optimization is based on the convexity concept. This applies both to functions and sets, i.e. to the functions domains.

A set $S \in \mathbb{R}^n$ is a convex set if all the points of the segment connecting two points arbitrarily chosen in S, lie themselves into S, i.e.:

$$\alpha\, x + (1-\alpha)\, y \;\in\; S \quad \forall\, \{x,\, y\} \in S\,; \forall\, \alpha \in [0,1] \tag{4.5}$$

Figure 4.2 show three examples of sets, to graphically represent the concept of convexity for a set.

A function is, similarly, defined convex if:

$$f(\alpha\, x + (1-\alpha)\, y) \;\leq\; \alpha\, f(x) + (1-\alpha)\, f(y) \quad \forall\, \alpha \in [0,1] \tag{4.6}$$

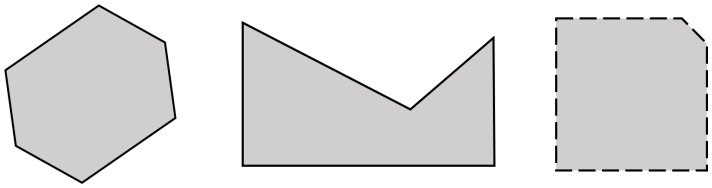

Figure 4.2: Three simple examples of sets, with the dark area representing the points included within the set, and the black outlines the boundary points included into the set. The set on the left is a convex set, while the other two are not: for the one in the center, it is easy to see that there are line segments connecting two of its points and lying partially out of the set. The set on the right is not convex because some of its boundary points are not included into the set.

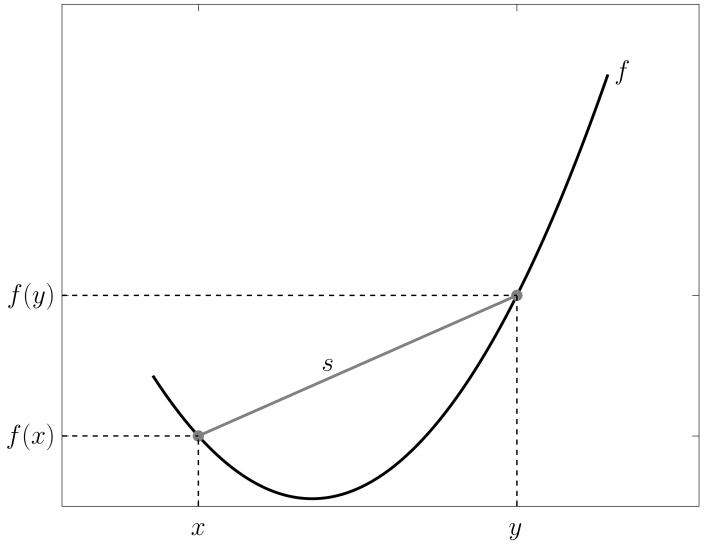

Figure 4.3: An example of convex function. $s = \alpha\, f(x) + (1 - \alpha)\, f(y)$.

that is, the straight line connecting $(x, f(x))$ and $(y, f(y)$ is always above f. Figure 4.3 shows a simple example with a quadratic function.

As noted in [74, 75], convexity helps in solving optimization problems, because stronger claims can be made about the convergence of algorithms, and the problem solving is, in terms of complexity and reliability, comparable to least-squares or linear optimization.

Convexity and Extrema

One of the most useful property valid for convex optimization problems can be here introduced: it can be proved that when the objective function f is convex, any local minimizer $\boldsymbol{x}^*$ is a global minimizer of f. If in addition f is differentiable, then any stationary point $\boldsymbol{x}^*$ is a global minimizer of f[1]. Duality is valid for maxima.

Unfortunately, when non-linear functions are involved in the problem, it is likely that convexity does not characterize the system [76]. As a consequence, it is more

[1]See [74] for further details.

difficult to guarantee that a local optimum is also the global optimum of the problem. On the contrary, sometimes there is not even a simple way to demonstrate that a nonlinear problem is a convex problem for all the feasible points.

Nevertheless, some considerations can be done on a function convexity, using its Hessian matrix $\underline{\underline{H}}(\boldsymbol{x})$. More specifically, as done in [76], the latter can be used to identify the character of extrema. The Hessian matrix, also noted $\nabla^2 f(\boldsymbol{x})$ or Hf, is the matrix of the second partial derivatives of f respect to each component of $\boldsymbol{x} = \{x_1, x_2, \dots x_n\}$ [2]. For clarity, it is worth to recall that if $\boldsymbol{f} = \{f_1, f_2, \dots, f_m\}$, i.e. $\boldsymbol{f}(\boldsymbol{x}) : \mathbb{R}^n \to \mathbb{R}^m$, an Hessian matrix can be written for each component of $\boldsymbol{f}$.

The nature[3] of the Hf can tell important information about f: the table 4.1 summarizes the different cases.

Table 4.1: Relation between Hessian matrix, its eigenvalues and convexity of a function.

$Hf(\boldsymbol{x})$	Eigenvalues of Hf	$f(x)$
Positive-definite	> 0	Strictly Convex
Positive-semidefinite	≥ 0	Convex
Negative-definite	< 0	Concave
Negative-semidefinite	≤ 0	Strictly Concave
Indefinite	$\gtrless 0$	Neither

Necessary and Sufficient Conditions

After providing a general definition of a function local minimizer, it is possible to define more rigorously the necessary and sufficient conditions for a point to be a solution for a minimization problem. An optimal point $\boldsymbol{x}^*$ is completely specified by satisfying those conditions. The description will be related to a minimum problem, but can be extended to maximum with an easy duality.

[2]
$$Hf = \begin{bmatrix} \frac{\partial^2 f}{\partial x_1^2} & \frac{\partial^2 f}{\partial x_1 \partial x_2} & \cdots & \frac{\partial^2 f}{\partial x_1 \partial x_n} \\ \frac{\partial^2 f}{\partial x_2 \partial x_1} & \frac{\partial^2 f}{\partial x_2^2} & \cdots & \frac{\partial^2 f}{\partial x_2 \partial x_n} \\ \vdots & \vdots & \ddots & \vdots \\ \frac{\partial^2 f}{\partial x_n \partial x_1} & \frac{\partial^2 f}{\partial x_2 \partial x_n} & \cdots & \frac{\partial^2 f}{\partial x_n^2} \end{bmatrix}$$

[3]If the quadratic form of a square matrix $\underline{\underline{A}}$ is the scalar $Q(\boldsymbol{x}) = \boldsymbol{x}^T \underline{\underline{A}}\, \boldsymbol{x}$, the following definitions can be adopted, $\forall\ \boldsymbol{x} \neq 0$:

1. Positive-definite: $Q(\boldsymbol{x}) > 0$.
2. Positive-semidefinite: $Q(\boldsymbol{x}) \geq 0$.
3. Negative-definite: $Q(\boldsymbol{x}) < 0$.
4. Negative-semidefinite: $Q(\boldsymbol{x}) \leq 0$.
5. Indefinite: $Q(\boldsymbol{x}) \gtrless 0$.

For defining the conditions for the optimum point $\boldsymbol{x}^*$ of $f(\boldsymbol{x})$, it is helpful to start from the Taylor series expansion of $f(\boldsymbol{x})$ [76], written in a neighborhood of $\boldsymbol{x}^*$ with the hypothesis that f is a smooth function, of class C^∞:

$$f(\boldsymbol{x}) = f(\boldsymbol{x}^*) + \nabla^T f(\boldsymbol{x}^*)\,\Delta\boldsymbol{x} + \frac{1}{2}\,\Delta\boldsymbol{x}^T\,\nabla^2 f(\boldsymbol{x}^*)\,\Delta\boldsymbol{x} + o(\Delta\boldsymbol{x}) \tag{4.7}$$

where $\Delta\boldsymbol{x} = \boldsymbol{x} - \boldsymbol{x}^*$ is the perturbation from $\boldsymbol{x}^*$.

The definition of the existence of a local minimum in $\boldsymbol{x}^*$ is, as already seen above, that

$$f(\boldsymbol{x}) - f(\boldsymbol{x}^*) \geq 0 \tag{4.8}$$

and $\boldsymbol{x}^*$ is a global minimum if the relation holds for any $\boldsymbol{x}$ in the domain of interest. Focusing on the second term of the RHS in eq.(4.7), $\nabla^T f(\boldsymbol{x}^*)\,\Delta\boldsymbol{x}$, one can notice that the perturbation from the minimum, being arbitrary, can be either positive or negative. It follows that it could be possible that

$$\nabla^T f(\boldsymbol{x}^*)\,\Delta\boldsymbol{x} < 0 \Rightarrow f(\boldsymbol{x}) - f(\boldsymbol{x}^*) < 0 \tag{4.9}$$

that is in contrast with the condition expressed in eq.(4.8). The only way to assure that eq.(4.8) holds true for any perturbation $\Delta\boldsymbol{x}$ from $\boldsymbol{x}^*$, is that

$$\nabla f(\boldsymbol{x}^*) = 0 \tag{4.10}$$

This is indeed a necessary condition for a minimum of $f(\boldsymbol{x})$: the gradient of f has to be null at $\boldsymbol{x}^*$, i.e. $\boldsymbol{x}^*$ is a stationary point. Given that the condition is imposed on the gradient of the function, it is also referred to as "first order necessary condition".

The third term of the RHS in eq.(4.7) can characterize the stationary point to be a minimum, maximum or saddle point. More specifically, the information can be withdrawn from $\nabla^2 f(\boldsymbol{x}^*)$, combining also the specific properties related to convexity, seen in sec.4.1.1 and the information of table 4.1. The following table 4.2 can express those considerations, that represent the "second order necessary condition".

Table 4.2: Second order necessary conditions. Reproduced from [76].

$\nabla^2 f(\boldsymbol{x}^*) \equiv Hf$	$\Delta\boldsymbol{x}^T\,\nabla^2 f(\boldsymbol{x}^*)\,\Delta\boldsymbol{x}$	f near $\boldsymbol{x}^*$
Positive-definite	> 0	Increases
Positive-semidefinite	≥ 0	Possibly Increases
Negative-definite	< 0	Decreases
Negative-semidefinite	≤ 0	Possibly Decreases
Indefinite	$\gtrless 0$	Not defined

Interpreting the information of the table 4.2, it is possible to say that the Hessian matrix, or equivalently the second order term of the Tayor series expansion of f, defines the behavior of the function in the neighborhood of the stationary point $\boldsymbol{x}^*$. Once this behavior is understood, it is possible to say if the point is a mamixum, a minimum, or it might be a saddle point.

Table 4.3: Second order sufficient conditions. Reproduced from [76].

$\nabla^2 f(\boldsymbol{x}^*) \equiv Hf$	$\boldsymbol{x}^*$
Positive-definite	Isolated minimum
Negative-definite	Isolated maximum

Among the second order necessary conditions, the cases where the quadratic form of Hf evaluated in $\boldsymbol{x}^*$ is strictly larger or smaller than zero, define the second order sufficient conditions, reported in table 4.3.

It is eventually possible to summarize the conditions to guarantee that $\boldsymbol{x}^*$ is an extremum:

1. $f(x)$ is twice differentiable at $\boldsymbol{x}^*$.
2. $\nabla f(\boldsymbol{x}^*) = 0$. Consequently, $\boldsymbol{x}^*$ is a stationary point.
3. $Hf(\boldsymbol{x}^*)$ is positive-definite (/negative-definite) for a minimum (/maximum) to exist in $\boldsymbol{x}^*$.

With the first two points of the list being the necessary conditions, and the third the sufficient condition. It is also important to say that it is not always possible to prove those conditions in the point of interest, which could be anyway an extremum.

4.1.2 Review of Algorithms

After the general treatment of the previous section about definitions and relevant aspects of optimization problem, a short overview of some important algorithms and/or numerical methods used in this field is here provided. It is clearly not aiming to be a comprehensive treatment of the topic, for which a number of references can be used, including [74–79].

Generally speaking, once the optimization problem is set up, one or more algorithms are applied to search for the optimum point. Usually the algorithm moves towards the problem solution from a starting point $\boldsymbol{x}_0$, generating a sequence of iterations. The main differences between different algorithms are in how the iteration k brings the problem from the attempt $\boldsymbol{x}_{k-1}$ to $\boldsymbol{x}_k$. A main differentiation is classically done between "line search" and "trust region" methods. In the following some peculiarities of the two classes of methods are reported.

Line Search

The algorithms based on the line search strategy, search for a possible new iteration from $\boldsymbol{x}_k$ choosing a direction p_k. Once this is fixed, the step length from one iteration to the other in principle is defined by a sub-problem:

$$\min_{\alpha>0} f\left(x_k + \alpha\, p_k\right)$$

which would probably lead to increase the computational efforts. More often, the step α to take along p_k is chosen with several trial steps.

Clearly the crucial aspect in this class of methods is the definition of the direction along which the method will move the step at each iteration. There are several options for this task, and among them it is worth to cite the "steepest descent direction" and the "Newton direction", briefly described in the following, together with some similar approaches.

Steepest Descent This method is the straightforward choice, using the opposite of the gradient to select the direction that is, by definition, the one pointing toward the function most rapid decrease:

$$p_k = \nabla f_k \tag{4.11}$$

Being the gradient perpendicular to the function contour, it is also possible to pick a direction forming with $-\nabla f_k$ and angle smaller than $\pi/2$, and being still sure to point toward a function decrease. Figure 4.4 shows both the cases.

Newton The search direction is defined using a second-order Taylor series, approximating $f(x_k + p)$:

$$f(x_k + p) \approx f_k + p^T \nabla f_k + \frac{1}{2} p^T \nabla^2 f_k \, p \tag{4.12}$$

The direction is defined with the vector p that minimizes this approximation, found differentiating the expression and setting it to zero, leading to [74]:

$$p_k = -\left(\nabla^2 f_k\right)^{-1} \nabla^2 f_k \tag{4.13}$$

Two important considerations can be made about this method. The second order approximation brings a small error when p is small, and is then acceptable. In addition, clearly this approach requires the computation of the Hessian matrix, and then of all the second derivatives of f_k, that has also to be inverted. This effort is not required by the gradient method, where only the first derivatives have to be computed. Important to notice is also that $(\nabla^2 f_k)^{-1}$ might not be defined, and then modifications have to be used. The advantage of the Newton methods is a super-linear rate of convergence. It is very quick to converge, especially if the starting point is close to the solution, but can also diverge in some cases [77].

Quasi-Newton Clearly related to the Newton class methods, they reduce the impact of computing the Hessian matrix at each iteration by using, in place of $H\ f$, a matrix to approximate it. This matrix is updated using information about the changes in the gradients, based on the simplifying hypothesis [74] that

$$\left(\nabla^2 f_{k+1}\right)(x_{k+1} - x_k) \approx \nabla f_{k+1} - \nabla f_k \tag{4.14}$$

More information about the Newton and quasi-Newton methods are reported in the appendix A to this thesis, where the 1D cases are better detailed for the two methods.

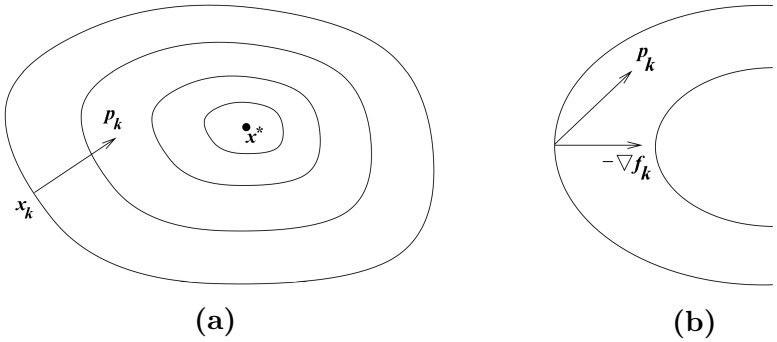

Figure 4.4: (a) The direction p_k is given by the opposite of the gradient, computed in x_k, where is then perpendicular to the contour of f. (b) The direction p_k forms an angle smaller than $\pi/2$ with the gradient direction, and is consequently pointing toward the decrease of f, even if not following the path of the most rapid descent. Reproduced from [74].

Trust Region

When the iterations are at the point $\boldsymbol{x}_k$, the trust region based algorithms build a model function m_k, whose behavior is similar to f in the vicinity of the current point, i.e. in that specific "trust region". Once the model function is built, the algorithm searches for the next step using m_k and not f, solving a sub-problem within the trust region:

$$\min_p m_k(x_k + p) \tag{4.15}$$

If the decrease in the model does not produce a sufficient reduction in the value of f, the trust region is changed in size and/or shape. It is common that the model function is a quadratic approximation of the objective function, with the second order term being either the Hessian or an approximation to it.

The size of the trust region is critical, for an effective method behavior: when it is too small, extra-time is spent when a bigger step could have been made toward the solution; if it's too big, the model minimizer could not bring a satisfying result for the objective function, and the region size might be shrunk. Usually a parameter is used to adjust the size of the trust region, given a step p_k:

$$\rho_k = \frac{f(x_k) - f(x_k + p_k)}{m_k(0) - m_k(p_k)} = \frac{\text{Actual Reduction}}{\text{Predicted Reduction}} \tag{4.16}$$

Being the denominator always positive[4] it follows that if $\rho_k < 0 \Rightarrow f(x_k + p_k) > f(x_k)$ and then the step has to be rejected. If $\rho_k > 0$ then the step can be accepted by the algorithm. Additionally, if $\rho_k \simeq 1$, it is safe to stretch the size of the trust region, having the model function and the objective function a very similar behavior.

Within the trust region, several methods can be used to minimize the model function, including models similar to the one seen for the line search methods.

[4]It includes the value of $m_k \equiv m_k(0)$, while all the possible steps p_k from $m_k(0)$ are made toward a decrease of the model function.

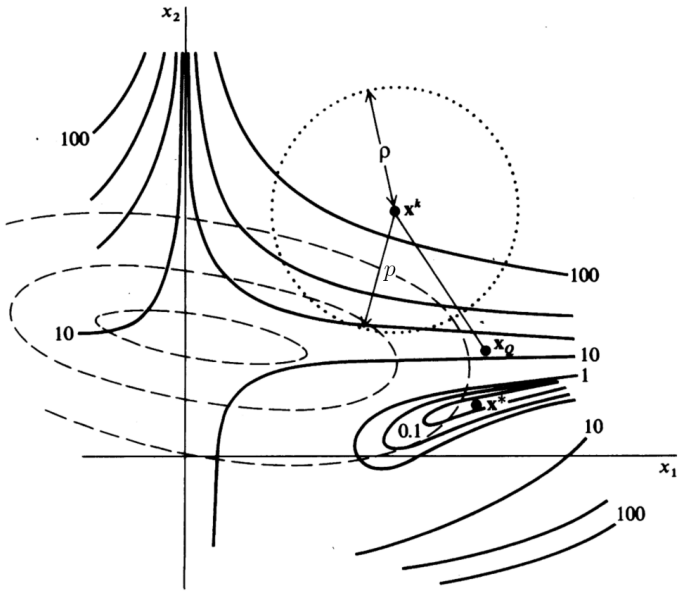

Figure 4.5: Representation of the trust region to select the step length. Solid lines are contours of $f(\boldsymbol{x})$. Dashed lines are contours of the convex quadratic approximation of $f(\boldsymbol{x})$ at $\boldsymbol{x}_k$. The dotted circle is the trust region boundary in which δ is the step length $\boldsymbol{x}_0$, is the minimum of the quadratic model m_k. Reproduced from [76].

Genetic Algorithm in MATLAB®

The genetic algorithm, as implemented in MATLAB® and detailed in [80], is based on [81–83]; some relevant aspects are here summarized.

The logic behind this class of methods is inspired by the process driving biological evolution. The progresses of the algorithm toward the solution are based on a "population" of "individuals", i.e. possible values of the design variables, candidates to be the solution. An individual is a possible (set) of values for the design variables, and the population is formed by a number of possible solutions. Figure 4.6 presents a sketched representation of some of these features. Using a population of individuals means that at each iteration a number of possible solutions are generated, rather than only one. A score is given to each of the possible solutions, i.e. each of the individual of the population, on the basis of ifs performance with respect to the objective function. At each iteration i, named in this case "generation", the $(i+1)$-th generation is composed using information from the individuals of the i-th generation, with the characteristics of an individual being referred to as "genes". Some of the individuals of the generation i are then the "parents" of the individuals of the generation $(i+1)$, indeed often referred to as "children".

The algorithm mixes deterministic calculations and random number generation to perform the evolution from a generation to the next one. The selection rules are regulating the process of selecting, modifying and combining the parents individuals that will contribute to the evolution. The evolution criteria may be different, depending on the specific implementation, but common approaches are used. The most relevant are listed below, together with important aspects involved in the process. Figure 4.7 reports a sketched visual representation of the evolution process.

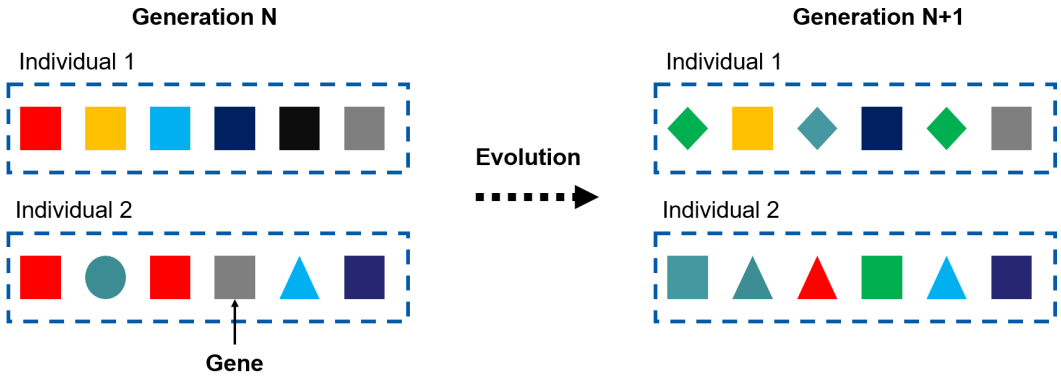

Figure 4.6: Sketched representation of some features of a genetic algorithm. Each generation is composed by a population of individuals (two, in the case of the sketch). Each individual is composed by genes. Through the evolution process the algorithm generates new individuals, mixing deterministic calculations and random number generation.

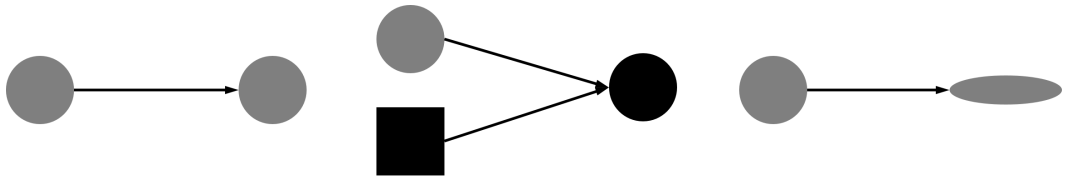

(*a*) Elite Child (*b*) Crossover (*c*) Mutation

Figure 4.7: Basic principles to evolve from a generation to the next one, with the arrow representing the evolution: (a) Elite Child: a parent individual, without modifications, becomes a child of the next generation; (b) Crossover: two parents with different characteristics are combined to form a child, which will have combined characteristics from the parents.; (c) Mutation: a parent individual is modified in some of its characteristics to form a child.

Elite Child Some of the parents might be selected to become elite child, i.e. individuals staying the same through the evolution.

Crossover With this mechanism, two "parents" are combined to form the next generation children, named "crossover child". A crossover child has mixed characteristics from the parents. Genes can be randomly selected among the two parents and mixed or concatenated to form children. Also, it can represent a weighted average of the parents. Other possibilities are, for example, to create a child that lies on the line containing the two parents. The position on the line is determined thanks to the score of each of the parents.

Mutation Is the case when individual parents are modified to form children. For example, randomly selected genes might be altered to generate a child. Different approaches are possible. The Gaussian procedure adds a random number, chosen from a Gaussian distribution with 0 mean, to each entry, i.e. each gene, of the parent vector. The amount of mutation is proportional to the standard deviation of the distribution, set as an initial parameter, and can be defined in order to decrease across generations. The "uniform" mutation selects a fraction of the genes

to be mutated, depending on user defined values, and replaces them with random numbers selected uniformly within the allowed values. This mutation function is then particularly useful when bounds are imposed on the problem. Other approaches are possible to compete with constrained optimization problems.

4.2 Data Processing: Mathematical Formulation of the Calibration Routine

As anticipated in the summary of this chapter, sec.4.2 is dedicated to present the results of the analysis and synthesis procedures operated on the data processing system, when operated in calibration mode. A mathematical structure will be presented for the Raman/Rayleigh data processing system, with specific details about the calibration procedure, in sec.4.2.1. Some fundamental quantities involved in the data processing, introduced in the previous chapter, are here characterized depending on their mathematical properties. In fact, the tuners of the Raman matrix, the signal and number densities vectors are analyzed. Also, the characteristics of the functions describing the Raman responses and the crosstalks are presented.

In sec.4.2.2 and sec.4.2.3 the problem setup and its formulation are presented. This last section introduces an alternative formulation for the problem, which will be detailed in the next chapter.

4.2.1 Problem Variables

The scope of the calibration routine in the data processing is to find one value for each of the system tuners, k's, as presented in 3.2.4. As already said, this process is based on the use of reference calibration data, acquired in known conditions, and the values assigned to the tuners are kept constant in the unknown conditions.

Tuners

Recalling the Raman equation, (3.6):

$$\boldsymbol{S} = \underline{\underline{M}}(T)\boldsymbol{N} \tag{4.17}$$

the tuners are included into the Raman matrix, $\underline{\underline{M}}$, as one of the two components of the $m_{ij} = k_{ij} \cdot c_{ij}(T)$. While the $c(T)$'s are polynomial functions in the temperature domain, the tuners are defined such that

$$k_{ij} \in \mathbb{R}^+ \tag{4.18}$$

meaning that they are positive real numbers, and 0 is not a feasible value for their definition. This limitation is due to the obvious reason that a null multiplier would cancel the effect of the correspondent Raman response or crosstalk. There is also an additional reason for imposing $k_{ij} > 0$ and not $k_{ij} \geq 0$, and it becomes clear when adding more details about the treatment of the tuners within the data processing routine. More specifically it is important to point out that the species multipliers, i.e. the tuners $k_{ij} : i = j$, are treated in the routine as $1/k_{ij}$. Clearly, $\lim_{k_{ij}\to 0} 1/k_{ij} = \infty$.

Additionally one may point out that, being the whole routine executed with machine based computations, the existence itself of all the elements $\mathbb{R}^+$ is questionable in this context, due to the round-off procedure which excludes the set of the irrational numbers. Intrinsically $\mathbb{R}^+$ could be restricted only to the positive rational numbers, $\mathbb{Q}^+$, as it is done in practice when it comes to practically find a solution for the Raman equation. With this in mind, but considering that in the following a more general

mathematical description will be given, $\mathbb{R}^+$ will be kept as reference set for the k's domain of existence.

A peculiarity of the k's, already mentioned but worth to stress, is that each of the tuner, k_{ij}, has to take one and only one value, valid for all the thermochemical states possibly processed through the Raman equation, when they are referring to the same measurement slot[5].

If one refers to the Raman matrix as written in (3.9), the tuners are 23, one for each non-zero element of M. In other configurations, this number can change.

Raman responses and Crosstalks Polynomials

In sec.3.2 details have been given about the procedure for the construction of the Raman responses and the crosstalks. Here some peculiarities related to their polynomial structures are shown.

As explained in 3.2 some of the $c(T)$'s are pre-defined functions, while others come from the integration of the convoluted spectra. The pre-defined functions are 3rd to 5th order polynomials, in the temperature domain. Figure 4.8 shows as an example the polynomial functions representing the crosstalks from CH_4 (4.8a) and H_2O (4.8b) onto the other species channels. In this case all the functions are 4th or 5th order polynomials. Accordingly, they can present up to 3 or 4 local extrema and up to 2 or 3 inflection points, respectively, as it can be observed from the figure. This last characteristic will be relevant in the next discussions throughout the present work. Similar specifics are highlighted from the crosstalks functions obtained from the convoluted spectra integration: different scales and inflections are clearly visible from fig.4.9, where the crosstalks from H_2 onto the other species channels are shown.

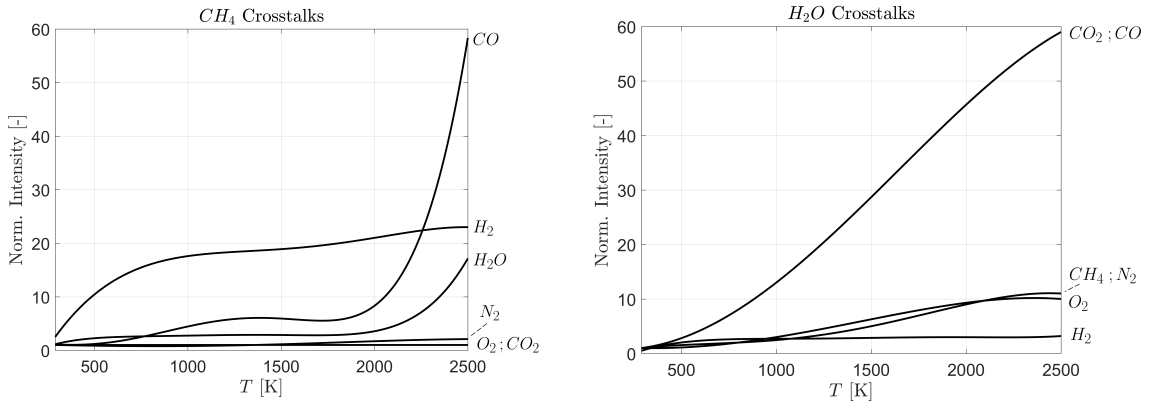

Figure 4.8: Polynomial functions expressing the crosstalks from (a) CH_4 and (b) H_2O onto the other species channels. The shown functions are 4th or 5th order polynomials.

[5]As previously mentioned, special cases can require the need to modify some of the tuners within one slot. This can happen, for example, when the measurement slot is prolonged in time, and the system hardware may encounter some drift.

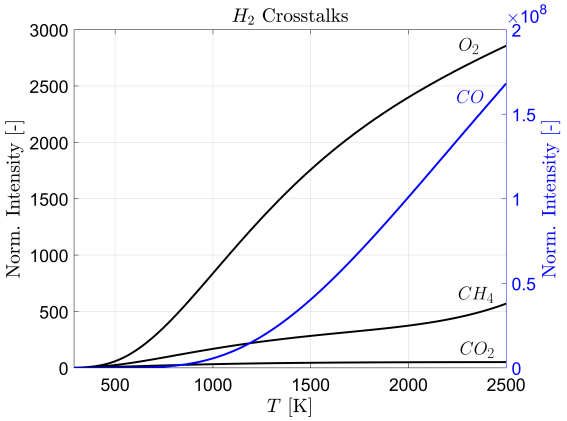

Figure 4.9: Polynomial functions expressing the crosstalks from H_2, as obtained from the convoluted spectra integrations.

Inverting the point of view, it is possible to visualize the contributions to a species channel from different sources. Specifically, in each channel there will be signal coming from its own species as well as the crosstalks from other species. Figures 4.10a and 4.10b show, as an example, the different contributions to the CO_2 and O_2 channels, respectively. Several important aspects can be noted. First, again it is clear how the single contributions are very different, in terms of maximum intensity and shape. In addition, it is clear in the CO_2 channels as the relative importance of the contribution can vary with the temperature: while H_2 gives the most relevant part of the signal up to about 2000 K, for higher temperatures the one from H_2O becomes the most intense crosstalk signal.

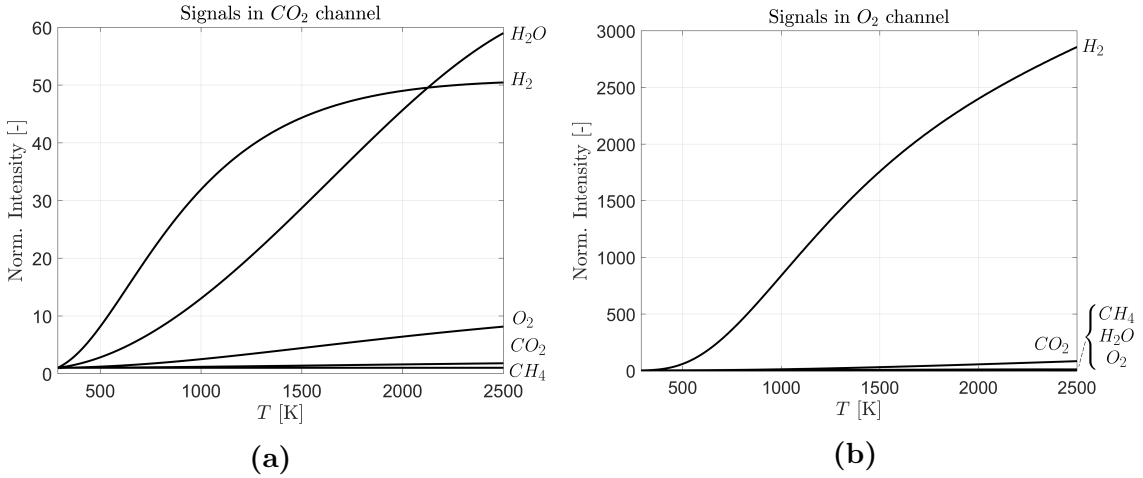

Figure 4.10: Individual contributions to (a) CO_2 and (b) O_2 channels, as from the look-up tables.

Signal and Number Densities Vectors

The elements of the signal vector are positive scalars such that:

$$\boldsymbol{S} \in \mathbb{R}^n \tag{4.19}$$

if n is the number of species. Also in this case, considering that the information processed comes from digital signals, rigorously one could replace $\mathbb{R}$ with $\mathbb{Q}$. For the elements of the signal vector, 0 is in principle a feasible value, even though in practice a certain signal intensity is always present due to noise or other disturbances; as a consequence it is hardly possible that any element of $\boldsymbol{S}$ is exactly equal to zero. The same principles for $\boldsymbol{S}$ apply to the Rayleigh signal as well as the number density vector N.

4.2.2 Problem Setup

Overview

Figure 4.11 shows a block scheme of the elements to process the Raman/Rayleigh measurement to obtain the temperature and concentrations. The core of the central block is composed by solving the Raman equation, through the loop shown in fig.3.15.

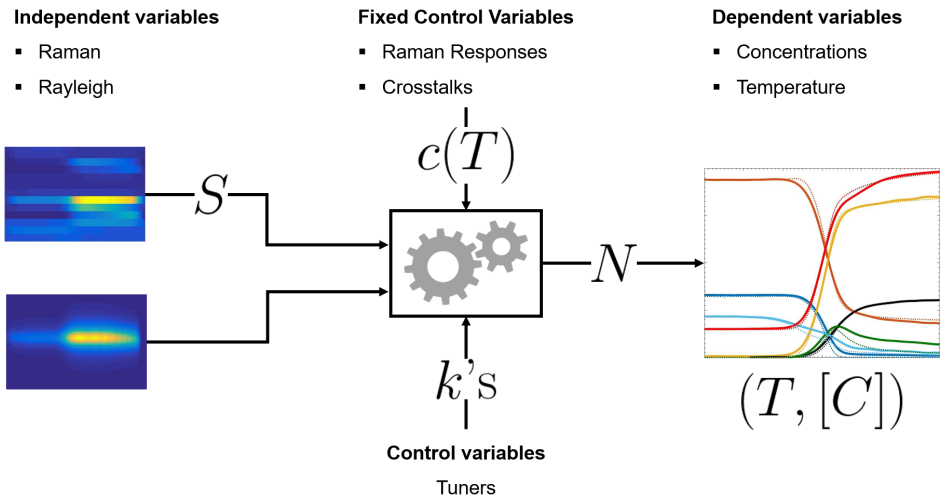

Figure 4.11: Block scheme with the main components of the Raman/Rayleigh data processing system.

With the variables so far analyzed, it is possible to look at the Raman/Rayleigh processing system shown in fig.4.11, from two different perspectives, illustrated in the following.

Processing Mode When the system is in "Processing Mode" the goal is to obtain the thermochemical state $(T, [C])$, starting from the signal vector $\boldsymbol{S}$ and from the Rayleigh measurement. The c's are given with the already discussed procedure. In this operation mode the tuners k's are already adjusted and the system is calibrated. The vector $\boldsymbol{N}$ and T represent the unknowns of the Raman equation. The thermochemical state is not known beforehand and the correct calibration is crucial to obtain the correct "translation" from the signals to the temperature and concentrations. It can be helpful to recall that $\boldsymbol{S}$ and $\boldsymbol{N}$ are discretized, and then for each 1-D single shot, each segment is processed independently from the other, to contribute to the 1-D output profiles.

Calibration Mode The block system stays the same, and also the variables format does not change. The fundamental difference is that, in this mode, the tuners can be seen as "design variables" and their values are not fixed yet: the goal of this operating mode is to find the right values for the set of k's. This is possible because the measurement of $\boldsymbol{S}$ and the Rayleigh signals are acquired in known conditions, and then the system output $(T, [C])$ can be compared with an expected value, $(T^{\text{th}}, [C]^{\text{th}})$. The system is calibrated in the given condition when

$$(T, [C]) = (T^{\text{th}}, [C]^{\text{th}}) \tag{4.20}$$

Accounting for non-idealities, the condition may be considered satisfied when eq.(4.20) is respected with a given tolerance.

Figure 4.12 shows the same block scheme as the fig.4.11, with an additional section including a generic known calibration state, identified by $(T_i, [C]_i)$, that is measured. The system output $(T, [C])$, obtained from processing this measurement, is compared with $(T_i, [C]_i)$ for the calibration purposes.

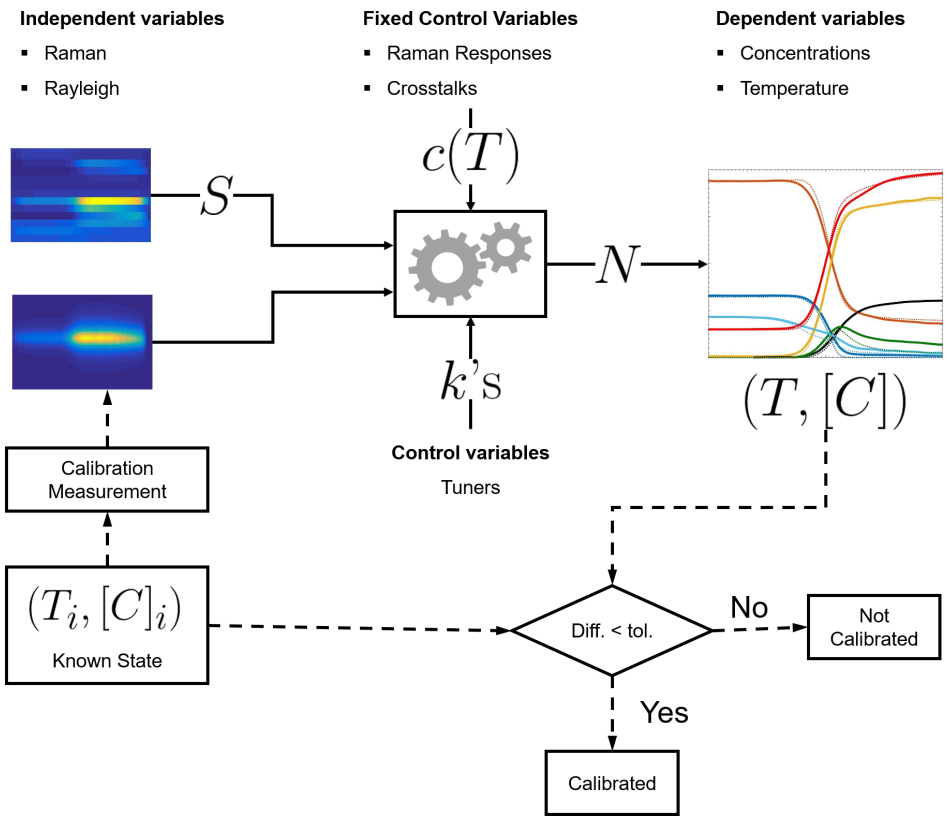

Figure 4.12: Block scheme with the main components of the Raman/Rayleigh data processing system operated for the calibration purpose. The system output is compared with the input, whose specifics are known beforehand. If there is a good correspondence, the system is assumed to be well calibrated.

In the following part a focus on the calibration mode is given, explaining how the tuners calibration is performed in the previous approach and modified in the present work.

Goal

It has been already clarified that the calibration goal is to find out the optimal set of values for the tuners. At this point it is important to highlight that the mentioned unique set must be valid in all the calibration conditions, given by the thermochemical states presented in 3.3.2. The crucial aspects of the procedure can be summarized as follows:

- The tuners adjusted according to one specific condition, could (and probably will) not fit for another condition, unless adjustments are made.
- The tuner's effects are coupled: several tuners act on the same system output variable, as sketched in fig.4.13a.
- The tuner's effects spread over all the system output: a single tuner may affect the behavior of several output variables sketched in fig.4.13b.

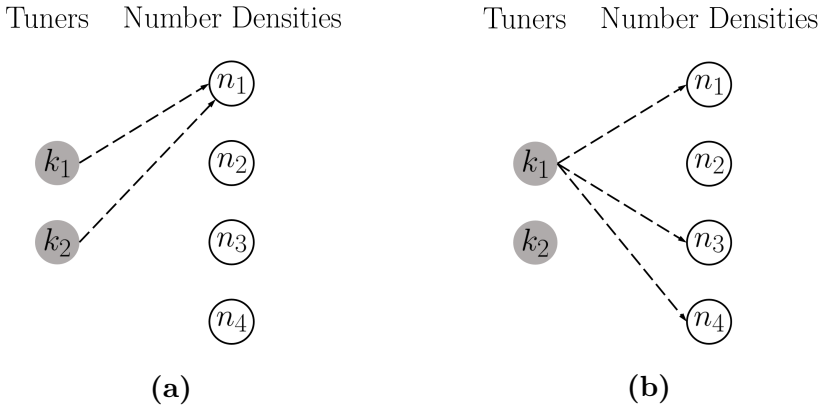

Figure 4.13: Example with 2 tuners, k_1 and k_2, and four output variables $\{n_1, n_2, n_3, n_4\} \in N$. (a) Coupled effects of the two tuners on n_1. (b) The tuner k_1 affects several variables in the system output.

The effects described in the second and third points of the bullet list will be characterized respect to a real set of data in sec.4.3.2.

4.2.3 Problem Formulation

Previous Approach

To reach the goal described above, an empiric or semi-empiric approach has been employed in the previous calibration procedures of the Raman / Rayleigh data, processed with the Hybrid Method. The procedure can be summarized by the loop in fig.4.14, and explained as follows.

Tuners Adjustment

1. All the calibration conditions are measured and available. A generic condition is marked as $(T_i, [C]_i)$.
2. A first guess for all the tuner values is done.
3. Using these tuners, the first condition of the set, $(T_1, [C]_1)$, is processed. The output is $(T_1^*, [C]_1^*)$
4. One or more tuners are adjusted, in order to bring the system output close to the expected output $(T_1^{\text{th}}, [C]_1^{\text{th}})$. The set values found can be noted as $[k]|_1$. In the loop of fig.4.14 it is assumed that $(T_i^{\text{th}}, [C]_i^{\text{th}}) = (T_i, [C]_i)$ for brevity, but non ideality, due for example to precision and accuracy errors, would make those sets differ. This step is repeated as many times as required to obtain the correspondence between input and output.
5. A different calibration condition, say $(T_2, [C]_2)$ is processed, giving $(T_2^*, [C]_2^*)$ as output.
6. Adjustments are made on the tuners, as for the point 4, bringing the values from $[k]|_1$ to $[k]|_2$.
7. The procedure continues for all the n calibration setpoints.
8. At the end of the first iteration, the tuners could have values $[k]|_n \neq [k]|_1 \neq [k]|_2 \neq [k]|_i$. The loop is repeated in order to find a compromise that would finally lead to a unique set of k's, $[k]$, good for all the calibration setpoints.

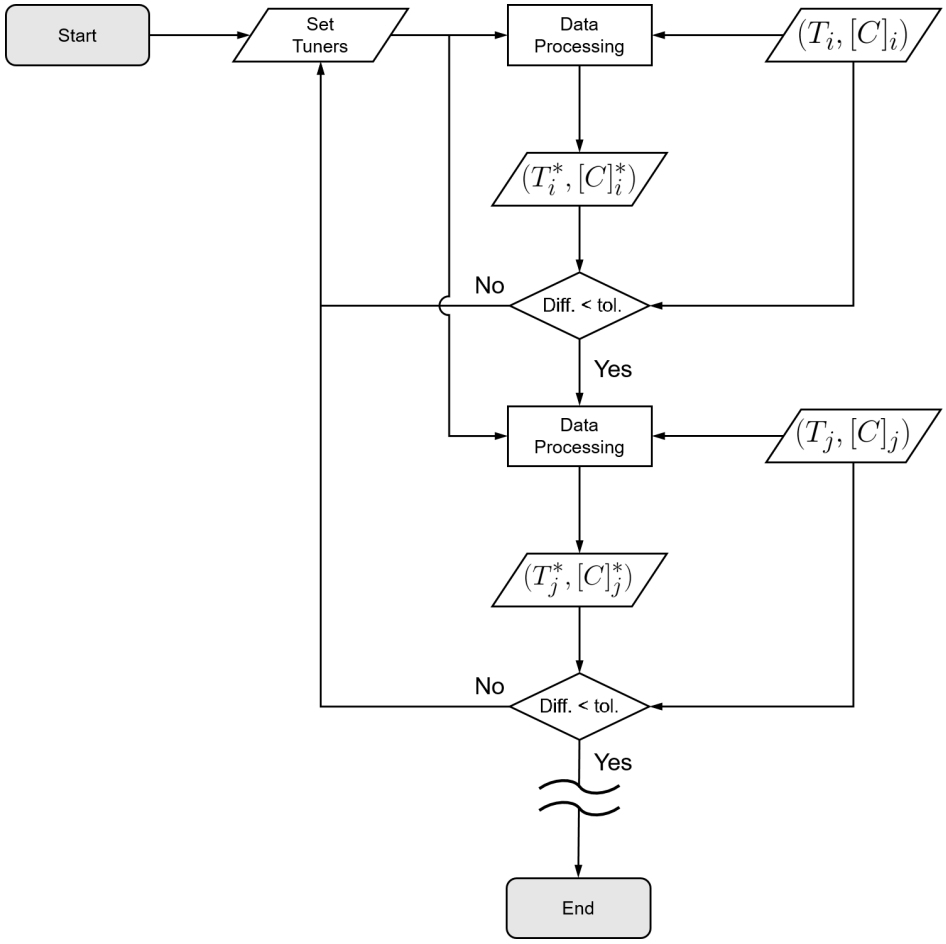

Figure 4.14: Flow chart of the tuners adjustment according to the previous approach. The flow refers to two calibration setpoints measured, $(T_i, [C]_i)$ and $(T_j, [C]_j)$. The starred points are the output of the data data processing. All the procedure, from the start to the end, is done in a loop (not shown in figure), until all the starred outputs are equal to the correspondent input (considering a defined tolerance).

The procedure presented above has some weak points. First, it can be very time consuming, because the loop may require a number of iterations, before finding the best $[k]$. In addition to that, a certain level of empiricism is present, given that the decision to stop the iterations is left to the operator. Moreover, a deep expertise about the system behavior and dynamics is required to the operator, in order to understand which adjustments apply to the tuners during the loops. Last but not least, the response of the data processing system might be different with modified conditions, and this adds further complexity to the procedure.

Modified Routine

Those weaknesses highlighted the need to propose a different approach to the routine used to find the tuners values, introduced here and detailed in the next sections.

The proposed routine attempts to address some critical aspects, such as removing a part of the procedure intrinsic empirism, and the strong dependence on the operator's expertise and actions. The fundamental idea is to move the focus from a loop

with intensive man-based iterations to a routine mostly machine-based. This vision is achieved by providing to the routine several calibration setpoints that are accounted for simultaneously, in order to obtain as an output a tuners set already optimized for all the provided setpoints.

The problem can then be set as an optimization problem. For the i-th calibration condition, the fundamental variables indicating the setpoint and the data processing output are set as:

$T_i^{\text{th}}, [C]_i^{\text{th}}$ is the setpoint

$T_i^*, [C]_i^*$ is the data processing output

where it is worth to remember that $[C]_i$ is for the species of interest concentrations in the condition i, and is then a array of values.

It is possible to compute an error e_i, accounting for the differences between the desired output, marked with the superscript "th", and the actual output, marked with the "$*$". Given that an error e_i can be computed for each calibration condition, a vector of error functions can also be composed: $\boldsymbol{e} = \{e_1, e_2, \ldots, e_{n_c}\}$, where n_c is the number of calibration conditions used in the procedure. The goal of the routine can clearly be identified as finding a set of tuners k's, noted $\boldsymbol{k}$, such that the error function $\boldsymbol{e}$ is minimum:

$$\boldsymbol{k} \,:\, \min_{\boldsymbol{k}} \boldsymbol{e}(\boldsymbol{k}) \tag{4.21}$$

More specifically, if n_k is the size of the tuners vector

$$\boldsymbol{e}(\boldsymbol{k}) \,:\, \mathbb{R}^{n_k} \rightarrow \mathbb{R}^{n_c} \tag{4.22}$$

then the routine goal is to find a set of k's, $\boldsymbol{k}_{\text{opt}}$, such that

$$\boldsymbol{k}_{\text{opt}} \in \mathbb{R}^{n_k} \,:\, \boldsymbol{e}(\boldsymbol{k}_{\text{opt}}) \leq \boldsymbol{e}(\boldsymbol{k}) \quad \forall\, \boldsymbol{k} \in \mathbb{R}^{n_k} \tag{4.23}$$

It can be useful to list all the variables introduced:

k one of the system tuners.

$\boldsymbol{k}$ the set of tuners.

$\boldsymbol{k}_{\text{opt}}$ the set of tuners chosen at the end of the routine, such that the system outputs are as close as possible to their correspondent expected outputs.

n_k number of tuners, i.e. size of $\boldsymbol{k}$.

$(T_i^{\text{th}}, [C]_i^{\text{th}}$ expected output from the data processing for the calibration condition i.

$(T_i, [C]_i)$ real thermochemical state of the calibration condition i. Due to non ideality, it can be that $(T_i, [C]_i) \neq (T_i^{\text{th}}, [C]_i^{\text{th}})$

$(T_i^*, [C]_i^*)$ data processing output, when the calibration condition i is processed.

n_c number of calibration conditions used within the routine.

e_i error function describing the difference between $(T_i^{\text{th}}, [C]_i^{\text{th}})$ and $(T_i^*, [C]_i^*)$. It is possible to identify n_c error functions.

$\boldsymbol{e}$ error function, array composed by the e_i.

In the next section, the implementation of the problem formulated in eqs.(4.21) - (4.23) is detailed.

4.3 Automated Calibration Routine

After presenting the problem setup for the calibration routine in sec.4.2, in this section the details about the implementation of the alternative approach introduced in sec.4.2.3 are given. Further, results of the application will be illustrated. In the following, the modified routine will be referred to as "Automated Calibration Routine" (ACR).

4.3.1 Non Linear Programming problem formulation

It is worth to recall the basic problem formulation, as stated in eq.(4.21), considering the main objective function variables:

$$\min_{\boldsymbol{k}} \boldsymbol{e}(\boldsymbol{k}, \boldsymbol{T}, \underline{\underline{C}}) \quad \text{with} \quad \boldsymbol{e} : \mathbb{R}^{n_k} \rightarrow \mathbb{R}^{n_c} \tag{4.24}$$

remembering that $\boldsymbol{e}$ is the vector of the error functions e_i, n_k is the size of the tuners vector, n_c is the number of calibration conditions used in the procedure, and the tuner set $\boldsymbol{k}$ is the design variables set. $\boldsymbol{T}$ is the set of temperatures corresponding to the n_c conditions, and $\underline{\underline{C}}$ is the set of species concentrations for the same set. Giving that for each calibration condition one temperature and seven species are defined, the dimension of these variables are

$$\boldsymbol{T} = [1 \times n_c] \quad ; \quad \underline{\underline{C}} = [7 \times n_c] \tag{4.25}$$

while for the design variables:

$$\boldsymbol{k} = [1 \times n_k] \tag{4.26}$$

The nature of the functions involved into the routine has already been briefly introduced, highlighting the non-linearity. Because of this aspect, the routine can be framed within the Non Linear Programming problems, characterized by multidimensional input and output.

With this being said, it is important to understand if constraints or boundaries are present. To clarify this aspect, considerations related to the physics, as well as to the physical model, have to be done. The first consideration which can be done is about the variables $\boldsymbol{T}$ and $\underline{\underline{C}}$. Being temperatures and concentrations, clearly negative values have to be rejected:

$$\boldsymbol{T} > 0 \; ; \; \underline{\underline{C}} \geq 0. \tag{4.27}$$

The lower boundary for the temperature might also be selected on the base of the lowest temperature present in the measurement system in terms of measured flows (and accounting for heat losses). It is worth highlighting that those constraints are not imposed directly on the design variables, nor on the objective function, but rather on the sub-functions that compose the objective function. If these limits are set by the physics of the problem, the model used at the base of the Hybrid Method, and more specifically the Raman matrix M composed by the tuners and by the Raman responses and crosstalks, clearly set that

$$\boldsymbol{k} > 0. \tag{4.28}$$

The requirement of eq.4.28 is necessary to avoid negative elements of the Raman matrix, which would have no physical meaning. Even if in principle no upper boundaries are needed on the design variables, some considerations can be done. Reasonably the tuners have to be limited, i.e. $k < \infty$, but also their upper limit could be restricted on the base of practical considerations derived from the knowledge of the model: considering the model sensitivity, later explored, a "high" value could have the same effects as ∞. For example, for most of the cases the tuners are in the order of $10^0 - 10^1$. Upper boundaries may be set also on the base of user's expertise.

The full problem formulation can then be expressed using (4.21), (4.27) and (4.28) as

$$\min_{\boldsymbol{k}} \boldsymbol{e}\left(\boldsymbol{k}, \boldsymbol{T}, \underline{\underline{C}}\right) \quad \text{with} \quad \begin{cases} 0 < \boldsymbol{k} < \mathbf{ub} \\ \boldsymbol{T}(\boldsymbol{k}) > 0 \\ \underline{\underline{C}}(\boldsymbol{k}) \geq 0 \end{cases} \tag{4.29}$$

where in $\boldsymbol{e}(\boldsymbol{k}, \boldsymbol{T}, \underline{\underline{C}})$ the dependence on $\boldsymbol{k}$ of temperatures and concentrations is implicit, but formally it is simply $\boldsymbol{e} = \boldsymbol{e}(\boldsymbol{k})$. $\boldsymbol{T}$ and $\underline{\underline{C}}$ are explicit in the formulation because of the important role they play in defining the objective function, and also because they represent the link with the physical problem treated.

4.3.2 Objective Function Characterization

A fundamental point to decide how to solve the NLP, is to perform a characterization of the objective function, $\boldsymbol{e}(\boldsymbol{k})$, in the design space. Given the multidimensional spaces of the function domain and codomain, it is practically impossible to analytically perform this task, but some preliminary considerations can be done.

As already mentioned, the error function is constructed on the base of the physical quantities characterizing the thermochemical states, $(T_i, [C]_i)$. The reference values are clearly constant, once the states are fixed. The outputs from the processing routine, as previously explained in sec.4.2.2, depend on the tuners but also on the functions describing the Raman responses and the crosstalks, whose peculiarities were presented in sec.4.2.1. It is possible to graphically verify, from fig.4.8a, fig.4.8b or fig.4.9, that the functions involved are clearly non convex in the space of T.

Moreover, a necessary and sufficient condition for a function $f(x)$ to be convex in an interval $[a, b]$ is that its second derivative, if it exists, has to be greater than zero: $f''(x) \geq 0 \ \forall x \in [a, b]$ [6]. This condition can be checked in a representative example, shown in fig.4.15. Here are shown the graphs of the numerically approximated (finite differences) first and second derivatives of the function representing the crosstalk $CO_2 << H_2$.

From fig.4.15 the graph of the second derivative confirms that there is a change in the crosstalk function convexity, that is indeed non-convex: the second derivative changes twice its sign, and indeed it's not verified that $d^2f/dT^2 \geq 0$ for all the temperatures in the domain.

[6] If this condition is not met, several scenarios could be verified: for example, the function could be concave or inflections points could be noted.

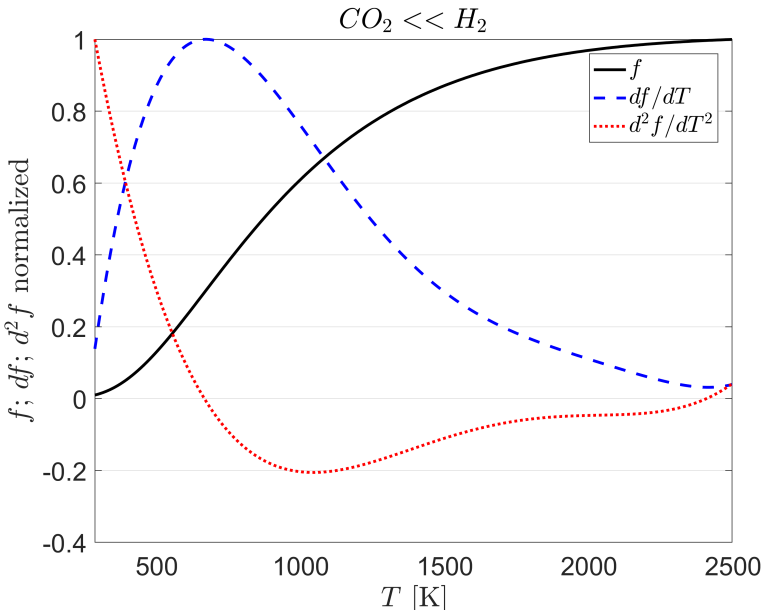

Figure 4.15: The function f represents the crosstalk $CO_2 << H_2$. The first and second derivatives respect to the temperature are approximated with the finite difference method. The second derivative changes of sign confirm that f is not convex in the temperature domain of interest (290 – 2500 K).

While there are theorems which help to identify as convex a combination of convex elements (functions, sets, ...) following specific criteria, there are no guaranties that a combination of non convex functions can always lead to a convex function. For this reason, it is safer to assume the worst case scenario, with a non-convex problem. That is, $\boldsymbol{e(k)}$ is not assumed to be convex.

System Response Characterization

For an indirect understanding of the objective function behavior, it is useful to characterize the system response to the changes in the design variables, because the objective function depends on the system output. The plot in fig.4.16 shows the system response in terms of CO_2 and CO to the variation of two of the tuners. It is possible to notice how the response is characterized by peaks and wells, highlighting the possible existence of local extrema, as well as local slow slopes which could slow down search algorithms.

Another aspect to point out, is the problem stiffness. It can be already noted in the Raman response and crosstalk functions (fig.4.8, fig.4.9, fig.4.10) that the several functions can differ one from the other in intensity for several orders of magnitude. The example of system response shown in fig.4.16 confirms that significant differences can be present in the function sign and magnitude from one local extremum to another.

Moreover, it has been previously pointed out that several tuners may act on one system output variable. This aspect can be visualized with the graph in fig.4.17, where is shown the variation of one of the system outputs with the change of several tuners.

Figure 4.18 shows another important effect: the variation of a single tuner causes changes on several output variables (major species and temperature are shown).

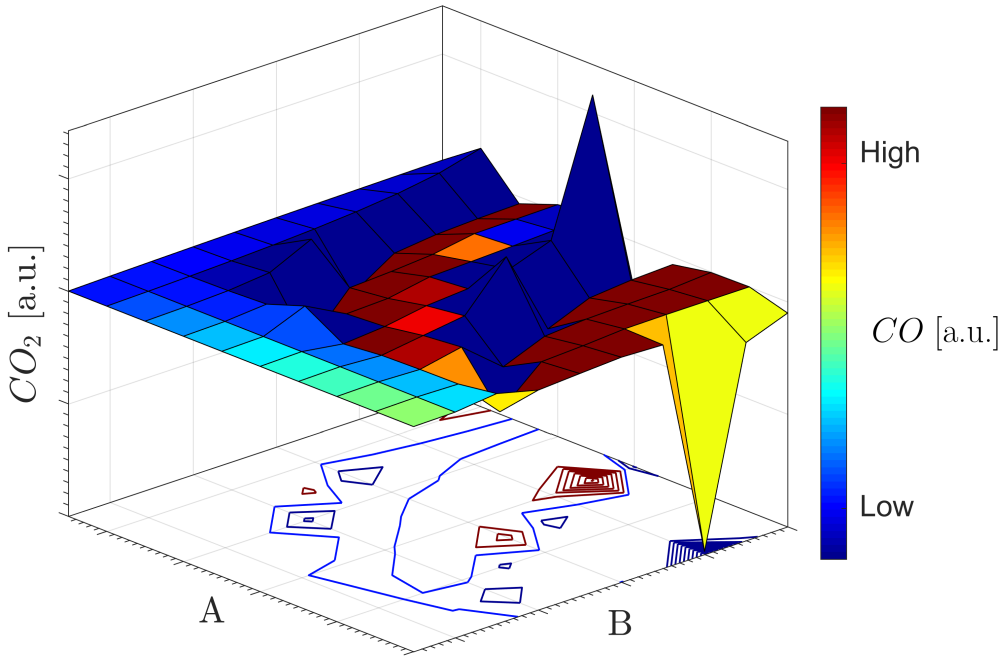

Figure 4.16: System output behavior to variations of two parameters. The output is measured in terms of CO_2 and CO. The two parameters, A and B, are k_{CO_2} and $k_{CO_2<<O_2}$.

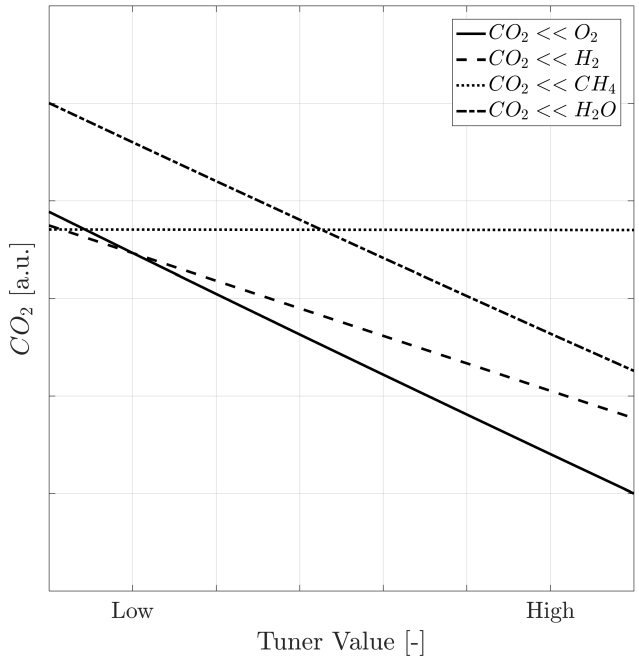

Figure 4.17: Effect on one of the system outputs (CO_2, in this case) changing different tuners. Clearly the variable is affected by different tuners, with different sensitivities.

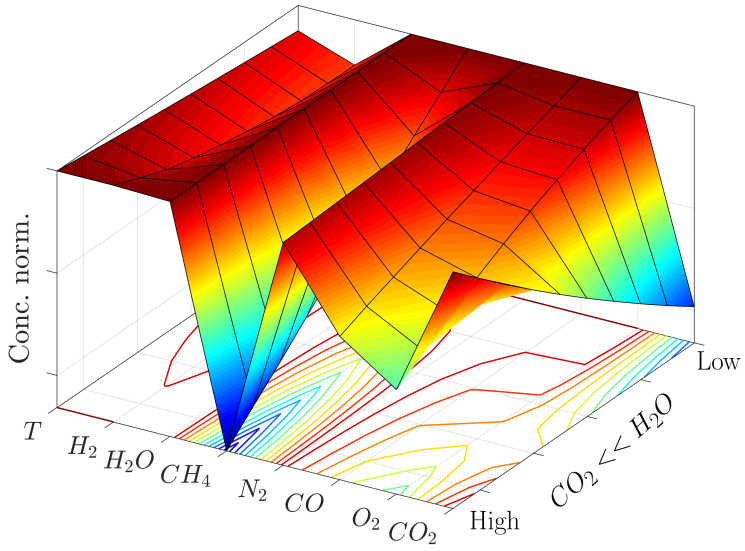

Figure 4.18: Effect on several system outputs caused by the change of one of tuners. It is possible to see how a single tuner affects several outputs, with different sensitivities. Note that the system output is presented as a surface for better rendering the irregular trend of the different outputs, but there is no continuity between one output and the other.

4.3.3 Solving the Non Linear Programming Problem

The Non Linear Programming problem so far characterized has been set to be solved using MATLAB® by MathWorks®. Several approaches have been tested, starting from the simplest line search to global search based algorithms. Given the problem features already presented, such as the existence of local extrema, a "global" approach has been chosen, using a genetic algorithm. The genetic algorithm implemented in MATLAB® can not assure to identify the global optimum among local solutions, but its intrinsic logic may be helpful to find the global rather than a local solution[7].

Implementation

The objective function is defined in a dedicated script, where the setpoint values are compared with the system output to form the vectorial error function, as introduced in eq.(4.22) and eq.(4.29). More in details, if i is used to mark the i-th setpoint of the calibration condition, a matrix can be build in the following form:

$$\begin{bmatrix} \varepsilon_{s1,1} & \varepsilon_{s1,2} & \cdots & \varepsilon_{s1,n} \\ \varepsilon_{s2,1} & \varepsilon_{s2,2} & \cdots & \varepsilon_{s2,n} \\ \vdots & \vdots & \ddots & \vdots \\ \varepsilon_{T,1} & \varepsilon_{T,2} & \cdots & \varepsilon_{T,n} \\ \varepsilon_{\sigma,1} & \varepsilon_{\sigma,2} & \cdots & \varepsilon_{\sigma,n} \end{bmatrix} \tag{4.30}$$

[7] https://it.mathworks.com/help/gads/example-global-vs-local-minima-with-ga.html

The element $\varepsilon_{A,i}$ is the error in the calibration condition i for the quantity A. The quantities used are the seven measured species, the temperature and also the Rayleigh cross section σ. Each column of the matrix is summed to obtain one element of $\boldsymbol{e}$:

$$\boldsymbol{e} = \begin{bmatrix} e_1 & e_2 & \dots & e_n \end{bmatrix} \tag{4.31}$$

Because of the limitations of the genetic algorithm solver in MatLab, the elements of $\boldsymbol{e}$ are summed to obtain a scalar global error.

The ε's are obtained comparing the system output to its setpoint, but also a normalization has to be performed. Indeed the Raman/Rayleigh spectroscopy, as applied for this work, leads to the species quantification in terms of concentrations and the temperature in Kelvin. As a consequence, the different system outputs may have different order of magnitudes, from $\propto 10^{-6}$ for species not present in the probe volume (for example products in the unburnt mixture) to $\propto 10^{+3}$ for the temperature of burnt gases. In addition to that, the same output can assume different values depending on the condition used for the calibration: consider for example that a mixture with given components, switching from rich to lean conditions, sees the fuel getting closer and closer to null concentration in the burnt condition while ϕ decreases. As normal consequence, the contribute of the different ε_i's in the several conditions to the error function e_i's may differ significantly if a simple summation is done. A proper normalization is then applied to the ε_i's, leading to the following formulation:

$$\varepsilon_{A,i} = \sqrt{\frac{(A_i - A_i^{\text{th}})^2}{\left(\overline{A^{\text{th}}}\right)^2}} \tag{4.32}$$

The structure in eq.(4.32) defined for ε_i includes the power and square root operations to avoid the unintended suppression of errors with same magnitude and different sign. The value used for the normalization is obtained from the mean theoretical value of the given quantity A, averaged over the calibration condition setpoints[8].

Penalty Factors (PF) Looking at the problem structure as presented in eq.(4.29), it is clear that the constraints on temperature and concentrations being non-negative present two complications: first, they are non-linear, given the polynomial structure discussed above. In addition, in order to verify whether the constraint is violated or not, the whole cycle of fig.4.11, i.e. the data processing routine, has to be executed. To handle those constraints with a relatively easy procedure, a penalty factors method is implemented. The principle of using penalty factors, as for example explained in [76], is in treating the constrained objective function somehow as unconstrained: in other words, the constraints are implicitly accounted for. There are several ways to implement such a method, and mostly they depend on the nature of function and constraints.

In this case there is no analytic formulation for the objective function, and the factors are applied on the elements of the error function matrix in eq.(4.30), i.e. the ε's presented in eq.(4.32). More in details, the error is augmented by a factor, PF > 1, in case the given quantity results to be smaller than zero, accounting for a defined tolerance:

$$\varepsilon_{A,i} = \text{PF} * \varepsilon_{A,i} \quad \text{if} \quad A|_i - 0 < \text{tol.} \tag{4.33}$$

[8] An exception is made for quantities where $\overline{A^{\text{th}}} = 0$, for obvious reasons.

Clearly, the more the constraint is violated, the higher will be the penalization.

Two different sets of penalty factors are used, one for the reactive cases and another for the non-reactive cases. For the reactive cases the error is augmented by 30%, while for the non-reactive cases the penalty factor is 60%. The values are identified with a heuristic procedure. This strategy is intended to attribute a higher penalty to the non-reactive case respect to the reactive cases, when negative concentrations are returned as a feasible solution. Given that the non-reactive cases have higher species concentrations (depending on the calibration condition, the volume fractions are in the order of tens percentiles), a negative value has to be a marker for the algorithm to be very far from a possible solution. Figure 4.19 compares selected outputs of a case run with 100 algorithm generations, with and without the use of penalty factors. The figure demonstrates that the use of the penalty factors avoids the feasible solution to include negative concentrations, and also returns a better result for the other species.

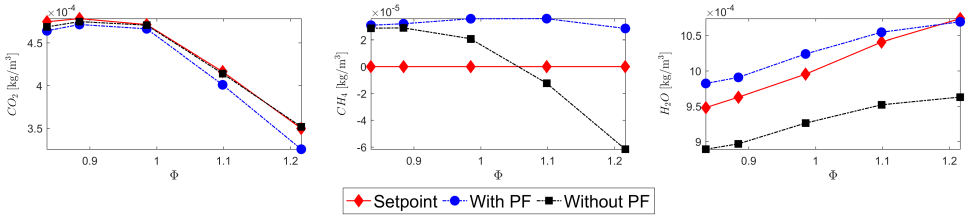

Figure 4.19: Comparison of a 100 generations run with (●) and without (■) the use of penalty factors. Setpoint = ♦.

Other approaches to impose the factors are possible, for example using of "logarithmic barriers" is typical (see [75, 82]), but the presented implementation is lighter in terms of computational effort. To give a value to PF, it is important to consider that the highest the penalty factor is, the closer the modified unconstrained problem will be to the original, constrained, one [76]. On the other hand, when the factors are applied to the objective functions and are too high, it might be that the problem becomes ill-conditioned.

Weights In the ACR it is implemented the use of weighting factors. Scalar factors might be applied to single species to reduce their impact on the global error value. This strategy may be applied by the user for quantities where higher uncertainty is reported, for example, or to guide the algorithm to focus on some quantities rather than others in the error reduction. The weights are found with a heuristic procedure, and are intended to reduce the impact of one or more quantities on the error. Values applied may vary between a reduction of 30% up to 90%, when a significant reduction of the contribution of a quantity is needed.

Scaling It is common practice to scale the design variables of an optimization problem, leading (especially) non-linear algorithms to perform better [78]. When the absolute values of these quantities lie within a few orders of magnitude of each other, the algorithms (if solutions exist) tend to solve faster and with fewer numerical difficulties [76]. For this purpose, several methods may be applied; choosing wisely the

variables unit might be sufficient in some cases, but in problems like the one here studied this is not an option, given that the variables are non-dimensional. For this reason a slightly more complex method is tested to perform the scaling procedure on the tuners: using the upper and lower bounds imposed on the individual tuners, the following formula has been applied:

$$k' = \frac{k - lb}{ub - lb} \tag{4.34}$$

where k is one of the tuners, lb and ub are its lower and upper bounds, respectively. With this method, all the tuners may vary in the interval $[0;1]$. It is easy to verify that when $k = lb \Rightarrow k' = 0$; and that when $k = ub \Rightarrow k' = 1$. Consequently, the bounds for all the scaled tuners, k', are $lb' = 0$ and $ub' = 1$, for all the tuners.

A test is performed running the routine over 100 generations, using the exact same settings with and without the scaling operation performed on the tuners. The results, represented in fig.4.20 for three outputs, clearly show that the user scaling is not beneficial for the problem, with a solution far from the set points.

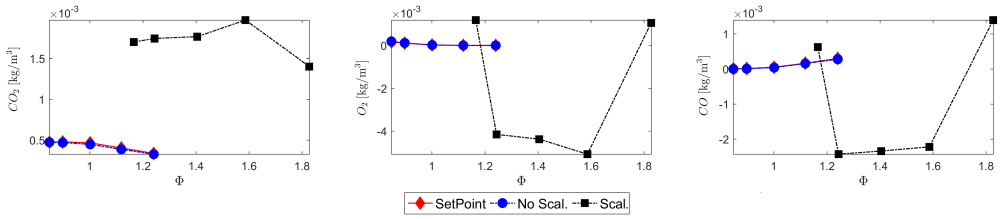

Figure 4.20: Comparison of a 100 generations run with (•) and without (■) the scaling. Set points = ♦. The case without the scaling and set point markers are almost coincident, in this scale.

The worst algorithm performances are also confirmed by the error function progression through the generations, as shown in fig.4.21 where the functions are normalized by the maximum value: in the case where the scaling is applied the objective function decrease stops at about 70% of its starting value, while in the other case it is assessed below the 10%.

The worst performance registered with the design variable scaling might be due to a conflict with the built-in scaling operations performed by the MATLAB® genetic algorithm. Normalization methods applied to genetic algorithms have been subject of research (e.g. [84], [85]). It has been demonstrated in [86] that normalization plays a role in reducing the dimension of the search space of genetic algorithms. On the other hand, the same authors stress out that the normalization method employed has to be designed in accordance with the specific implementation of the genetic algorithm. A crucial role is particularly played by the encoding scheme determining the relation between individuals' genes space and the solution space. Moreover, it has to be taken into account that normalization alters the search space [86]. A uniform normalization, as the one tested in this case, is not the most effective choice for the encoding scheme implemented in MATLAB®. More complex scaling approaches may allow for better performances. Nevertheless, the finality of the optimization problem presented here does not justify the increase in complexity derived by the application of a more complex normalization procedure, considering the satisfying results obtained without

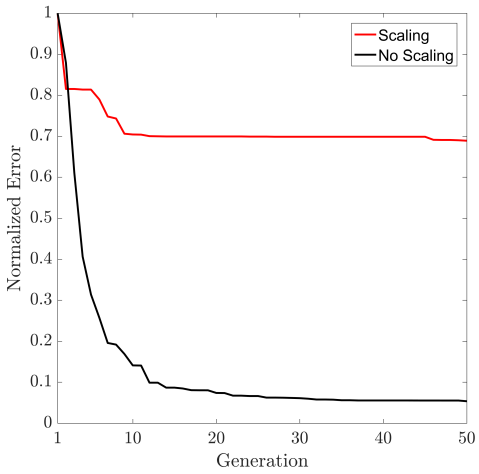

Figure 4.21: Error function progression though the algorithm generations (detail): comparison between two identical cases with and without the scaling operation.

the scaling. Indeed, it has to be taken into account that the inner structures of the problem (e.g. eqs.(3.6) - (3.9) used to evaluate the objective function) must have in input the unscaled variables, in order to preserve the physical models on which they are based upon. Iterative scaling and unscaling operations would then be required, adding significant computational effort in the case of more complex normalization procedures.

Results of the ACR application on two different FF data sets

The results from the ACR implementation on two different FF data sets are shown here. The two data sets belong to two different measurement campaigns, and are acquired with test rigs having comparable specifics. A random ACR starting point has been used for the design variables in both the cases. The first data set, "FF data set 1", includes 5 configurations of the Flat Flame Burner, bringing a total of 10 "series" of setpoints. Referring to the error composition expressed in eq.(4.30) and eq.(4.31), a "series" of setpoints is one column of the matrix, i.e. it is composed by the setpoints for the species, the temperature and the Rayleigh cross section in one given condition. The matrix of eq.(4.30) has then 10 columns and the error vector $\boldsymbol{e}$ has 10 elements. The configurations cover the range of equivalence ratio from $\phi = 0.841$ to $\phi = 1.23$. The second data set, "FF data set 2" is composed by more FF configurations, with a total of 18 series of setpoints covering an equivalence ratio range from $\phi = 0.856$ to $\phi = 1.34$. The matrix in eq.(4.30) has then size $[9 \times 18]$, while $\boldsymbol{e}$ $[=]$ $[1 \times 18]$.

Figure 4.22 shows the results of the ACR applications on FF data set 1. Figure 4.23 refers instead to FF data set 2. Both the figures show the nine system outputs used to build the error function in the routine, compared to the relative setpoints. The quantities are plotted in the equivalence ratio domain for the reactive cases. The non reactive cases are used to define the ϕ's of the setpoints. The species are expressed in [kg/m^3], the temperature in K, Rayleigh Cross Sections are dimensionless.

Analyzing fig.4.22 and fig.4.23 it is possible to notice how for both the cases the monitored quantities are in good qualitative agreement with the setpoints. The quantitative analysis highlights that the optimal solution identified for FF data set 1 returns

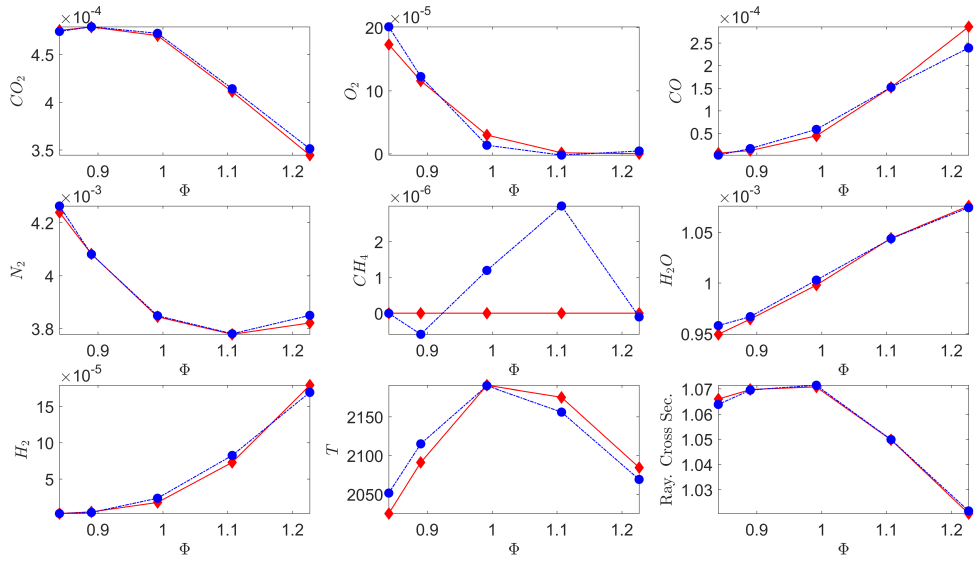

Figure 4.22: Application of the ACR on FF Data set 1 - 10 FF configurations (5 non reacting and 5 reacting cases): setpoints (♦) and system output (•). The species are expressed in [kg/m^3], the temperature in K, Rayleigh Cross Sections are dimensionless.

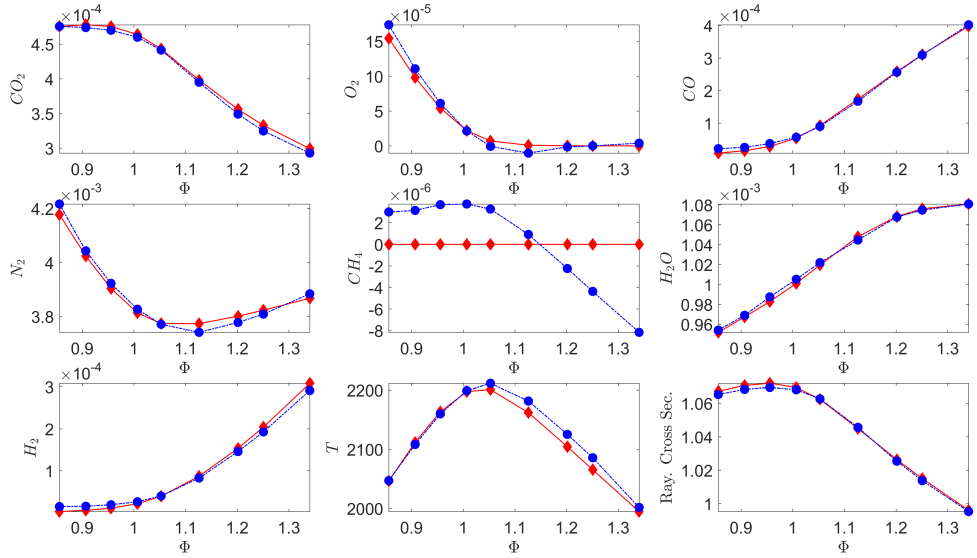

Figure 4.23: Application of the ACR on FF Data set 2 - 18 FF configurations (9 non reacting and 9 reacting cases): setpoints (♦) and system output (•). The species are expressed in [kg/m^3], the temperature in K, Rayleigh Cross Sections are dimensionless.

a relative error, computed after eq.(4.32) and averaged in the ϕ domain, below 4% for all the quantities, except for a value of 8% for CO and higher values for O_2. It might be useful to anticipate that oxygen has shown also higher errors in terms of precision, as it will be seen in the next chapter. In addition to that, it is also important to notice that the O_2 theoretical setpoints in rich conditions are very close to the absolute zero, and then a small deviation in the system output from the setpoint returns a significant relative error. For this type of cases, the weighting factors are implemented.

The FF data set 2 shows even better performances of the optimal solution, respect to the setpoints. Indeed, the relative error is assessed below 3% for all the quantities, while still remaining higher for the oxygen.

As mentioned, the overall correspondence between the system outputs and the setpoints may be judged as satisfying, in comparison to the measurement campaigns conducted in similar studies where Raman/Rayleigh spectroscopy is used as diagnostic tool in turbulent combustion [7, 12, 17, 25, 57, 65, 87, 88].

Results of the ACR on Other Calibration Conditions

It has been clarified in sec.3.3 that the set of tuners identified by the routine has to be valid for all the conditions used for the system calibration. The conditions typically used for experiments in turbulent flames using methane as fuel have been presented in sec.3.3.2. In addition to the FF (whose results have been shown in sec.4.3.3) the conditions include also gas mixtures at ambient temperature and vertical flames.

In fig.4.22 the performance of the tuners identified by the ACR applied to a FF data set have been shown (FF data set 1). In this section, it is demonstrated the validity of the same tuners used to process the data from other calibration conditions used in the same measurement campaign. The gas mixtures at ambient temperature used have the following compositions, in % vol.:

1. 20% CH_4 ; 80% N_2.
2. 20% CO_2 ; 80% N_2.
3. 2% CO ; 35%H_2 ; 63% N_2.
4. 21% O_2 ; 78% N_2 (dry ambient air).

The results are shown in tables 4.4 - 4.7, where the setpoint is compared with the system output (spatially averaged and meaned over 100 realizations). The relative error is computed applying the same formula of eq.(4.32).

In table 4.4 the results for the CH_4/N_2 mixture are shown. It is possible to notice that the error is null for several monitored quantities. The largest value is registered for N_2, with a value that remains low (0.03). Table 4.5 refers to the mixture of CO_2/N_2.

Table 4.4: Output of calibration procedure for mixtures at ambient temperature. Calibration gas: 20% CH_4; 80% N_2 [Mole Fractions]

	Out	**Setpoint**	**Rel.Error**
CO_2	0.00	0.00	0.00
O_2	0.01	0.00	0.01
CO	0.01	0.00	0.01
N_2	0.78	0.80	0.03
CH_4	0.20	0.20	0.00
H_2O	0.00	0.00	0.00
H_2	0.00	0.00	0.00
T	283	290	0.02

Table 4.5: Output of calibration procedure for mixtures at ambient temperature. Calibration gas: 20% CO_2; 80% N_2 [Mole Fractions]

	Out	**Setpoint**	**Rel.Error**
CO_2	0.20	0.20	0.00
O_2	0.00	0.00	0.00
CO	0.00	0.00	0.00
N_2	0.78	0.80	0.03
CH_4	0.00	0.00	0.00
H_2O	0.00	0.00	0.00
H_2	0.00	0.00	0.00
T	285	290	0.02

Table 4.6: Output of calibration procedure for mixtures at ambient temperature. Calibration gas: 2% CO; 35% H_2; 63% N_2 [Mole Fractions]

	Out	**Setpoint**	**Rel.Error**
CO_2	0.00	0.00	0.00
O_2	0.00	0.00	0.00
CO	0.02	0.02	0.00
N_2	0.62	0.63	0.02
CH_4	0.01	0.00	0.01
H_2O	0.00	0.00	0.00
H_2	0.35	0.35	0.00
T	280	290	0.03

Table 4.7: Output of calibration procedure for mixtures at ambient temperature. Calibration gas: 21% O_2; 78% N_2 [Mole Fractions]

	Out	**Setpoint**	**Rel.Error**
CO_2	0.00	0.00	0.00
O_2	0.20	0.21	0.05
CO	0.01	0.00	0.01
N_2	0.77	0.78	0.01
CH_4	0.00	0.00	0.00
H_2O	0.00	0.00	0.00
H_2	0.00	0.00	0.00
T	290	290	0.00

In this case, the error is null for all the quantities, except for N_2 (0.03) and T (0.02). Table 4.6 reports the results for the gas mixture composed by CO, H_2 and N_2. Here all the species result in zero error, except for N_2 (0.02) and CH_4 (0.01); the temperature has also a low error. Table 4.7 contains results for dry ambient air. Oxygen reports an error of 0.05, CO and CH_4 a relative error of 0.01, while all the other monitored quantities have zero errors.

The overall results of the application of the tuners previously found with the ACR to the gas mixtures at ambient temperature is satisfactory. Low relative errors are observed for all the monitored quantities, with a maximum of 0.05 for only one species in one case, and the other errors that vary in the range [0.00 ; 0.03].

It is important to remark that the thermochemical conditions of the analyzed gas mixtures are significantly different from the ones of the FF data set 1 of fig.4.22. Nevertheless, the same set of tuners identified by the ACR for FF data set 1 returns good results for the mixtures measured for the calibration in the same measurement campaign.

The same set of tuners has been used to process data measured on VF configurations, during the same measurement campaign of FF data set 1 and the gas mixtures described above. Figure 4.24 reports scatter plot in the temperature domain of the monitored quantities for one of the VF configurations, at ϕ = 0.80. The VF is used

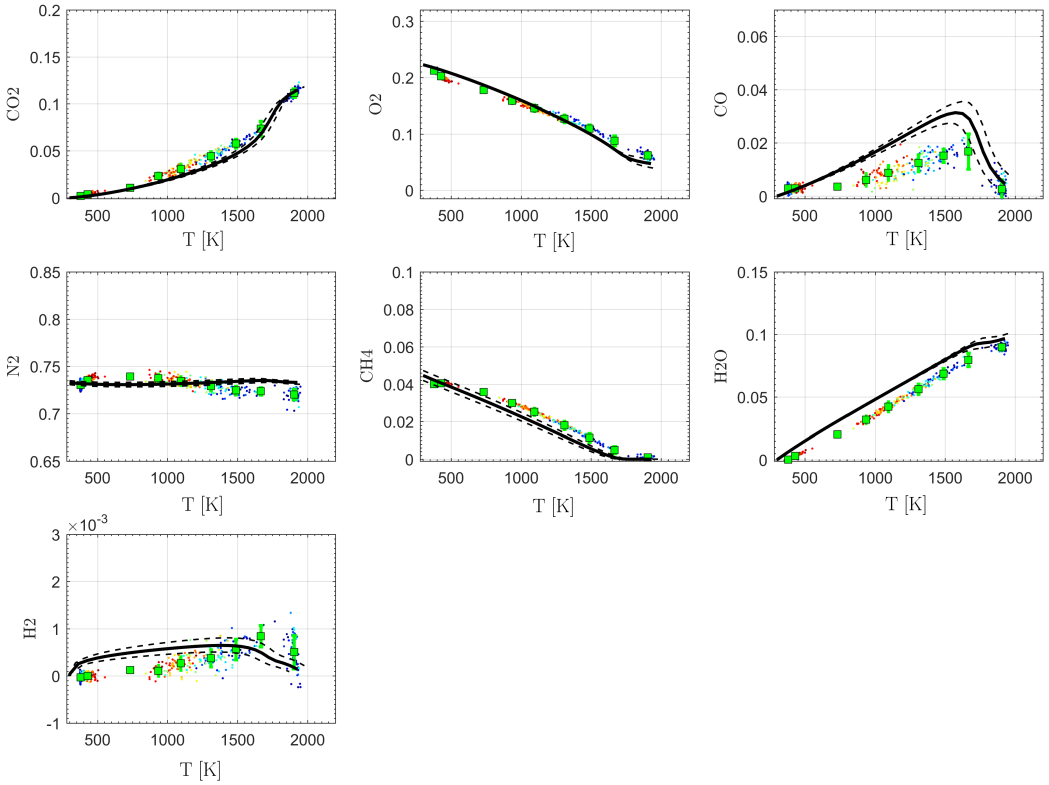

Figure 4.24: Scatter plot in the temperature domain of the species [mass fractions] and temperature [K] for VF at ϕ = 0.80. The solid, upper dashed and lower dashed black line refers to laminar steady flamelet at ϕ = 0.80, ϕ = 0.85 and ϕ = 0.95, respectively.

as a reference in the calibration procedure because it allows for an evaluation of the

system behavior in presence of a flame front. This evaluation is not possible with the FF, where the probe line is placed in the burnt products and in the unburnt mixture, without crossing the flame front. Observing fig.4.24 it is possible to conclude that the tuners application to the VF is satisfying, with a good agreement between the scattered data and the reference flamelet in the burnt and unburnt region, as well as in the flame front zone.

As a final remark, it is also relevant to mention that the results shown in this section, about the use of the tuners in gas mixtures and VF, as well as the one shown for FF data set 1 (sec.4.3.3) should also take into account the precision characterizing the measurements. This information are included in the next chapter. Here it is enough to consider that precision would add a tolerance to the results above illustrated, to account for all the fluctuations present in the measurements. This tolerance would further improve the discussed ACR performances, thanks to a better agreement among the set points and the calibration outputs, which is guaranteed by the inclusion of the precision ranges in the evaluation.

Comparison of ACR implementation with Old Approach

It has been remarked that the ACR is intended as a modified version of another routine, used for the identification of the optimal set of tuners. This has been detailed in sec.4.2.3, where it has been described as an empiric-based routine. Here a comparison between the ACR results and the previous approach is proposed, respect to the FF data set 2. A direct comparison is shown in fig.4.25. Here, the ACR output and its setpoints are compared with the output obtained with the old approach on the same data set. The species are expressed in [kg/m^3], the temperature in K, Rayleigh Cross Sections are dimensionless. The comparison of fig.4.25 doesn't highlight relevant differences between the outputs of the two methods. The qualitative agreement is good for both the outputs.

For a quantitative evaluation, each approach is compared with its own setpoint[9] and the error is computed according to the formula of eq.(4.31). The results are shown in table 4.8, where the error averaged over the setpoints is shown. Being the errors of eq.(4.31) always positive, there is no risk of deleting opposite errors in the averaging process. It can be observed from the quantitative comparison of table 4.8 that the

Table 4.8: Errors computed after eq.(4.31) and averaged over the respective setpoints, resulting from the application of the ACR and of the old approach on the same data set (FF data set 2).

	CO_2	O_2	CO	CH_4	N_2	H_2O	H_2	T	Ray.C.Sec.
Old Appr.	0.00	0.09	0.03	0.00	0.00	0.00	0.01	0.01	0.00
ACR	0.00	0.05	0.02	0.00	0.00	0.00	0.00	0.01	0.00

ACR obtains for all the monitored quantities better performances in terms of error, respect to the old approach. Indeed, the ACR allows for lower or equal performance in

[9] A minor difference is indeed present, due to the fact that the setpoints are defined on the base of the measurement in non-reactive cases. These depends on the set of tuners used.

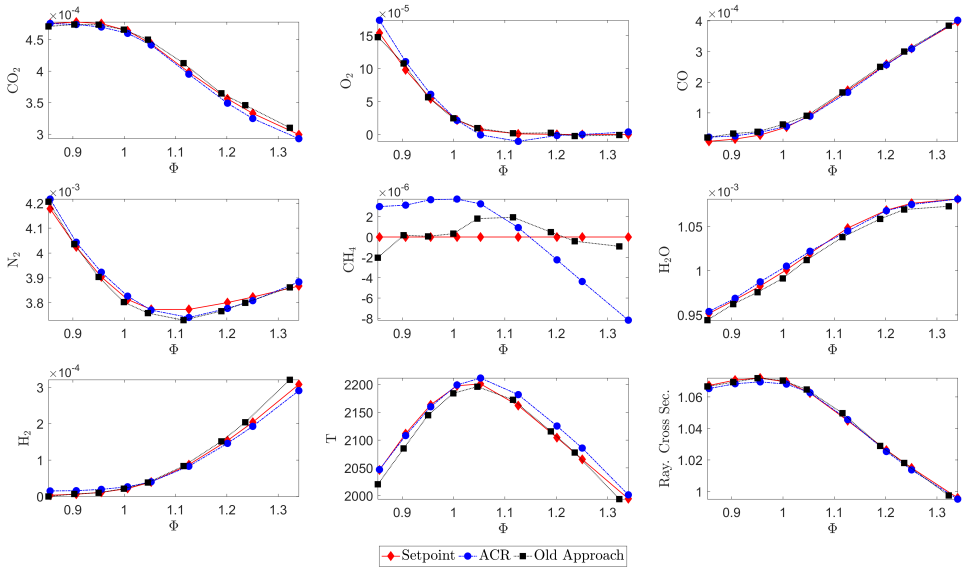

Figure 4.25: Comparison of the ACR and the old approach on the data set 2 - 18 FF configurations (9 non reacting and 9 reacting cases): ACR setpoint (♦) and output (●); old approach output (■). The species are expressed in [kg/m^3], the temperature in K, Rayleigh Cross Sections are dimensionless.

terms of normalized average errors respect to the previous approach: for example on the oxygen the normalized average error is reduced from 0.09 to 0.05, on the carbon monoxide from 0.03 to 0.02 and on the hydrogen from 0.01 to 0.00.

In addition to the better quantitative results of the ACR respect to the old approach, other considerations have to be done. With the previous approach, a trial and error procedure has to be applied by the user, in order to identify the optimal set. This procedure may be significantly time consuming, because manual adjustments have to be performed. These adjustment have to be done by the user, after the comparison between output and setpoint. The ACR identifies the optimal set of tuners in a wall time in the order of 24 hours, running on a 2-core machine and using parallel computation. Not only this aspect is significant. On the contrary, it is even more important to highlight that the manual adjustment requires a significant user expertise, differently from the ACR that is instead user-independent in the search for the optimum. The user expertise may play a role when defining weights (described in sec.4.3.3) in the case the ACR should highlight a lack of performances in searching for the optimal solution. On the other side, changing the weights is not required for each data processing procedure. In addition, it is easy to identify for any user if there are quantities far from the optimal solution in the routine output and, in case, act on the weights to balance the output.

Limits of Standard Algorithms

The standard algorithms proposed to solve non-linear programming problems have encountered some limits on this application, as seen in a series of tests conducted on the same case (FF data set 1). The performance from two algorithms included

in the MATLAB® Optimization Toolbox™ are compared here with the presented implementation of the ACR, in terms of ability to find the optimal solution.

More in details, one of the algorithms whose performance are shown is defined "interior-point". It uses a Line Search to solve with a Newton-like method a linear approximation of the first order necessary conditions for constrained optimization[10]. In some cases, for example when the approximate problem is not locally convex near the starting point of the iteration[11], the algorithm uses a trust region based method, rather than the line search, solving a quadratic approximation instead of the linear one.

The other algorithm tested is referred to as "Sequential Quadratic Programming" (SQP in the following) and is based on the work by Nocedal and Wright [74]. It is intended to work as a Newton method, but dealing with constrained optimization. A quasi-Newton method is used to approximate the Hessian matrices. The equation, with the approximated (positive definite by definition) Hessian, is then solved as a quadratic subproblem, finding the search direction for a line search procedure applied to find the new iteration. The step length along the defined search direction is determined by an appropriate line search procedure.

Figure 4.26 shows a direct comparison between the error function evolution through the progresses of the three algorithms. Despite the very low tolerance (tol $< 1E-10$), both interior point and SQP algorithms reach a stationary point after few iterations.

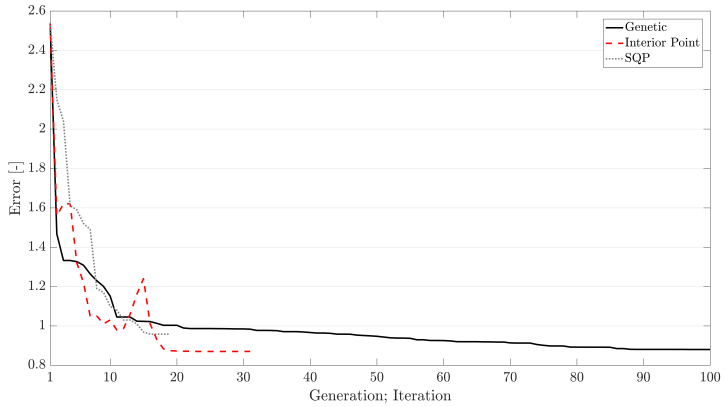

Figure 4.26: Error function progression through the algorithms steps: comparison of the genetic, "interior point" and sequential quadratic programming (SQP) algorithms.

The "interior point" is capable of reaching an absolute value of the error function almost as low as the genetic algorithm, but an analysis of the solution identified as optimal shows differences between the two results. A direct comparison of selected system outputs is reported in fig.4.27.

From the comparison of selected systems outputs obtained with the interior point, the SQP and the genetic algorithms, it is possible to deduce that the optimal solutions

[10]The first order necessary conditions for constrained optimization are represented by eq.(A.9), that describes a relation between the gradient of the objective function and the one of the equality constraints, and by the feasibility condition (i.e. the relation stating that the constraints have to be respected).

[11]This condition is verified from the Hessian included in (A.9), similarly to what has been seen in sec.4.1.

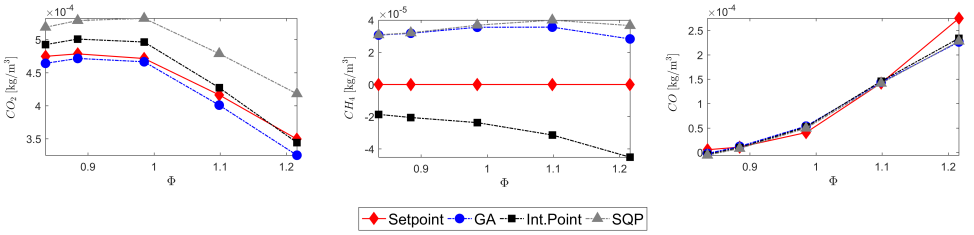

Figure 4.27: Comparison of selected system outputs after the application of the genetic, "interior point" and sequential quadratic programming (SQP) algorithms.

identified by the first two methods are local rather than global. The CO calibration is for example almost coincident for all the methods, while the CH_4 is returned in negative concentrations by the interior point algorithm, and the "SQP" gives a worst result for the CO_2 respect to the genetic algorithm.

Chapter 5

Application on Turbulent Premixed Methane/Air Jet Flames

Summary

This last chapter presents an application of the Automated Calibration Routine to a turbulent premixed methane/air flame, investigated using the single-shot simultaneous Raman/Rayleigh spectroscopy. The test rig used for the measurement campaign has already been described in sec.3.1. The flame represent a test case for the routine, as well as is of interest for its specifics. In the last section, sec.5.3, preliminary results from a second turbulent premixed methane/air are presented.

5.1 Investigated Flame

5.1.1 Flame Configuration

The flame investigated is a premixed turbulent flame, stabilized above the stratified burner (described in sec.3.1.2). The main feature of such a flame may be anticipated as follows. First, it is remarkable the reduced impact of the pilot flame, which is indeed positioned upstream, inside the pilot tube. Only the pilot exhaust are in contact with the fresh gas mixture, assuring that the flame is anchored to the burner. Moreover, the independent control of the burner slots allows for establishing a reduced shear between the mixture and the air flows.

The flame is named "Flame C" (Fl.C). Table 5.1 reports the Fl.C inlet conditions. The mixture issuing from the slot 1 is composed by methane and filtered, dried, ambient air. The same composition is used for the pilot flame. The slot 2 is fueled solely with air. Note that the bulk velocity of the pilot is intended as issuing from the pilot tube, and not as fresh mixture. From the inlet conditions reported, the estimated Reynolds number is $Re_{\text{Fl.C}} \simeq 13\text{e}+3$ based on the hydraulic diameter.

Table 5.1: Fl.C inlet specifics.

Pilot ϕ = **0.95**	**Slot 1** ϕ = **0.95**	**Slot 2** **Air**
u_P [m/s]	u_1 [m/s]	u_2 [m/s]
10	10	10

Shear

The pilot bulk velocity is considered at the exit of the pilot tube: the pilot flame fresh mixture is slower, with the combustion products accelerating to a velocity intended to be as close as possible to the one of the slot 1, for not having a significant shear between the two flows. Low shear is also present on the interface slot 1/slot 2.

Classification in the regime diagram

The investigated flame can be located in the Borghi-Peters regime diagram, as reported in sec.2.3.3, on the base of the experimental characterization done on a series of flames by Seffrin in [88] and by Seffrin et at. in [12]. The turbulent flames series covers several configurations, established on the already mentioned Stratified Burner, close to the Fl.C specifics. Figure 5.1 reports the positions of the above mentioned series in the Borghi-Peters diagram.

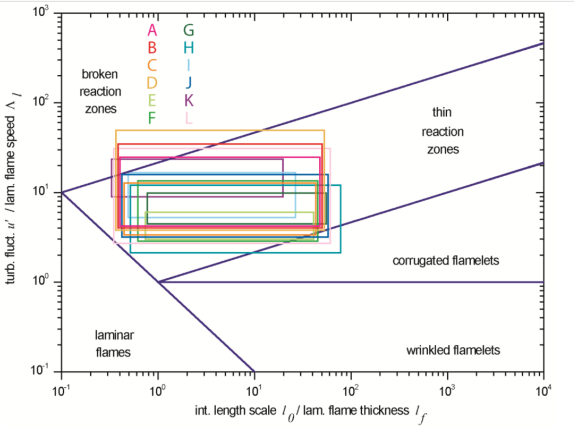

Figure 5.1: Regime diagram including the configurations investigated by Seffrin in [88].

According to the characteristics of the mentioned flame series, Fl.C might be said to be close to the TSF_A or TSF_G. The configuration of interest lie in the thin reaction zone, with possibly some overlapping into the broken reaction zone area.

Investigated Locations

In fig.5.2 and fig.5.3 time-averaged chemiluminescence images show the Fl.C topology. In fig.5.3 the spatial reference coordinates are superimposed. The investigated axial positions are: 30, 45, 60, 75, 90 and 120 mm above the burner top edge. At each height, the 1-D probe line is placed at different radial positions, in order to acquire information along a continuous line in the range from −2.5 to 40.0 mm, with the zero being center at the axis of radial symmetry. From these probe lines, 1-D radial profiles of scalars are extracted through the routine described in sec.3.2.

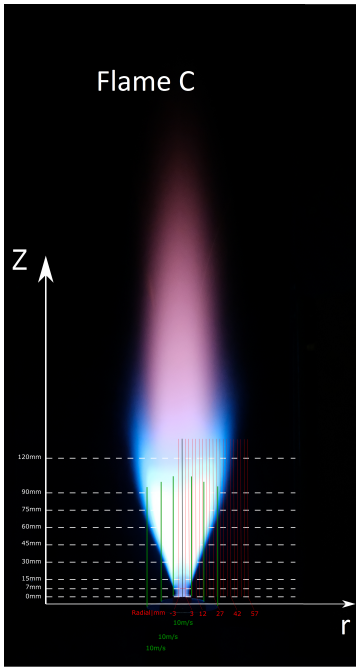

Figure 5.2: Time-averaged chemiluminescence images of Fl.C.

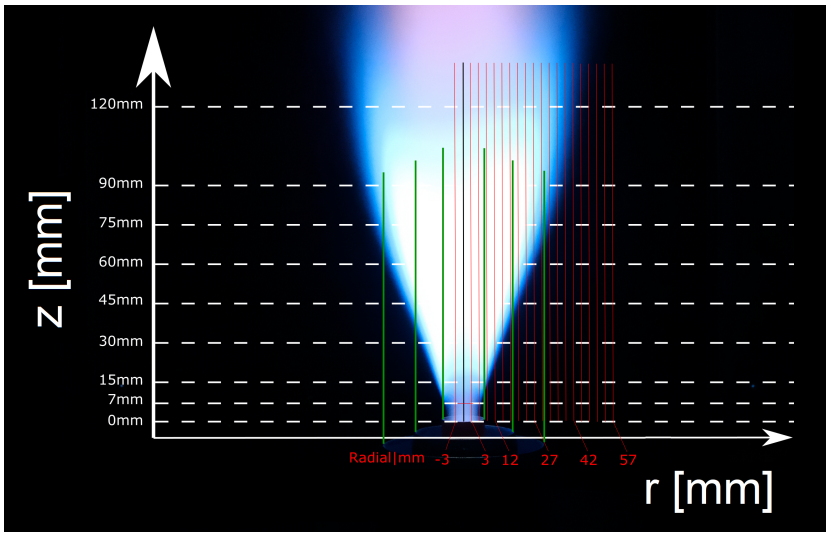

Figure 5.3: Time-averaged chemiluminescence images of Fl.C (detail), with superimposed the coordinate system in the laboratory reference.

5.1.2 Calibration, Precision and Accuracy

Precision and Accuracy

Table 5.2 shows representative values for precision and accuracy in the scalar measurements analyzed in this work. The quantities are averaged over the central portion of the probe line and computed as percentage of the mean value. Mean values for species are expressed in mass fractions, while the temperature is in K. The obtained errors are comparable with similar measurements, including [10, 13, 25, 37].

Table 5.3 includes the estimated precision for the equivalence ratio in five FF calibration files.

System Calibration

The calibration conditions available for this set of flames consist of a FF data set, VF configurations and gas mixtures at room temperature, as described in 3.1.3. The Automated Calibration Routine has been applied to reacting and non reacting cases from the Flat Flame burner. Figure 5.4 shows the species of interest in the space of the equivalence ratio for the FF reactive cases. The markers represent the measured values, averaged over the probe line. The error bars give a range of $\pm 1\,\sigma$ (standard deviation) computed over the samples acquired for each condition. The continuous lines are linear interpolations of the set points used for the calibration. The system

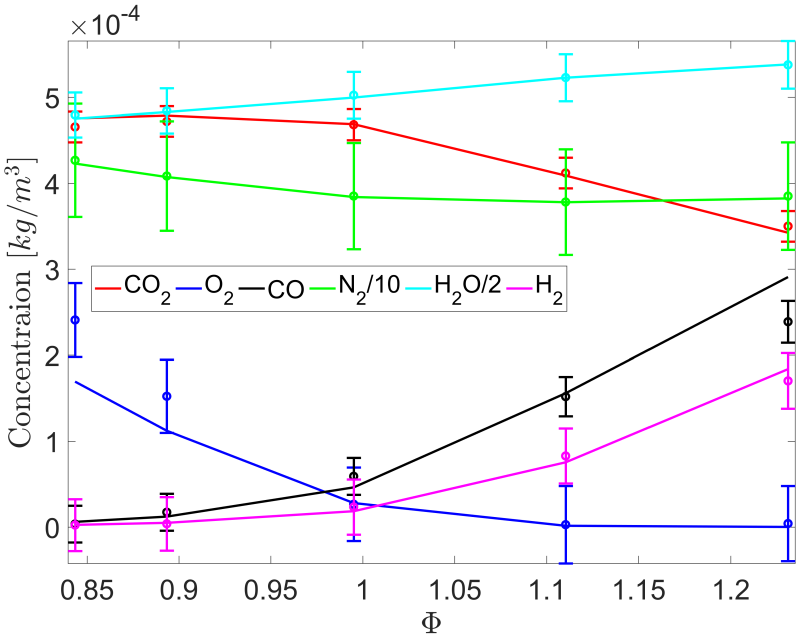

Figure 5.4: Calibration conditions: species of interest in the space of the equivalence ratio for the FF reactive cases. The markers represent the measured values and the error bars give a range of $\pm 1\sigma$ (standard deviation), computed over the samples acquired for each condition. The lines are linear interpolations of the set points used for the calibration

calibration agree with those of similar studies available in the literature, e.g. Magnotti and Barlow [10].

Table 5.2: Representative values of precision and accuracy from the analyzed measurements, expressed as percentage of the mean value. Mean values for the species are in mass fractions, temperature is in K. The column "FF" reports the correspondent FF case where the calculation have been computed.

Scalar	**Precision σ %**	**Accuracy %**	**FF**	**Mean Value**
T	0.18	0.7	ϕ = 1.22	2069
CO_2	0.64	0.2	ϕ = 0.890	0.134
O_2	5.38	5.5	ϕ = 0.890	0.025
CO	1.63	16.3	ϕ = 1.22	0.045
CH_4	0.00	0.1	ϕ = 0.890	0.000
H_2O	0.47	0.3	ϕ = 0.890	0.121
H_2	3.11	5.3	ϕ = 1.22	0.002
N_2	0.16	0.2	ϕ = 0.890	0.720

Table 5.3: Estimated precision for the equivalence ratio, as computed in five calibration conditions, from FF data set. Information are taken from the central strip of the 1-D line, recorded over a series of 100 laser shots.

ϕ	
0.831	±0.035
0.899	±0.039
1.03	±0.045
1.13	±0.049
1.20	±0.050

The Vertical Flame burner has been used to verify the proper calibration across a flame front, and to compensate the camera reciprocal alignment. The calibration conditions verified in a VF case and with the gas mixtures relative to the measurement campaign analyzed in this chapter have been presented in sec.4.3.3 (fig.4.24 and tables 4.4 - 4.7). To avoid repetitions, they are not reported here.

5.2 Results and Discussion

5.2.1 Position of the Mean Flame Brush

To get quantitative information about the flame topology, the position of the mean flame brush is identified. For this purpose, the position of the flame brush is tracked using the location of the maximum temperature fluctuation [37]. The figure 5.5 shows the identified locations at the heights of interest. A linear regression is performed from

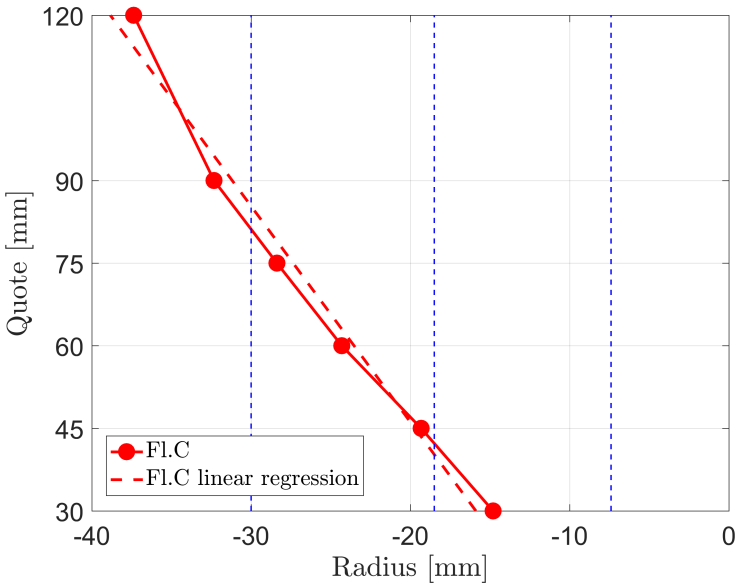

Figure 5.5: Position of the Fl.C mean flame brush at the different heights. Linear regression is performed, plotted with the dashed lines, in order to obtain information about the flame angle. The vertical dashed lines represent the virtual prolongation of the burner sections.

the data, in order to obtain an overall flame angle. The flame presents a monotonic trend going from the lower to the upper heights, and the angle is estimated in 14° with the vertical line.

5.2.2 Single Shot 1-D Profiles Analysis

In this section an analysis is proposed to understand the flame structures. For this goal, single shot 1-D profiles in different locations of the flame are here reported. The 1-D profiles are selected from areas with significant heat release, in order to be as close as possible to the regions where reactions are taking place, as well as from positions where the reaction is in a different stage.

Considering a laser pulse duration of about 500 ns, a single sample (obtained from one laser shot) is able to capture an instantaneous realization of the shortest turbulent time scales [41].

One dimensional laminar flames calculations are used in order to perform a comparison. Indeed, these 1D laminar flames are chosen with the aim to compare the investigated flame with the flamelet model, being the latter an established model that well describes the flamelet regimes of turbulent premixed flames. The flamelet model has

been introduced in sec.2.3.3, and here it is sufficient to recall that it is established when the chemical time scales are significantly faster than the turbulence characteristic time. In terms of length scales, the flame thickness is smaller than the size of the Kolmogorov length scale, leading thus to a laminar flame embedded within, and not significantly affected by, the turbulent structures. The chemical structures of the investigated flame are then compared with the ones predicted by the mentioned laminar flame calculations to verify whether the hypothesis of the flamelet model are fulfilled or not, and if the investigated flame highlights some differences with respect to the flamelet regime of turbulent premixed combustion. The calculations are obtained simulating a steady state unstretched unidimensional laminar flame using multi-component transport and then eventually accounting for preferential diffusion effects, such as the mechanisms described in sec.2.3.3 and sketched in fig.2.19. The kinetic mechanism used for the calculations is is the GRI-Mech 3.0 .[1]

In the following, the results of the analysis are shown for each investigated plane. All the plots have the same structure, and are composed by two sub-plots. The left one shows spatial profiles of Y_{CO_2}, Y_{CO}, T (scaled) and ϕ (scaled). These quantities may help to have an overview of the thermochemical state along the probe line. When present, the vertical dashed line reports the positions of the burner sections limits. The sub-plot on the right shows instead scatter plot of Y_{CO} in the temperature space, together with three references obtained from the mentioned laminar steady flamelet at ϕ = 0.85, 0.95 and 1.05. The CO evolution in the temperature domain, as presented in 5.2.3, is characterized by a first section at about $T < 1500$ K. This section represent the carbon monoxide formation consequent to the methane oxidation. Y_{CO} is very low in the fresh gas mixture and in air, and increases up to a maximum value in correspondence of $T \simeq 1500$ K. For $T > 1500$ the CO oxidation to CO_2 is dominant, and part of the carbon monoxide produced is converted into carbon dioxide. The detailed chemistry involving these two species includes a number of reactions, and the direct conversion of CO into CO_2 is not the only one taking place in reality. For the scope of this work, it is sufficient to consider the role of the carbon monoxide as a combustion intermediate that, spanning the combustion evolution from reactants to products, is formed, reaches a peak in the concentration, and then is partially consumed.

Note that the spatial plots refer to the negative half-plane of the radial coordinate. Nevertheless, the axial symmetry hypothesis allows for the discussion to be done in terms of the positive half-plane.

General Comments The analysis has been performed at each plane, and is proposed with this format. For clarity, a brief summary is here proposed, considering the most relevant aspects that will be found in the following. In the lowest planes the majority of the profiles where significant heat release is present are characterized by steep gradients of the analyzed quantities. The flame width appears to be thin, with the variation from unburnt to burnt state taking place in less than 1 mm. Moreover, the mixing process between reacted mixture and fresh gases is observed. With increasing heights, other phenomena become observable. The preheat of cold gas is present in more realizations. In addition, the interaction between the flame and the turbulent structures is clear in

[1] Gregory P. Smith, David M. Golden, Michael Frenklach, Nigel W. Moriarty, Boris Eiteneer, Mikhail Goldenberg, C. Thomas Bowman, Ronald K. Hanson, Soonho Song, William C. Gardiner, Jr., Vitali V. Lissianski, and Zhiwei Qin `http://www.me.berkeley.edu/gri_mech/`

a relevant number of profiles. This interaction, present for example in about 4% of the realizations at $z = 45$ mm, affects the flame preheat zone, but does not appear to have an impact in the flame reacting structures. It is deduced so, thanks to the comparison of the carbon monoxide with flamelet profiles in the temperature domain. Thickening effects are observed also at higher planes. The observed thickening is likely caused by turbulent eddies smaller than the flame thickness (but larger than the reaction layer) penetrating the flame preheat zone, without affecting the flame reaction zone. This mechanism is typical of the thin reacton zone regime for turbulent premixed flames, introduced by Peters [55]. From $z = 75$ mm fluid dynamics phenomena, such as wrinkling and mixing become more relevant in terms of number of profiles affected. As a final remark, in the highest plane it is possible to notice that the reactivity is generally reduced. It is deduced so, because in the location around the mean flame brush position, there is an increasing number of profiles describing mixing without reaction. Some of them evidence mixing between reacted and unreacted fluid, without reactivity. Others involve only unreacted fluids, typically fresh mixture and air. The ϕ profiles highlight, in some cases, a variation from the fresh mixture equivalence ratio, that will be discussed later (sec.5.2.5).

Plane $z = 30$ mm

At $z = 30$ mm the mean flame brush, as shown in sec.5.2.1, is located in the slot 1 area, at about $r = 15$ mm. At inner radial locations respect to this position, the 1-D profiles correspond indeed to fully reacted states. These are indicated by the absence of a gradient in the observed quantities, which are instead characterized by flat profiles. Moreover, the temperature values are in the order of 2000 K, carbon monoxide is almost absent and high values of CO_2 are measured. These peculiarities are shown in two representative profiles, in fig.5.6.

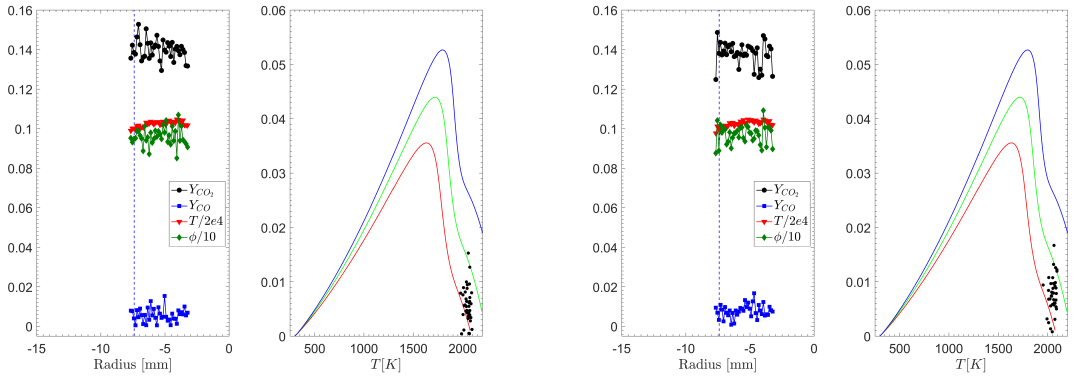

(a) Shot a **(b)** Shot b

Figure 5.6: For each shot: (left) Fl.D 1-D single shot profile of Y_{CO_2} [−], Y_{CO} [−], T [K] and ϕ [−] at $z = 30$ mm, $5 \leq r \leq 10$ mm; the blue dashed line virtually extends the pilot tube / slot 1 limit. (right) CO scatter plot of the same single shot in the temperature space; flamelet calculation at $\phi = 0.85$ (–), 0.95 (–) and 1.05 (–).

The analysis of the CO in the temperature domain respect to the laminar flamelet confirms that the samples are in the conditions of fully reacted state, i.e. positioned at the right-end of the flamelet profile, with high temperature and $Y_{CO} < 0.01$. Less than

1% of the observed shots at $r < 8$ mm deviates from the described behavior. In the mentioned locations, the influence of the exhaust from the pilot might be significantly relevant, as noted also in similar configurations by Schneider in [57].

At the plane $z = 30$ mm the flame front position appears located most likely at about $10 \leq r \leq 20$ mm. At this coordinate the fresh gas and burnt gas sections, as well as the flame structures, are scattered around the unstretched adiabatic flamelet profile, as can be seen for example in fig.5.7. Here two different shots show a similar

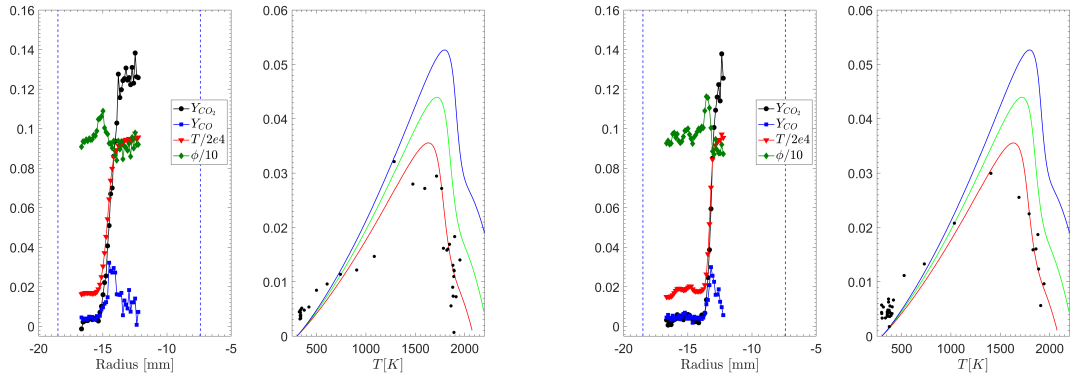

(a) Shot a **(b)** Shot b

Figure 5.7: For each shot: (left) Fl.D 1-D single shot profile of Y_{CO_2} [−], Y_{CO} [−], T [K] and ϕ [−] at $z = 30$ mm, $5 \leq r \leq 10$ mm; the blue dashed line virtually extends the burner sections limits. (right) CO scatter plot of the same single shot in the temperature space; flamelet calculation at $\phi = 0.85$ (–), 0.95 (–) and 1.05 (–).

behaviour, with the spatial profile including a section of unreacted fluid (low temperature, low CO, low CO_2) and one of reacted fluid (high T, high CO_2). Between these sections there is a portion in which the quantities have a steep variation. This part may include the reaction zone, which is indeed characterized by such a rapid change in the species and temperatures. Moreover, it may be noted that the increase/decrease takes place in 7 discretized steps (average value among all the analyzed profiles), with one step corresponding to ca. 0.12 mm. From this observation it might be deduced that the turbulence structures are not small enough to penetrate in this length scale and change significantly the reacting structures, at least for the location where heat release is present. It can be observed that, crossing the flame region, an increase in the equivalence ratio is noted.

The majority of the 1-D profiles at the mentioned locations highlights the discussed characteristics. Nevertheless, it has to be noted that 2% of the profiles correspond to pockets of fresh gas. Those are detected in the slot 1 section close to the slot 2, at $r > 12$ mm, and are signal of the mixing process that happens between the flows of the two slots (remembering that slot 1 is fueled with the flammable mixture, while slot 2 with air).

The cases exemplified in fig.5.7, where reacting structures are not significantly affected by the turbulent ones are present in more than 90% of the profiles. The remaining cases, apart from the mentioned fresh gas pockets, present remarkable peculiarities. Two exemplifications are shown in 5.8.

The profiles shown in fig.5.8 are notably different from the one described in fig.5.7.

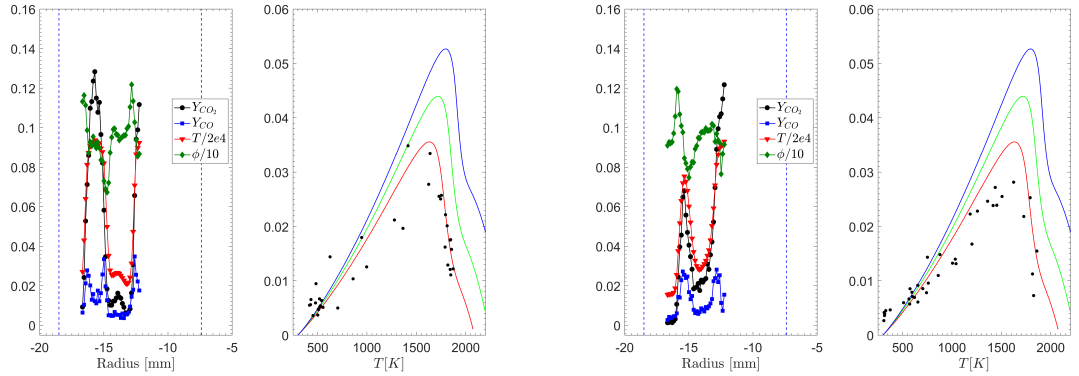

(a) Shot a **(b)** Shot b

Figure 5.8: For each shot: (left) Fl.D 1-D single shot profile of Y_{CO_2} [−], Y_{CO} [−], T [K] and ϕ [−] at $z = 30$ mm, $5 \leq r \leq 10$ mm; the blue dashed line virtually extends the bruner slots limits. (right) CO scatter plot of the same single shot in the temperature space; flamelet calculation at $\phi = 0.85$ (–), 0.95 (–) and 1.05 (–).

Indeed, the spatial variations are not monotonic, but rather characterized by stationary and inflection points. High temperature portions are interrupted by sections at about 400 K. The CO_2 and CO profiles are coherent with the temperature trend, with high/low carbon dioxide presence in correspondence of high/low temperature. The CO peaks aligned with the temperature gradients suggest the presence of reaction activity. This behavior might be explained by the mixing process taking place between reacted/reacting structures and fresh gas. The analysis of the carbon monoxide in the temperature domain shows a qualitative and quantitative correspondence to the flamelet. This indicates that the observed phenomenon does not affect significantly the flame structures, that are indeed well reconstructed by the flamelet model.

Plane $z = 45$ mm

At $z = 45$ mm the mean flame brush is located into the slot 2 area, near the boundary with the slot 1, as seen from sec.5.2.1. The analysis of the 1-D profiles at this height suggest that the interaction between the slot 1 gas mixture and the slot 2 air plays a relevant role in defining the spatial profiles.

Several conditions are detected, when focusing the analysis at $18 \leq r \leq 22$ mm. Flame structures similar to the one of fig.5.7 are present, with flat profiles interrupted by steep gradients that indicate the presence of the flame. Here, the temperature, CO_2 and CO profiles are coherent one to each other, with the same relations already described (low/high T corresponds to low/high CO_2, CO peaks where T gradients are located). The flamelet is still able to reconstruct the carbon monoxide distribution in the temperature domain. Examples of these profiles are shown in fig.5.9, and are representative of ca. 20% of the shots.

10% of the profiles are clearly belonging to unreacted cold gas. It is interesting to show profiles that differ from the flame structures already presented and from the mentioned unreacted gas gas. Two examples are shown in fig.5.10. In fig.5.10a the preheat of cold gas is evident, with the temperature slowly rising from its inlet value. The presence of carbon monoxide, but the absence of reactivity, suggest that the heating

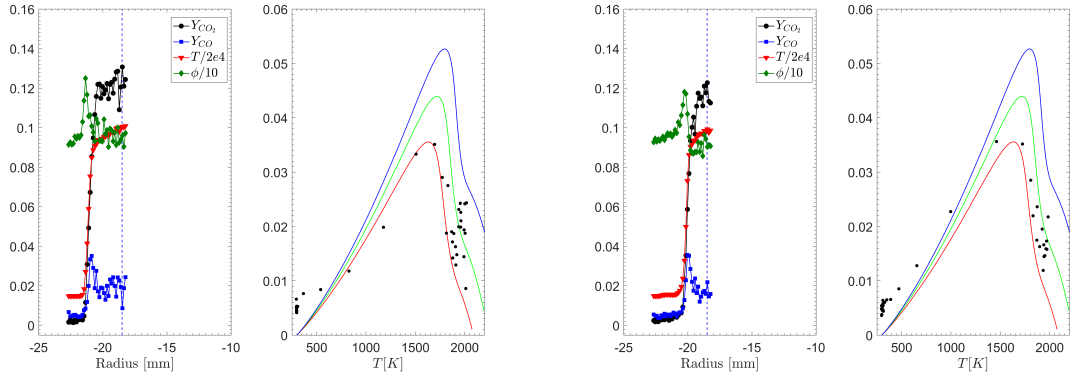

(a) Shot a **(b)** Shot b

Figure 5.9: For each shot: (left) Fl.D 1-D single shot profile of $Y_{CO_2}\,[-]$, $Y_{CO}\,[-]$, $T\,[K]$ and $\phi\,[-]$ at $z = 45$ mm, $5 \leq r \leq 10$ mm; the blue dashed line virtually extends the slot 1 / slot 2 limit. (right) CO scatter plot of the same single shot in the temperature space; flamelet calculation at $\phi = 0.85$ (–), 0.95 (–) and 1.05 (–).

process may be due to mixing with hot, reacted gases. The equivalence ratio present in the profile, close to the one of the mixture, is a marker that the mixing takes place among reacted and non reacted pockets of mixtures, rather than with air.

The profiles of fig.5.10b suggest that the interaction of the turbulence and flame structures is intense. Indeed, steep non-monotonic spatial variations are present, indicating the possible penetration of eddies inside the flame. Such a behavior is evident in ca. 4% of the analyzed realizations, and results in an overall flame thickening. This must anyway affect only the flame preheat zone and leave untouched the flame reaction zone, as it is proven by the CO – T evolution, following the flamelet prediction.

Plane $z = 60$ mm

At $z = 60$ mm the mean flame brush position is located at $r = 24$ mm. The analysis is then focused on $18 \leq r \leq 25$ mm. At this plane similar profiles to ones observed at $z = 45$ mm are evidenced. They will not be shown, but the same considerations are valid. A different condition is instead present, not noted at lower heights. In about 2% of the profiles where reactivity is present, less steep gradients are observed, as shown in fig.5.11. While in the previous commented profiles the evolution from unreacted to reacted takes place in ca. 7 discretized steps, here it is doubled in the size. The flat profiles in reacted and unreacted states are not affected significantly by the observed phenomenon. Also, the flamelet describes qualitatively the CO evolution in the temperature space. The effect observed in fig.5.11 of a thickened flame structure, is likely due to the probe line not intersecting the flame front perpendicularly. Indeed a strong impact on the flame reaction zone is not evident, as it is proven by the carbon monoxide in the temperature domain, that is not strongly different from the cases where steeper gradients are observed (e.g. fig.5.7). While in fig.5.10b the impact of the turbulent structures on the thickening effects is clear, in this case it is not possible to notice the same impact. It is still present an increase in the equivalence ratio when crossing the flame zone, as noted in the lower planes.

In more than 10% of the profiles, fully reacted gases are detected.

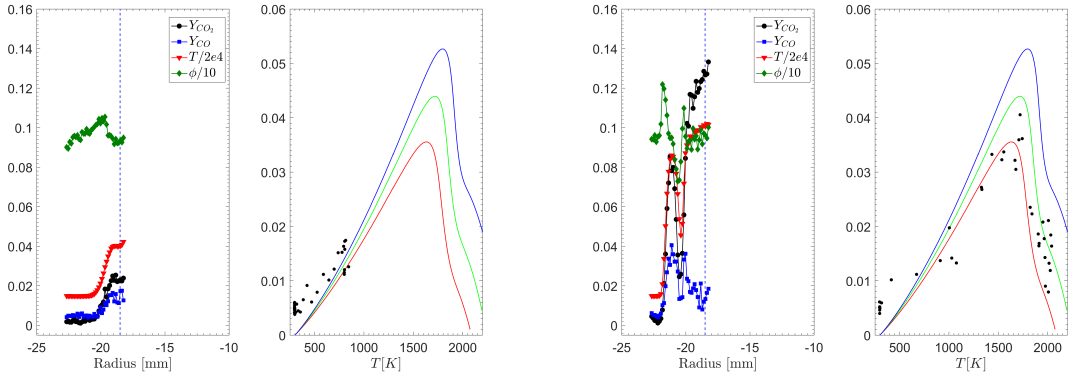

(a) Shot a **(b)** Shot b

Figure 5.10: For each shot: (left) Fl.D 1-D single shot profile of Y_{CO_2} [−], Y_{CO} [−], T [K] and ϕ [−] at z = 45 mm, 5 ≤ r ≤ 10 mm; the blue dashed line virtually extends the pilot slot 1 / slot 2 limit. (right) CO scatter plot of the same single shot in the temperature space; flamelet calculation at ϕ = 0.85 (–), 0.95 (–) and 1.05 (–).

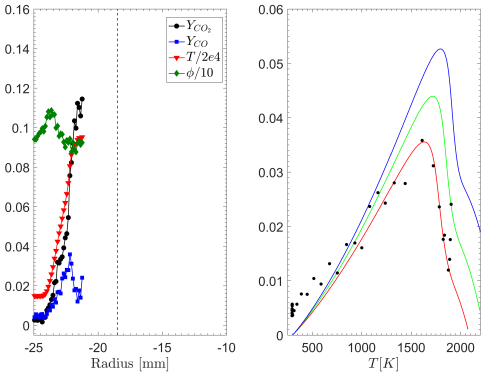

Figure 5.11: For each shot: (left) Fl.D 1-D single shot profile of Y_{CO_2} [−], Y_{CO} [−], T [K] and ϕ [−] at z = 60 mm, 5 ≤ r ≤ 10 mm; the blue dashed line virtually extends the pilot tube / slot 1 limit. (right) CO scatter plot of the same single shot in the temperature space; flamelet calculation at ϕ = 0.85 (–), 0.95 (–) and 1.05 (–).

Plane z = 75 mm

The mean flame brush at z = 75 mm is close to the limit of the slot 2. It is indeed located at ca. r = 28 mm. The analysis is then conducted for 23 ≤ r ≤ 30 mm. At this plane the same kind of profiles described at the lower heights are observed. Two interesting profiles are shown as examples of effects not evidenced at the lower planes. Figure 5.12a presents irregular profiles, where the mixing between fluid at $\phi \simeq 0.95$ and ϕ of about 0.50/0.70 takes place. A marked peak is not evident for carbon monoxide, and it is not possible in this case to be sure about the reaction activity. In this condition the temperatures and species evidence a profile that may be connected to the flame wrinkling. In about 10% of the shots the (thin) flame front is identified with the same characteristics as e.g. fig.5.7. Figure 5.12b shows a profile where the mixture from slot 1 and air are in contact. This is clearly indicated by the equivalence ratio, which is very low on the left side of the profile, while at about the inlet condition on the right

side. In between, at about r = 25 mm, there is a ϕ gradient that connects the two sections. The interaction between the two flows is similar to cold mixing, as it is clear from the flat temperature profile and the absence of CO_2 and CO. This kind of profiles are ca. 1% of the total for the locations of interest.

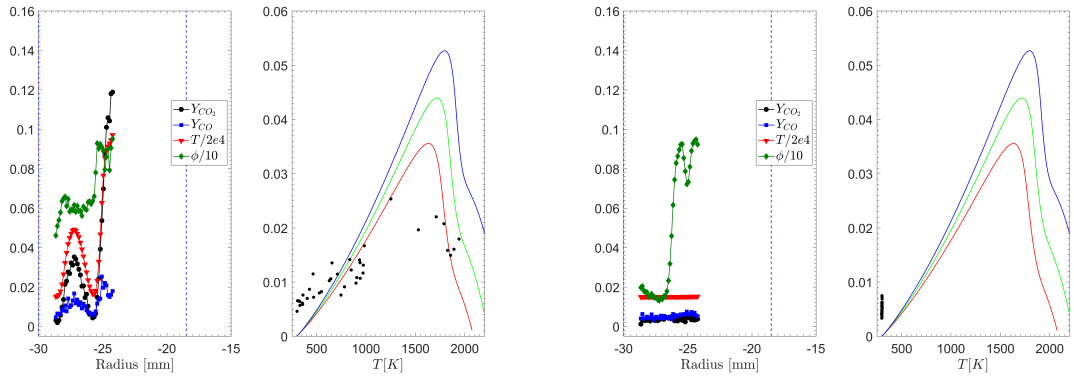

(a) Shot a **(b)** Shot b

Figure 5.12: For each shot: (left) Fl.D 1-D single shot profile of Y_{CO_2} [−], Y_{CO} [−], T [K] and ϕ [−] at z = 75 mm, 5 ≤ r ≤ 10 mm; the blue dashed line virtually extends the burner sections limits. (right) CO scatter plot of the same single shot in the temperature space; flamelet calculation at ϕ = 0.85 (–), 0.95 (–) and 1.05 (–).

Effects that may connected to flame wrinkling or to the formation of unreacted pockets are also shown, as it is possible to notice from the profiles in fig.5.13. In fig.5.13a the presence of unreacted fluid surrounded by fully reacted gas is highlighted. The impact of flame wrinkling may be the cause for the profiles shown in fig.5.13b, where a thin flame front is detected, with opposite orientation respect to what discussed before (where the unreacted section is placed on the left of the profile, and the reacted one on the right side).

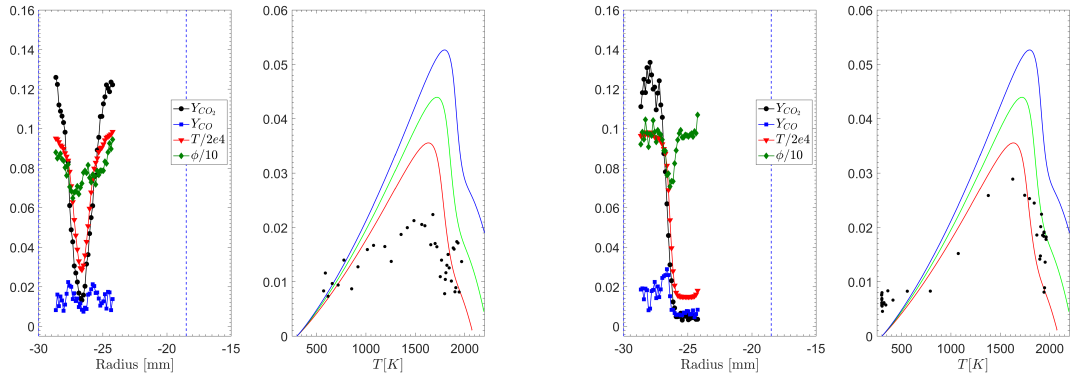

(a) Shot a **(b)** Shot b

Figure 5.13: For each shot: (left) Fl.D 1-D single shot profile of Y_{CO_2} [−], Y_{CO} [−], T [K] and ϕ [−] at z = 75 mm, 5 ≤ r ≤ 10 mm; the blue dashed line virtually extends the pilot tube / slot 1 limit. (right) CO scatter plot of the same single shot in the temperature space; flamelet calculation at ϕ = 0.85 (–), 0.95 (–) and 1.05 (–).

Plane $z = 90$ mm

Being the mean flame brush positioned at ca. $r = 34$ mm, the analysis at this plane contains profile in the radial locations $28 \leq r \leq 35$ mm. At this place about 20% of the shots present mixing without reaction. This statistics is evenly distributed among two types of profiles. One type is characterized by mixing between hot gas and unreacted gas at the same equivalence ratio, as in fig.5.14a. The other type presents a flat temperature profile at about room temperature, confirming that none of the fluid has reacted, and an equivalence ratio gradient. This last aspect is instead the marker for the layer between the fresh mixture issued by the slot 1 and the air issued from slot 2, and is observable in fig.5.14b.

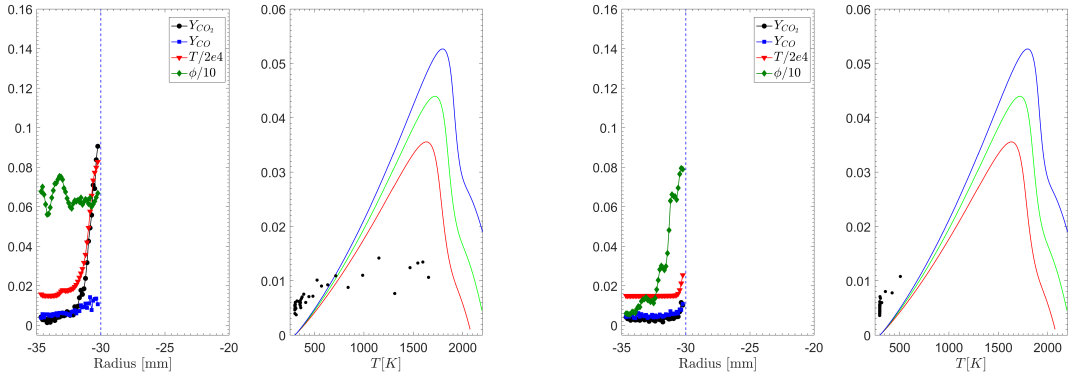

(a) Shot a **(b)** Shot b

Figure 5.14: For each shot: (left) Fl.D 1-D single shot profile of Y_{CO_2} [−], Y_{CO} [−], T [K] and ϕ [−] at $z = 90$ mm, $5 \leq r \leq 10$ mm; the blue dashed line virtually extends the pilot tube / slot 1 limit. (right) CO scatter plot of the same single shot in the temperature space; flamelet calculation at $\phi = 0.85$ (–), 0.95 (–) and 1.05 (–).

Plane $z = 120$ mm

At $z = 120$ mm, the mean flame brush is located at about $r = 38$ mm. Consequently, the analysis is focused on $34 \leq r \leq 41$ mm. In these locations, ca. 5% of the CO profiles suggest that there is reactivity. The majority of the profiles are instead characterized by fully reacted fluid, or pockets where mixing has taken place. In this second case, the CO spans all the temperature range, from ca. ambient temperature to ca. 2000 K, but no peaks highlight the presence of reactivity.

5.2.3 Scalars Radial Profiles

Radial profiles of selected scalars measured with the Raman/Rayleigh spectroscopy are shown in the following. The scalars are reported with the Reynolds decomposition: as seen in 2.3.2: a generic quantity may be expressed as $x = \bar{x} + x'$. In the present study, the mean part is obtained averaging every point of the spatial discretization over the shots sequence, while the fluctuations, x', are expressed through the standard deviation. Given that the probe lines are placed in order to have an overlap of half the length, for each radial location 1000 measurement samples are available.

The temperature, reported in fig.5.15, is expressed in Kelvin; the species, in figs.5.16, 5.17 and 5.18, are expressed in terms of mass fractions. The plots show the radial profiles at the different heights above the burner exit: 30; 45; 60; 75; 90; 120 mm. The vertical dashed lines are drawn in correspondence of the burn sections limits, $r_P = 7.4$ mm, $r_{S_1} = 18.5$ mm and $r_{S_2} = 30$ mm. Going from the right to the left in the horizontal axis (i.e. from 0 to −40), it is possible to identify the regions above pilot tube, slot 1, slot 2 and air co-flow. In all the plots reporting the radial profiles, the left column shows the mean value, and the right one the fluctuations. In this section, as for the previous ones, the axial symmetry assumption allows for using the positive half-plane of the radial coordinates within the discussion.

Temperature

The analysis of the mean temperature, left column in fig.5.15, highlights a smooth profile. The maximum temperature gradient is located in the slot 1 area, at about $r = 15$ mm, for $z = 30$ mm. This is expected, given the presence of the fresh mixture in this location. With increasing height, the radial locations of the max T gradient shifts gradually toward the outer radial zones. At $z = 45$ mm the temperature ramp is across the limit between slot 1 and slot 2 ($r = 18,5$ mm). At $z = 60$ mm it is located in the slot 2 region, about $r = 25$ mm. At $z = 120$ mm the temperature ramp is located in the co-flow region, $r > 30$ mm.

The analysis of the fluctuating components, right column of fig.5.15, confirms the described topologies. In fact, the peak of the temperature fluctuation is usually located in the same region where the highest gradients are present for T. As observed for $\overline{T}$, the maximum of the T' at $z = 30$ mm is located at about $r = 15$ mm. At $z = 45$ mm it is positioned on the slot 1/slot 2 boundary, and at the $z = 120$ mm it is in the co-flow region, $r > 30$ mm.

Linking the maximum of the temperature fluctuations to the heat release zone, as done for the mean flame brush position detection, one may notice that the Fl.C flame zone shifts toward outer radial positions with increasing z. The combustion reaction is not expected to be significantly affected by the presence of the air from slot 2 at $z = 30$ mm, but already from $z = 45$ mm the reaction may be affected by the interaction between the two flows. This is indeed confirmed by the single shot analysis proposed in sec.5.2.2, e.g. fig.5.10b.

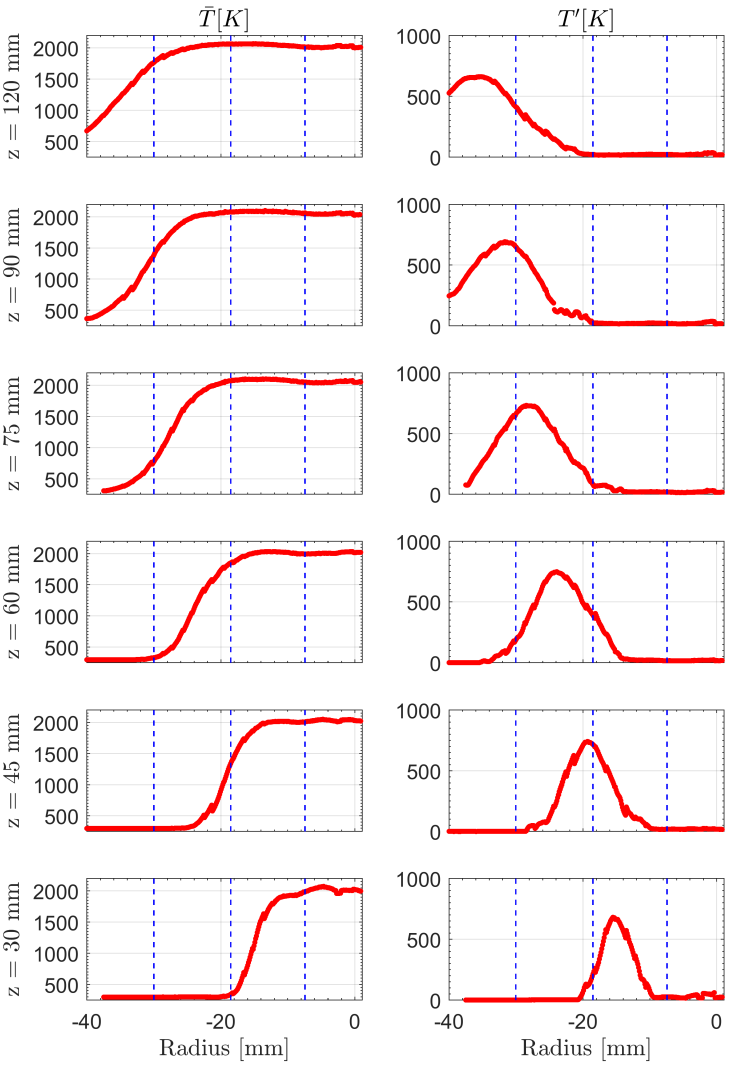

Figure 5.15: Fl.C temperature radial profiles at six heights above the burner. *Left*: Reynolds average. *Right*: standard deviation. Blue dashed lines show the burner sections limits.

Species

Figures 5.16, 5.17 and 5.18 show radial profiles of CO_2, O_2 and CO mass fractions, respectively. The species are selected as representative of a product, a reactant and an intermediate. As already seen for the temperature, the dashed lines are traced in correspondence with the burner sections. In the three figures, the left column reports the shot-averaged value and the right one shows the fluctuation.

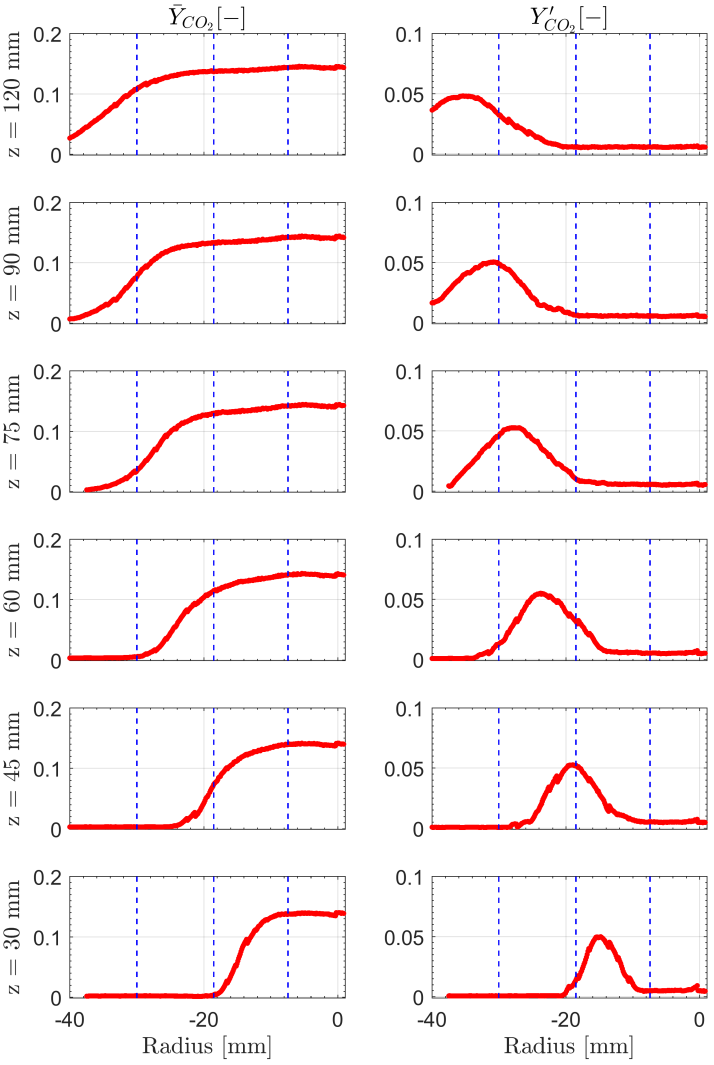

Figure 5.16: CO_2 mass fraction radial profiles at six heights above the burner. *Left*: Reynolds average. *Right*: standard deviation. Blue dashed lines show the burner sections limits.

At $z = 30$ mm the carbon dioxide (fig.5.16) increases smoothly in the slot 1 region, i.e. about $7 < r < 18$ mm, from the reactant concentration to the product one. With increasing z, the area where this increase takes place is shifted to the outer radii. At $z = 60$ mm, indeed, it is located in the slot 2 region, about $r = 30$ mm.

The CO_2 fluctuating components of the flame C show, at $z = 30$ mm, a flat profile

for $r > 20$ mm, with very low value. The peak is located at about half of the slot 1 region. At $z = 45$ mm the peak is located almost exactly on the slot 1/slot 2 boundary. At $z = 60$ mm is positioned in the middle of the slot 2, about $r = 23$ mm, and at $z = 120$ mm it can be found in the co-flow area, while it is almost flat for $r < 20$ mm.

It is possible to notice that the carbon monoxide and the temperature have very similar qualitative mean radial profiles, confirming the expectations. Indeed, with the reaction progress, the CO_2 is formed and the temperature increases from ambient temperature (in this case) to ca. 2000 K. The trend of the two mean components of these quantities are then connected. It has also been shown in the analysis of the 1-D profiles that there are cases, where the reaction is not active, where T and CO_2 are disconnected.

In terms of fluctuating part, there is also a strong qualitative correspondence in terms of radial profiles. This is true not only for T and CO_2, but also for the other species. Indeed, on the fluctuating part there is the strong impact of the turbulence. It can be observed that the locations of the fluctuating parts maxima are aligned in the radial position for temperature and species.

Figure 5.17 reports the radial statistics O_2 profiles. At $z = 30$ mm, the mean value is very low in the region above the pilot flame. This is in line with the expectations, given that the flow issued by the pilot pipe is designed to be in fully reacted state. The same holds true at all the axial positions. The values reached by the mean O_2 in the outer region of the jet are slightly above 0.20. This is well explained by the fact that in this location the jet is composed solely by air (which has indeed ca. $Y_{O_2} = 0.23$). Between these two extrema, there is a difference in the spatial evolution of the mean profile, depending on the height above the burner. At the lowest plane the profile reaches a plateau in the slot 2, as expected given the inlet composition. With increasing heights, the mixing process between the slot 1 mixture and the slot 2 air of becomes dominant in the region above the slot 2. This is confirmed by the fact that the maximum gradient is shifted toward outer radial positions with increasing z, and is positioned in the slot 2 area for $z = 45$ to $z = 90$ mm. Further downstream, it is positioned out of the slot 2 region. It can be noted that the mean profiles of CO_2 and O_2 at each z are specular respect to the radial coordinate. This is in line with the fact that the oxygen necessary for the carbon dioxide formation is provided by the oxygen consumption.

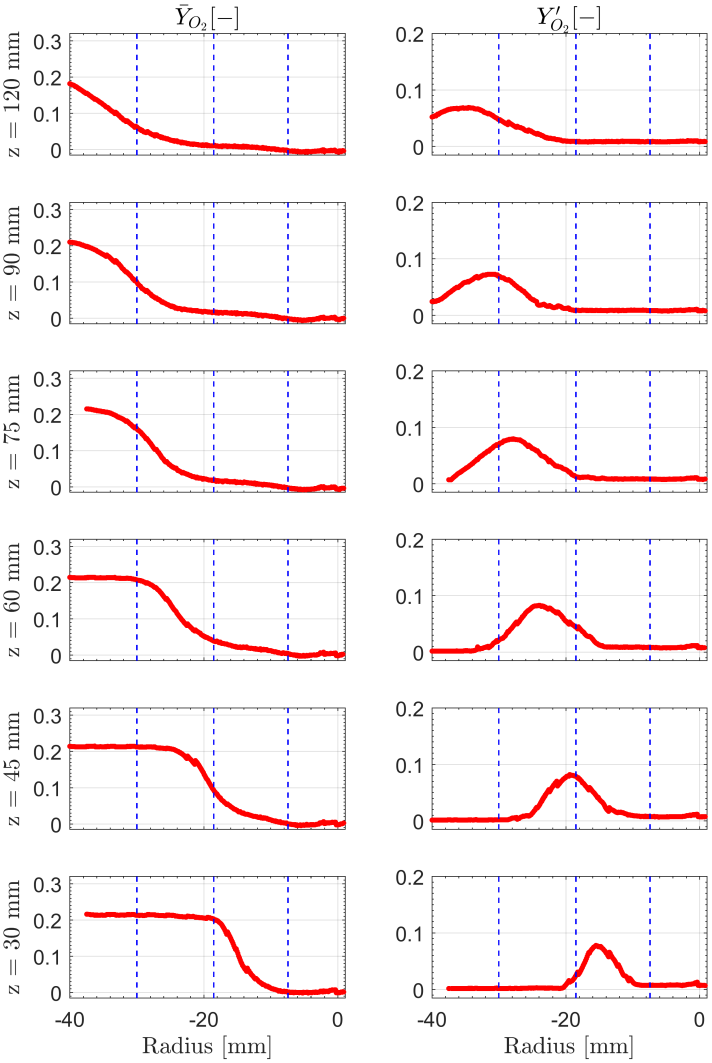

Figure 5.17: O_2 mass fraction radial profiles at six heights above the burner. *Left*: Reynolds average. *Right*: standard deviation. Blue dashed lines show the burner sections limits.

The last species analyzed in this section is the carbon monoxide, and its profiles are shown in fig.5.18.

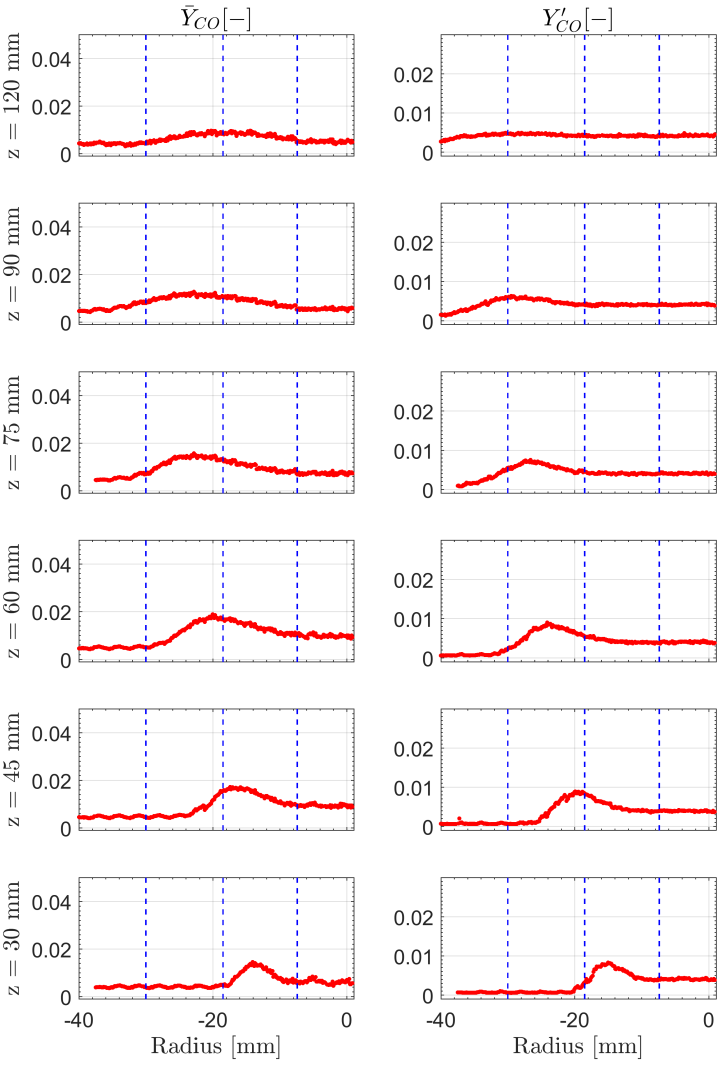

Figure 5.18: CO mass fraction radial profiles at six heights above the burner. *Left*: Reynolds average. *Right*: standard deviation. Blue dashed lines show the burner sections limits.

At z = 30 mm, $\overline{Y}_{CO}$ is at null concentration for r > 20 mm, and is also close to zero in the pilot area. As already commented, in this area and in the vicinity of the burner's exit, the flow is expected to be dominated by the pilot exhaust. According to laminar flamelet calculations (as the one used in the single shot analysis) at ϕ = 0.95 Y_{CO} < 0.005 for the highest T.

A peak of less than 0.02 is shown in the middle of the slot 1 area. With increasing height, this peak shifts toward outer radii and the value above the pilot rises to about 0.01 at z = 45 to z = 90 mm. At z = 120 mm again the mass fraction is close to zero. At this plane, the clear peak shown at lower z is less distinct.

The CO fluctuating component is in line with the profiles already described, showing peaks in the same locations of the other analyzed quantities.

General Comments In this brief paragraph, closing this section, some of the observations stated above are unified and integrated, in order to provide an overview of the analysis of the radial profiles.

Being the CO_2 a product of the combustion reaction, it is in very low concentration in the region where only air or fresh mixture is present. The carbon dioxide concentration increases with the reaction progress, up to the maximum value in the product region. This species, indeed, follows the same trend as the temperature. The oxygen, being a combustion reactant, has the opposite trend. It is low where the reaction has taken place and it has all been consumed; it is high where no reaction has taken place or in the reaction zone. The flat $\overline{O_2}$ plateau shown at z = 30 mm for r > 20 mm is corresponding to the unreacted air composition, for example. The locations where the oxygen concentration increases from low to high mass fractions includes the mean reaction zone.

The mean CO mass fraction is a marker for the area where the reaction zone is likely to be located. Indeed, in the flame condition here studied, the carbon monoxide is mainly formed starting from CH_4 and then oxidated to CO_2. A peak in the CO presence is registered around the reaction zone. After the reaction the peak is lowered by the CO oxidation[2] to CO_2. A simplified schematization of this process is given in the kinetic mechanisms used to describe the methane/air combustion referred to as "2 step - global" as the one applied in [89]:

$$CH_4 + 1.5\, O_2 \Rightarrow CO + 2\, H_2O \tag{5.1}$$

$$CO + 0.5\, O_2 \Leftrightarrow CO_2 \tag{5.2}$$

where the first reaction represents the methane oxidation, and the second one the $CO - CO_2$ equilibrium. Mechanisms as simple as the one above reported indicate in fact that the carbon monoxide is produced from the methane reactions, and is then considered a combustion intermediate. Global mechanisms are extreme simplifications of the kinetics controlling the combustion processes. A more realistic representation of the chemical pathways involved in cases similar to the one of interest is reported by Warnatz et al. in [45] or described by (more) detailed kinetics mechanisms. A detailed treatment about the kinetic mechanisms characterizing the CO (as well as the other species) reactions in the system is out of the scope of this work, especially because reaction chains involve radicals and intermediate species that are not available within the data set used here.

Variations of the CO may happen not only in the reaction zone, but may be present also in the preheat zone and in the post flame zone. For a more precise localization of the reaction zone, intermediate species such as CH and HCO [90] have to be studied.

The combined analysis of the profiles above reported show consistency in the trend of reactant, product and intermediate species, in accordance with the temperature, for both the flames. Similar profiles are in fact shown for premixed methane–air flames

[2]The predominant reaction leading to carbon monoxide oxidation in hydrocarbon combustion is the CO reaction with OH, producing CO_2 and H [4].

by Peters in [5].

5.2.4 Comparison with Flamelet Model

For a better understanding of the combustion process taking place in Fl.C, the data from the investigated flame have been compared to results from laminar steady flamelet calculations. This comparison is often used as a reference in similar studies, e.g. [25, 65, 87].

Introduction Figures 5.19, 5.20, 5.21 report the CO_2, O_2 and CO mass fractions in the temperature domain. These species are chosen as representative of a product, a reactant and an intermediate species, respectively. If plotted in the temperature domain, reactants and products have monotonic trends. With increasing temperature the reactants are heated up and then are consumed by the reaction progress. On the contrary, the products are in low concentrations at low temperature (depending on the fresh mixture composition) and are formed through the reaction. During the reaction and in the post-flame zone, they are heated up by the reaction heat release. The effects of other processes that might be present, such as non-reactive mixing, may change these trends. The CO has instead a change in the trend at about 1600 K. Considering the case of premixed methane/air mixture at ambient temperature, carbon monoxide is formed with T increasing from $\simeq$ 290 K to $\simeq$ 1600 K. At about 1600 K the carbon monoxide oxidation becomes dominant, especially because of the CO reaction with OH, which produces CO_2 and H. Consequently, at temperatures higher than $\simeq$ 1600 K the presence of CO in the system decreases. These aspects have been already commented in the final comments to sec.5.2.3.

The plots are reported at the heights of 30, 45, 60, 75, 90 and 120 mm above the burner top edge. Superimposed on the scattered data, green markers and error bars show the mean and standard deviation computed over a 200 K temperature binning.

At the end of this section, a discussion considering the interconnections between the species of the interest is proposed.

Scatter Plots Figure 5.19 reports the CO_2 scatter plots in the temperature domain. At z = 30 mm there is a good correspondence between the data and the flamelet profiles. The carbon dioxide follows the trend indicated by the flamelet at low, intermediate and high temperature. At higher planes the trend is not significantly different, but some differences can be noted. With increasing z, the upper limit of the data does not follow the same curvature of the flamelet. This effect is evident especially from z = 75 mm, and is clear at z = 120 mm. Such a behavior might be reflecting the presence of non-reactive mixing. The relevance of this process at z = 75 mm has already been noted in the single-shot analysis, see fig.5.12b, where non reactive mixing is noted.

Figure 5.20 shows the scatter plots for oxygen. As noted for CO_2, also this species is in good agreement with the flamelet profiles at all the analyzed planes. The effects of the non-reactive mixing highlighted for carbon dioxide is here less observable.

In fig.5.21the CO scatter plots are shown. In line with what noted for the species above illustrated, also carbon monoxide highlights a good qualitative agreement with the flamelet profiles at the lowest planes, from z = 30 mm to z = 60 mm. Here the two

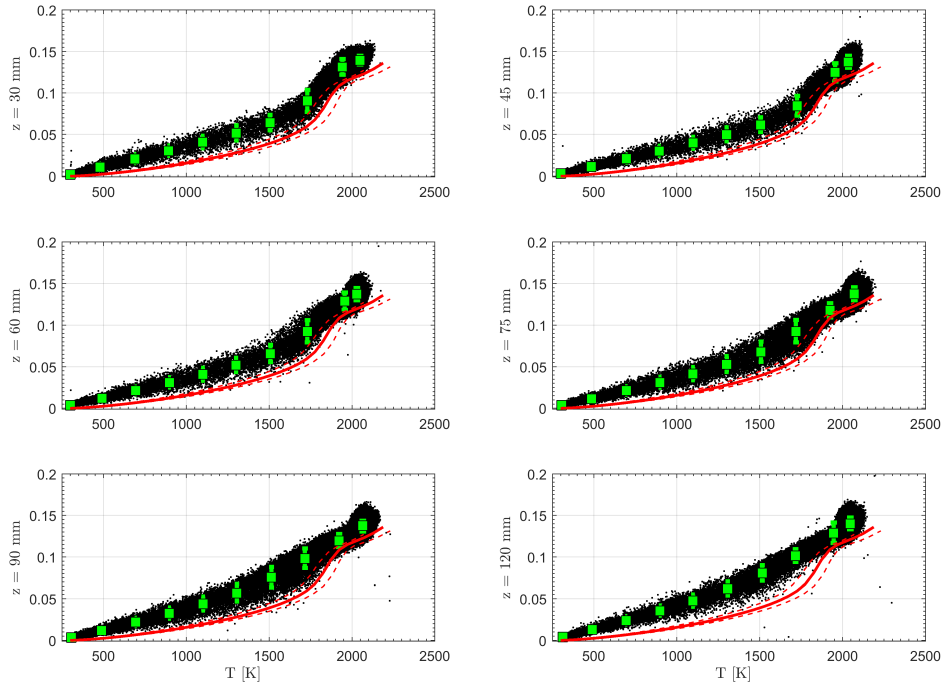

Figure 5.19: CO_2 mass fraction in the temperature space. Red lines report the steady, unstretched, flamelet solutions at ϕ = 0.95 (solid), ϕ = 0.85 (lower dashed) and ϕ = 1.0 (higher dashed). Green squares and bars are mean and standard deviation computed over a 200 K binning.

paths of the CO evolution in the temperature space are clear. The first section, at T lower than ca. 1600 K, reflects the CO formation as the reactants are oxidated. The second path, at high temperature, clearly shows the carbon monoxide oxidation. At z = 90 mm and z = 120 mm a significant number of samples are located in the area below the flamelet profile. At z = 120 mm it is not possible to notice from the mean values the presence of the production peak. As said, this is coherent with the fact that the reactivity has been demonstrated to be less intense at the higher planes, where the influence of cold mixing is notable.

General Comments As seen, a good qualitative agreement with the profiles identified by the flamelet model is noted. Given the strong interconnections in the combustion process between the species shown, it is possible to highlight some aspects emerging from the analysis of the scatter plots. Looking at the CO_2 and O_2 plots, it is possible to notice that a direct connection is present between the two species, in terms of their correspondence with the flamelet profile. Indeed, almost all the conditional mean values plotted (green markers) for carbon dioxide are slightly above the flamelet values. At the same time, O_2 conditional means are positioned slightly below the flamelet profiles.

The impact of cold mixing is clear at z = 90 mm and z = 120 mm. Here, the carbon monoxide distribution shows that the mass fraction is almost constant in the temperature space, assuming a quasi-constant value close to the one at CO at 2000 K (at ϕ = 0.95, $Y_{CO} \simeq 0.005$). This is a confirmation that at z = 120 the fluid is mainly

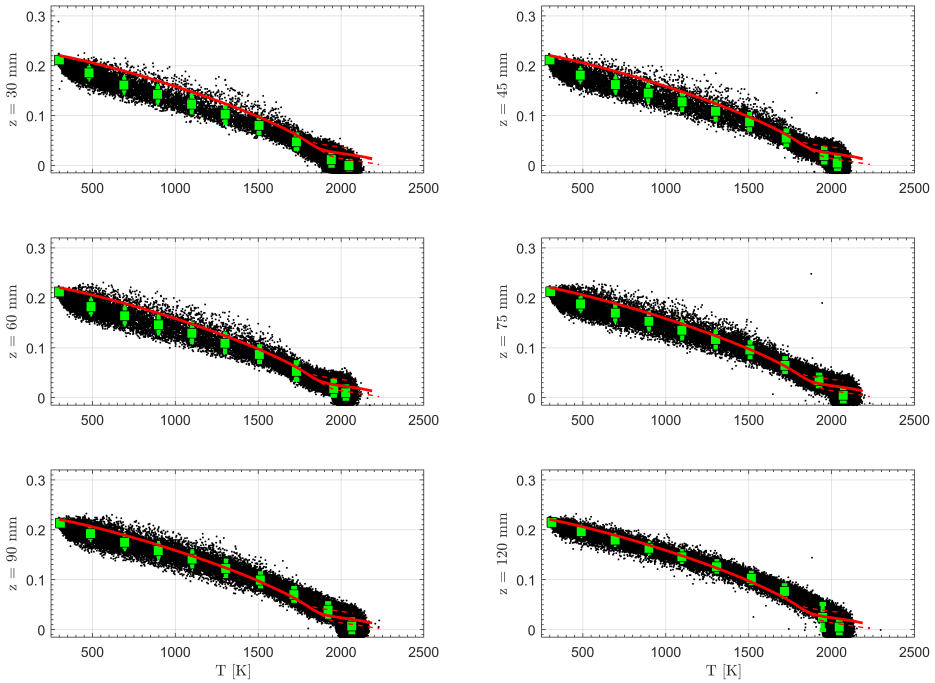

Figure 5.20: O_2 mass fraction in the temperature space. Red lines report the steady, unstretched, flamelet solutions at ϕ = 0.95 (solid), ϕ = 1.0 (lower dashed) and ϕ = 0.85 (higher dashed). Green squares and bars are mean and standard deviation computed over a 200 K binning.

involved in cold mixing, without reaction.

To have a better understanding of the observed effects, and to provide a quantitative analysis, in the next section the comparison with the flamelet model is proposed on the base of multiple conditioned analysis conducted on the data set.

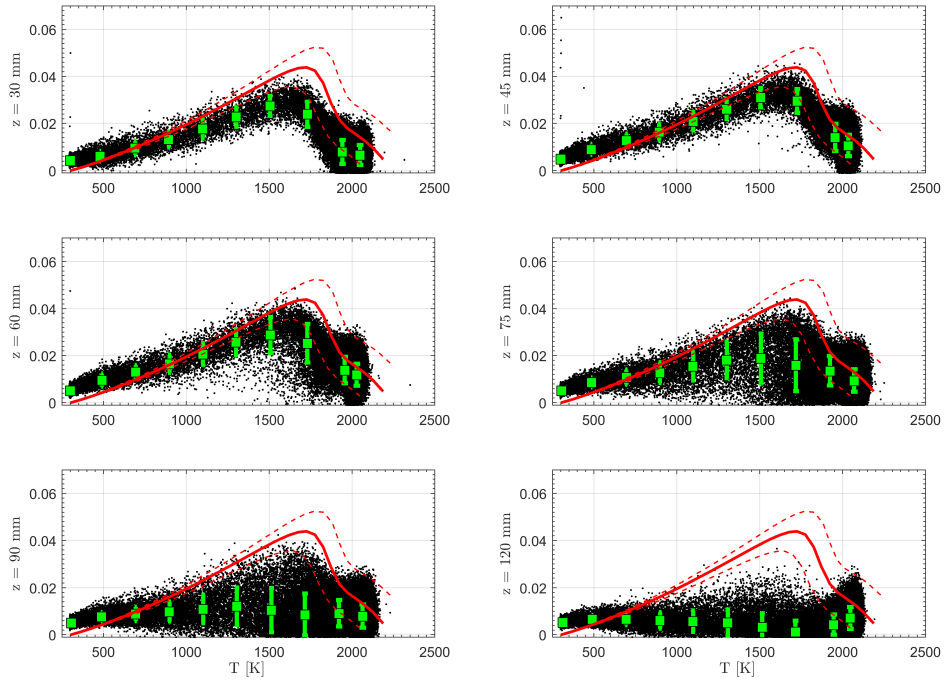

Figure 5.21: CO mass fraction in the temperature space. Red lines report the steady, unstretched, flamelet solutions at $\phi = 0.95$ (solid), $\phi = 0.85$ (lower dashed) and $\phi = 1.0$ (higher dashed). Green squares and bars are mean and standard deviation computed over a 200 K binning.

5.2.5 Multiple Conditioned Analysis

Data conditioning on the local equivalence ratio has been applied to the data set. This is a procedure often applied to isolate the physical phenomena on the base of the local composition, given that significant changes may occur in the combustion physics and in the fluid dynamics depending on this aspect (e.g. [13], [37]). The results shown in this part belong to the conditioned database.

The equivalence ratio is computed according to Barlow et al. [67] as the oxygen required divided by the oxygen available, based on the mole fractions of the same seven major species:

$$\phi = \frac{X_{CO_2} + 2X_{CH_4} + X_{CO} + 0.5\left(X_{H_2O} + X_{H_2}\right)}{X_{CO_2} + X_{O_2} + 0.5\left(X_{CO} + X_{H_2O}\right)} \tag{5.3}$$

The equivalence ratio chosen for the conditioning is the one characterizing the inlet fresh mixture, i.e. $\phi = 0.95$. A range of $\phi \pm 0.05$ is added to the conditioning equivalence ratio, to account for the determined precision.

The aspect of the plots is the same as the one presented in the previous sec.5.2.4. As before, also in this case CO_2, O_2 and CO are chosen as representative of products, reactants and intermediate species. The plots are reported at the heights of 30, 45, 60, 75, 90 and 120 mm above the burner top edge. Superimposed on the scattered data, green markers and error bars show the mean and standard deviation computed over a 200 K temperature binning.

Figure 5.22 reports the conditioned scatter plots for CO_2. Similarly to what already seen for the unconditioned database, at $z \leq 60$ mm the samples have a good qualitative agreement with the trend defined by the flamelet profiles. In this case, differently from the unconditioned database, the same is observable at the higher planes. Indeed, excluding the samples in leaner conditions, the effects of (cold) mixing is less evident, as expected. With increasing z it is noted that less samples are present in the mid-temperature range. This is particularly clear at $z = 120$ mm. This reflects the fact that, at the higher planes, less samples in the conditional range analyzed are involved in the active reaction. At $z = 120$ mm it is indeed evident that the majority of the samples, conditioned on $\phi = 0.95 \pm 0.05$, are in fully reacted conditions (high temperature, high mass fraction).

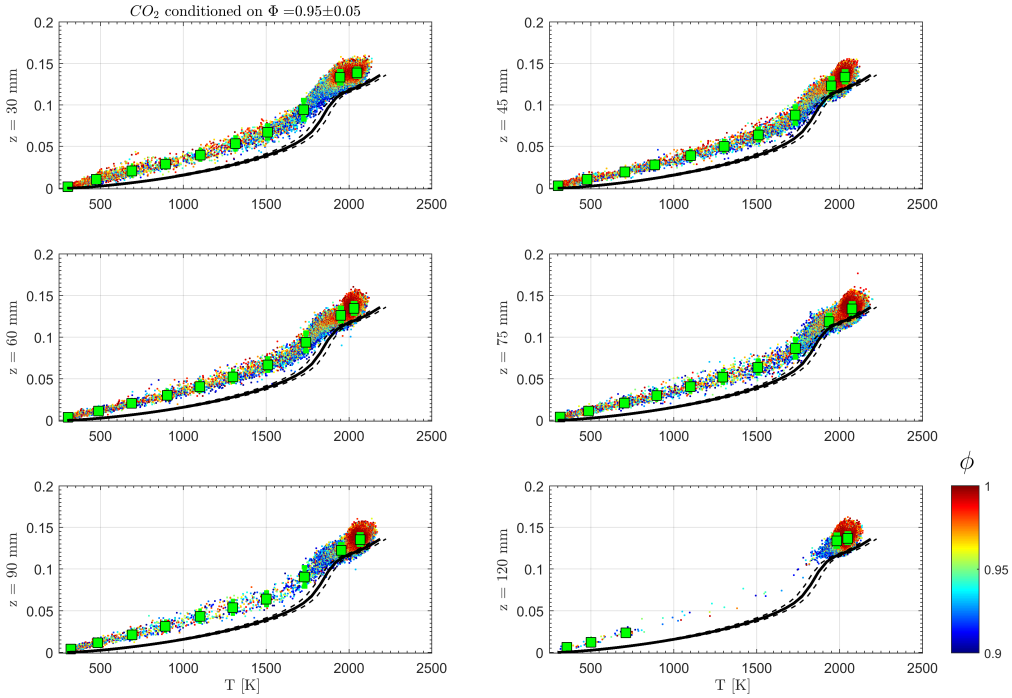

Figure 5.22: CO_2 mass fraction in the temperature space, conditioned on $\phi = 0.95 \pm 0.05$. Black lines report the steady, unstretched, flamelet solutions at $\phi = 0.95$ (solid), $\phi = 0.90$ (lower dashed) and $\phi = 1.0$ (higher dashed). Green squares and bars are mean and standard deviation computed over a 200 K binning.

Figure 5.23 shows conditioned scatter plots for the oxygen. The qualitative agreement between the scattered data and the flamelet profiles is good. The mean conditional values computed with the 200 K binning follow the trend identified by the model, especially in the high temperature region. Apart from the already mentioned absence of samples at $T < 1800$ K for $z = 120$ mm, there are no evident differences visible among the different planes. The color code helps to identify a stratification of the samples depending on the equivalence ratio. As expected, the samples characterized by (slightly) richer conditions, i.e. the red color on the plot, are positioned below the samples with leaner conditions, i.e. blue color on the plot. The positioning of the conditioned samples on the mass fraction - temperature plane reflect the expected

behavior described by the flamelet model.

As already observed for the unconditioned database, also in this case there is consistency between the CO_2 and the O_2 relative positions with the respective flamelet profiles. For example, at z = 45 mm, the oxygen mean mass fraction at the highest temperature is 0.0138, while the flamelet is at 0.023, i.e. the mean value is positioned below the flamelet profile. On the contrary, mean CO_2 in the same position is 0.134, with the flamelet at 0.123, i.e. the mean value is positioned above the flamelet.

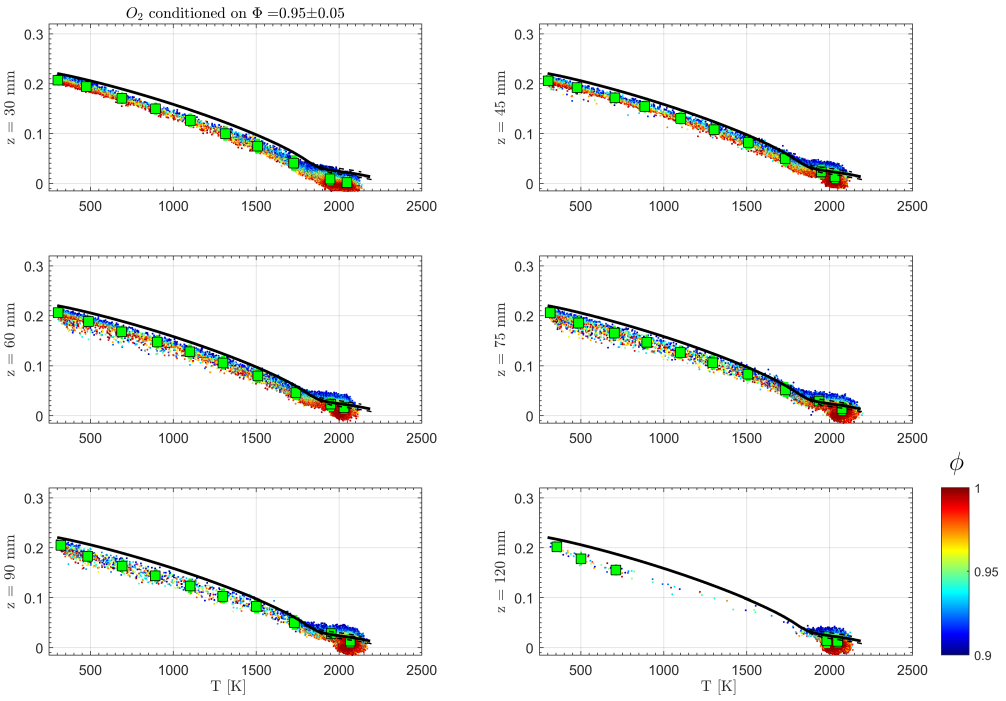

Figure 5.23: O_2 mass fraction in the temperature space, conditioned on $\phi = 0.95 \pm 0.05$. Black lines report the steady, unstretched, flamelet solutions at ϕ = 0.95 (solid), ϕ = 1.0 (lower dashed) and ϕ = 0.90 (higher dashed). Green squares and bars are mean and standard deviation computed over a 200 K binning.

Figure 5.24 includes scatter plot in the temperature space for carbon monoxide. Significant differences are shown between the conditioned database and the unconditioned one (fig.5.21) in terms of CO. The conditioned scatter plots, indeed, exclude a relevant number of the samples present below the flamelet profile, especially at $z \geq 75$ mm. A good agreement is observed between the scatter plot and the flamelet model, at all the heights.

General Comments To conclude the analysis of the multiple conditioned database, in this paragraph the comments highlighted above are summarized and integrated. The first aspect that can be noted from the conditioned scatter plots, and that confirms what remarked in the unconditioned analysis, is that at z = 120 mm the reactivity is low in the flame, and most of the fluid is in reacted conditions. This is confirmed by the absence of an observable peak in the carbon monoxide scatter plot. In addition, almost no samples at $\phi = 0.95 \pm 0.05$ are present (for all the species) at $T < 1800$ K.

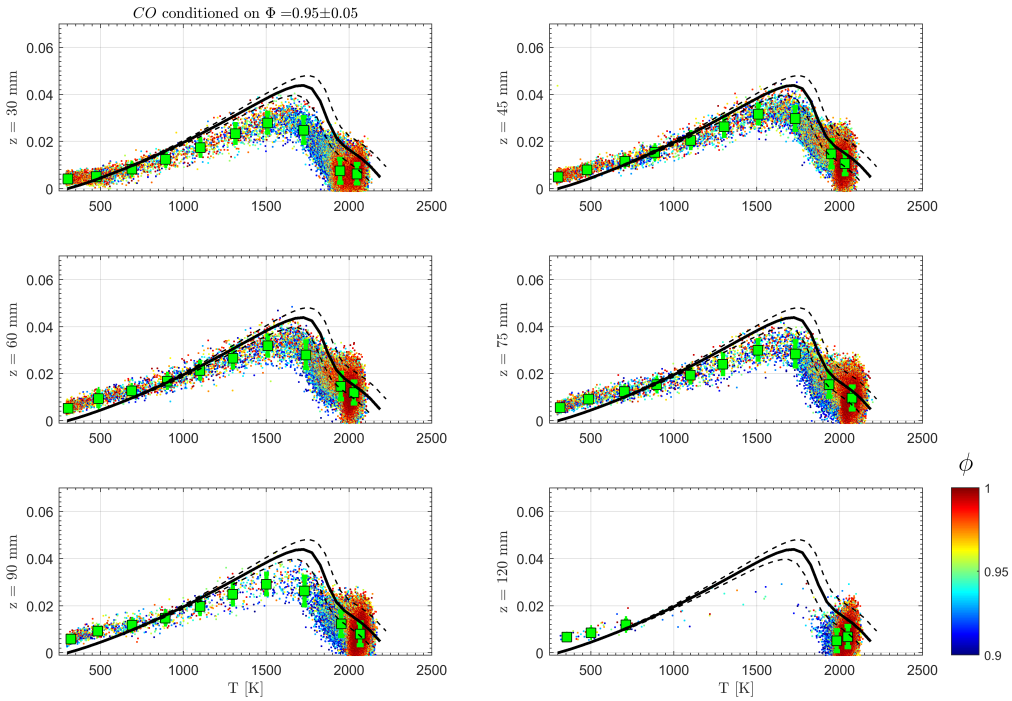

Figure 5.24: CO mass fraction in the temperature space, conditioned on $\phi = 0.95 \pm 0.05$. Black lines report the steady, unstretched, flamelet solutions at $\phi = 0.95$ (solid), $\phi = 0.90$ (lower dashed) and $\phi = 1.0$ (higher dashed). Green squares and bars are mean and standard deviation computed over a 200 K binning.

Further, as a general remark, it might be observed from the species scatter plots that the conditioned database is well described by the profiles of the flamelet model. The qualitative agreement is good at all the investigated planes. Quantitative differences are observed, especially for carbon dioxide and (less evident) for oxygen. The observed deviations are coherent one to each other, i.e. where the CO_2 mass fraction is higher than the flamelet profile, the oxygen results to be lower. This bahvior might be caused by the effects of preferential diffusion [91]. Barlow et al. in [11] report from single shot Raman/Rayleigh experiments on turbulent premixed methane/air flames that, in presence of relevant preferential diffusion effects, the equivalence ratio may increase of more than 10% across the turbulent flame brush. Such a behavior can be observed in the present work, e.g. in fig.5.10a, 5.10b and fig.5.11. A statistical analysis of the database composition, conducted on the base of the equivalence ratio, shows that with increasing z, an increasing number of samples are detected in $\phi > 1.0$, while simultaneously the samples with $0.90 \leq \phi \leq 1.0$ decreases in number, as it can be seen in fig.5.25. Here the database composition is analyzed, at the different heights, considering the relative number of samples in different ϕ ranges, respect to the total number (at the relative z). The increase with z of the samples wiht $\phi > 1.0$ may be explained by the fact that the effects of preferential diffusion are stronger with lower levels of turbulence [11]. Indeed, relaminarization with increasing distance from the burner outlet is usually observed in turbulent premixed flames, as consequence of the

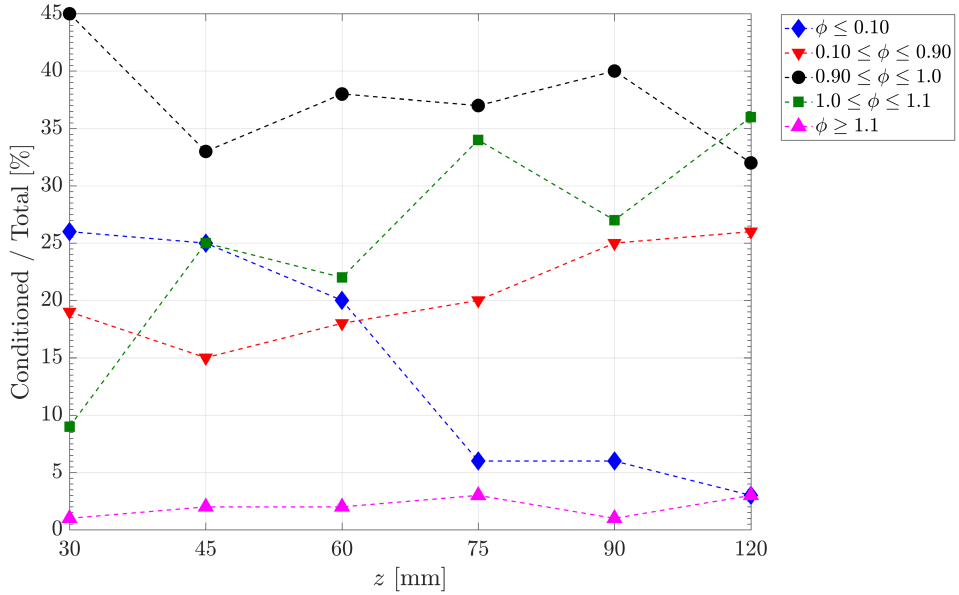

Figure 5.25: Database composition at the different heights. At each z, the relative composition is determined as the ratio between the number of samples in a given ϕ range and the total number of samples at the given z.

heat release [92], as discussed in sec.2.3.3.

The possible impact of preferential transport is confirmed by the hydrogen scatter plots, obtained from the conditioned database, shown in figure 5.26. Indeed, the mean values of the H_2 mass fractions are positioned below the laminar flamelet, and are rather aligned on a linear trend. Similar behavior of the hydrogen has been addressed as a marker for the presence of preferential diffusion by the mentioned work by Barlow et al. Further, the preferential transport effect is observed also on the mean condi-

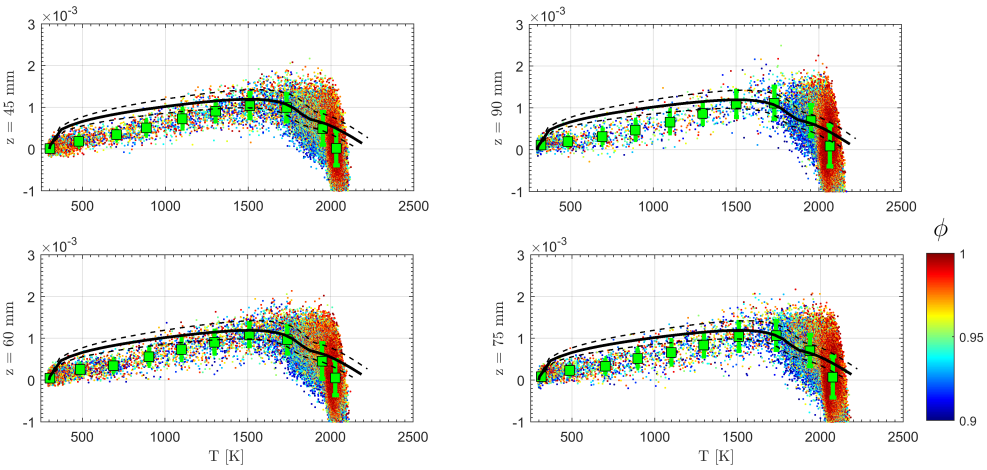

Figure 5.26: H_2 mass fraction in the temperature space, conditioned on $\phi = 0.95 \pm 0.05$. Black lines report the steady, unstretched, flamelet solutions at $\phi = 0.95$ (solid), $\phi = 0.90$ (lower dashed) and $\phi = 1.0$ (higher dashed). Green squares and bars are mean and standard deviation computed over a 200 K binning.

tional atom ratios, in agreement with the observations in [11]. Barlow and coworkers measured an increase of about 10% in the C/N, C/H and C/O in the products respects to the reactants. In the present database, an increase in the conditional mean of the mentioned atom ratios in the products respect to the reactants is also observed. The computed increases are: C/N = 7%; C/H = 5%; C/O = 3% at z = 60 mm. Multiple conditioned scatter plots in the temperature space are shown in the appendix A to this thesis. The reduced magnitude of the effects, respect to the mentioned work, is explained by the key role that, in the investigation by Barlow and coworkers, plays the presence of a strong recirculation zone, which enhances the observable effects of preferential diffusion of the H-containing molecules, respect to the others. In the present study, where a piloted jet is investigated, a strong recirculation zone is not present.

5.2.6 Focus on the Equivalence Ratio

For a further understanding of the effects linked to the equivalence ratio, a dedicated focus is proposed in this section. First, a sensitivity analysis is performed, to verify the impact of the single species on the equivalence ratio, when it is computed according to the formula of eq.(5.3). Further, the evolution of quantities of interest respect to ϕ in the investigated flame will be analyzed. This analysis will demonstrate that at the lowest investigated planes the flame behavior well reflects the one expected by a turbulent premixed flame. It will be seen that the maximum temperature is slightly over predicted by the flamelet model. A maximum temperature lower than the flamelet prediction has been observed in the above-mentioned study by Barlow et al. [11]. In that case, the presence of a heat exchange with the bluff body was causing doubts in addressing the observed reduction to preferential diffusion. In this case, where a pilot flame is used to anchor the flame, it can be said that the observed reduction may be an effect of the preferential diffusion. With increasing height, the effects of the preferential diffusion become more clear, especially on the products, as well as the mixing processes taking place due to cold-mixing between products and air. Also, indications that the fluid previously involved in mixing processes participates to the reaction (at $\phi < 0.95$) are found.

Sensitivity Analysis

To estimate the impact of the single species on the equivalence ratio, a sensitivity analysis is performed, with the scope of excluding errors in the observations about the database composition (fig.5.25) and about the preferential transport.

For this purpose, two measured conditions are selected as starting points for this procedure. More specifically, the two conditions refer to two points where the shot averaged local ϕ results to be rich in one case and lean in the other. From the two real conditions, a linear perturbation is imposed on the species, to simulate an error with different magnitudes. The consequent values of the local equivalence ratio are computed, to estimate the impact of the simulated error on ϕ.

Figure 5.27 shows the results of the sensitivity analysis of ϕ on the carbon monoxide. The horizontal axes shows the variation in the measured CO values, normalized respect to the two initial (measured) values. The vertical axis shows the resulting values of the local ϕ, normalized with respect to the values computed in the two starting points. The two relations are described by the two plotted lines: the black one refers to the

Table 5.4: Equivalence ratio sensitivities on the species of interest, according to the formula of eq.(5.3).

	CO_2	O_2	CO	CH_4	H_2O	H_2
Lean Start	±1%	±3%	±2%	±1%	±1%	±0%
Rich Start	±1%	±5%	±1%	±0%	±1%	±0%

starting point in lean conditions, the red line to the rich case. The linear perturbation applied to the carbon monoxide value is of ±20% of the measured values. The computed perturbed ϕ highlights a deviation from the starting value that is contained below ±2%.

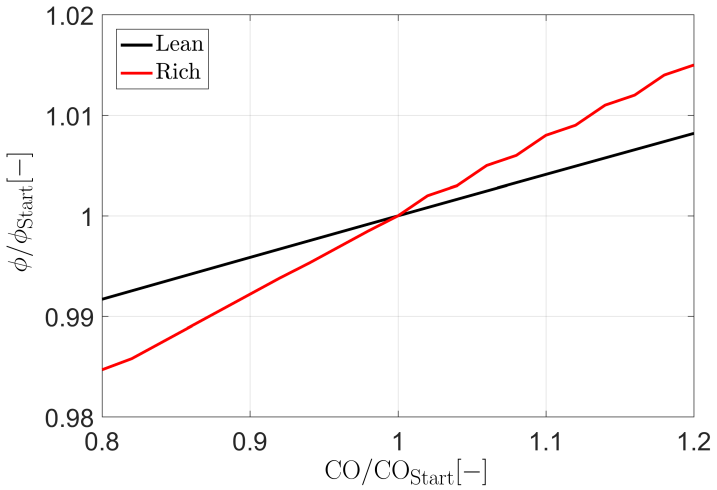

Figure 5.27: Sensitivity analysis of the equivalence ratio on carbon monoxide variations, as resulting from the formula (5.3) used by Barlow et al. [67]. The red line refers to a starting point in rich conditions, the black one to a starting point in lean conditions. The CO and ϕ variations are normalized respect to the values assumed in the two starting points.

Table 5.4 shows the computed ϕ sensitivities starting from the perturbations applied on selected species. It is noted that in none of the cases the effect on the equivalence ratio exceed ±2%, except for the oxygen where it can be up to ±5%.

It is concluded that the effects on the equivalence ratio observed in sec.5.2.5 are not likely to be affected by any error on the species measurement, also considering the values of the uncertainties presented in 5.1.2, that are below the ±20% perturbation applied on the species.

Process Evolution in the Equivalence Ratio Domain

In this section an analysis is proposed, to investigate the evolution of quantities of interest respect to the local equivalence ratio. Figures 5.28 to 5.30 show scatter plots of T, Y_{CH_4} and Y_{CO} in the space of the equivalence ratio. The color map identifies the sample radial locations, with the bar ticks defined on the base of the burner geometry. Black dots show maximum T and maximum Y_{CO}, in the respective plots, as computed

from laminar flamelets.

An overall look to fig.5.28, which refers to z = 30 mm, confirms the expected behavior for a turbulent premixed flame. It is clear in the temperature plot the evolution from reactants to product, which is aligned about the reactants equivalence ratio. The two different states are clearly identified by the clouds of points at low and high temperature. The points aligned at $T \simeq 300$ K that span the space from $\phi \simeq 0.0$ to $\phi \simeq 0.90$ belong to fluid located above the slot 2 and co-flow, as confirmed by the light blue color. The products, marked by the red color, belong to the region above the pilot/slot 1. The CH_4 plots show clearly, as for the temperature, the locations of reactants and products, that are confirmed to be aligned about the vertical line at $\phi \simeq 0.95$, as expected given the inlet composition of the fresh mixture. The points aligned in the region at $\phi \simeq 0.95$ belong to samples where the reaction is taking place. The reacting samples come from the center of the slot 1 (yellow dots), confirming the analysis conducted on the radial profiles and on the mean flame brush position. Other than reactants, products and the reaction progress, in the CH_4 plots is also clearly visible the presence of a mixing area. This is identified by the points aligned onto the straight line connecting the axis origin and the reactant cloud. This mixing takes place between the air in the slot 2 and the fresh mixture present in the slot 1 region, as clearly shown by the color code. The CO plots show clearly the increase and the decrease (burnout) with the reaction progress. The two parts are almost superimposed, given that the reaction takes place about the vertical line at $\phi \simeq 0.95$.

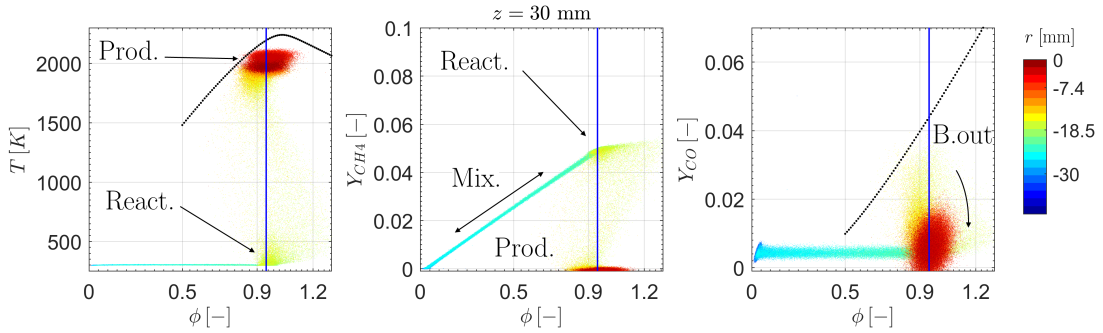

Figure 5.28: Scatter plots of T, CH_4 and CO in the ϕ space, z = 30 mm. The color code stands for the radial position of the samples. The colorbar labels mark the inner radii of the different burner sections. Blue vertical line is aligned on ϕ = 0.95. Black dots show maximum T and maximum Y_{CO}, in the respective plots.

At the plane z = 75 mm, fig.5.29, Fl.C has a sample distribution resembling the one at z = 30 mm, even if differences may be observed. At z = 75 mm there is a lack of reactants respect to z = 30 mm, as it can be deduced by the smaller clouds at high methane concentration and low temperature. Also, the reaction radial location is now identified in the slot 2 area, as it is possible to see from the light blue color of the points aligned on $\phi \simeq 0.95$. The clouds identifying the products are elongated in the horizontal axis, reflecting the small shift in the equivalence ratio caused by the preferential transport. Moreover, mixing between products and surrounding fluid is present, and is indicated by a second group of points aligned on a straight line

departing from the products clouds. Part of the samples located in correspondence of this group of points might belong to product of reactions taking place in leaner conditions. This may be caused by mixing of fresh mixture with air from slot 2, and can be visualized on the T plot. Indeed, samples are present in the area between the elongated, oblique cloud at high temperature and the one aligned at ambient T. Further, mixing between reactants and air is still clearly visible, as in the lower plane.

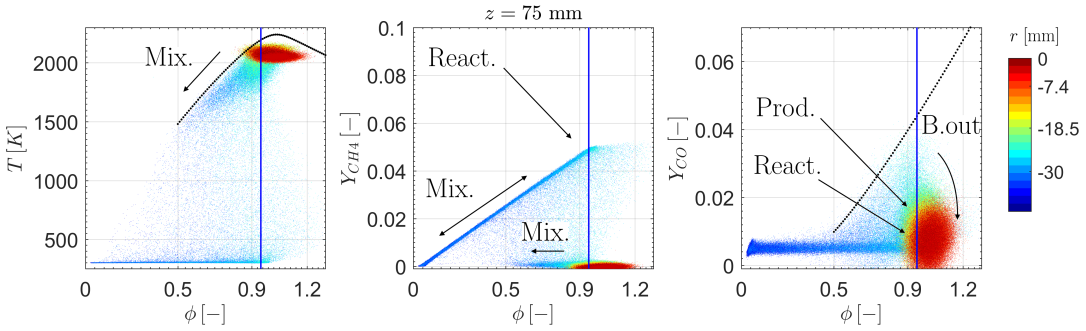

Figure 5.29: Scatter plots of T, CH_4 and CO in the ϕ space, z = 75 mm. The color code stands for the radial position of the samples. The colorbar labels mark the inner radii of the different burner sections. Blue vertical line is aligned on $\phi = 0.95$. Black dots show maximum T and maximum Y_{CO}, in the respective plots.

Figure 5.30 refers to the plane at 120 mm from the burner exit. Here it is clear that no reactants from the fresh mixture are available. Indeed the sample cloud centered at $T \simeq 300$ and $\phi \simeq 0.95$ is not present. The same might be said for methane, where no samples accumulation is visible with high CH_4 value. Both T and CH_4 evidence a strong presence of mixing, in the same locations where the process has been observed at $z = 75$ mm. Looking at the temperature, it is deduced that the mixing process brings a part of the fluid in slot 2 area (light blue) to a temperature $T > 1500$ K, thanks to the interaction with the products at $T > 2000$ K. The light blue samples might also belong to transported products of the reactions at $\phi < 0.95$ that have been observed at $z = 75$ mm. Indeed, the T values well follow the black curve indicating the maximum product temperature as a function of the equivalence ratio. Mixing with the outer region of the slot 2 and with the co-flow (dark blue) is also still present. The samples aligned to the vertical line at $\phi \simeq 0.95$, indicating the ones participating to the reaction, are not present in this case. The samples positioned between the reactants and the products clouds are now located mostly at $\phi < 0.50$, i.e. below the lower flamability limit in the condition of interest. ($\phi \simeq 0.55$, indicated by the red arrow in the plot). The CO production peak is not visible in the plot, and the max CO mass fraction is about 0.02. This is a further indication that there is no high reactivity at $z = 120$ mm, confirming what observed in the analysis conducted so far.

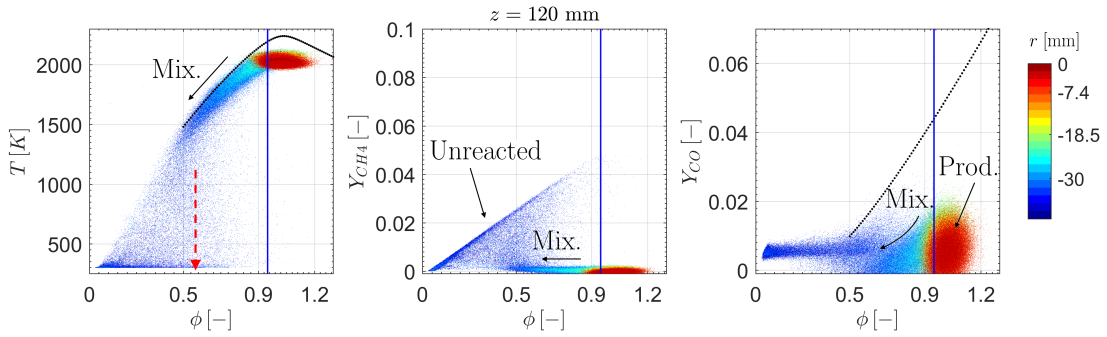

Figure 5.30: Scatter plots of T, CH_4 and CO in the ϕ space, z = 120 mm. The color code stands for the radial position of the samples. The colorbar labels mark the inner radii of the different burner sections. Blue vertical line is aligned on ϕ = 0.95. Black dots show maximum T and maximum Y_{CO}, in the respective plots. The red arrow is positioned at about the lower flammability limit.

5.3 Preliminary Results on an Additional Target Flame

In this section preliminary results on a second target flame are shown, named "Flame D" (Fl.D). As it will be seen in sec.5.3.1, Fl.C and Fl.D have comparable inlet characteristics in terms of composition, but different shear between the slot 1 flow and the surrounding fluid. The investigated axial locations are the same used for Fl.C in terms of coordinate system respect to the burner. The results of the analysis, shown in sec.5.3.2 and sec.5.3.3, will focus on multiple conditioned analysis of the database, conducted on the planes[3] $z = 30$ mm and $z = 120$ mm.

5.3.1 Flame Configuration

Fl.D is characterized by the inlet conditions reported in table 5.5. It can be noted that the flame has comparable conditions with Fl.C in terms of composition. The slot 1 flow bulk velocity is 60 m/s, while for Fl.C it is 10 m/s. The different velocity configuration induces in this case a relevant shear between the slot 1 and the surrounding fluid.

Table 5.5: Fl.D inlet specifics.

Pilot $\phi = \mathbf{0.95}$	**Slot 1** $\phi = \mathbf{0.95}$	**Slot 2** **Air**
u_P [m/s]	u_1 [m/s]	u_2 [m/s]
10	60	10

From the inlet conditions reported, the Fl.D estimated Reynolds number is $Re_{\text{Fl.D}} \simeq 74\text{e}+3$ based on the hydraulic diameter.

Fl.D data have been acquired within the same measurement campaign of Fl.C, then the information about precision and accuracy presented in sec.5.1.2 are here valid.

Classification in the Regime Diagram

Fl.D can be located in the turbulent premixed regime diagram, as it has been done for Fl.C in sec.5.1.1. According to the characteristics of the flame series presented in [12,88], Fl.D might be said to be close to TSF_C or TSF_E, with possibly an upward shift in the diagram, due to the higher inlet velocity of the slot 1. The configurations of interest lie in the thin reaction zone, with possibly some overlapping into the broken reaction zone area.

Investigated Locations

In fig.5.31 and fig.5.32 time-averaged chemiluminescence images show the Fl.D topology, compared with Fl.C. In fig.5.32 the spatial reference coordinates are superimposed. The investigated axial positions are the same used for Fl.C: 30, 45, 60, 75, 90 and 120

[3] The other planes are excluded from the discussion because of inconsistency found in the results, which require a further analysis on Fl.D, possibly repeating the experimental investigation.

mm above the burner top edge. The radial investigated locations and the probe line characteristics are the same mentioned for Fl.C.

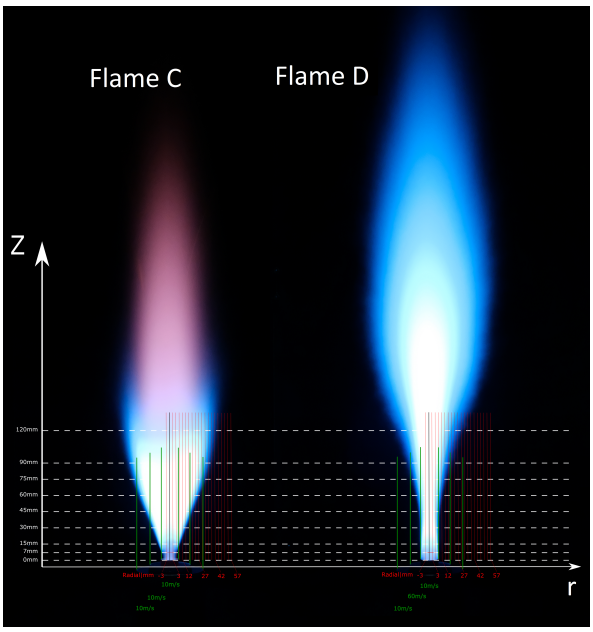

Figure 5.31: Time-averaged chemiluminescence images of Fl.C and Fl.D.

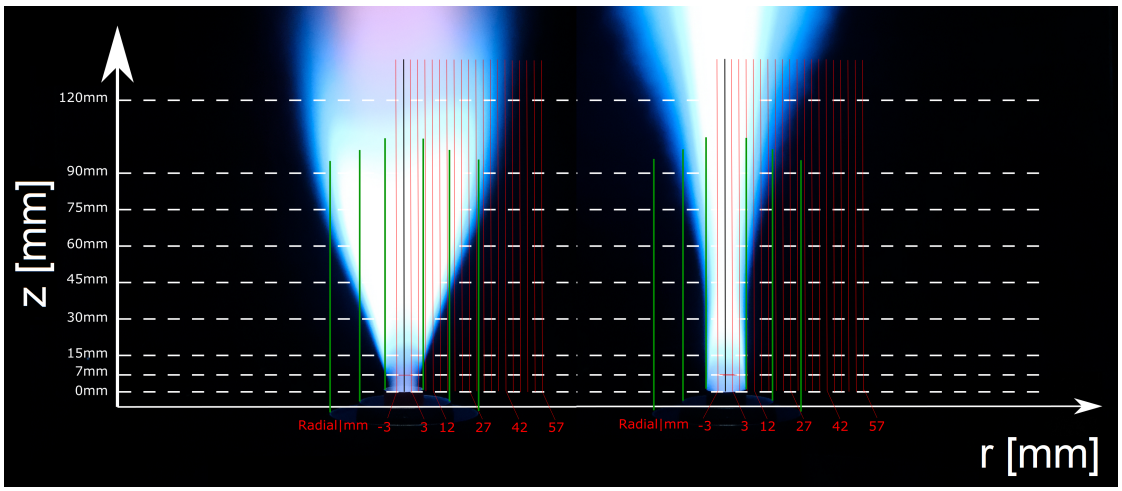

Figure 5.32: Time-averaged chemiluminescence images of Fl.C and Fl.D (detail), with superimposed the coordinate system in the laboratory reference.

5.3.2 Position of the Mean Flame Brush

The positions of the mean flame brush at the different planes, estimated using the same methodology applied for Fl.C (sec.5.2.1), are shown in fig.5.33. Positions estimated for Fl.C are also reported, for a direct comparison. Fl.D is characterized by a contracting section, up to $z \leq 45$ mm, followed by expansion at $z > 45$ mm. In the lower part an angle of $-5°$ is computed, while in the upper section it results to be equal to $4°$ from the vertical.

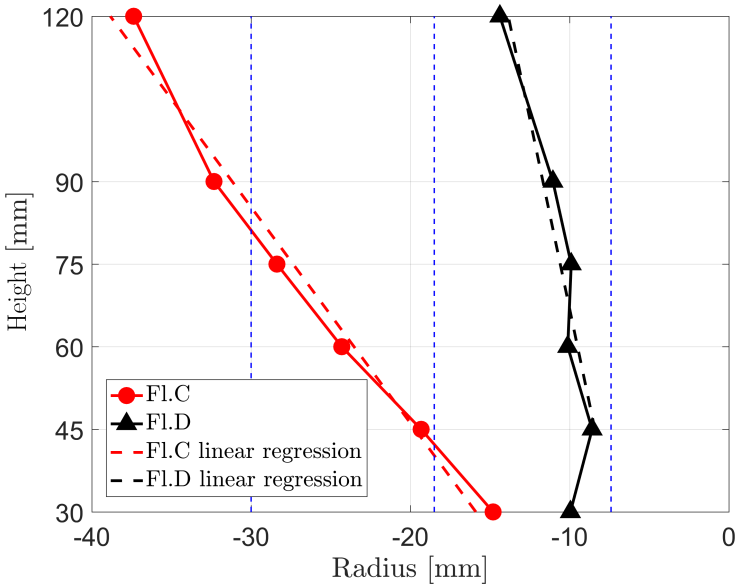

Figure 5.33: Position of the mean flame brush for Fl.C and Fl.D at the different heights. Linear regressions are performed, plotted with the dashed lines, in order to obtain information about the flame angles. The vertical dashed lines represent instead the virtual prolongation of the burner sections.

5.3.3 Multiple Conditioned Analysis

Multiple conditioned analysis is presented for Fl.D, with the same criteria illustrated for Fl.C. The equivalence ratio and the temperature are used for the database conditioning, as seen in sec.5.2.5. As for Fl.C, Y_{CO_2}, Y_{O_2} and Y_{CO}, representative of a product, a reactant and an intermediate, are conditioned on $\phi = 0.95 \pm 0.05$ and analyzed as scatter plots in the temperature domain. The plots are reported at $z = 30$ and $z = 120$ mm above the burner top edge. Superimposed on the scattered data, green markers and error bars show the mean and standard deviation computed over a 200 K temperature binning. The sample color code represents the local equivalence ratio.

As it will be seen from the plots, the flamelet model qualitatively well reproduces the distribution of the conditional mean values obtained from the scatter plots at the analyzed planes. At $z = 30$ mm carbon dioxide and oxygen follow a nearly linear trend in the temperature space. A similar behavior, in turbulent premixed methane/air flames, has been indicated by Magnotti and Barlow in [10] as an effect present in highly strained flames.

Figure 5.34 reports conditional scatter plots for the carbon dioxide. The low temperature area, $T \simeq 300$ K shows a good agreement with the laminar flamelet for both the planes. The same might be said for the high temperature range, ca. $T > 1800$ K. The plane $z = 30$ reaches a maximum temperature lower than the one predicted by the flamelet. Moreover, the conditional mean values, especially at the lowest plane, don't follow the flamelet curvature in the intermediate temperature range. The difference highlighted are less pronounced at $z = 120$ mm.

Figure 5.35 shows scatter plots for Fl.D oxygen. Here a good qualitative agreement is observed at both planes. In the intermediate temperature range, the mean values are located slightly below the correspondent flamelet prediction. As a reference, at ca.

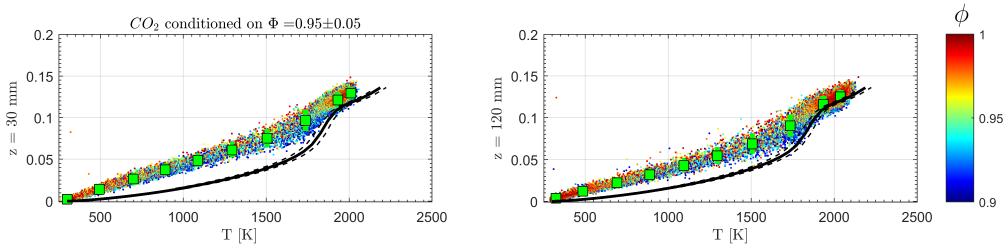

Figure 5.34: Fl.D CO_2 mass fraction in the temperature space, conditioned on ϕ = 0.95 ± 0.05. Black lines report the steady, unstretched, flamelet solutions at ϕ = 0.95 (solid), ϕ = 0.90 (lower dashed) and ϕ = 1.0 (higher dashed). Green squares and bars are mean and standard deviation computed over a 200 K binning.

1300 K, the $\overline{Y}_{O_2}$ is about 85% of the correspondent flamelet value.

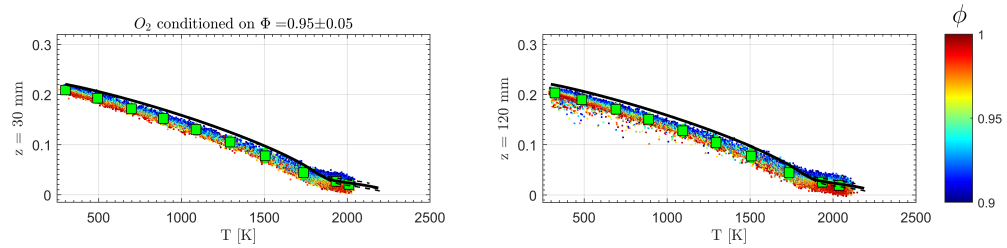

Figure 5.35: Fl.D O_2 mass fraction in the temperature space, conditioned on ϕ = 0.95 ± 0.05. Black lines report the steady, unstretched, flamelet solutions at ϕ = 0.95 (solid), ϕ = 1.0 (lower dashed) and ϕ = 0.90 (higher dashed). Green squares and bars are mean and standard deviation computed over a 200 K binning.

In fig.5.36 the carbon monoxide scatter plots are shown. It can be observed that the laminar flamelets well represent the conditional species distribution in both the planes. As observed for CO_2 and O_2, quantitative differences are highlighted at z = 30 mm, where the peak of the mean carbon monoxide values is placed below the flamelet profile. A lower Y_{CO} respect to the flamelet might be due to effects of preferential transport, already observed for Fl.C, as noted in [10].

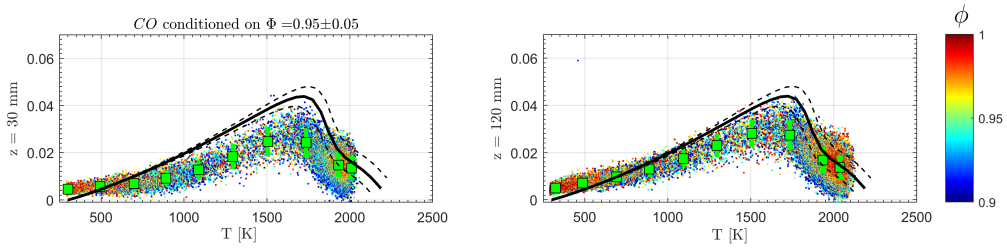

Figure 5.36: Fl.D CO mass fraction in the temperature space, conditioned on ϕ = 0.95 ± 0.05. Black lines report the steady, unstretched, flamelet solutions at ϕ = 0.95 (solid), ϕ = 0.90 (lower dashed) and ϕ = 1.0 (higher dashed). Green squares and bars are mean and standard deviation computed over a 200 K binning.

As a conclusion, it can be noted that also for Fl.D, as for Fl.C, the laminar flamelet well reconstructs the qualitative trend of conditional means in the temperature space for the analyzed cases. In both the flames indications of a significant effect of preferential

transport is noted. Moreover, in Fl.D a strain is induced on the flame by the high shear established around the locations of the mean flame brush, i.e. between the pilot exhaust and the fresh mixture from slot 1. The effects of this strain are observed in the tendency of carbon dioxide and oxygen to follow a linear trend in the temperature space, especially in the mid-temperature range. Figure 5.37 reports a direct comparison of CO_2 conditional means in the temperature space for Fl.C and Fl.D at z = 30 mm, together with unstretched flamelet at ϕ = 0.95. Linear interpolations of the mean values are plotted, too. It is evident the difference in the trends followed by the carbon dioxide in the two flames, with the Fl.D mean values less curved, as it can be clearly noted by the comparison of the liner interpolations. A similar behavior is usually noted in presence of strong mixing.

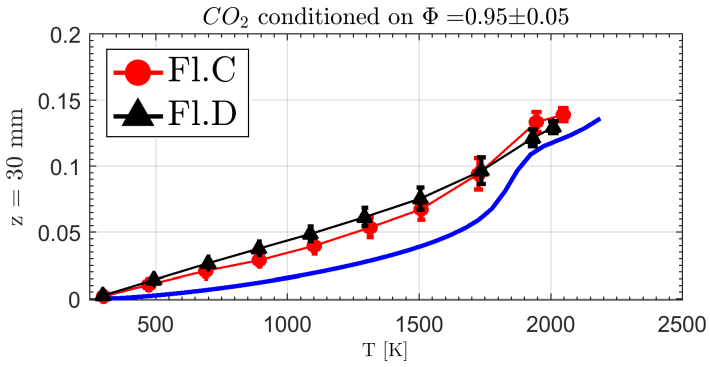

Figure 5.37: Fl.C and Fl.D CO_2 mass fraction conditional means (and respective linear interpolations) in the temperature space. Blue line reports the steady, unstretched, flamelet solutions at ϕ = 0.95. The vertical bars show the range of 1 standard deviation, computed over a 200 K binning.

It has been mentioned that a similar effect has been observed by Magnotti and Barlow in [10]. In fig.5.38 it is reported a figure from their work, where they plot the measured conditional mean Y_{CO_2} from the bluff-body flame series with 3 ratios of reactant bulk velocity to the laminar flame speed (the arrow shows the increase of this ratio). On the same plot, they also show Chemkin laminar unstrained flame results (dashed black line) and opposed flow calculations (dashed red line) for a strain rate of 3500 s^{-1}, using the same chemical (GRI-mech 3.0) and transport (multi-component) mechanisms applied throughout this thesis. It can be noted that one of the effects of the strain is to align the carbon dioxide mass fraction toward a straight line. This may be a confirmation that the effect observed in fig.5.37, with the different Y_{CO_2} trends of Fl.C and Fl.D, is due to a higher strain present in the high-shear case Fl.D, respect to Fl.C (where lower shear is expected between the flows, given the inlet conditions reported in table 5.1.).

Further downstream, where the shear between the Fl.D flows is reduced, the effects observed are less strong, and also the differences of alignment between Fl.D and Fl.C species mass fractions are less evident.

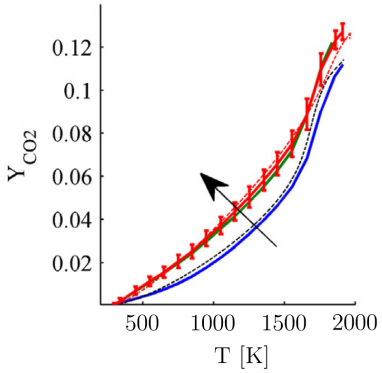

Figure 5.38: Reproduced from Magnotti and Barlow [10]: measured conditional mean Y_{CO_2} from the bluff-body flame series with 3 ratios of reactant bulk velocity to the laminar flame speed (the arrow shows the increase of this ratio). Chemkin laminar unstrained flame results (dashed black line) and opposed flow calculations (dashed red line) for a strain rate of 3500 s^{-1} are included. It is interesting to notice that the presence of strain has the effect of aligning the carbon dioxide mass fraction towards a straight line.

Chapter 6

Conclusions

This work presents the development of an optimized hybrid data reduction strategy in 1D Raman/Rayleigh spectroscopic measurements of turbulent flames.

The hybrid data reduction strategy has been previously developed by Fuest et al. [24, 65], and its effectiveness strongly depends on the correct calibration of the system used for the data reduction. In this thesis, a modified version of the calibration procedure is proposed. It is based on optimization techniques applied to solve a non linear programming (NLP) problem. The analysis of the calibration system is conducted, in order to obtain the problem characterization necessary to identify the most effective optimization routine to implement. The result of this characterization highlights that the use of global optimization methods is fundamental to identify the global optimal solution. For this purpose, a genetic algorithm is selected as best option to solve the NLP problem, after a comparison with other available algorithms.

The implementation of the modified routine is presented, and its performances are tested in different test cases. The results of the test show that the implemented routine is capable of identifying an optimal solution within predefined levels of tolerance. Respect to the original calibration procedure, it allows for several benefits. Considering that the original procedure is fundamentally based on an try and error method guided by the user's inputs, the intrinsic automated nature of the modified routine removes empiricism from the process. Moreover, a significant reduction of the time needed for identifying the optimal solution is noted. Indeed, the modified procedure converges to a solution in about 24 hours of wall time when running on standard commercially available machines, against the several days needed by the user with the try and error procedure. Lastly, the result of the modified routine does not depend strongly on the user's experience, differently from the previous version, where a deep system knowledge is crucial for identifying a satisfying solution.

The modified routine has been applied to calibrate the data processing system for a data set provided by an experimental investigation of two turbulent premixed methane/air jet flames, Fl.C and Fl.D. The data set is composed by multiple scalars, including major species (CO_2, O_2, CO, CH_4, N_2, H_2O, H_2) and temperature, simultaneously measured with single shot 1D Raman/Rayleigh spectroscopy. Results from Fl.C are presented, based on data acquired at six planes located at different heights above the burner top edge. The flame topology is discussed thanks to the computed positions of the mean flame brush, as well as to the analysis of radial profiles of relevant measured scalars. The flame structures are discussed through the analysis of instantaneous 1D profiles of key scalars measured in several locations. Moreover, a multiple

conditional analysis is performed on the data set, and a comparison with the flamelet model is proposed. From the comparison, it is highlighted that the flamelet model well reproduces the evolution of key scalars in the different thermochemical states. At the same time, it is noted that quantitative differences are present, and are justified by the effects of preferential diffusion, based on the analysis conducted on similar configurations. It is possible to conclude that the investigated flame belongs to the flamelet regime of the turbulent premixed combustion, as identified in the so-called "Borghi diagram" [55,56], even if differences are observed due to effects of preferential diffusion.

In the last part of the thesis, preliminary results for Fl.D are shown, from two of the six investigated planes of the flame. The similar inlet compositions of the two flames allow for a comparison of the effects induced by the different shear present on the two flames. More in detail, in Fl.D a high shear exists between the different flows composing the jet, which is not present instead for Fl.C. Similar analysis presented for Fl.C is applied for Fl.D, resulting in comparable results for the two flames. It is also highlighted that the strain induced by the high shear is responsible of a modification of the conditional distributions of key scalars for Fl.D. Additional analysis are suggested to address the reasons of inconsistencies found in the other axial locations where the experimental investigation of Fl.D has been performed.

Outlook

The developed modified routine is flexible to applications with different fuels, within the limits of its original version [24, 65]. Moreover, it does not depend on the test rig setup, e.g. on the calibration burner configurations. Testing with different fuels has not being conducted within this work, and is suggested for future applications, together with additional burners configurations.

Regarding the physical phenomena treated in this thesis, several aspects still require further investigations, which could be conducted with the instantaneous multi-scalar technique applied throughout this work. For example, the considerable impact of the preferential diffusion, which has been observed in the discussion in chapter 5, has to be carefully taken into account when adding hydrogen to the fuel in the mixture. The strategy of H_2 addition is of great interest in turbulent combustion because it allows for using considerably lean mixtures [93, 94], with benefits on the pollutant emissions. Investigations on these configurations have been conducted, e.g. by Schneider et at. on stratified turbulent cases [17]. The valuable quantity of information that simultaneous single shot 1-D Raman/Rayleigh can provide would be beneficial for a better understanding of the effects connected to H_2 addition to the fuel in the mixture.

The potentiality of Raman/Rayleigh spectroscopy could also be of great advantage in investigating turbulent combustion regimes significantly far from the flamelet, e.g. the broken reaction zone (sec.2.3.3).

Moreover, in the context of the energy mix presented in the introduction to this thesis, and considering the fundamental role of (turbulent) combustion in modern technological applications, the use of renewable fuels, such as "biofuels", is of high interest [3]. Single shot Raman/Rayleigh would allow for gaining important insights in the combustion physics of these fuels, e.g. contributing to the understanding of

the flame structures, but also providing experimental database for the validation of combustion models and chemical schemes developed for simulations [6].

Appendix A

Newton and Quasi-Newton methods in 1-D

Explaining the Newton and quasi-Newton methods in a single variable case might come very helpful to fully understand the results of the methods in a multi-variable case. The key ideas at the base of the two methods are:

1. Using the first order necessary condition to find a minimum, i.e. the function derivative (gradient, in N-D) has to be null. In other words, the goal is to find the zero of the objective function first derivative.

2. To find the zero of the first derivative, the latter is approximated at each iteration with its tangent (Newton) or secant (quasi-Newton).

A basic explanation of the Newton method is shown in fig.A.1a. The first derivative f' of the objective function f is called $y(x)$, i.e. $y(x) \equiv f'$. When the algorithm is at the generic iteration k, to find x_{k+1} using the Newton method first one has to write the tangent $t(x)$ to $y(x)$ in x_k:

$$t(x) = y(x_k) + y'(x_k)\,(x - x_k) \tag{A.1}$$

The point x_{k+1} is set in the zero of $t(x)$, then:

$$t(x) \stackrel{!}{=} 0 \;\Rightarrow\; y(x_k) + y'(x_k)\,(x - x_k) = 0 \;\Rightarrow\; x_{k+1} = x_k - \frac{y(x_k)}{y'(x_k)} \tag{A.2}$$

Remembering that $y(x) \equiv f'$ it follows that, expressing the formula for the objective function:

$$x_{k+1} = x_k - \frac{f'(x_k)}{f''(x_k)} \tag{A.3}$$

The algorithm will proceed computing the tangent in x_{k+1} and finding its zero in x_{k+2}.

To approximate at each iteration the function whose zero has to be found, the quasi-Newton method uses the secant instead of the tangent, as it can be seen in fig.A.1b. If again the first derivative of f is called $y(x) \equiv f'$, its secant at the points x_k and x_p may be written as

$$s(x) = y(x_k) + \frac{y(x_k) - y(x_p)}{x_k - x_p}\,(x - x_k) \tag{A.4}$$

It follows then:

$$s(x) = 0 \;\Rightarrow\; y(x_k) + \frac{y(x_k) - y(x_p)}{x_k - x_p}\,(x - x_k) = 0 \;\Rightarrow\; x_{k+1} = x_k - \frac{y(x_p)}{(y(x_k) - y(x_p)) \;/\; (x_k - x_p)} \tag{A.5}$$

and changing back the formula in terms of objective function f:

$$x_{k+1} = x_k - \frac{f'(x_p)}{(f'(x_k) - f'(x_p)) \;/\; (x_k - x_p)} \tag{A.6}$$

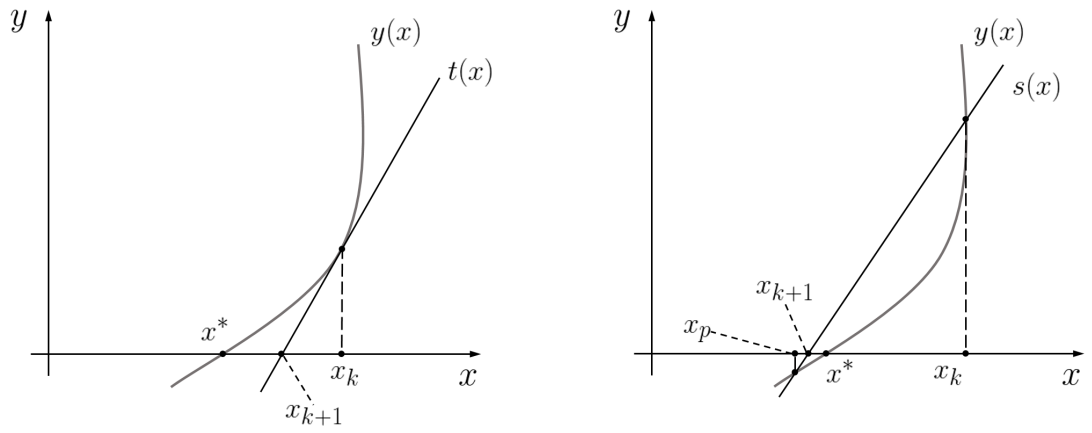

(a) Newton **(b)** Quasi-Newton

Figure A.1: Representation of the Newton and quasi-Newton method: to find the zero of $y(x)$, an iterative procedure is used approximating the function at each step with its tangent (a) or secant (b).

It is then very clear, comparing eq.(A.3) and eq.(A.6), that the advantage of the quasi-Newton method respect to the Newton method, is that for the quasi-Newton there is no need to compute the second derivatives. One can notice, indeed, that the second terms at the rhs of the two equations are the same, except for the difference that the second derivative present in eq.(A.3) is substituted with a combination of information from the first derivative. This substitution is the 1-D case of the more general reported in eq.(4.14).

The relation with the multidimensional case is already clear with the analogies between derivatives and gradient / hessian, but is even more evident if one notices that it is possible to obtain the same result of the Newton method, in (A.3), by setting to zero the derivative of a second order Taylor approximation of f, as done with the expression in eq.(4.12) for the multidimensional Newton method.

Constrained Optimization

When the problem presents constraints, as shown in the general structure (4.1), specific treatment is required to limit the search of the optimum within the limits imposed. A first procedure usually applied sees the inequality constraints translated into equality constraints, using some proper slack variables, say b_i:

$$g_i(\boldsymbol{x}) < 0 \;\Rightarrow\; g_i(\boldsymbol{x}) = b_i \quad \text{with} \quad b_i < 0 \tag{A.7}$$

For this reason it is possible to focus on optimization problems constrained by only equalities.

An important concept to introduce is the so called "Lagrangian function", L. The use of this function comes from the fact that "at any local optimum of any equality constrained NLP involving smooth functions" [74], must hold the relation:

$$\nabla f(\boldsymbol{x}^*) + \boldsymbol{\lambda}^* \nabla h(\boldsymbol{x}^*) = 0$$

which means that, at a local optimum, the objective function gradient and the constraint gradient are collinear, but point into opposite directions. Also, the two might be scaled by a scalar λ, called "Lagrangian multiplier". Defining the Lagrangian function as:

$$L(\boldsymbol{x}, \boldsymbol{\lambda}) = f(\boldsymbol{x}) + \lambda\, h(\boldsymbol{x}) \tag{A.8}$$

the previous relation between the gradients becomes:

$$\nabla_x L(\boldsymbol{x}, \boldsymbol{\lambda})|_{(\boldsymbol{x}^*, \boldsymbol{\lambda}^*)} = 0 \tag{A.9}$$

The relation expressed in (A.9), together with the feasibility condition $h(\boldsymbol{x}) = 0$ represent the first order necessary condition for constrained optimization.

As an example, in [74] given a NLP with m constraints and n variables written as

$$\min_{\boldsymbol{x}} f(\boldsymbol{x}) \quad \text{with} \quad h_j(\boldsymbol{x}) = b_j\,;\; j = 1, \ldots, m \tag{A.10}$$

where $x = \{x_1, x_2, \ldots, x_n\}$ and each b_j is a constant, the Lagrangian function is formulated as

$$L(\boldsymbol{x}, \boldsymbol{\lambda}) = f(\boldsymbol{x}) + \sum_{j=1}^{m} \lambda_j \left[h_j(\boldsymbol{x}) - b_j\right] \tag{A.11}$$

An inequality constraint is said to be "active" when the problem solution lies on the constraint[1]. With that being said, it is possible to state the so called "Kuhn-Tucker conditions" by saying that if inequality constraints are present, it is possible to verify [74] that at $\boldsymbol{x}^*$, ∇f lies within the space generated by the negative gradients of the active constraints. In formula this can be expressed by

$$\nabla f(\boldsymbol{x}^*) = \sum_{j=I} u_j^* \left[-\nabla g_i(\boldsymbol{x}^*)\right] \tag{A.12}$$

where u_j^* are non negative scalars and I is the set with all the indexes of the active constraints. It is then possible to write a Lagrangian function, when both inequality and equality constraints are present:

$$L(\boldsymbol{x}, \boldsymbol{\lambda}, \boldsymbol{u}) = f(\boldsymbol{x}) + \sum_{i=1}^{m} \lambda_i \left[h_i(\boldsymbol{x}) - b_i\right] + \sum_{j=1}^{r} u_j \left[g_j(\boldsymbol{x}) - c_j\right] \tag{A.13}$$

Flame C Atom Ratio Plots

In fig.A.2 scatter plots of relevant Fl.C atom ratios are shown. The database is conditioned on $\phi = 0.95 \pm 0.05$ and the ratios are plotted in the temperature space at $z = 60$ mm and $z = 120$ mm. The red line shows results from the laminar flamelet calculation,

[1] When the constraint is not a strict inequality, in which the points on the feasible domain limit are not included into the set of the feasible solutions.

green markers are conditional means over 200 K T-binning. As discussed in sec.5.2.5, an increase in the ratios is observed in the products respect to the reactants, at the lower axial locations of the flame. At z = 60 mm the computed increases are: C/N = 7%; C/H = 5%; C/O = 3%. As discussed in the mentioned sections, with increasing height (z = 120 mm) the increase is less evident.

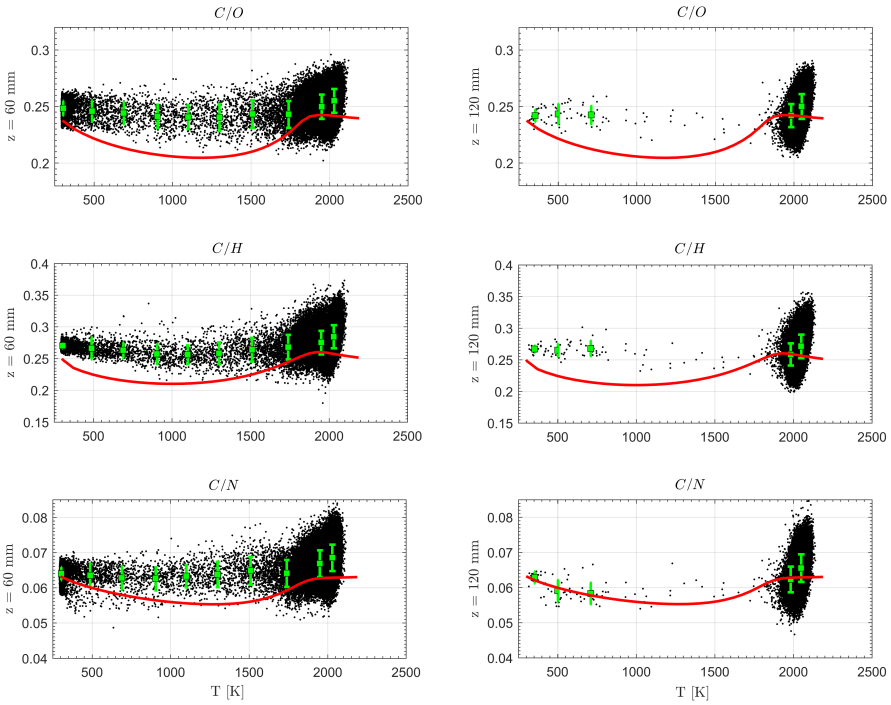

Figure A.2: Fl.C scatter plot of relevant atom ratios in the temperature space. The database is conditioned on ϕ = 0.95 ± 0.05. The red solid line reports the results of laminar flamelet calculations. Green squares and bars are mean and standard deviation computed over a 200 K binning.

Abstract

Keywords: Optimization; Combustion; Data.

A variety of technical applications in energy conversion are based on turbulent combustion, which has a crucial role in terms of design, control and safety. Despite the advanced contest of operation, (turbulent) combustion science is at a relatively young stage.

Detailed investigations of benchmark flames are essential to achieve a better understanding of the physics behind the mentioned processes, as well as to provide reliable database for validating numerical models developed to simulate turbulent combustion problems. Raman/Rayleigh spectroscopy is a highly valuable technique which allows to access simultaneous information on temperature and main chemical species concentration within the flame structures. The data reduction strategy applied with this technique is crucial, in order to extract reliable information from the experimental investigations. For this purpose, the hybrid data reduction and calibration strategy has been developed by Fuest et al. which to a large extent is empirical, time-consuming and presumes specific expertise.

In this thesis, a modified version of the calibration procedure is proposed. It is based on optimization techniques applied to solve a nonlinear programming (NLP) problem. The calibration system characterization highlights that the use of global optimization methods is fundamental to identify the global optimal solution. After reviewing various algorithms, a genetic algorithm is selected as best option to solve the NLP problem. Implementation and performance of the modified routine are proven in different test cases, demonstrating its ability to effectively identify an optimal solution to the NLP. Moreover, several advantages respect to the previous version are noted. The intrinsic automated nature of the modified routine removes the empiricism previously present in the calibration system. A significant reduction of the time needed for the problem solving is obtained. The user's expertise necessary to finalize the calibration is drastically reduced.

The modified routine has been applied to calibrate the data processing system for a data set provided by an experimental investigation of two turbulent premixed methane/air jet flames, Fl.C and Fl.D. The data set is composed by multiple scalars, including major species and temperature, simultaneously measured with single shot 1D Raman/Rayleigh spectroscopy.
Data from six planes located at different heights above the burner top edge reveal several Fl.C characteristics. The flame topology is analyzed thanks to the computed positions of the mean flame brush and to the analysis of radial profiles of relevant measured scalars. The flame structures are discussed by means of the analysis of

instantaneous 1D profiles of key scalars. Moreover, a multiple conditional analysis is performed on the data set, and a comparison with the flamelet model is proposed. From the comparison, it is highlighted that the flamelet model well describes the conditional distributions of key scalars. At the same time, it is noted that quantitative differences are present in the scalars distributions in the temperature space, which are justified by the effects of preferential diffusion, based on studies available in literature for similar configurations. It is possible to conclude that the investigated flame belongs to the flamelet regime of the turbulent premixed combustion.

Fl.D presents the same inlet composition of Fl.C, but differs from the latter for the presence of high shear between the coaxial flows composing the jet. Preliminary results from selected Fl.D planes show that the flame is in a combustion regime similar to the one of Fl.C. It is also highlighted that the strain induced by the high shear is responsible of a modification of the conditional distributions of key scalars for Fl.D. Additional analysis are suggested to address the reasons of inconsistencies found in some Fl.D axial locations.

German Abstract

Schlüsselwörter: Optimierung; Verbrennung; Daten.

Eine Vielzahl von technischen Anwendungen in der Energiekonversion basiert auf der turbulenten Verbrennung. Dies spielt bei der Auslegung, der Steuerung und der Sicherheit dieser Applikationen eine entscheidende Rolle. Obwohl technische Systeme auf Grundlage turbulenter Verbrennungsprozesse seit langer Zeit eingesetzt werden, ist das Verständnis der turbulenten Verbrennung noch in einem relativ frühen Stadium.

Um ein besseres Verständnis der zugrunde liegenden physikalisch-chemischen Prozesse zu entwickeln, ist die detaillierte experimentelle Untersuchung von generischen Flammen essentiell, die wichtige Eigenschaften technischer Prozesse abbilden. Neben dem erforderlichen Prozessverständnis kann außerdem eine Datenbasis für die Validierung von numerischen Modellen, mit welchen die turbulenten Verbrennungsprozesse bei der Auslegung simuliert werden, bereitgestellt werden. Um insbesondere Informationen über den thermochemischen Zustand turbulenter Verbrennungsprozesse zu erhalten, ist die Raman/Rayleigh-Spektroskopie eine einzigartige Messtechnik, welche lokal die simultane Messung von Temperatur und Hauptspezieskonzentrationen auch innerhalb der Flammenstruktur ermöglicht.
Innerhalb der Raman/Rayleigh-Spektroskopie ist eine geeignete Datenreduktionsstrategie essentiell, um die gewünschte Information verlässlich aus den Messdaten zu extrahieren. Die bisher in diesem Kontext von Fuest et al. entwickelte hybride Datenreduktions- und Kalibrationsstrategie folgt einer empirischen Vorgehensweise, die zeitaufwändig ist und in besonderem Maße Expertenwissen voraussetzt.

In der vorliegenden Arbeit wird deshalb eine modifizierte Version der Kalibrationsprozedur vorgestellt. Sie basiert auf Optimierungstechniken für die Lösung von *Non Linear Programming Problems* (NLP). Die Charakterisierung des Kalibrationssystems zeigt auf, dass die Nutzung von globalen Optimierungstechniken für die Identifizierung einer global optimalen Lösung von besonderer Wichtigkeit ist. Nach einem Vergleich existierender Algorithmen wird ein generischer Algorithmus ausgewählt, der am Besten für die Lösung des NLP Problems geeignet ist. Die Implementierung und die Leistung der modifizierten Routine werden in verschiedenen Testfällen geprüft, um die Eignung für die effektive Identifizierung einer optimalen Lösung des NLP zu verifizieren. Darüber hinaus werden einige Vorteile gegenüber der bisherigen Version vorgestellt. Der intrinsisch automatisierte Charakter der modifizierten Routine verhindert das bisher empirische Vorgehen. Zusätzlich wird der Prozess deutlich beschleunigt und für die Anwendung der Routine wird kein besonderes Expertenwissen benötigt.

Die modifizierte Routine wurde genutzt, um eindimensionale Raman/Rayleigh-

Einzelschussmessungen von zwei turbulenten vorgemischten Methan/Luft Jet-Flammen, Flamme C (Fl.C) und Flamme D (Fl.D), auszuwerten. Es wurden sechs Ebenen verschiedener Höhen über dem Brenneraustritt untersucht. Flammentopologien wurden anhand der zeitlich gemittelten Flammenposition (engl. Flamebrush) sowie der Analyse der radialen Konzentrationsprofile analysiert. Lokale Flammenstrukturen wurden unter Nutzung der instantanen 1D-Profile untersucht. Im Rahmen einer doppelt-konditionierten Auswertung wurden die Flammenstrukturen mit dem Flamelet-Modell verglichen. Für die Flamme Fl.C. zeigt sich generell eine gute Übereinstimmung, wobei die beobachteten Unterschiede bei einer Auftragung im Zustandsraum auf Einflüsse der präferentiellen Diffusion hindeuten. Diese Beobachtungen werden im Kontext anderer Studien diskutiert. Aus diesen Ergebnissen ergibt sich, dass die Flamme Fl.C. innerhalb des Regime-Diagramms vorgemischter turbulenter Flammen in das Flamelet-Regime eingeordnet werden kann.

Die Flamme Fl.D besitzt am Einlass dieselbe Gaszusammensetzung wie Fl.C, aber unterscheidet sich in Folge unterschiedlicher Einströmgeschwindigkeiten durch starke Scherung zwischen den koaxialen Jets. Vorläufige Ergebnisse ausgewählter Messpositionen zeigen, dass die Flamme trotz hoher Scherraten in einem ähnlichen Regime wie Fl.C. brennt. Es wird aufgezeigt, dass die durch die hohe Scherung induzierte Streckung für die Änderung der konditionierten Verteilungen einiger chemischer Spezies verantwortlich ist. Diese Untersuchungen sind jedoch noch nicht abgeschlossen und bedürfen einer weitergehenden Untersuchung.

French Abstract

Mots clés: Optimisation; Combustion; Data.

Nombreuses applications techniques sont basées sur la combustion turbulente, qui joue un rôle crucial en termes de conception, de contrôle et de sécurité.

Des études détaillées des flammes de référence sont essentielles pour mieux comprendre la physique sous-jacente aux processus mentionnés, ainsi que pour fournir une base de données permettant de valider les modèles numériques développés pour simuler des problèmes de combustion turbulents. La spectroscopie Raman/Rayleigh est une technique utile qui permet d'accéder simultanément à des informations sur la température et la concentration en espèces chimiques principales au sein des structures de flammes.
La data reduction strategy appliquée avec cette technique est cruciale pour extraire des informations fiables des investigations expérimentales. À cette fin, la *hybrid data reduction strategy* a été développée par Fuest et al. et son efficacité dépend fortement du bon étalonnage du système utilisé pour le traitement des données.

Dans cette thèse, une version modifiée de la procédure d'étalonnage est proposée. Il repose sur des techniques d'optimisation appliquées pour résoudre un *non linear programming (NLP) problem*. La caractérisation du système d'étalonnage montre que l'utilisation de méthodes d'optimisation globales est fondamentale pour identifier la solution optimale globale. Après une comparaison avec les algorithmes disponibles, un algorithme génétique est sélectionné comme meilleure option pour résoudre le problème de la NLP. La mise en œuvre et les performances de la routine modifiée sont prouvées dans différents cas de test, démontrant ainsi sa capacité à identifier efficacement une solution optimale à la NLP. Plusieurs avantages par rapport à la version précédente sont notés. La nature automatisée de la routine modifiée supprime l'empirisme précédemment présent dans le système d'étalonnage. Une réduction significative du temps nécessaire à la résolution du problème est obtenue. L'expertise de l'utilisateur nécessaire pour finaliser l'étalonnage est également considérablement réduite.

La procédure modifiée a été appliquée pour l'étalonnage du système de data reduction pour des données expérimentales de deux jet flames pré-mélangées turbulentes de méthane/air, Fl.C et Fl.D. La base de données est composée de plusieurs scalaires, y compris les principales espèces et la température, mesurés simultanément avec la 1D *single-shot* spectroscopie Raman/Rayleigh.
Les données de six niveaux révèlent caractéristiques de la flamme. La topologie est analysée à l'aide des positions calculées du *mean flame brush*, ainsi que de l'analyse des profils radiaux des scalaires mesurés. Les structures de flammes sont

discutées au moyen de l'analyse des profils 1D instantanés de scalaires. Une *multiple conditional analysis* est effectuée sur les données et une comparaison avec le modèle Flamelet est proposée. La comparaison montre que le modèle Flamelet décrit bien les distributions conditionnelles des scalaires. Dans le même temps, il est noté que des différences quantitatives sont présentes dans les distributions scalaires dans l'espace de température, lesquelles sont justifiées par les effets de la diffusion préférentielle, sur la base des études disponibles dans la littérature pour des configurations similaires. La Fl.C étudiée appartient au régime Flamelet de la combustion pré-mélangée turbulente.

Fl.D présente la même composition de Fl.C, mais diffère de celle-ci par la présence d'un fort *shear* entre les flux coaxiaux composant le jet. Les résultats préliminaires montrent que Fl.D est dans un régime de combustion similaire à celui de Fl.C. Il est mis en évidence que la déformation induite par le fort *shear* est responsable d'une modification des distributions conditionnelles des scalaires pour Fl.D. Des analyses supplémentaires sont suggérées pour traiter les effets de le strain dans les configurations à haute Reynolds.

Bibliography

[1] Directorate-General for Energy. *EU energy in figures 2018*, volume 2018 of *Statistical pocketbook*. Publications office of the European Union, Luxembourg, 2018.

[2] V. Masson-Delmotte, P. Zhai, H. O. Pörtner, D. Roberts, J. Skea, P. R. Shukla, A. Pirani, W. Moufouma-Okia, C. Péan, R. Pidcock, S. Connors, J. B. R. Matthews, Y. Chen, X. Zhou, M. I. Gomis, E. Lonnoy, T. Maycock, M. Tignor, T. Waterfield. *Global warming of 1.5°C*. Special report. IPCC, [Geneva, Switzerland], 2018.

[3] Edenhofer, O., R. Pichs-Madruga, Y. Sokona, E. Farahani, S. Kadner, K., editor. *Climate change 2014: Mitigation of climate change Working Group III contribution to the Fifth Assessment Report of the Intergovernmental Panel on Climate Change*. Cambridge University Press, New York NY, 2014.

[4] Richard C. Flagan and John H. Seinfeld. *Fundamentals of air pollution engineering*. 1988.

[5] Norbert Peters. *Turbulent Combustion*. Cambridge University Press, Cambridge, 2000.

[6] Andrei Lipatnikov. *Fundamentals of premixed turbulent combustion*. Taylor & Francis, Boca Raton, FL, 2013.

[7] R. S. Barlow. Laser diagnostics and their interplay with computations to understand turbulent combustion. *Proceedings of the Combustion Institute*, 31(1):49–75, 2007.

[8] Kathleen M. Tacina and Werner J. A. Dahm. Effects of heat release on turbulent shear flows. part 1. a general equivalence principle for non-buoyant flows and its application to turbulent jet flames. *Journal of Fluid Mechanics*, 415:23–44, 2000.

[9] Mark S. Sweeney, Simone Hochgreb, M. J. Dunn, and R. S. Barlow. The structure of turbulent stratified and premixed methane/air flames i: Non-swirling flows. *Combustion and Flame*, 159(9):2896–2911, 2012.

[10] Gaetano Magnotti and R. S. Barlow. Effects of high shear on the structure and thickness of turbulent premixed methane/air flames stabilized on a bluff-body burner. *Combustion and Flame*, 162(1):100–114, 2015.

[11] Robert S. Barlow, Matthew J. Dunn, Mark S. Sweeney, and Simone Hochgreb. Effects of preferential transport in turbulent bluff-body-stabilized lean premixed ch4/air flames. *Combustion and Flame*, 159(8):2563–2575, 2012.

[12] F. Seffrin, F. Fuest, D. Geyer, and A. Dreizler. Flow field studies of a new series of turbulent premixed stratified flames. *Combustion and Flame*, 157(2):384–396, 2010.

[13] M. Mustafa Kamal, R. S. Barlow, and Simone Hochgreb. Conditional analysis of turbulent premixed and stratified flames on local equivalence ratio and progress of reaction. *Combustion and Flame*, 162(10):3896–3913, 2015.

[14] B. Bedat and R. K. Cheng. Experimental study of premixed flames in intense isotropic turbulence. *Combustion and Flame*, 100(3):485–494, 1995.

[15] Mark S. Sweeney, Simone Hochgreb, Matthew J. Dunn, and Robert S. Barlow. The structure of turbulent stratified and premixed methane/air flames ii: Swirling flows. *Combustion and Flame*, 159(9):2912–2929, 2012.

[16] A. R. Masri. Partial premixing and stratification in turbulent flames. *Proceedings of the Combustion Institute*, 35(2):1115–1136, 2015.

[17] S. Schneider, D. Geyer, G. Magnotti, M. J. Dunn, R. S. Barlow, and A. Dreizler. Structure of a stratified ch4 flame with h2 addition. *Proceedings of the Combustion Institute*, 2018.

[18] Olivier Gicquel, Nasser Darabiha, and Dominique Thévenin. Liminar premixed hydrogen/air counterflow flame simulations using flame prolongation of ildm with differential diffusion. *Proceedings of the Combustion Institute*, 28(2):1901–1908, 2000.

[19] Jacqueline B. Chen and Hong G. Im. Stretch effects on the burning velocity of turbulent premixed hydrogen/air flames. *Proceedings of the Combustion Institute*, 28(1):211–218, 2000.

[20] Katharina Kohse-Höinghaus, Robert S. Barlow, Marcus Aldén, and Jürgen Wolfrum. Combustion at the focus: laser diagnostics and control. *Proceedings of the Combustion Institute*, 30(1):89–123, 2005.

[21] A. R. Masri, R. W. Dibble, and R. S. Barlow. The structure of turbulent nonpremixed flames revealed by raman-rayleigh-lif measurements. *Progress in Energy and Combustion Science*, 22(4):307–362, 1996.

[22] D. Geyer, A. Kempf, A. Dreizler, and J. Janicka. Turbulent opposed-jet flames: A critical benchmark experiment for combustion les. *Combustion and Flame*, 143(4):524–548, 2005.

[23] R. S. Barlow, C. D. Carter, and Pitz R.W. Multiscalar diagnostics in turbulent flames. In K. Kohse-Höinghaus and J.B. Jeffries, editor, *Applied Combustion Diagnostics*, pages 384–407. Taylor & Francis, New York, 2002.

[24] F. Fuest. *1D Raman/Rayleigh-scattering and CO-LIF measurements in laminar and turbulent jet flames of dimethyl ether using a hybrid data reduction strategy.* Phd, 2011.

[25] G. Kuenne, Florian Seffrin, F. Fuest, T. Stahler, A. Ketelheun, D. Geyer, J. Janicka, and A. Dreizler. Experimental and numerical analysis of a lean premixed stratified burner using 1d raman/rayleigh scattering and large eddy simulation. *Combustion and Flame*, 159(8):2669–2689, 2012.

[26] Ewen Smith and Geoffrey Dent. *Modern Raman Spectroscopy - A Practical Approach*. John Wiley & Sons, Ltd, Chichester, UK, 2004.

[27] John R. Ferraro, Kazuo Nakamoto, and Chris W. Brown. *Introductory Raman spectroscopy*. Academic Press, Amsterdam and Boston, 2nd ed. edition, 2003.

[28] R. P. Feynman, R. B. and Leighton, and M. Sands. *The Feynman Lectures on Physics, Vol. I.* Addison-Wesley, 1963.

[29] Ronald K. Hanson, R. Mitchell Spearrin, and Christopher S. Goldenstein. *Spectroscopy and Optical Diagnostics for Gases*. Springer International Publishing, Cham, 2016.

[30] R. P. Feynman, R. B. and Leighton, and M. Sands. *The Feynman Lectures on Physics, Vol. II.* Addison-Wesley, Reading. reprinted, 1977.

[31] D. A. Long. *The Raman effect: A unified treatment of the theory of Raman scattering by molecules*. Wiley, Chichester, 2002.

[32] D. Geyer. *1D-Raman, Rayleigh experiments in a turbulent opposed-jet*. Phd thesis, TU Darmstadt, 2005.

[33] Gerhard Herzberg. *Molecular Spectra and Molecular Structure - Vol I*. Read Books Ltd, 2013.

[34] Gerhard Herzberg and Bryce L. Crawford. Infrared and raman spectra of polyatomic molecules. *The Journal of Physical Chemistry*, 50(3):288, 1946.

[35] Peter Larkin. *Infrared and Raman Spectroscopy: Principles and Spectral Interpretation*. Elsevier, 1st edition, 2011.

[36] Richard B. Miles, Walter R. Lempert, and Joseph N. Forkey. Laser rayleigh scattering. *Measurement Science and Technology*, 12(5):R33, 2001.

[37] T. Stahler, D. Geyer, G. Magnotti, P. Trunk, M. J. Dunn, R. S. Barlow, and A. Dreizler. Multiple conditioned analysis of the turbulent stratified flame a. *Proceedings of the Combustion Institute*, 36(2):1947–1955, 2017.

[38] C. DeMichelis. Laser induced gas breakdown: A bibliographical review. *IEEE Journal of Quantum Electronics*, 5(4):188–202, 1969.

[39] Jun Kojima and Quang-Viet Nguyen. Laser pulse-stretching with multiple optical ring cavities. *Applied Optics*, 41(30):6360, 2002.

[40] S. B. Pope. *Turbulent flows*. Cambridge University Press, Cambridge, 2000.

[41] C. Schneider, A. Dreizler, and J. Janicka. Fluid dynamical analysis of atmospheric reacting and isothermal swirling flows. *Flow, Turbulence and Combustion formerly: Applied Scientific Research*, 74(1):103–127, 2005.

[42] W. Meier, R. S. Barlow, Y.-L Chen, and J.-Y Chen. Raman/rayleigh/lif measurements in a turbulent ch4/h2/n2 jet diffusion flame: experimental techniques and turbulence–chemistry interaction. *Combustion and Flame*, 123(3):326–343, 2000.

[43] James R. Janesick. *Scientific charge-coupled devices*, volume PM83 of *SPIE Press monograph*. SPIE, Bellingham, WA, 2000.

[44] Thierry Poinsot and D. Veynante. *Theoretical and numerical combustion*. 3rd edition, 2011.

[45] J. Warnatz, U. Maas, and Robert W. Dibble. *Combustion: Physical and chemical fundamentals, modeling and simulation, experiments, pollutant formation*. Springer, Berlin and New York, 4th ed. edition, 2006.

[46] Chung K. Law. *Combustion physics*. Cambridge University Press, Cambridge, 2006.

[47] Irvin Glassman and Richard A. Yetter. *Combustion*. Academic, Amsterdam and London, 4th ed. edition, 2008.

[48] Octave Levenspiel. *Chemical reaction engineering*. Wiley, New York, 3rd ed. edition, 1999.

[49] U.S. Department Of Energy. *Thermodynamics, Heat Transfer, and Fluid Flow - Vol. 3*, volume 3 of *DOE Fundamentas Handbook*. U.S. Department Of Energy, 2016.

[50] Thierry Poinsot and D. Veynante. *Theoretical and numerical combustion*. Edwards, Philadelphia, 2nd ed. edition, 2005.

[51] Franciano Scremin Puhales, G. Demarco, Luis Gustavo Nogueira Martins, Otávio Costa Acevedo, G. A. Degrazia, Guilherme Sausen Welter, Felipe Denardin Costa, Gilberto Fernando Fisch, and Ana Cristina Avelar. Estimates of turbulent kinetic energy dissipation rate for a stratified flow in a wind tunnel. *Physica A: Statistical Mechanics and its Applications*, 431:175–187, 2015.

[52] Adam M. Steinberg and James F. Driscoll. Straining and wrinkling processes during turbulence–premixed flame interaction measured using temporally-resolved diagnostics. *Combustion and Flame*, 156(12):2285–2306, 2009.

[53] Nilanjan Chakraborty and R. S. Cant. Influence of lewis number on curvature effects in turbulent premixed flame propagation in the thin reaction zones regime. *Proceedings of the Royal Society A: Mathematical, Physical and Engineering Sciences*, 17(10):105105, 2005.

[54] Norbert Peters. Laminar flamelet concepts in turbulent combustion. *Symposium (International) on Combustion*, 21(1):1231–1250, 1988.

[55] Norbert Peters. The turbulent burning velocity for large-scale and small-scale turbulence. *Journal of Fluid Mechanics*, 384:107–132, 1999.

[56] R. Borghi, Michel Destriau, and Gérard de Soete. *Combustion and flames: Chemical and physical principles / Roland Borghi, Michel Destriau ; with the collaboration of Gérard de Soete ; translated from the French by Richard Turner*. Technip, Paris, 1998.

[57] S. Schneider. *Auswirkungen der Wasserstoff-Zumischung auf die Flammenstruktur turbulenter stratifizierter Methan-Luft-Flammen*. Phd, TU Darmstadt, 2017.

[58] M. Gregor and A. Dreizler. A quasi-adiabatic laminar flat flame burner for high temperature calibration. *Measurement Science and Technology*, 20(6):065402, 2009.

[59] R. Merkel. *Aufbau und Inbetriebnahme einer Verzögerungsstrecke für Laserpulse*. Master thesis, TU Darmstadt, 2017.

[60] Jun Zhao. Image curvature correction and cosmic removal for high-throughput dispersive raman spectroscopy. *Applied spectroscopy*, 57(11):1368–1375, 2003.

[61] K. Kohse-Höinghaus and J.B. Jeffries, editor. *Applied Combustion Diagnostics*. Taylor & Francis, New York, 2002.

[62] R. W. Dibble, S. H. Strner, A. R. Masri, and R. S. Barlow. An improved method of data aquisition and reduction for laser raman-rayleigh and fluorescence scattering from multispecies. *Applied Physics B Photophysics and Laser Chemistry*, 51(1):39–43, 1990.

[63] P. A. Nooren, M. Versluis, T. H. van der Meer, R. S. Barlow, and J. H. Frank. Raman-rayleigh-lif measurements of temperature and species concentrations in the delft piloted turbulent jet diffusion flame. *Applied Physics B: Lasers and Optics*, 71(1):95–111, 2000.

[64] V. Bergmann, W. Meier, D. Wolff, and W. Stricker. Application of spontaneous raman and rayleigh scattering and 2d lif for the characterization of a turbulent ch 4 /h 2 /n 2 jet diffusion flame. *Applied Physics B: Lasers and Optics*, 66(4):489–502, 1998.

[65] F. Fuest, R. S. Barlow, D. Geyer, F. Seffrin, and A. Dreizler. A hybrid method for data evaluation in 1-d raman spectroscopy. *Proceedings of the Combustion Institute*, 33(1):815–822, 2011.

[66] H. C. Cutcher, R. S. Barlow, G. Magnotti, and A. R. Masri. Turbulent flames with compositionally inhomogeneous inlets: Resolved measurements of scalar dissipation rates. *Proceedings of the Combustion Institute*, 36(2):1737–1745, 2017.

[67] R. S. Barlow, Gaetano Magnotti, Hugh C. Cutcher, and Assaad R. Masri. On defining progress variable for raman/rayleigh experiments in partially-premixed methane flames. *Combustion and Flame*, 179:117–129, 2017.

[68] Mark S. Sweeney, Simone Hochgreb, Matthew J. Dunn, and Robert S. Barlow. Multiply conditioned analyses of stratification in highly swirling methane/air flames. *Combustion and Flame*, 160(2):322–334, 2013.

[69] G. Magnotti, D. Geyer, and R. S. Barlow. Interference free spontaneous raman spectroscopy for measurements in rich hydrocarbon flames. *Proceedings of the Combustion Institute*, 35(3):3765–3772, 2015.

[70] A. Brockhinke, P. Andresen, and K. Kohse-Höinghaus. Double-pulse one-dimensional raman and rayleigh measurements for the detection of temporal and spatial structures in a turbulent h_2–air diffusion flame. *Optics Letters*, 21(24):2029, 1996.

[71] Michael Knapp, Andreas Luczak, Volker Beushausen, Werner Hentschel, Peter Manz, and Peter Andresen. Polarization separated spatially resolved single laser shot multispecies analysis in the combustion chamber of a realistic si engine with a tunable krf excimer laser. *Symposium (International) on Combustion*, 26(2):2589–2596, 1996.

[72] Friedrich Rabenstein and Alfred Leipertz. One-dimensional, time-resolved raman measurements in a sooting flame made with 355-nm excitation. *Applied Optics*, 37(21):4937, 1998.

[73] Sandra Hartl, D. Geyer, A. Dreizler, Gaetano Magnotti, R. S. Barlow, and Christian Hasse. Regime identification from raman/rayleigh line measurements in partially premixed flames. *Combustion and Flame*, 189:126–141, 2018.

[74] Jorge Nocedal and Stephen J. Wright. *Numerical optimization*. Springer series in operations research. Springer, New York, 1999.

[75] Stephen P. Boyd and Lieven Vandenberghe. *Convex optimization*. Cambridge University Press, Cambridge, 2004.

[76] Thomas F. Edgar, David Mautner Himmelblau, and Leon S. Lasdon. *Optimization of chemical processes*. McGraw-Hill chemical engineering series. McGraw-Hill, Dubuque, Iowa, 2nd ed. edition, 2000.

[77] Alan R. Parkinson, Richard J. Balling, and Jhon D. Hedengren. *Optimization Methods for Engineering Design: Applications and Theory*. Brigham Young University, 2013.

[78] J. E. Dennis and Robert B. Schnabel. *Numerical methods for unconstrained optimization and nonlinear equations*, volume 16 of *Classics in applied mathematics*. Society for Industrial and Applied Mathematics, Philadelphia, 1996.

[79] Stephen G. Nash and Ariela Sofer. *Linear and nonlinear programming*. McGraw-Hill series in industrial engineering and management science. McGraw-Hill, New York, [nachdr.] edition, 2003.

[80] The MathWorks Inc. Global optimization toolbox: User's guide: (r2016a).

[81] David E. Goldberg. *Genetic algorithms in search, optimization, and machine learning*. Addison-Wesley, Reading, Mass. and Wokingham, 1989.

[82] A. R. Conn, Nick Gould, and Ph. L. Toint. A globally convergent lagrangian barrier algorithm for optimization with general inequality constraints and simple bounds. *Mathematics of Computation*, 66(217):261–289, 1997.

[83] Andrew R. Conn, Nicholas I. M. Gould, and Philippe Toint. A globally convergent augmented lagrangian algorithm for optimization with general constraints and simple bounds. *SIAM Journal on Numerical Analysis*, 28(2):545–572, 1991.

[84] Thang Nguyen Bui and Byung Ro Moon. Genetic algorithm and graph partitioning. *IEEE Transactions on Computers*, 45(7):841–855, 1996.

[85] So-Jin Kang and Byung-Ro Moon, editors. *A Hybrid Genetic Algorithm for Multiway Graph Partitioning*, San Francisco, CA, USA, 2000. Morgan Kaufmann Publishers Inc.

[86] Sung-Soon Choi and Byung-Ro Moon. Normalization in genetic algorithms. In Erick Cantú-Paz, editor, *Genetic and evolutionary computation - GECCO 2003*, volume 2723 of *Lecture notes in computer science, v. 2723 0302-9743*, pages 862–873. Springer, Berlin, 2003 London.

[87] M. A. Gregor, F. Seffrin, F. Fuest, D. Geyer, and A. Dreizler. Multi-scalar measurements in a premixed swirl burner using 1d raman/rayleigh scattering. *Proceedings of the Combustion Institute*, 32(2):1739–1746, 2009.

[88] Florian Seffrin. *Geschwindigkeits- und Skalarfeld-Charakterisierung turbulenter stratifizierter Vormischflammen.* Phd, 2011.

[89] Benedetta Franzelli, Eleonore Riber, Laurent Y.M. Gicquel, and Thierry Poinsot. Large eddy simulation of combustion instabilities in a lean partially premixed swirled flame. *Combustion and Flame*, 159(2):621–637, 2012.

[90] Bo Zhou, Christian Brackmann, Zhenkan Wang, Zhongshan Li, Mattias Richter, Marcus Aldén, and Xue-Song Bai. Thin reaction zone and distributed reaction zone regimes in turbulent premixed methane/air flames: Scalar distributions and correlations. *Combustion and Flame*, 175:220–236, 2017.

[91] A. N. Lipatnikov and J. Chomiak. Molecular transport effects on turbulent flame propagation and structure. *Progress in Energy and Combustion Science*, 31(1):1–73, 2005.

[92] D. Geyer, M. Gregor, C. Schneider, A. Nauert, and A. Dreizler, editors. *Turbulent combustion: a challenge for laser diagnostics*, 2005.

[93] Fanhua Ma and Yu Wang. Study on the extension of lean operation limit through hydrogen enrichment in a natural gas spark-ignition engine. *International Journal of Hydrogen Energy*, 33(4):1416–1424, 2008.

[94] S. S. Shy, Y. C. Chen, C. H. Yang, C. C. Liu, and C. M. Huang. Effects of h2 or co2 addition, equivalence ratio, and turbulent straining on turbulent burning velocities for lean premixed methane combustion. *Combustion and Flame*, 153(4):510–524, 2008.

This project has received funding from the European Union's Horizon 2020 Programme for research, technological development, and demonstration under grant agreement no. 643134-CLEAN-Gas.